# Experimental Investigations of Core-Loc Armour Units

Adrian Raul Simpalean

Thesis submitted to the
Faculty of Graduate and Postdoctoral Studies
in partial fulfillment of the requirements for the degree of
Master of Applied Science in Civil Engineering

Academic advisors: Dr. Ioan Nistor and Dr. Andrew Cornett

University of Ottawa, Canada
Faculty of Engineering, Department of Civil Engineering
January 2019

# Abstract

Rubble mound breakwaters serve as the first line of defense against shoreline erosion and storm-induced flooding. Despite their vital importance in coastal areas, breakwater design guidelines currently lack a clear physically-based relationship between processes associated with wave induced flow through the structure`s armour layer, and corresponding hydrodynamic response. This has been the subject of many studies, however, the main challenge researchers face is evaluating the complex nature of wave induced loading on individual units. As a result, the current design provisions ignore the physical-based processes governing armour layer stability, and rely heavily on empirical constants derived from limited scaled laboratory tests and past design experience drawn from decades of trial-and error. The primary motivation for the current work is to help alleviate the aforementioned problem, by analyzing the primary destabilizing hydrodynamic forces of individual armour units occurring during wave action.

This research is part of an ongoing collaborative comprehensive research project, undertaken to generate new rubble mound structures practical design knowledge and tools. In the present study, the influence of geometric scale, unit orientation (alternatively, flow direction), and the dimensionless Reynold and Keulegan-Carpenter quantities on the hydrodynamic response of Core-Loc armour units is explored through a series of physical modelling tests under unsteady and oscillatory flow conditions. The standard hydrodynamic force model used in coastal engineering design is Morison equation, derived to estimate the drag and inertia force components on cylindrical structures in oscillatory flow. This study evaluates it`s applicability and limitations in estimating the hydrodynamic response of individual concrete armour units. A novel automated non-intrusive camera-based tracking system utilizing image processing techniques to track armour unit motion is presented, devised to obtain detailed kinematic analysis in unsteady flow conditions.

The forces and fluid kinematics measured during the experimental program are used to derive the drag and inertia force coefficients representative of the Core-Loc geometry, and evaluate their dependency on the Keulegan-Carpenter and Reynolds numbers, unit scale and orientation. The results showed significant differences in flow development and resistance experienced by specific Core-Loc orientations in similar flow conditions. This highlights the importance that placing patterns can have on the overall stability of an armour layer. Tests with different model scales indicated that as the scale increases and the flow conditions approach prototype conditions, the drag forces become predominant over inertia forces. The empirical force coefficient analysis showed good agreement with previous studies on the relative importance of drag forces over inertia forces in oscillatory flow for constant Keulegan-Carpenter numbers. The comparison of the measured forces and the Morison model, indicated that the model does not yield accurate estimates of the unit`s hydrodynamic response. The model underestimates the peak forces, with increasing inaccuracy as the flow transitions from inertia to drag dominated regime.

# Acknowledgements

This thesis is the result of research carried out at the Oceans, Coastal, and River Engineering Laboratory of the National Research Council of Canada (NRC-OCRE), and the University of Ottawa Hydraulic Laboratory (UO). I would like to use this opportunity to express my gratitude to everyone who supported me throughout this project. This study would not have been possible without the NSERC-CRD grant funding received for the project.

First and foremost, I would like to offer a sincere thanks to my academic supervisor, Dr. Ioan Nistor, who has constantly supported and steered me in the right direction throughout my master's degree. During the last two years, besides his technical knowledge and support, Dr. Nistor provided me with many opportunities to travel and work on different projects. He was a guide and a mentor throughout the entire process, providing me without exception any advice and resources needed to complete this project. Dr. Nistor`s passion for his students, his work ethic and attention to detail, without mentioning his technical background, motivated me to improve not only as a student but as a person.

Furthermore, I would like to thank my second supervisor, Dr. Andrew Cornett, for providing additional resources, facilities and personal time all essential for the completion of this study. Dr. Andrew`s experience in physical modelling was incredibly helpful and greatly improved the results of the project. I would also like to thank Seth Logan, who on behalf of Baird W.F. & Associates, provided unique insight and expertise in the area of rubble mound breakwater design and construction.

I would like to express my appreciation and gratitude for Steven Douglas and Derek Eden, my research partners, for their contributions and constant support during this unique experience. Without their help and input, this study would not have been successfully completed. I would also like to acknowledge personnel at NRC-OCRE, UO, the UO-Richard L`Abbe Makerspace members, and the Imperial College London (ICL) team members, who provided additional help and insight in the setup and running of the experiments.

Last but not least, I would like to thank my family and friends for their moral support during the difficult parts of my degree. I could not have asked to be part of a better team for this research study, and without them, none of the work conducted would have been possible.

Thank you!

# Table of Contents

# List of Figures

# List of Tables

# List of Symbols

## Latin Characters

| Symbol | Description | Unit |
|---|---|---|
| $H_s$ | Significant wave height | $m$ |
| $T_m$ | Mean wave period | $s$ |
| $T_p$ | Peak wave period | $s$ |
| $D$ | Water depth | $m$ |
| $L$ | Wave length | $m$ |
| $L_0$ | Deep water wave length | $m$ |
| $g$ | Gravitational acceleration | $m/s^2$ |
| $H_0$ | Deep water wave height | $m$ |
| $R_{u2\%}$ | 2% run-up height | $m$ |
| $q$ | Overtopping discharge | $m^3/s$ |
| $R_c$ | Relative armour crest level | $m$ |
| $z_A$ | Elevation referenced from the still water level | $m$ |
| $C_{v2\% \, or \, h2\%}$ | Empirical coefficients for velocity and flow thickness calculations | - |
| $H_{s,toe}$ | Significant wave height at the toe of the structure | $m$ |
| $C_T$ | Transmission coefficient | - |
| $C_r$ | Reflection coefficient | - |
| $H_i$ | Incident wave height | $m$ |
| $H_r$ | Reflected wave height | $m$ |
| $a, b$ | Empirical coefficients | - |
| W | Weight of the armour pieces | - |
| $N_a$ | Practical dimensionless coefficient | - |
| $K_d$ | Hudson`s dimensionless stability coefficient | - |
| $\Delta$ | Relative buoyant density of the rock | - |
| $D_{n50}$ | Nominal median diameter of armour blocks | $m$ |
| $W_{50}$ | 50% value of the mass distribution curve | $kg$ |
| $P$ | Core permeability factor | - |
| $S$ | Dimensionless damage level | - |
| N | Number of waves | - |
| $H_{2\%}$ | Largest 2% wave heights | $m$ |
| $V$ | Armour unit volume | $m^3$ |
| $C_L$ | Armor unit characteristic length | $m$ |
| $D_n$ | Equivalent cube unit size | $m$ |
| $n$ | Packing density | - |
| $N$ | Number of units | - |
| $F_g$ | Force of gravity | $N$ |
| $F_W$ | Friction force | $N$ |
| $F_i$ | Interlocking force | $N$ |
| $F_D$ | Drag force | $N$ |
| $F_I$ | Inertia force | $N$ |
| $F_L$ | Lift force | $N$ |

| | | |
|---|---|---|
| $F_B$ | Buoyant force | $N$ |
| $F_m$ | Measured force | $N$ |
| $F_H$ | Total hydrodynamic force | $N$ |
| $t$ | Time | $s$ |
| $u$ | Flow velocity | $m/s$ |
| $a$ | Flow acceleration | $m/s^2$ |
| $C_D$ | Drag force coefficient | - |
| $C_{Dp}$ | Prototype drag force coefficient | - |
| $C_M$ | Inertia force coefficient | - |
| $C_L$ | Lift force coefficient | - |
| $A$ | Unit total projected area perpendicular to the flow direction | $m^2$ |
| $n_L$ | Length scale factor | - |
| $Re$ | Reynolds number | - |
| $K_c$ | Keulegan-Carpenter number | - |
| $m$ | Mass | $kg$ |
| $x, y, z$ | Cartesian co-ordinate system | - |

## Greek Symbols

| Symbol | Description | Unit |
|---|---|---|
| $\beta$ | Wave angle of attack | $^o$ |
| $\gamma$ | Wave breaking index | - |
| $\xi_0$ | Surf similarity parameter | - |
| $\alpha$ | Slope angle | $^o$ |
| $\gamma_f$ | Slope roughness reduction factor | - |
| $\gamma_\beta$ | Oblique wave attack reduction factor | - |
| $\gamma_b$ | Bern effect reduction factor | - |
| $\gamma_f$ | Shape reduction factor | - |
| $\gamma_s$ | Safety factor | - |
| $\gamma_r$ | Specific weight of stone or rock | $kN/m^3$ |
| $\gamma_w$ | Specific weight of water | $kN/m^3$ |
| $\rho_r$ | Density of the rock | $kg/m^3$ |
| $\rho_w$ | Density of the water | $kg/m^3$ |
| $\rho_c$ | Density of concrete | $kg/m^3$ |
| $\phi$ | Packing density coefficient | - |
| $\mu_f$ | Friction coefficient | - |
| $\mu$ | Dynamic viscosity of the fluid | $Ns/m^2$ |
| $\nu$ | Kinematic viscosity of the fluid | $m^2/s$ |
| $\sigma$ | Error term | - |

## Mathematical Operators

| Symbol | Description |
|---|---|
| $\|\ \|$ | Absolute value |
| $\Delta \boldsymbol{d}$ | Change in parameter $d$ |
| $\equiv$ | Equivalent |
| $\int$ | Integral |
| $\boldsymbol{\partial / \partial t}$ | Partial derivative with respect to t |

## Abbreviations

| Symbol | Description |
|---|---|
| NRC | National research council Canada |
| OCRE | Ocean, coastal and river engineering |
| UO | University of Ottawa |
| NSERC | Natural sciences and engineering research council of Canada |
| CRD | Collaborative research and development grant |
| ICL | Imperial College London |
| CAU | Concrete armour unit |
| SWF | Steel wave flume |
| CIRIA | Construction industry research and information association |
| USACE | U.S. Army corps of engineers |
| WES | Waterways experiment station |
| CLI | Concrete layer innovations |
| SWL | Still water level |
| 3D/2D | Three and two dimensional |
| LS | Least squares |
| WLS | Weighted least squares |
| PVC | Polyvinyl chloride |
| FEM/DEM | Finite/Discrete element method |
| CAD | Computer-aided design |
| PLA | Polylactic acid |
| MP | Megapixel |
| FPS | Frames per second |
| LED | Light-emitting diode |
| RGB | Red, Green and Blue – color model |
| SXOX | Scale x, Orientation x |
| AWA | Active wave absorption |
| GDAC | Data acquisition and control system |
| NDAC | Laboratory data acquisition and control software |
| GEDAP | Data analysis software package |
| WG | Wave gauge |
| DAQ | Data acquisition |
| ADV | Acoustic Doppler velocimetry |
| CSV | Comma-separated values |
| Q-Q | Quantile-Quantile |

# Chapter 1 Introduction

## 1.1 Research Background

With the average population density in coastal regions three times higher than the global average and with significant anticipated climate-related changes, mitigation procedures for coastal damage due to intensification and increased frequency of extreme natural events is paramount to engineers and coastal zone planners. Buildings codes or guidelines that contain design criteria and provisions for wave induced loading are either limited, outdated or rarely implemented for the design of coastal defense structures. Although breakwaters serve as the first line of defense against shoreline erosion and storm-induced flooding, they are currently designed using the same procedure as 50 years ago and the current design prescriptions are based on limited laboratory tests findings and decades of trial-and-error. These structures are typically built as multilayered systems of various-sized rock, commonly referred to as rubble mound structures (see Figure 1-1). The core is the innermost layer forming the bulk of the structure and is made from quarry run or gravel. To protect the core, one or more filter layers are typically installed. These are built with larger size stone, providing a more efficient transition between the finer core and the outer layer. The outermost layer is the most important component of the breakwater, providing protection to the under-layer by dissipating wave energy through the porous armoring made of natural rocks or concrete armour units (CAUs) massive enough to withstand wave action. The current breakwater design approaches are based on simplified empirical constants, neglecting the actual physical processes associated with the hydraulic stability of the main armour layers, and thus, limiting the range of conditions to which a design can be applied.

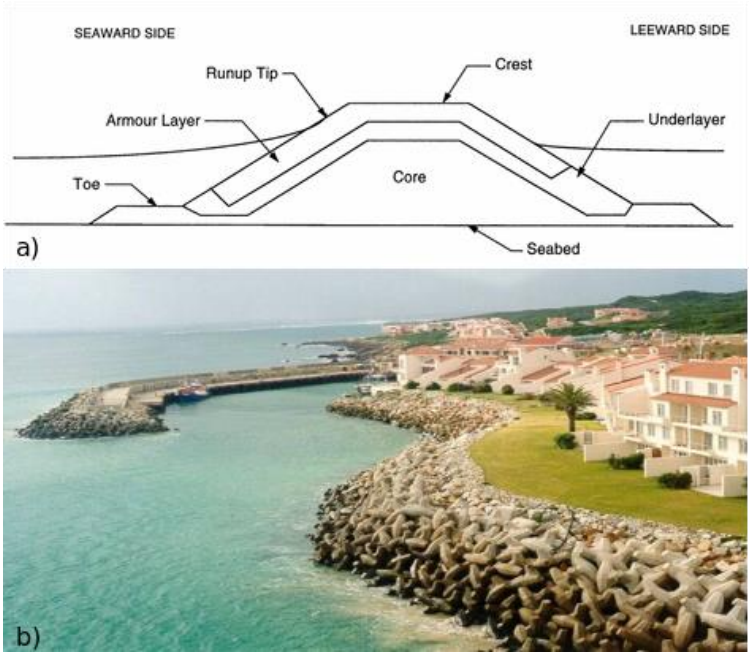


Figure 1-1: Rubble mounds breakwaters. (a) Typical cross section (Palmer and Christian, 1998); (b) Breakwater in Port St. Francis, South Africa (Core-Loc Africa, n.d.).

A conducted literature review revealed gaps in the current breakwater design techniques. The parameters of concern during design are run-up and run-down levels on the seaward face of the structure, which determine the transmission, the reflection, the overtopping levels, and the armour layer size required to withstand the given wave conditions. These parameters are generally limited by safety criteria for a case-to-case basis. Although the factors that influence these levels are determined and understood, no physical relation is present in the current breakwater design provisions. The latest formulas given in the EurOtop Manual (2016) account for the effects of various armour layer configurations using empirically derived reduction factors. In an attempt to narrow the knowledge gap, the study is focused on investigating and quantifying the primary armour layer destabilization forces, which are the drag, inertia and lift forces that occur during wave run-up and run-down.

A series of detailed experimental investigations were designed at University of Ottawa Hydraulic Laboratory (UO) and National Research Center -Ocean, Coastal and River Engineering Research Center (NRC-OCRE), to investigate the hydrodynamics of Core-Loc armour units under different flow conditions. The analysis focused on extracting the drag and inertia force coefficients for different model scales and unit orientations. Additionally, the influence of geometric scale, Reynold`s number, and unit orientation on the individual armour unit`s hydrodynamic loading was investigated. The research project has been conducted as part of a joint academic-industry collaborative project between UO, NRC-OCRE, and Bairds W.F. & Associates consulting firm, co-funded by NRC and an NSERC-CRD grant. Another partner of this research endeavor is Imperial College London (ICL), London, UK, which over the past few years conducted similar work from a numerical modeling perspective. The goal of the research program is the design of a detailed experimental investigation that can be used to quantify spatial and temporal hydrodynamic patterns and structural responses of armour units during wave actions. The study will be used for the implementation and validation of a multi-body dynamics numerical model with novel capabilities for simulating the behavior of armour unit layers under wave action, undertaken by ICL (Figure 1-2).

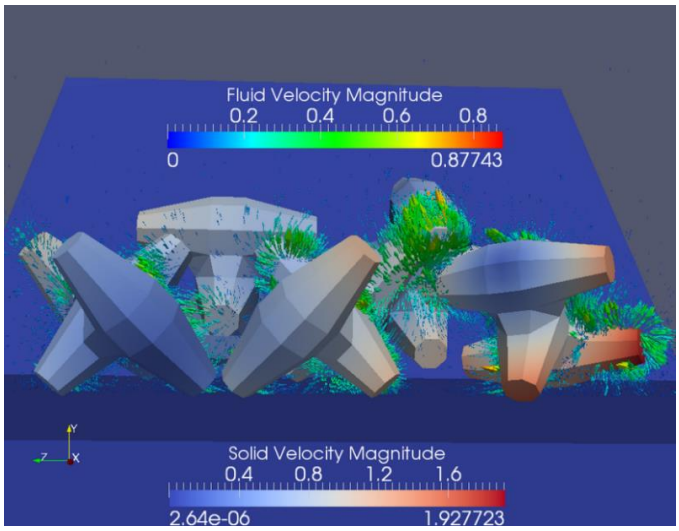


Figure 1-2: Two-way coupled motion of Core-Loc units modelled with Y3d/Fluidity (Milthaler et al., 2013).

The successful development and validation study of the numerical model will aid ICL in further developing the first practical rubble mount breakwater design tool that will accurately reflect real physical processes associated with rubble mound breakwater stability. Additionally, several aspects concerning the design and construction of rubble mound breakwaters will be experimentally investigated. The long-term value of the research is that it will one day enable coastal engineers to design concrete armour units and breakwaters both more efficient and with a greater level of confidence than has been previously possible. The proposed project will also narrow the knowledge gap in structural engineering when it comes to breakwater design, as the physics-based processes associated with breakwaters layer stability will be investigated and quantified. Ultimately, the concepts, methods and tools developed during the research project will be used to develop new standards and guidelines for the design and construction of rubble mound coastal protection structures, after being reviewed by pertinent committees.

## 1.2 Objectives and Research Needs

Before optimizing the construction and design of breakwater, the relationships between the processes associated with hydrodynamic forces exerted on the individual armour units of the breakwater layers must be well understood. Breakwater design guidelines currently lack a clear physically-based relationship between processes associated with wave induced flow through the armour layers, hydrodynamic loading, and the resultant armour units' response. Therefore, a comprehensive experimental investigation of the drag and inertia forces, which are the primary destabilization forces acting on individual armour units is required. In this study, the influence of geometric scale, Reynold's number, and unit orientation (alternatively, flow direction) on the hydrodynamics and response of Core-Loc armour units, in unsteady and oscillatory flow conditions, are explored through a series of physical modeling tests.

**Experiment 1**

To assess the flow development around Core-Loc armour units, a series of controlled hydrodynamic drop tests were designed and performed at University of Ottawa. The study outlines a simple and cost-effective method to extract accurate estimates for the drag and inertia force coefficients of Core-Loc armour units that can be easily extended to other geometric shapes.

The main focus of the experiments was to evaluate the effect of varying geometric scale, unit orientation, and flow velocity on the hydraulic response of Core-Loc armour units. Four geometric scales and unit orientations were examined in this study. To simulate a full-range of flow velocities, four different volume-averaged unit densities were considered. The second objective of the study was to develop a novel and non-intrusive displacement tracking system to obtain the displacement, velocity, and acceleration time histories of free falling Core-Loc units through a column of water. The results were used to optimize the balance of the forces acting on the falling unit and extract the drag and inertia force coefficients using Morison`s predictions of the total hydrodynamic force acting on a submerged object.

**Experiment 2**

The second experiment was focused on the hydrodynamic analysis of Core-Loc armour units under oscillatory flow conditions. The experiments were performed in the Steel Wave Flume (SWF) at the NRC-OCRE. Preliminary analysis of the results from the first experiment indicated different development of flow around different Core-Loc orientations. Therefore, the study was focused on three additional unit orientations. The main objective of the study was to examine the effect of different wave conditions on the unit response and the drag and inertia force coefficients. Using two geometric scales, seven Core-Loc orientations were examined. For this study, only regular wave conditions were analyzed.

Both studies will summarize discrepancies in the incoming flow development around different Core-Loc armour unit orientations and scales, and therefore their stability. Additionally, the analysis will assess Morison`s equation applicability and limitations in predicting the CAUs response under wave-loading. The results will be beneficial in the evaluation of force distribution inside a pack of units build on a slope, where specific orientations should be treated separately.

## 1.3 Novelty and Contribution of the Study

When designing a breakwater, the primary concern is the stability of the armour layer on the seaward side of the structure. A reasonable approach to design the armour layer would be based on force balance between the induced loading during wave action, and the forces that hold the individual armour units in place. Due to the complex flow development though the armour layer, the assessment of the hydrodynamic forces on individual armour units has been difficult, leading researchers to treat the armour system as a single structural component. It is for this reason that current design equations and provisions rely on empirical coefficients derived from limited scaled laboratory experiments, which neglect the actual forces that influence the stability of the armour layer. In this sense, the novelty of this work is primarily contained in the evaluation of the primary destabilizing forces during wave run-up on individual armour units. The work presented here is the first that examined the Core-Loc armour unit orientation effect on the flow development, and implicitly the drag and inertia forces. The experimental setting also allowed the analysis of other variables, such as scale effects, and different flow conditions.

Finally, the unique, non-invasive, and cost-effective methods used during this study to extract estimates of the hydrodynamic forces around Core-Loc units can be extended to other CAUs and hydraulic engineering applications. These methods are based on the semi-empirical Morison equation, traditionally used to estimate the wave loads on cylindrical piles.

## 1.4 Thesis Structure

This thesis has been divided into five chapters. Chapter 1 provides an introduction of the general setting of the research, outlining the motivations, objectives, and novelty of the work presented.

Chapter 2 presents an in-depth literature review of rubble mound breakwater design and hydrodynamic force coefficients. First, the literature review focuses on the hydrodynamic and structural parameters of interest for breakwater design, and their influence on the stability of the structure`s armour layer. The second part covers methods of estimating the forces acting on objects and armour units with respect to the surrounding fluid motion. This section will provide the necessary technical background used for this research, and identify the literature knowledge gaps on the topics.

Chapter 3 examines the results of the controlled drop tests performed at University of Ottawa. In this section, the analysis of the hydrodynamics effect of four geometric scales and armour unit orientations examined under different flow velocities are summarized. The same section covers the technical details of a non-invasive and cost-effective displacement tracking method developed.

Chapter 4 presents the results of the physical modelling performed in the SWF at NRC-OCRE. In this section, the experimental design details and fabrication of the model will be detailed. The results of the determined force coefficients are analyzed with respect to changing wave properties and armour unit orientations.

The results and analysis conclusions discussed in the previous chapters are summarized in Chapter 6, along with recommendations for future work.

# Chapter 2 Literature Review

## 2.1 Rubble Mound Breakwaters

Shoreline protection structures are primary build to change the effects of ocean waves, currents, and sediment transport in the near shore areas. Coastal structures that absorb wave energy and prevent erosion include revetments, sea walls, bulkheads, jetties, or breakwaters. These structures protect shore-based infrastructure, provide shore stability control, flood protection and stabilize navigation. Breakwaters reflect and dissipate the energy and force of waves and thereby reduce coastal erosion and provide safe harborage. According to their structural features, breakwaters can be classified into mound, monolithic, composite, and special types. Mound breakwaters are characterized by large heaps of elements such as gravel, quarry stone or concrete blocks. The stability of those breakwaters is governed by the size and relative density of the elements used during construction and the site wave conditions. These are the primary factors that determine the ratio between the applied and resisting load. Furthermore, mound breakwaters can be subcategorized into two main types: gravel or sandy beaches, and statically stable breakwaters, also known as rubble mound breakwaters, which counteract the wave forces using the weight of the elements in armour layer.

Rubble mound breakwaters are preferred over other types due to their higher energy dissipation as a result of the porous slope. To build such a structure a large quantity of rock materials of various grading and qualities is required. The natural stones are supplied from quarries, and due to the nature of their exploitation (blasting), the output creates discontinuous patterns of size and shape of the blocks used. This in turn affects breakwaters functionality and durability. Furthermore, using natural armour stones may not be the most cost-effective option. This shortcoming, lead to the creation of artificial concrete armour units (CAUs), having the advantage of unit interlocking with high permeability and porosity. Artificial blocks are also required when breakwater design requires heavier (<10-15 tons) rocks, which are hard to produce and supply in sufficient quantities by quarries.

## 2.2 Concrete Armour Units - CAUs

The first CAUs used in the construction of rubble mound breakwaters were the cubes. It was only after the Second World War when other shapes started to be introduced. Tetrapods were introduced in 1950 by the SOGREAH hydraulic laboratory of Dauphinois, shape that enabled better interlocking of the units, which in turn increased the porosity of the armour layer, decreased wave run-up, and as a results, increased wave energy dissipation. Many other concrete armour units were developed in time. A summary of the most popular CAUs is given in Figure 2-1, classified based on their placement and geometric properties, and their main stability contributor. The worldwide leading CAUs are the Accropode, Core-Loc and A-jack units. These units are used due to high interlocking mechanism and single layer use, which increases the breakwater`s hydraulic performance and decreases construction costs.

| Placement pattern | Number of layers | Shape | Stability factor (main contribution) | | |
|---|---|---|---|---|---|
| | | | Own weight | Interlocking | Friction |
| Random | Double layer | Simple | Cube, Antifer Cube, Modified Cube | | |
| | | | Tetrapod, Akmon, Tripod | | |
| | | Complex | | Stabit, Dolos | |
| | Single layer | Simple | Cube | | Cube |
| | | Complex | | Stabit, Accropode, Core-loc, Xbloc | |
| Uniform | Single layer | Simple | Haro | | Seabee, Haro |
| | | Complex | | | Cob, Shed, Tribar, Diode |

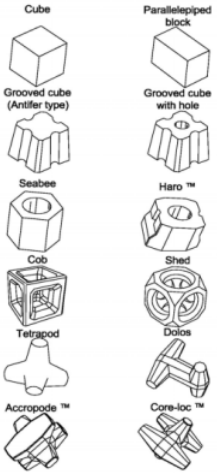


Figure 2-1: Breakwater concrete armour unit's classification by shape, placement and stability factor (adapted from CIRIA, 2007).

## Core-Loc Armour Units

Core-Loc armour units were developed as a result of research done in 1995 at the U.S Army Corps of Engineers (USACE) Waterways Experiment Station (WES) by Dr. Jeffrey Melby and Mr. George Turk. Core-Loc units are an advanced and refined version of the Accropode units, designed to be placed in a single layer, providing a cost-effective system for breakwater applications. Their design consists of symmetrically-tapered octagonal members, as shown in Figure 2-2(a), which allows a high degree of interlocking between units, while maintaining a high layer porosity. This provides a superior hydraulic stability of breakwaters constructed using Core-Locs. Until 2018, over 65 breakwater structures have been build using this CAU across the world (CLI, 2012). For this research, Core-Loc armour units were chosen as they are widely used in North America, and by the project`s industrial collaborator, Bairds W.F. & Associates (Figure 2-1(b)).

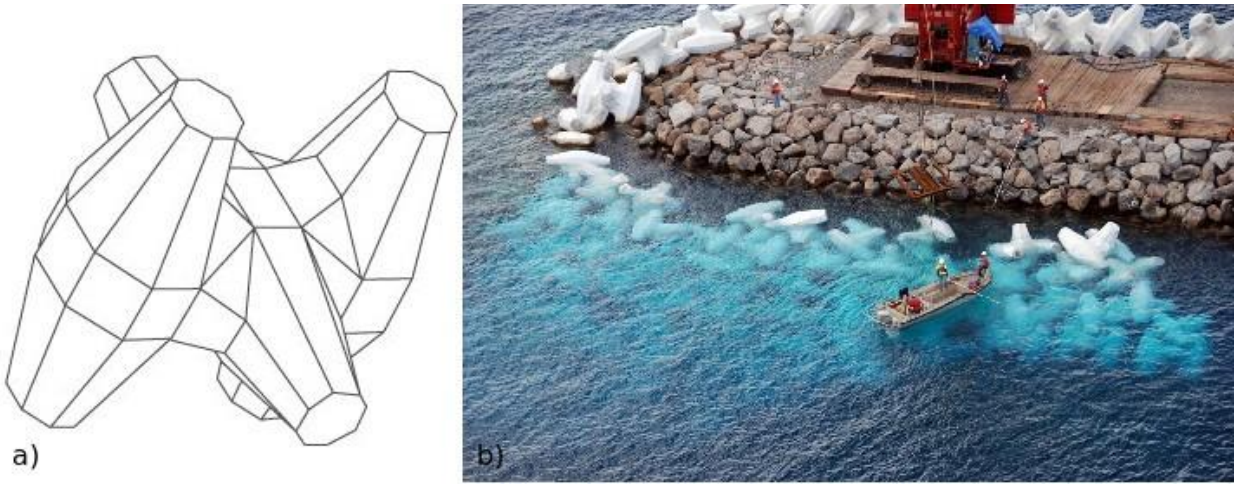


Figure 2-2: Core-Loc armour unit. (a) Symmetrical geometry (Arhur de Graauw, 2007); (b) Kaumalapau breakwater repair (Bairds W.F. & Associates, n.d).

## 2.3 Wave-Structure Interactions

To assess a breakwater performance, the wave-structure interactions must be understood. The structure`s hydraulic stability is governed by the maximum wave run-up and run-down, and wave reflection and transmission levels. Due to the complex flow through the porous armour layer, these parameters are often derived based on limited physical models experiments.

### 2.3.1 Waves

A stable coastal structure depends on the assessment of the offshore wave climate or nearshore bathymetry. The wave conditions are characterized by the wave height, length or period, maximum water levels due to tides or storm surges, predicted sea level rises, tides, and wind and wave induced currents. Most formulae used to determine the stability of armour units are based on the significant incident wave height ($H_s$) at the toe of the structure, the mean or peak wave period ($T_m$ or $T_p$) , the wave angle of attack ($\beta$) and the water depth ($D$). In deep water conditions, the difference between both definitions of significant wave height is about 10-15%. The wave period determines the wave length ($L$) which related to the wave height determines the wave steepness. The wave period is used in the determination of run-up and overtopping rates.

Waves are mainly generated by wind action on water. Waves are characterized by their height, length, period and propagation direction. Wave frequency is often used in wave theory to distinguish between low-frequency waves which travel faster compared to high-frequency ones. The waves that moved away from the generation area and are no longer influenced by wind are called swell waves, relatively regular long crested waves. Contrary, wind waves can be characterized as irregular, short crested and steep, with different frequencies and directions. Once formed, waves spread in area and travel vast distances while maintaining their wavelength and period. As they approach the shoreline, the wave speed and length decrease in shallow water and the wave height increases due to energy conservation between deep and shallow water. This process is called wave shoaling, illustrated in Figure 2-3. Another factor affecting the wave characteristics as they approach the shoreline is wave refraction, also a result of varying bathymetry. The waves travel slower in shallow water compared to deep water, causing the waves to “bend”. When the travelling waves encounter obstacles, such as islands or artificial structures (e.g. breakwaters), the passing waves spread the energy along the crest, which causes the waves to diffract.  These processes are illustrated in Figure 2-4.

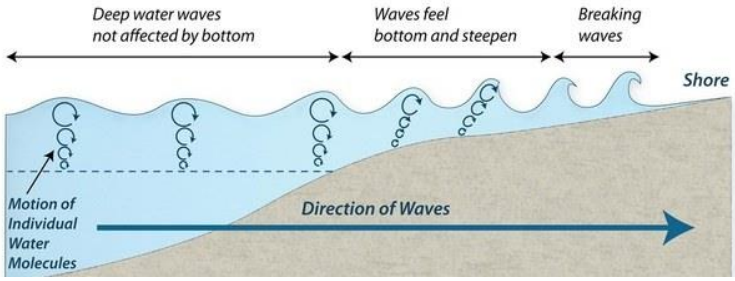


Figure 2-3. Wave shoaling (n.d, 2010).

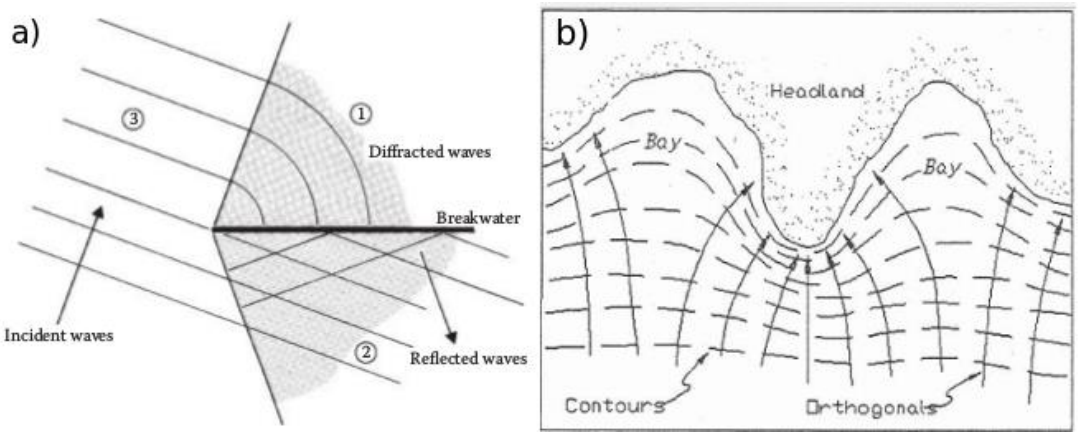


Figure 2-4: Wave energy. (a) Refraction; (b) Diffraction (adapted from USACE, 2002).

**Breaker Type**

As a consequence of waves progress, the relationship between water depth and wave height results in an unstable waveform causing breaking of the waves. Wave steepness and breaking index are the criteria that determines wave breaking, as shown below. Russell (1840) was the first to theoretically determine the steepness and $H/D$ limits based on a solitary wave (single wave).

Wave Steepness : $H/L < 1/7$

Breaking index: $\gamma = \frac{H}{D} = 0.78$

**Iribarren Number**

To describe the wave action on a slope, the surf similarity parameter ($\xi_0$), also known as Iribarren number ($Ir$) is often used. The parameter can be used to describe the type of wave breaking on a beach or structure illustrated in Figure 2-5. The Iribarren number relates the slope angle ($\alpha$) to the wave height and deep water wavelength ($L_0$) as shown below.

$$Ir = \xi_0 = \frac{tan\alpha}{\sqrt{H_0/L_0}} \; ; With\; L_0 = \frac{g}{2\pi}T^2$$

| breaker type | $\xi_0$–range | $\xi_b$–range |
|---|---|---|
| surging or collapsing | $\xi_0 > 3.3$ | $\xi_b > 2.0$ |
| plunging | $0.5 < \xi_0 < 3.3$ | $0.4 < \xi_b < 2.0$ |
| spilling | $\xi_0 < 0.5$ | $\xi_b < 0.4$ |

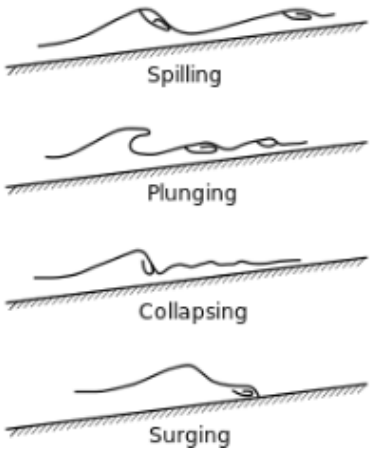


Figure 2-5: Breaking wave types (S.L. Douglas and J. Krolak, FHWA, 2015)

### 2.3.2 Wave Run-up and Run-Down

The vertical oscillations of water height on a structure are referred to as run-up and run-down (Figure 2-6). The level of the structure crest is governed by the design run up while the lower extent of armour protection is determined using the run-down level. Both parameters are defined with respect to the still-water levels (SWL)—this is the average water elevation excluding local variations due to waves but including the effects of tides or storm surges. Generally, the run up level is higher than the incident wave heights.

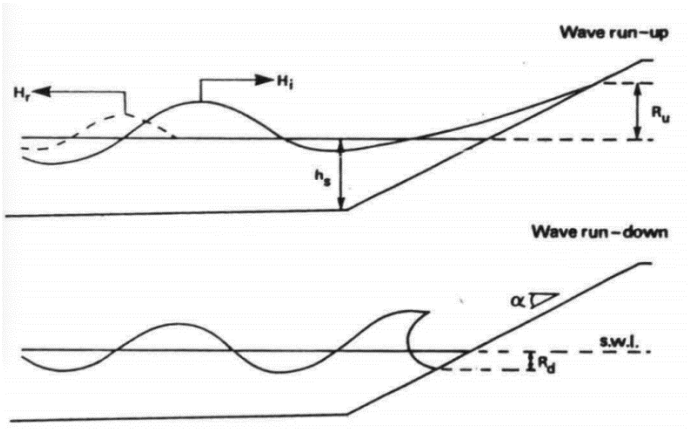


Figure 2-6: . Wave run-up and run-down schematics (J.W. Van Der Meer, 1995).

The general run-up formula for a smooth slope was given by Van der Meer (1995), as a function of the significant wave height and the surf similarity parameter. The equation also includes a reduction factor which takes into consideration the effects of slope roughness ($\gamma_f$), oblique wave attack ($\gamma_\beta$), and a bern ($\gamma_b$). Further studies done by Seelig and Ahrens (1981) and Van der Meer and Stam (1992) indicated that rough porous slopes affect the relative run-up levels as a function of the surf similarity parameter. Therefore, two additional empirical equations were derived for run-up on rock slopes, based on different wave breaking parameter. All research indicates that the wave run-up decreases with increasing armour layer roughness and porosity. The latest run-up expressions are given by EurOtop Manual (2016) – Manual on wave overtopping of sea defences and related structures. The general wave overtopping formula estimates the 2% run-up height ($R_{u2\%}$) taking into account the effects of wave angle and slope roughness. The roughness factor is given in the Manual for different types of armour layer as shown in Figure 2-7. The reduction factors were derived empirically, based on the European research project CLASH. The factors were derived based on one slope angle of 1:1.5, breaker parameters ranging between 2.8 and 4.5, and three different wave steepness's. Therefore, the range of applicability of the current equations used to estimate the run-up height is limited.

$$\frac{R_{u2\%}}{H_0} = 1.65\gamma_b\gamma_f\gamma_\beta\xi_0$$

Maximum wave run-up is given by:

$$\frac{R_{u2\%}}{H_0} = \gamma_{f\ surging}\gamma_\beta\left(4 - \frac{1.5}{\sqrt{\gamma_b\xi_0}}\right)$$

$$\gamma_{f\ surging} = \gamma_f + \frac{(\xi_0 - 1.8)(1 - \gamma_f)}{8.2}$$

| Type of armour layer | $\gamma_f$ | Figure |
|---|---|---|
| Smooth impermeable surface | 1.00 | Figure 6.8 |
| Rocks (1 layer, impermeable core) | 0.60 | |
| Rocks (1 layer, permeable core) | 0.45 | |
| Rocks (2 layers, impermeable core) | 0.55 | |
| Rocks (2 layers, permeable core) | 0.40 | Figure 6.8 |
| Cubes (1 layer, flat positioning) | 0.49 | |
| Cubes (2 layers, random positioning) | 0.47 | Figure 6.8 |
| Antifers | 0.50 | Figure 6.8 |
| HARO's | 0.47 | Figure 6.9 |
| Tetrapods | 0.38 | Figure 6.9 |
| Dolosse | *0.43* | |
| Accropode™ I | 0.46 | Figure 6.9 |
| Xbloc®; CORE-LOC®; Accropode™ II | 0.44 | Figure 6.9 |
| Cubipods one layer | *0.49* | |
| Cubipods two layers | *0.47* | |

Figure 2-7: Roughness factor for permeable rubble mound structures with slope of 1:1.5 (EurOtop Manual, 2016)

The maximum run-down level of a wave on a slope is the lowest point where the water retreats with respect to SWL. In design, this parameter is generally less important compared to overtopping and run-up levels. In the EurOtop Manual, an estimate of the run-down on a straight rock slope is given, based on research conducted by Van der Meer (1988). The results are rather limited, as the method only gives graphical estimates for four slope configurations based on different breaker parameters. The effects of CAUs are not included.

### 2.3.3 Wave Overtopping

Wave overtopping is defined as the discharge ($q$) over breakwater in extreme cases and it is often the controlling hydraulic parameter in the design of rubble mound breakwaters. If extreme levels of run-up exceed the crest level, the structure will overtop. Some small mean overtopping discharge is expected under extreme wave conditions. Thus, $q$ must be below acceptable limits under the design conditions. Such limits are enforced by safety criteria (FEMA, 2005).

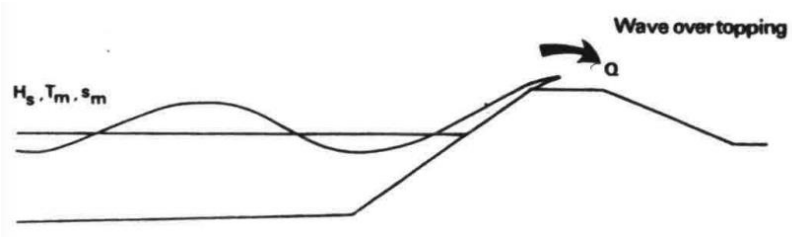


Figure 2-8: Wave overtopping schematic (J.W. Van der Meer, 1995).

The EurOtop Manual (2016) provides a mean wave overtopping discharge estimation for steep and rough breakwater slopes. The equations are based on the relative armour crest level, $R_c$, wave height and the shape reduction factor ($\gamma_f$) discussed above, and are valid for steep slopes of 1V:2H to 1V:4/3H.

$$\frac{q}{\sqrt{gH^3}} = 0.09\ exp\left[-\left(1.5\frac{R_c}{H\gamma_f\gamma_\beta}\right)^{13}\right]$$

The structural failure mechanisms cannot be assessed by estimating the run-up levels. Instead, the flow velocity and thickness are required. For rubble mound breakwaters, the wave energy is dissipated in the permeable layer, which results in a very different hydraulic behavior of the run-up between rubble mound and smooth slopes. For example, Core-Loc armour layers have a high porosity ratio, consisting of 60% air voids (CLI, 2012), resulting in a very effective wave energy dissipation. Therefore, the velocities and spatial distribution of the run-up water will be different. Currently, no provisions are given with respect to breakwaters constructed using CAUs. The run-up velocity and flow thickness exceeded by 2% of the up-rushing waves on dikes with respect to the elevation referenced from the still water level ($z_A$) can be estimated as shown below, equation based on the EurOtop Manual design equations. Both equations are based on $C_{v2\%}$ and $C_{h2\%}$ coefficients. Research attempting to estimate the correct coefficients was inconsistent, and therefore the Manual lists two recommended values for different slope configurations.

$$u_{A,2\%} = C_{v2\%}(g(R_{u2\%} - z_A))^{0.5}$$

$$h_{A,2\%} = C_{h2\%}(R_{u2\%} - z_A)$$

### 2.3.4 Wave Transmission

Waves with long periods cause wave energy transmission through relatively permeable structures. The transmission performance of breakwaters, defined as the transmission coefficient $C_t$, is dependent on the structure geometry, the crest freeboard and width, the water depth, the structure`s permeability and on the wave height ($H_{s,toe}$) and period at the toe of the structure. Van der Meer (1990), reanalyzed past research conducted by Seelig (1980), Powell and Allsop (1985) and Ahrens (1987), to develop a single method that relates $C_t$ to the relative crest freeboard $R_c/H_s$. The approach does not give a clear relation between constant $R_c$ and variable $H_s$ or vice-versa. Another method to estimate the transmission coefficient for rubble mound structures is given by Van der Meer (1998), which relates the crest height above the still water level and the incident significant wave height at the toe of the structure.

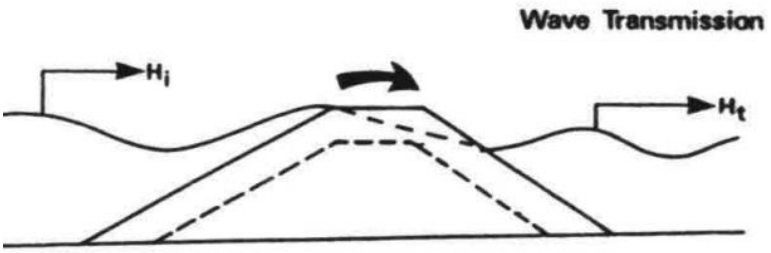


Figure 2-9: Wave Transmission Schematic (J.W. Van der Meer, 1995).

$C_T = 0.1\gamma_s \qquad for\ R_c/H_{s,toe} \geq 1.2$

$C_T = 0.8\gamma_s \qquad for\ R_c/H_{s,toe} \leq -1.2$

$C_T = -0.3\gamma_s(R_c/H_{s,toe}) + 0.45 \qquad for -1.2 < R_c/H_{s,toe} < 1.2$

$\gamma_s = safetyfactor\ of\ 1.2$

### 2.3.5 Wave Reflection

All coastal or shoreline structures will cause wave reflection, which can lead to unstable conditions and waves in front of the structure. Wave reflection also increases the sediment transport. A nonporous and steep structure will reflect 100% of the wave energy, while rubble slopes are designed to absorb the wave energy. The reflection performance is given by a reflection coefficient, $C_r$, which relates the incident and reflected wave heights, $H_i$ and $H_r$, respectively, as shown below. The first reflection coefficient estimated was developed by Seelig (1983) based on the equation developed by Battjes (1974) as functions of the surf similarity parameter. This method proved to underestimate the reflection coefficient (Van der Meer, 1995). Postma (1989) derived a new relationship that takes into consideration the effects of slope angle and wave steepness separately, thus giving a more accurate prediction. Zanuttigh B. and Van der Meer (2006) made further contributions, which developed a new formula that satisfied the shape requirements that can reproduce different slope types and it relates the roughness factor from the overtopping discharge formula presented earlier. The new formula shows good agreement for smooth and rock impermeable slopes, with the only limitation that the $C_r$ value is overestimated for armour units and rock permeable slopes when the surf similarity parameter is smaller than 4. The empirical coefficients required for the new formula are given in Figure 2-10 for different armour units.

$$C_r = \frac{H_i}{H_r}$$

$$C_r = tanh(a\xi_o^b)$$

**Table 3. Coefficient *a*, derived by directly fitting formula (5) on the armour units in Edinburgh dataset; for each unit the measured $\gamma_f$ is included; *b* is constant, 0.87.**

| *Armour unit* | $\gamma_f$ | *a* |
|---|---|---|
| Tetrapod, 2 layers | 0.38 | 0.102 |
| Core-Loc, 1 layer | 0.44 | 0.113 |
| Xbloc, 1 layer | 0.45 | 0.112 |
| Accropod, 1 layer | 0.46 | 0.115 |
| Antifer, 2 layers | 0.47 | 0.115 |
| Cube, 2 layers | 0.47 | 0.108 |
| flat | 0.47 | 0.120 |
| (1:2), rough | 0.47 | 0.105 |
| Cube, 1 layer | 0.50 | 0.120 |

**Table 2. Coefficients *a*, *b* to be included in formula (5).**

| | *a* | *b* | $\gamma_f$ |
|---|---|---|---|
| Rock permeable | 0.12 | 0.87 | 0.40 |
| Armour units | 0.12 | 0.87 | Various |
| Rock impermeable | 0.14 | 0.90 | 0.55 |
| Smooth | 0.16 | 1.43 | 1.00 |

Figure 2-10: Reflection Equation Coefficients for different armour layers (Zanuttigh B. And Van der Meer, 2006).

## 2.4 Current Design Guidelines for Rubble Mound Breakwaters

In 1933, De Castro and Briones presented the formula used in the selection of rock armour weight given a wave height. In 1938, inspired by the previous work done by De Castro, Iribarren published a new formula that combines the characteristics and height of waves with the resistance characteristics of the breakwater, the weight of the armour pieces (W) and density of the armour stone, and the slope of the structure.

$$W = \frac{NH^3d}{(cos\alpha - sen\alpha)^3(d-1)^3}$$

In this equation, $d = \gamma_s/\gamma_w$, where $\gamma_r$ and $\gamma_w$ is the specific weight of the rock and water, respectively, and $N$ is a practical dimensionless coefficient ($N \equiv N_a\gamma_w$), $N_a$ representing an empirical coefficient.

The article published by Iribarren was translated and published in the Bulletin of the Beach Erosion Board Office. Following this, Robert Y. Hudson developed an analogous formula to the Iribarren one based on a series of experiments conducted between 1942-1950 at the WES of USACE. The formula is very similar to the Iribarren formula, with the slope angle parameter modified. Hudson`s Equation was the first widely used and know formulae used by designers and planners to design rubble mound breakwaters.

### 2.4.1 Hudson`s Equation (1953)

Hudson`s formula is used to determine the required size of rock armour blocks to satisfy stability characteristics of rubble mound breakwaters under wave loading. The equation was derived from data analysis of physical model tests with relatively permeable cores under regular wave loading. The results of the tests concluded that the inter-unit friction coefficient varies with armour unit shape and placement patter but these effects were ignored and assumed to be included in a new empirical coefficient, $K_d$. The dimensionless parameter was assumed to account for the friction effects as well as all the other factors affecting armour stability but not accounted for directly in the equation. The determination of this coefficient was the primary focus of the research done at WES. It was traditionally used in the design because of its simplicity; however, it does not take into consideration the effects of irregular waves (random sea state- natural state) or storm duration. Another advantage

was the range of armour units and configurations for which the stability coefficient has been derived. Other limitations of the formula include potentials scale effects from the tests that were used to derive the equation, and the use of non-overtopped structures. Hudson`s equation in terms of the design weight of the armour pieces (W) is given as:

$$W = \frac{\gamma_r {H_{s,toe}}^3}{K_d \Delta^3 cot\alpha} \equiv M_{50} = \frac{\rho_r {H_{s,toe}}^3}{K_d \Delta^3 cot\alpha}$$

Where $\gamma_r$ represents the specific weight of the armour blocks Δ represents the relative buoyant density of the rock ($\Delta = \rho_r/\rho_w - 1$),and $\rho_r$ and $\rho_w$ represent the density of the rocks and water, respectively.

The stability dimensionless coefficient $K_d$ is used to account for the influence of other variables not present in the stability equation. The contributing factors are the shape of armour units, the number of layers, placing pattern (random or special), friction and interlocking of units, wave shape (breaking or nonbreaking), part of structure (trunk or head) and the wave angle of incidence. The coefficient is based on Hudson`s "no damage" condition which allows up to 5% of the armour units to be displaced from the armour layer at the design wave height. Examples of the stability coefficient for various concrete shapes are given in Figure 2-11, based on their placement location and wave type.

**Table 3.10 – Hudson's Stability coefficient values for various concrete armours**

| Breakwater section | Type of wave | Dolos | Antifer cube[2] | Core-Loc[3] | Xbloc[4] | Accropode / Accropode II |
|---|---|---|---|---|---|---|
| Trunk | Non-breaking wave | 31.8[1] | 7.5 | 16 | 16 | 15 / 16 |
| | Breaking wave | 15.8[1] | 6.5 | 16 | 16 | 11.5 / 12.3 |
| Head | Non-breaking wave | 16[2] | 5 | 13 | 13 | - |
| | Breaking wave | 8[2] | - | 13 | 13 | - |

[1] Refers to no damage criteria (<5% of displacement, rocking, etc.); if no rocking (<2%) the $K_D$ is reduced b 50% [SHORE PROTECTION MANUAL, 1984]

[2] Preliminary design purposes [SHORE PROTECTION MANUAL, 1984]

[3] Guidelines for design - Core-Loc .Design Guide Table

[4] Xbloc. Effective wave protection for breakwaters and shores

Figure 2-11: Hudson`s stability coefficient for various CAUs (Domingo V., 2012)

In the nineties, the formula was rewritten in terms of the nominal diameter ($D_{n50}$) and relative mass density of the armour block used.

$$\frac{H_{s,toe}}{\Delta D_{n50}} = \frac{(K_d cot\alpha)^{1/3}}{1.27}$$

$$D_{n50} - nominal\ median\ diameter\ of\ armour\ blocks(m) = (W_{50}/\rho_r)^{1/3}$$

$$W_{50} - 50\%\ value\ of\ the\ mass\ distribution\ curve(kg)$$

Further improvements of Hudson`s equation were done by Jackson (1968), who assessed the effects of waves higher than the original no-damage design wave, on the safety factor of rubble mound breakwaters.

### 2.4.2 Van der Meer`s Equation (1988)

Van der Meer developed the next widely used breakwater stability design equation, which takes into consideration the effects of wave period, number of waves (N), spectrum shape, and the permeability of the core (*P*). His work was based on an extensive series of test conducted earlier by Thomson and Shuttler (1975) which included a wide range of core/under layer permeability levels and wave conditions. Within the conditions tested, he concluded that the grading of the armour, the wave groupness and spectrum shape do not influence the stability of the breakwater armour layer. The new formulas take into account the storm duration and implicitly the number of waves by relating a dimensionless damage level ($S$), under the loading of N number of waves. To relate the wave period to external process such as waves breaking on a slope, the surf similarity parameter is used.

For plunging waves:

$$\frac{H_{s,toe}}{\Delta D_{n50}} = 6.2\, P^{0.18} \left(\frac{S}{\sqrt{N}}\right)^{0.2} \xi_o^{-0.5}$$

For surging waves:

$$\frac{H_{s,toe}}{\Delta D_{n50}} = 1.0\, P^{-0.13} \left(\frac{S}{\sqrt{N}}\right)^{0.2} \sqrt{\cot \alpha}\, \xi_o^{P}$$

The tests used to derive Van der Meer`s equations are limited to materials with mass density values between 2000 and 3100 $kg/m^3$. The structure is assumed to have reached equilibrium after 7500 waves. The wave steepness is limited between 0.005 and 0.6, range which almost covers all the possible range. The applicability range for structure permeability varies from a minimum of 0.1 corresponding to a layer with a thickness equal to $2D_{n50}$, to a maximum of 0.6 for a homogeneous rock fill structure.

Tests on a 1V:30H slope and a depth limited foreshore concluded that $H_{2\%}$ (largest 2% waves) give a better stability approximation compared to the significant wave height used in the original equations. Based on a Rayleigh distribution of the known ratios of $H_2/H_s$, the equations become:

For plunging waves:

$$\frac{H_{2\%}}{\Delta D_{n50}} = 8.7 P^{0.18} \left(\frac{S}{\sqrt{N}}\right)^{0.2} \xi_o^{-0.5}$$

For surging waves:

$$\frac{H_{2\%}}{\Delta D_{n50}} = 1.4 P^{-0.13} \left(\frac{S}{\sqrt{N}}\right)^{0.2} \sqrt{tan\alpha}\, \xi_o^{P}$$

Further improvement to the original equations were incorporated by Lathan et al. (1988) consisting of alternative coefficients that account for “nonstandard” armour shapes. Van Gent (2003) also published an updated version of the equation, accounting for the core permeability by relating the nominal diameter of the armour layer stone to the one used in the core, however, Van der Meer`s original equations remained popular for the design of rubble mound breakwaters.

### 2.4.3 Other Equations – Core-Loc

Following the development of Hudson`s and Van der Meer equations, more research has been conducted for specific types of CAUs. Generally, the design equations and recommendations available in literature are specific to one type of artificial armour unit, typically given by their manufacturer. This is another reason why the two previous equations are still used today, as they provided a simple and quick way to estimate the required size of the armour blocks given specific wave conditions. For Core-Loc armour units, the equation developed by Melby and Turk (1994) is valid for irregular, head-on waves within the tested parameters shown below. Concrete Layer Innovations (CLI), the Core-Loc exclusive manufacturer, specifies a Hudson`s stability coefficient of 16 and 13 for trunk sections and roundheads, specifically. A value of 2.8 is given for Van der Meer`s stability number.

$$\frac{H_s}{\Delta D_{n50}} = (K_D cot\alpha)^{1/3} \equiv M_{50} = \frac{\rho_c H^3}{K_D \left(\frac{\rho_c}{\rho_w} - 1\right)^3 cot\alpha}$$

Where, $D_{n50}$ is the equivalent length of a cube having the same mass as a Core-Loc unit, $\rho_c$ is the mass density of concrete. The formula is valid for the following parameters:

Wave parameters: $1.5 \leq T_p \leq 4.7\ s$

Structure Slope : $1V{:}\,1.33H\ and\ 1V{:}\,1.5H$

Surf similarity parameters: $2.13 \leq \xi_0 \leq 15.9$

Relative depth: $0.012 \leq D/L_o \leq 0.175$

Wave steepness: $0.001 \leq H_o/L_o \leq breaking$

- Geometric parameters given by the Core-Loc design table (CLI, 2012):

Unit volume ($m^3$): $V = 0.2211{C_L}^3$

Unit Height (Characteristic length) (m): $C_L = (V/0.2211)^{1/3}$

Equivalent Cube Size (m): $D_n = V^{1/3}$

## 2.5 Hydraulics Stability of Rubble Mound Breakwaters

### 2.5.1 Packing Density

Pacing density (*n*) is the number of units (*N*) per unit area (*A*) , expressed as a function of a non-dimensional parameter— packing density coefficient ($\phi$) , and the unit volume (*V*) as shown below. Generally, the smaller the packing density, less units are used, and therefore a cheaper system. On the other hand, more units increase the strength of the structure due to increased contact-forces between the units.

$$n = \frac{N}{A} = \phi V^{\frac{-2}{3}}$$

Traditionally, rubble mound breakwaters were build using double layers. The introduction of the Accropode, which was a more complex armour unit, enabled single-layer rubble mound breakwaters to be built, at a reduced cost compared to double layer breakwaters. Placing concrete units in a single layer requires special consideration to the damage levels and failure mechanism. Van Gent et al. (2001) concluded that higher packing density would result in higher stability, which is due to more units in the top layer which in turn will increase the strength as a results of increasing contact-forces between the units. A higher packing density also decreases the progressive damage sensitivity. Tests with a packing density of 0.4 and 0.3 showed that below the water level, the units become more compact, which causes gaps above. This in turn will increase the damage levels since the wave attack effects are considerably higher above the water level.

### 2.5.2 Placement Techniques and Unit Interlocking

Armour units' placement contributes to the stability of the breakwater, as a regular pattern which does not include isolated armour units, would reduce the effects of hydrodynamic forces on a single unit. Generally, the placement pattern depends on the type of armour unit used, as well as the number of layers. The placement pattern influences the packing density and interlocking properties, and therefore the stability. Armour units can be placed uniformly, patterned, oriented or randomly. The placement technique depends on the degree of interlocking and level of porosity sought. It is important to mention, that random placement refers to units placed in predefined locations; the term random come from the finished armour layer which resembles a random pattern. The idea of placement is to arrange the units in alternating and overlapping rows. This staggering pattern resembles diamond-shaped patter, characterized by the horizontal and upslope distance between units. This will ensure that each unit has enough contact points with the neighboring units, increasing the layer stability and reducing the forces exerted on individual blocks. Core-Loc armour units are placed in a random staggered patter (CLI, 2012).

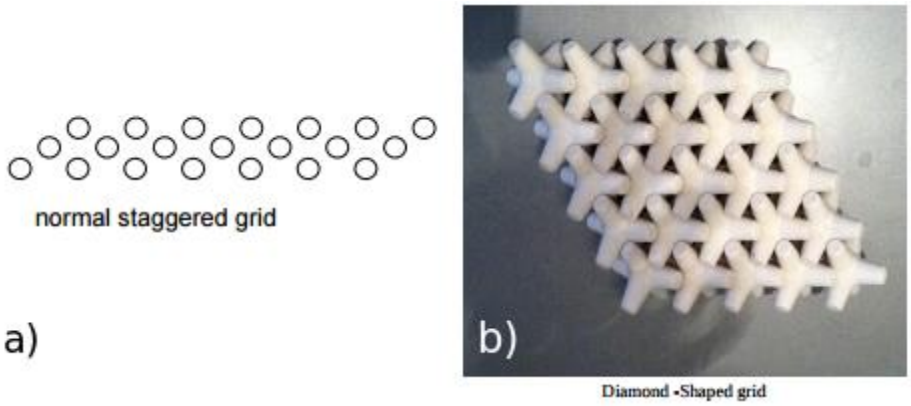


Figure 2-12: CAUS placement pattern. (a) Staggered pattern (Md. Salauddin, 2015); (b) Example Diamond-Shaped grid of Carblocks (Md. Salauddin, 2015).

### 2.5.3 Wave Induced Loading

The armour layer stability is the governing parameter following the preliminary design of the breakwater. Its structural integrity dictates its capability to withstand wave induced loading.

#### 2.5.3.1 Stabilizing Forces

The hydraulic stability of the armour layer is determined by the self-weight (gravity, $F_g$), the friction ($F_W$) and the interlocking ($F_I$) forces between the units. The magnitude of friction and interlocking forces depend on the friction coefficient ($\mu_f$), contact area and placement of the units. An armour layer made of rock would require larger volume of material to achieve the same hydraulic stability and performance as concrete armour units. Most rubble mound breakwaters are constructed using double layers, consisting of Cubes, Tetrapods, or Dolos. The Accropode was the first armour unit used in a single-layer application. The side slopes of breakwaters are generally steep, ranging from 1H:1.5V to 1H:3V, to reduce the volume of core material required. This influences the interaction between units, with steeper slope increasing the contribution of interlocking to stability as the unit's slope-parallel forces increase with increasing slope angle.

Figure 2-13 illustrates the static loads that determine the armour layer stability, with the gravity force decomposed into a parallel and perpendicular force to the side slope of the breakwater. An Xbloc armour layer is used for illustrative purposes.

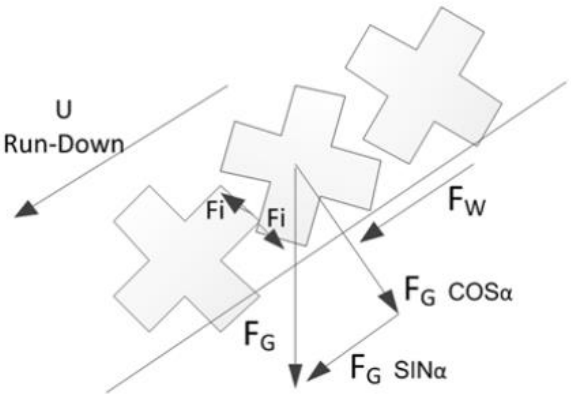


Figure 2-13: Individual armour unit static loads (I. Verdegaal, 2013).

$$F_G = (\rho_r - \rho_w) {D_n}^3 g$$

$$F_W = \mu_f (F_G) cos\alpha$$

#### 2.5.3.2 Destabilizing Forces

Interlocking units create a porous armour layer, which in turn dissipates more wave energy. The downside of increasing the porosity of the armour layer is increasing the effect of destabilization forces due to induced flow around the units during run-up and run-down. If several units lose the interlocking with adjacent units, the armour layer will progressively fail. Drag and lift forces ($F_D$ and $F_L$) are

generated by the flow velocities ($u$) between the units. Additionally, inertia forces ($F_I$) are generated in the direction of fluid motion due to wave motion on the slope. The wave motion causing a fluctuating hydraulic gradient in the armour layer also induces inflow forces and outflow forces.

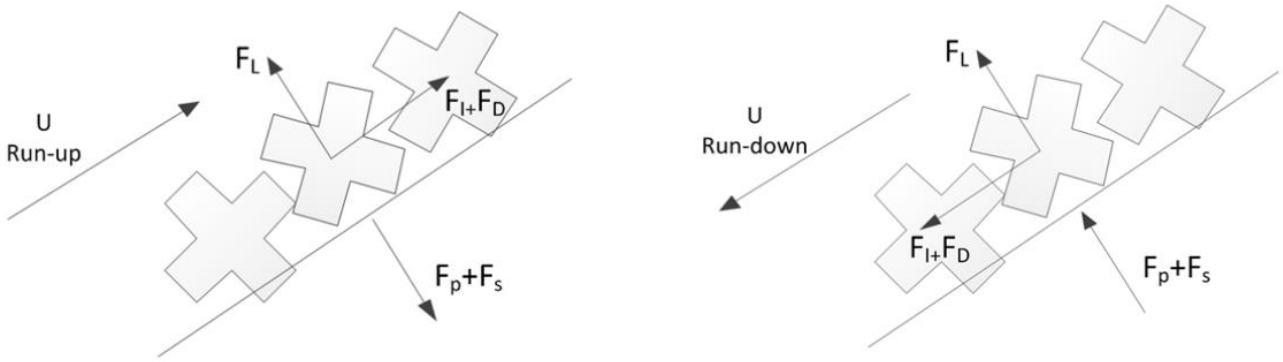


Figure 2-14: Individual armour unit loading during run-up and rundown (I. Verdegaal, 2013).

$$F_D = 0.5 C_D \rho_w V^2 \mathrm{A}$$

$$F_L = 0.5 C_L \rho_w u^2 A_L$$

$$F_I = C_M \rho_w \mathrm{V} \frac{\partial u}{\partial t}$$

Where $C_D$, $C_L$, and $C_M$ are empirical coefficients, and $A$ is the unit total projected area perpendicular to the flow direction ($A_L$ indicates that the projected area in the direction of lift is different). The first derivative of the velocity with respect to time ($\partial u/\partial t$) represents the instantaneous fluid acceleration.

## 2.6 Physical Modelling of Rubble Mound Breakwaters

In coastal engineering, physical modelling is still a widely used method to assess the hydraulic and structural performance of a structure, and to optimize its final design. For rubble mound breakwaters, physical models are employed when overtopping is a major design parameter, the bathymetry or structure geometry are complex, or when CAUs are used as armour. To reproduce realistic wave conditions, the main bottom contours of the bathymetry are constructed using elevation templates that are filled with gravel and capped with a concrete layer. The reproducible size of model armour units, maximum wave height and water depth in the flume, are the parameters that govern the scale ratio of the physical models. To analyze the interaction between waves and a breakwater structure, a 2D model representative of the structure`s cross section is sufficient. For more complicated wave patterns and complex geometry (i.e. roundheads), 3D models are employed (Frostick et al., 2011).

For a physical model to behave in the same manner as the prototype, geometric, dynamic, and kinematic similarity laws are used. For an accurate model, the geometric dimensions of a prototype must have a constant relationship to the corresponding lengths of the model. Similarly, the time depended processes must undergo similar time rates of motion change. Lastly, the dynamic similarity ensures that the forces in the model flow can be scaled to the corresponding forces in the prototype flow. Scale effects are introduced when the force ratios between the physical model and its prototype

are not identical. As a result, some forces are mode dominant in the model relative to the prototype. The significance of scale effects depends on the relative importance of the involved forces; therefore, it is important to understand which forces can be neglected and which forces are relevant. The two common nondimensional parameters used in hydrodynamic models are Froude and Reynolds numbers. Froud scaling is typically employed in free surface flows, characterized typically by rough regimes, and therefore the viscous effects can be neglected.

Reynolds similarity is used where viscous and inertial forces are important. Such situations correspond to fully enclosed flows (e.g. pipes, turbomachines), where the viscosity effects on the solid boundaries influence the relationship between model and prototype forces. For wave motion studies and wave loading, the prototype conditions are dominated by gravity effects and viscous effects can be ignored – with the condition that the model Reynolds number is maintained large enough such that the flow is turbulent (Chanson, 2004). Therefore, for hydraulic structures and for wave motion studies, to ensure that the forces acting on the real system are represented in the model in correct proportions, the models are geometrically similar to the full-scale structure and scaled using Froude scaling. The Froude Law scaling relationships between a prototype and a model are given below, expressed in terms of the length scale factor $n_L$.

Wave height (m): $n_H = n_L$

Time (s): $n_T = {n_L}^{0.5}$

Velocity (m/s): $n_u = {n_L}^{0.5}$

Acceleration ($m/s^2$): $n_L = 1$

## 2.7 Theoretical Background

In order to design any offshore structure able to withstand wave action, the fluid motion and resultant hydrodynamic loading must be understood. Fluid loading consists of two components, namely drag and inertia forces. Any submerged or partially submerged object will cause flow separation around it. Drag forces represent the resistance imposed by the object, acting in opposite direction of the oncoming flow velocity. Similarly, the inertia force is the resisting force that arises from the change in fluid velocity around the object. In fluid dynamics, the sum of the two force component can be determined using the semi-empirical Morison Equation (1950). Additionally, submerged bodies are subject to lift and buoyant forces acting in the perpendicular direction relative to the flow. Lift forces are a result of the pressure difference on the opposite sides of the object. Buoyant forces ($F_B$) are the result of fluid pressure exerted around the object. From basic hydrostatic principles, it is known that pressure increases as depth increases. This implies that the pressure at the top of an object will always be smaller compared to the bottom forces. This difference causes a net upward force, known as buoyancy, and its depended on the displaced fluid volume by the object, force estimated as shown below.

$$F_B = \rho_w \mathrm{V} g$$

### 2.7.1 Morison Equation

In 1950, Morison, O`Brien, Johnson, and Schaff presented an empirical formula for estimating hydrodynamic forces ($F_H$) acting on a fixed vertical pile. This equation is widely known as the Morison Equation (or MOJS). The formula represents the sum of the two inline forces acting on a body placed in an oscillatory flow and it's based on two empirical hydrodynamic coefficients – inertia and coefficients ($C_M, C_D$, respectively), determined from experimental data. The inertia principle comes from the added mass fluid mechanics principle, representing the accelerative force acting on a mass of water displaced, as a result of fluid flow distortion. The first component of Morison`s equation represents the inertia force contribution ($F_I$), proportional to the local fluid acceleration and object`s volume. The drag force ($F_D$) is proportional to the velocity squared and object projected area perpendicular to the flow. The two empirical coefficients account for the effects of the object`s surface roughness, and are found to be dependent upon Reynolds number ($Re$), Keulegan Carpenter number ($K_c$), and the geometry of the structure (Baba,2014). Reynolds number represents the ratio of fluid`s inertial force to its viscous force, which can be used to predict fluid flow changes. Its dimensionless form is used in fluid mechanics to measure the type of behavior of flow fluid. Keulegan-Carpenter number is a dimensionless quantity used to describe the relative importance of drag forces over inertia forces acting on an object in oscillatory flow (Keulegan and Carpenter, 1958). For small $K_c$ numbers, the inertia effects are predominant, while for larger numbers, which are associated with increased in turbulence (higher $Re$), the drag forces become predominant.

$$F_H = F_I + F_D = \rho C_M V \frac{\partial u}{\partial t} + \frac{1}{2}\rho C_D A u|u|$$

$$Re = \frac{\rho u L}{\mu} = \frac{uL}{\nu}$$

$$K_c = \frac{uT}{L}$$

Where $L$ is the characteristic length scale of the object (for example the diameter of a pile, $D$, or the characteristic length of an armour unit, $C_L$), $\mu$ is the dynamic viscosity of the fluid, and $\nu$ is the kinematic viscosity of the fluid. In the $K_c$ equation, $u$ is the maximum amplitude of the flow velocity oscillation, and $T$ is the period of the oscillation.

Morison equation was developed based on a simple experimental program (Morison et al., 1950). The method is applicable to small structures relative to the wave lengths ($D/L < 0.1$ to 0.2). The physics of the force fluctuations on an object in oscillatory flow is a complex fluid dynamics problem, leading to several limitations of the proposed formulation. Mainly, the forces due to vortex shedding were neglected and the derivation was based on the horizontal component of the orbital velocity and acceleration, implying that the vertical components` contributions do not contribute to the force (Lin, 1981). It has been indicated that the equation yields large errors for $K_c$ numbers between 8 and 25. Since its development, numerous attempts have been made to improve Morison equation with no satisfactory results (Sapkaya, 2010), but it remains a widely used method in coastal engineering design.

### 2.7.2 Methods for Fitting Force Coefficients

The original experimental investigations performed by Morison et al. (1950) were designed to measure the moment history on a pile subjected to wave action. Measurements of the wave profiles were used to determine the height, velocity and periods of the waves. There variables were then used to determine the coefficients $C_M$and $C_D$ by optimizing the solution of the proposed equation and the measured moment time history. Fitting the drag and inertia coefficients used in Morison`s equation to match the experimentally measured force time histories still remains a standard approach, with several methods proposed in literature.

**Morison`s Method**

In his original work, Morison derived the coefficients from the moment history at phase angles of $0, \pi/2, \pi, (3/2)\pi$ with respect to the wave crest. This approach allowed the drag and inertia components of the equation to be isolated. The assumption was that when velocity is maximum and acceleration zero, the only force contribution on the pile is due to drag, and therefore $C_D$ can be calculated directly as shown below in terms of the measured force ($F_m$). Similarly, the inertia term was computed based on the maximum acceleration and zero velocity instance. This process is illustrated in Figure 2-15. This approach however, was not very accurate and does not provide estimates for the forces occurring between wave crest phases angles, as only two instant in the time record are used and the results of this method imply that the two coefficients are time-invariant. This method is not widely used and will not be considered during this study. Keulegan and Carpenter (1958) proposed a method to isolate the force coefficients by using Fourier or time averaging of each wave cycle. Again this approach assumes that the velocity and acceleration time series are orthogonal.

$$C_D = \frac{2F_m}{\rho D u|u|}$$

$$C_M = \frac{4F_m}{\pi \rho D^2 \frac{\partial u}{\partial t}}$$

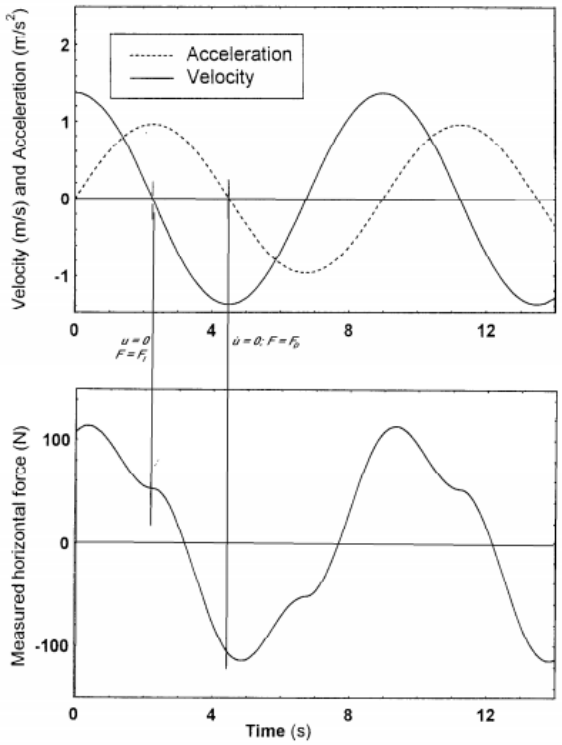


Figure 2-15: Phase relationship between water particle kinematics and measured forces (Morison et al., 1950).

## Least Squares Optimization

A method that yields better results is to optimize the drag and inertia coefficients using the least-squares approach (LS), which can be applied to the entire data set. In this method, the values chosen for the two coefficients are optimized so that the error term ($\sigma$) between the measured and the estimated force at each measured point is minimized. Studies comparing the two fitting techniques indicated that least-squares methods yields more accurate results compared to Morison's method (Isaacson et al. 1991). On the downside, this method does not yield accurate prediction of the forces close to zero, and there are many combinations of $C_M$ and $C_D$ that will give the same error estimate. Using all data points in the series ensures that each point has an equal influence in the determination of $C_M$ and $C_D$, which leads to some limitations of the method in predicting peak forces accurately.

$$\sigma(C_D, C_M) = \int_0^t \left[F(t)_{measured} - F(t, C_D, C_M)_{computed}\right]^2 dt$$

## Weighted Least Squares Optimization

A similar approach is to use weighted least squares method (WLS). The force coefficients are optimized using this approach by putting more emphasis on the measured force terms, as shown below. Therefore, the instances where the measured forces are small have little influence in the final optimization of the coefficients, leading to increased accuracy in the prediction of peak forces.

Wolfram and Naghipour (1999) reported that weighted least square method gave the best predictive accuracy when compared to least squares method, but only by a small margin.

$$\sigma(C_D, C_M) = \int_0^t [F(t)_{measured}]^2 - \left[F(t)_{measured} - F(t, C_D, C_M)_{computed}\right]^2 dt$$

**Alternative Methods**

Other coefficient fitting methods are available in literature such as spectral fitting method. This method is particularly helpful for irregular waves, where the coefficients are determined using the energy density spectra of the forces and velocities. This method will not be covered in this thesis.

### 2.7.3 Analysis of Drag and Inertia Force Coefficients and CAUs Hydrodynamics

Since Morison`s equation development, researchers conducted numerous laboratory tests to determine the $C_D$ and $C_M$ coefficients. Keulegan and Carpenter (1958), determined that the force coefficients can be plotted reasonable as functions of the dimensionless $K_c$ number, used since as the primary parameter for interpreting $C_D$ and $C_M$. Published literature results focus on the hydrodynamic interactions with different structures` geometries, orientations or roughness, and the resultant variation of the force coefficients with $Re$ and $K_c$. Variation of the force coefficients trends with respect to different Keulegan Carpenter numbers have been reported in literature. In general, it was shown that $C_D$ decreases with increase in $K_c$, while $C_M$ increases with increase in $K_c$, as shown in Figure 2-16 which represents a typical laboratory measurement result from Sarpkaya (1976).

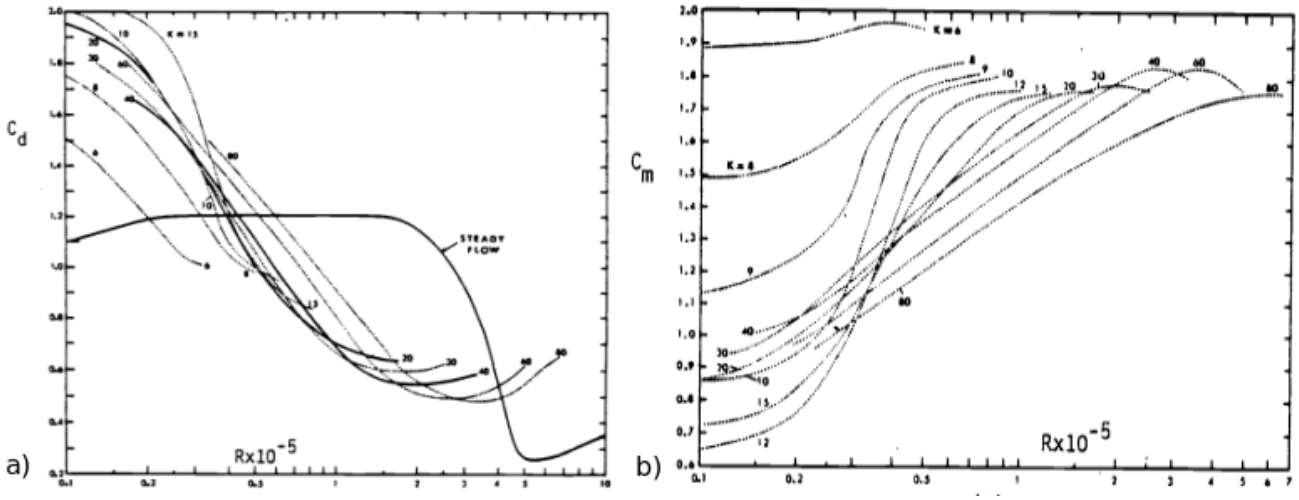


Figure 2-16: Drag and inertia force coefficients results for various $K_c$ values in oscillating flow. (a) $C_D$ versus Re; (b), $C_M$ vs Re (adapted from Sapkaya, 1976).

Based on the results, several observations of the variation of the force coefficients with respect to $K_c$ have been made. It has been showed that for low $K_c$ values ($K_c$<3), the inertia force contribution is dominant, and the drag effects can be neglected. The drag effects become significant for $K_c$ between 15 and 45, while high values of $K_c$ ($K_c$>45), the drag force is dominant. For the intermediate range until drag becomes significant (3<$K_c$<45), the drag is often linearized in analysis.

Although Morison's equation has been traditionally used to describe the wave resultant forces acting on fixed cylinders, its application extended to several experiments on the stability of armour units. Namely, Sakakiyama and Kajima (1990) investigated the scale effect of wave forces on Tetrapods. The relationship between the drag coefficient and Hudson's stability coefficients has been theoretically derived based on experimental results of the wave forces on an armour unit placed in an armour layer of a breakwater. To measure the wave force time history acting on armour units, various size Tetrapods has been connected to a load cell as depicted in Figure 2-17. The drag and inertia force coefficients were estimated using Morison equation and Fourier analysis of the measured forces and theoretical wave velocities and accelerations.

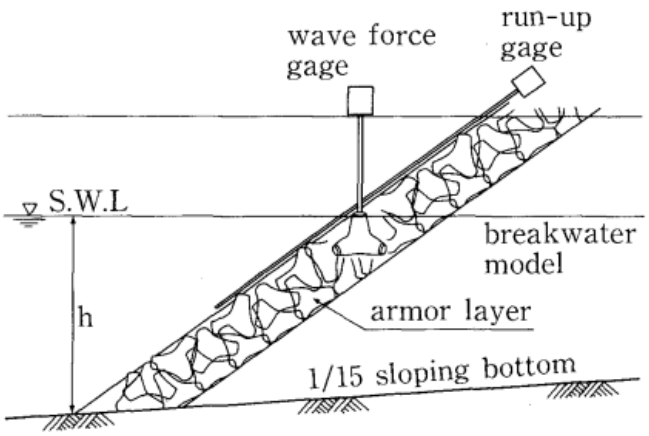


Figure 2-17: Experimental setup to measure wave forces acting on armour units (Sakakiyama and Kajima, 1990).

Based on the results as functions of the $K_c$ number and Reynolds Number, it was concluded that as $Re$ increases, inertia coefficient increases constantly at certain $K_c$ number, while drag decreases as shown in Figure 2-18(a) and (b). $K_c$ is a representation of the importance of drag force over the inertia force. The results indicate that at a constant $K_c$ number, the ratio of the forces changes with changing Reynolds number. Figure 2-18(c) show the drag to inertia force ratio as a function of $Re$ for each scale model used. It can be concluded that the drag force become predominant compared to the inertia force as Reynolds number increases.

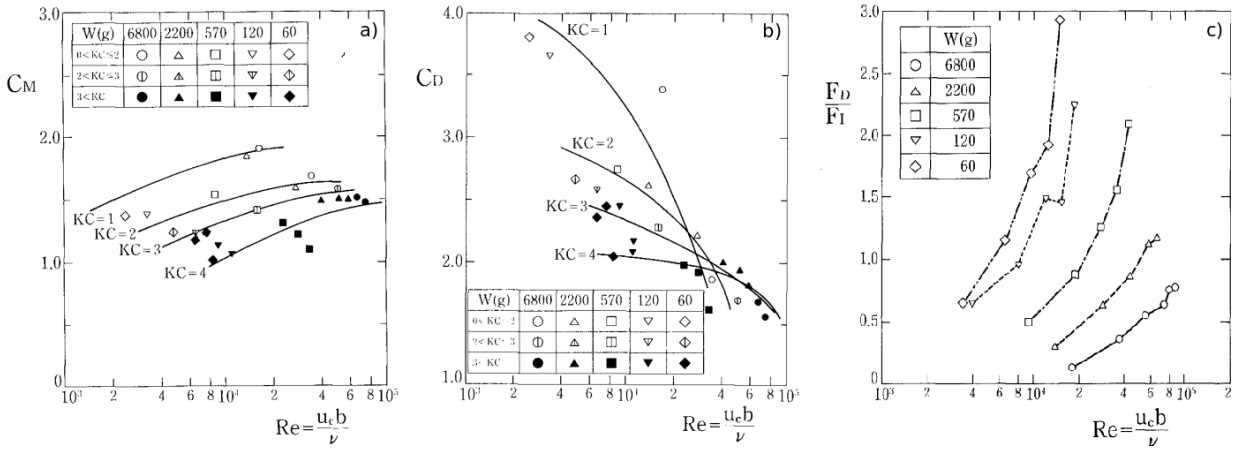


Figure 2-18: Force coefficients depending on model scale and $K_c$ number. (a) Inertia coefficient; (b) Drag Coefficient; (c) Drag to inertia force ratio (adapted from Sakakiyama and Kajima, 1990).

To examine the scale effects of drag force, a second experiment was performed using unsteady flow conditions. Various sizes of Tetrapod armour units with different weights were dropped in a water tank, as depicted in Figure 2-19(a). The experiments were designed on the condition that the drag force can be isolated and constant throughout the fall of the unit. The velocity was measured using a set of cameras that traced the displacement of the units at different levels, results shown in Figure 2-19(b). No significant changes can be observed in the fall velocity, and therefore, the tank was tall enough so that the armour units reached constant fall velocity (zero acceleration), implying that the inertia force can be ignored (proportional to the acceleration). In other words, the drag force was equal to the buoyant force acting on the individual size of the units. The drag coefficient results ($C_{Dm}$) were then normalized with respect to a prototype drag coefficient ($C_{Dp}$) of 0.6 and plotted against Reynolds number, as shown in Figure 2-19(c). The results indicated that the ratio $C_{Dm}/C_{Dp}$increases as Reynolds number decreases, meaning that the drag force increases as model scale decreases, and therefore, it can be concluded that small scaled models will experience relatively larger wave forces acting on armour units compared to large-scale model tests.

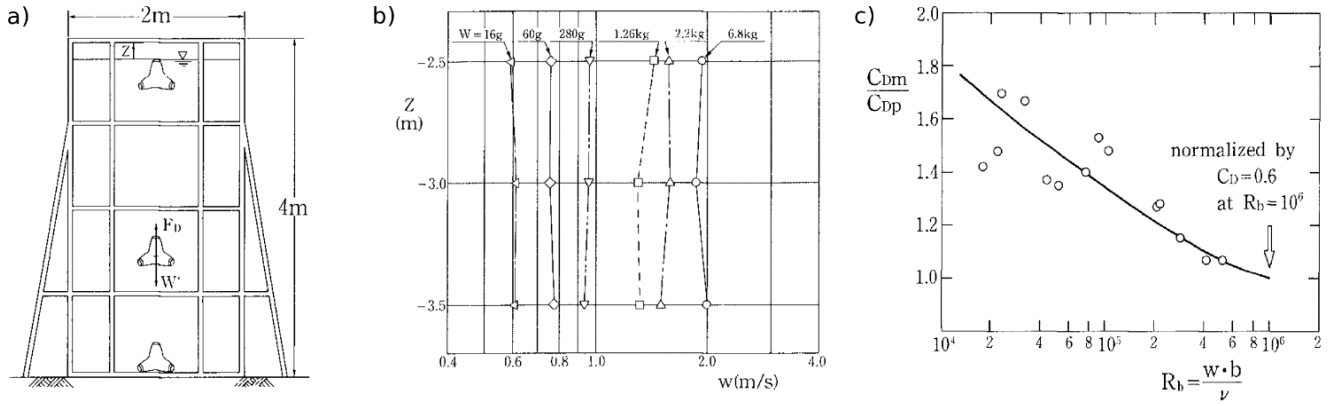


Figure 2-19: Drag force experiments (a) Water tank; (b) Tetrapod fall velocity resilts; (c) Normalized drag coefficient versus Re (adapted from Sakakiyama and Kajima, 1990).

Rubble mound breakwater research is largely focused on the overall hydraulic stability and structural integrity of the armour layer as a whole. This is a rational approach, considering that one of the major contributors to the layer stability is the interlocking forces that resist wave actions. However, this lead to design procedures that rely heavily on empirical coefficients, as the individual armour unit contributions on the overall stability of the armour layer are hard to quantify experimentally and theoretically. Therefore, not many resources are available in literature regarding the individual CAUs hydrodynamics. Another interesting experiment was done by E. ten Oever (2006), where the forces acting on a submerged Xbloc unit under oscillatory flow conditions were calculated using Morison Equation. The research was particularly helpful to predict the unit response during crane placement, concluding that the response of the armour unit is correlated to the wave period, and full amplitude is reached after three waves, and therefore full unit response occurs before the units are placed on the slope. The results were replicated numerically within reasonable agreement with the amplitude tests; however, the drag and inertia force coefficients were estimated based on coefficients given for various geometric shapes.

## 2.8 Discussion

Although breakwaters are the first line of defense against shoreline erosion and storm-induced flooding, the wave induced forces acting on the structure are not well understood and quantified in current design provisions. During the design stage, the hydraulic stability of the main armour layer on the seaward side of the structure is the primary concern. Breakwater failure occurs in a progressive manner as individual units are dislocated when the wave action loading exceeds the forces that hold the units in place. Therefore, a reasonable design approach should be based on this force balance. Due to the complex flow through the armour layer, the actual forces acting on the individual units has been difficult to quantify, and the factors that influence the stability of the armour layer are estimated using empirical parameters. These are derived from limited scaled laboratory tests and are assumed to account for the stability parameters and other sea state parameters not directly included in the design provisions.

Hudson`s equation, derived over 50 years ago, and Van der Meer`s equation, derived over 25 years ago, are the two widely used design equations for rubble mound breakwaters (Hudson, 1957) (Van der

Meer, 1988), both quantifying armour unit's hydraulic stability using a non-dimensional stability number, and empirically derived coefficients. Furthermore, these parameters were found to have several definitions in literature. This raises the question of reliability of the current formulas, which only focus on the hydraulic stability of the layer but ignore the effects of armour unit`s structural strength and the effect of the interlocking and friction forces between units. Since many definitions and estimation approaches are used, comparison between different equations is nearly impossible. As the equations are valid within the tested conditions, physical testing is still a standard and recommended practice for breakwater projects.

Shortcomings of using natural rock to build rubble mound breakwaters lead to the creation of artificial CAUs. Their shape allowed a high interlocking mechanism while maintaining a high degree of layer porosity. In turn, this increased wave energy dissipation and decreased wave run-up and overtopping, the main hydraulic parameters of concern when building a breakwater. Over the past 65 years, several units were introduced; however, one of the worldwide leading CAUs is the Core-Loc unit (CLI, 2016). This unit proved to be advantageous, as it can be placed in a single layer, while its geometry allows for high interlocking capabilities, overall increasing the breakwater`s hydraulic performance and decreasing the construction costs.

The structural integrity of the armour layer dictates its capability to withstand wave loading. This is determined by the armour units' self-weight, the friction and the interlocking forces between adjacent units. Although the self-weight of the layer is easily determined, the other forces are extremely hard to quantify experimentally and therefore not accounted for in the design equations. Similarly, the primary destabilization forces due to wave induced flow around the units during run-up and run-down are not included in current provisions. These are the main hydraulic and structural parameters that influence the overall stability of the breakwater, and although current design formulas are invaluable tools in the development of rubble mound breakwater designs, they may not accurately reflect the physical processes associated with rubble mound breakwater stability.

The standard method for predicting wave induced forces on submerged structures is Morison equation. This is an empirical method for estimating the hydrodynamic forces acting on a fixed vertical pile. The two inline force components acting on a structure, the drag and inertia forces, are linked using this method to the water particle kinematics using two empirical coefficients – inertia and drag coefficients ($C_M$, $C_D$) (Morison et al., 1953). The influence of piles structure geometry, orientation or roughness on the force coefficients has been the subject of many experimental studies (Sarpkaya, 1976), however, limited literature sources were found describing its applicability to wave induced loading on individual armour units. It was shown experimentally that drag forces become predominant over inertia forces as laboratory scale increases (Sakakiyama and Kajima, 1990). A known problem with the scaling of forces and force coefficients from physical models to prototype conditions is related to the scaling laws employed. It has been shown that the coefficients are a function of $K_c$ and $Re$ numbers, however using Froude`s law for the model scaling, the dependence of the hydrodynamic coefficient on $Re$ makes similitude impossible. The main reason is that the prototype $Re$ numbers cannot be reproduced experimentally. Model $C_D$ results were shown to decrease with increasing $Re$, indicating that lower

model $Re$ numbers correspond to model $C_d$ higher than the prototype. To minimize scale effects, the model velocity should be increased such that it approaches the prototype $Re$ number, however this is generally limited by the economical and practical aspects of physical models (Trenhaile and Lakhan, 1989). For scale-independent results, both $Re$ and $Fr$ scaling laws should be satisfied, and this is only possible using full-scale tests.

To reduce the knowledge gaps in the current breakwater design techniques and better understand the processes associated with armour unit stability, a detailed experimental investigation is needed. The study will be focused on investigating and quantifying the primary armour layer destabilization forces. The drag and inertia forces will be evaluated experimentally using Core-Loc armour units. The hydrodynamics of different scales and unit orientations, and implicitly flow direction, will be examined in unsteady and oscillatory flow conditions. A non-intrusive unit displacement tracking technique will be developed for the evaluation of individual armour unit kinematics. Those results will be used to optimize the two empirical coefficients used in Morison equation to evaluate the orientation and scale effects on the flow and force development of Core-Loc armour units.

# Chapter 3 Core-Loc Hydrodynamic Analysis via Controlled Drop Tests

## 3.1 Introduction

The drag and inertia forces, which are the primary destabilization forces acting on individual armour units during wave loading, were investigated through a series of physical modeling tests for different unit scales and orientations. In this section, a simple and cost-effective method to extract hydrodynamic variables of interest of Core-Loc armour units that can be easily extended to other geometric shapes is described.

## 3.2 Facilities, Instrumentation and Testing Program

This study is focused on investigating individual armour unit hydrodynamic forces, as a basis for quantifying armour layer stability. This is achieved through a series of experimental investigations designed and performed under controlled conditions in the Civil Engineering Hydraulics Laboratory of the University of Ottawa, Canada. In total, 320 tests were conducted to extract accurate estimates of the drag and inertia force coefficients for Core-Loc armour units with varying geometric scales, flow velocity, and orientations.

In the sections that follow, details will be provided on the experimental design process and the physical characteristics of the testing chamber, the design of the armour units, the instrumentation, and the experimental procedure.

### 3.2.1 Experimental Setup

#### 3.2.1.1 University of Ottawa Vertical Drop Test Chamber

Due to the geometric anisotropy of the Core-Loc unit, the development of drag and inertial forces are expected to be dependent upon the direction of the flow, alternatively, its orientation, given a single flow direction. To further explore the effects of unit orientations and scales, a series of controlled drop tests were designed in order to replicate different hydraulic conditions for different armour unit configurations. For this reason, four different scales and four respective orientations were used. Figure 3-1 represents the conceptual model of the experimental setup built for this research. The tests were designed on the principle that a free falling unit will reach terminal velocity in still water (unsteady flow). This ensures that the inertia force does not work on the relative drag force, as the inertia force is proportional to the acceleration, and the drag force is proportional to the velocity squared. A video recording system was used to record the tests, later used to derive the unit`s fall velocities. To maintain the armour unit falling trajectory and orientation constant throughout the tests, the units were mounted on a set of guide wire.

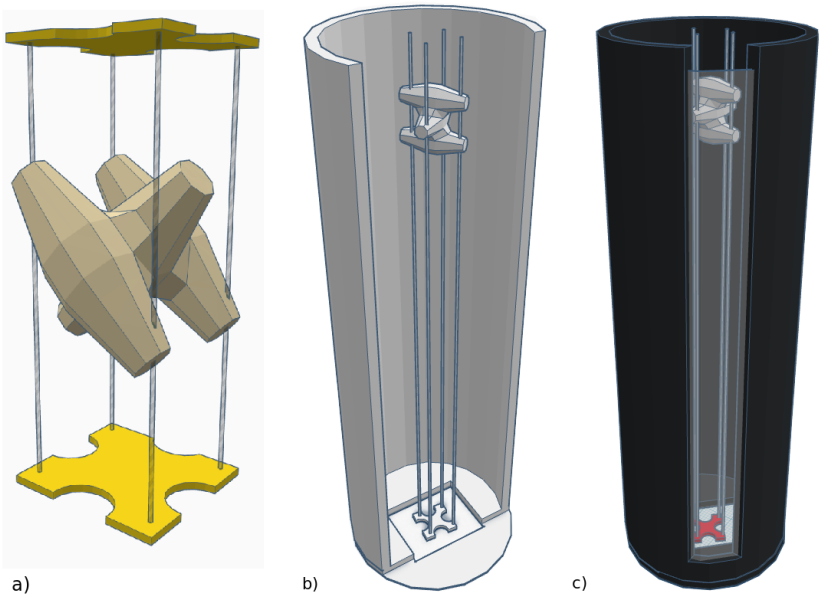


Figure 3-1: Vertical drop test chamber design prototype. (a) Sliding unit; (b) Guide wires installation; (c) Tank viewing window.

### 3.2.1.2 Experimental Design Process

The premise of the drop tests is that no inertia forces works on the units as the descend through the water column. For this, the vertical tank must be designed sufficiently high, such that the units reach terminal velocities. The required tank height was estimated based on the balance of the forces acting on a falling unit, illustrated in Figure 3-2, of different sizes and a density of 2200 $kg/m^3$. The buoyancy force, used to determine the submerged unit weight, was easily determined using the known unit mass and volume, while the drag force was estimated using four different guessed drag coefficients and the smallest projected area of a Core-Loc. The net difference between the forces represents the unit`s acceleration due to gravity ($F_g = m\ \partial u/\partial t$). The individual unit`s acceleration and velocity was calculated using these results and a time step of 0.001s. For this step, terminal velocity was defined as the point at which acceleration was smaller than $1mm/s^2$. Using basic kinematics principles, the velocities were converted into displacement. The final tank heights required for five unit sizes (5cm-25cm) and four drag coefficient guesses are summarized in Table 3.1. Realistically, the drag coefficient is greater than 1, and therefore, based on the results, a tank taller than 2.57 m will ensure that the falling model Core-Loc units will reach terminal velocity.

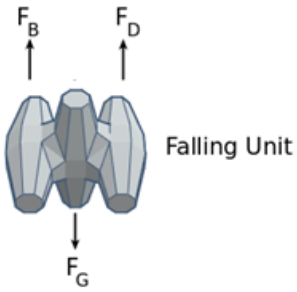


Figure 3-2: Diagram of the forces acting on a falling Core-Loc considered for the tank height determination

Table 3.1: Summary of the tank heights required to reach terminal velocity using different Core-Loc model sizes

| **Drag Coefficient** | **Tank Heights Required to Reach Terminal Velocity (m)** | | | | |
|---|---|---|---|---|---|
| | **Unit Characteristic Length, $C_L$ (m)** | | | | |
| | **0.05** | **0.1** | **0.15** | **0.2** | **0.25** |
| **0.5** | 1.023 | 2.055 | 3.085 | 4.114 | 5.143 |
| **1** | 0.512 | 1.026 | 1.540 | 2.055 | 2.570 |
| **1.5** | 0.341 | 0.684 | 1.026 | 1.369 | 1.711 |
| **2** | 0.255 | 0.512 | 0.769 | 1.026 | 1.284 |

To build the vertical tank, five recycled rain barrels were used (purchased locally). Four of the barrels` tops and bottoms were cut out, while the fifth barrel was used to create the connecting rings between the stacked barrels, as shown in Figure 3-3(a). These steps were required to maintain a consistent diameter along the length of the tank, while providing a secure connection. The rings were fixed using strong bonding PVC adhesive and a series of hexagonal bolts installed in a zigzag pattern along both sides of the connections. FLEXSEAL adhesive was used for all the connections, as this was proved to create the most reliable waterproof bond based on previous works. This sealant was applied along the inside and outside connections, to minimize any potential leakage. Once the construction was completed, a 0.12m opening was cut along the length of the barrel (as shown in Figure 3-3(a)), for the installation of a plexiglass window. The installation of the plexiglass was necessary in order to visualize and record the tests. The full technical drawing of the vertical tank is available in Appendix A.1. Additionally, a bottom window was installed to provide visual aid while mounting the bottom guide plates. Lastly, four bolt anchors were installed along the bottom of the barrel to install the fishing line used as guidelines, which can be seen in Figure 3-3(b).

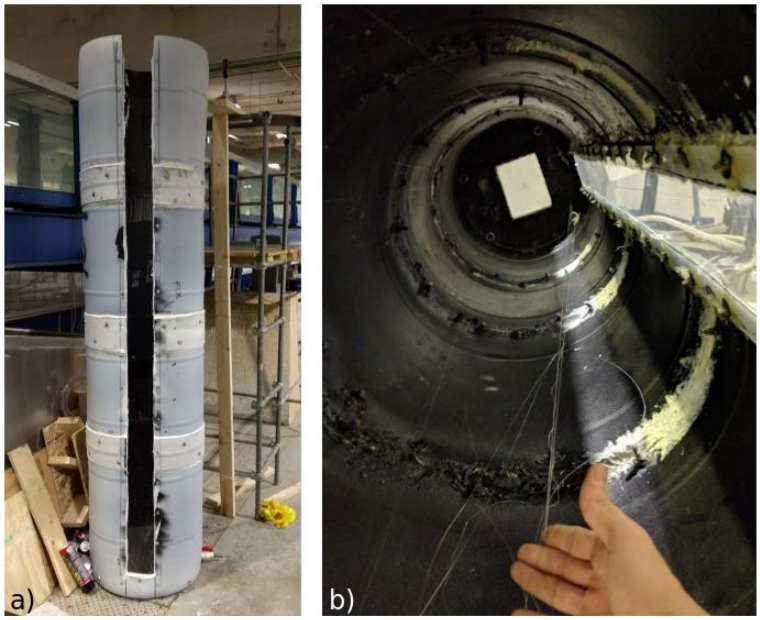


Figure 3-3: Vertical tank construction. (a) Rain barrels' connections; (b) Fishing line and hooks installation.

### 3.2.1.3 Test Chamber Physical Characteristics

The final testing chamber was 2.62 m tall, with a constant diameter of 0.56 m, giving a tank capacity of 0.6 $m^3$, or 600 $l$. In oeder to give access to the top of the tank and to prevent accidents, the tank was secured to a fixed scaffold work platform, visible in the background of Figure 3-4(a). A drain valve was installed at the bottom of the tank to ease draining. The tank was placed on a raised bottom support for easier access to the magnets holding the bottom guide plate. The upper frame support was required to provide a base for the top guide plate. To ensure a constant location of the upper frame throughout testing, a series of grooves were made along the rim of the top barrel. The last step was to paint and install LED lights at the top and bottom of the barrel. This step was required for the image processing, which required a high contrast between the color of the unit and its surroundings. More details regarding this will be provided in Section 3.2.4.

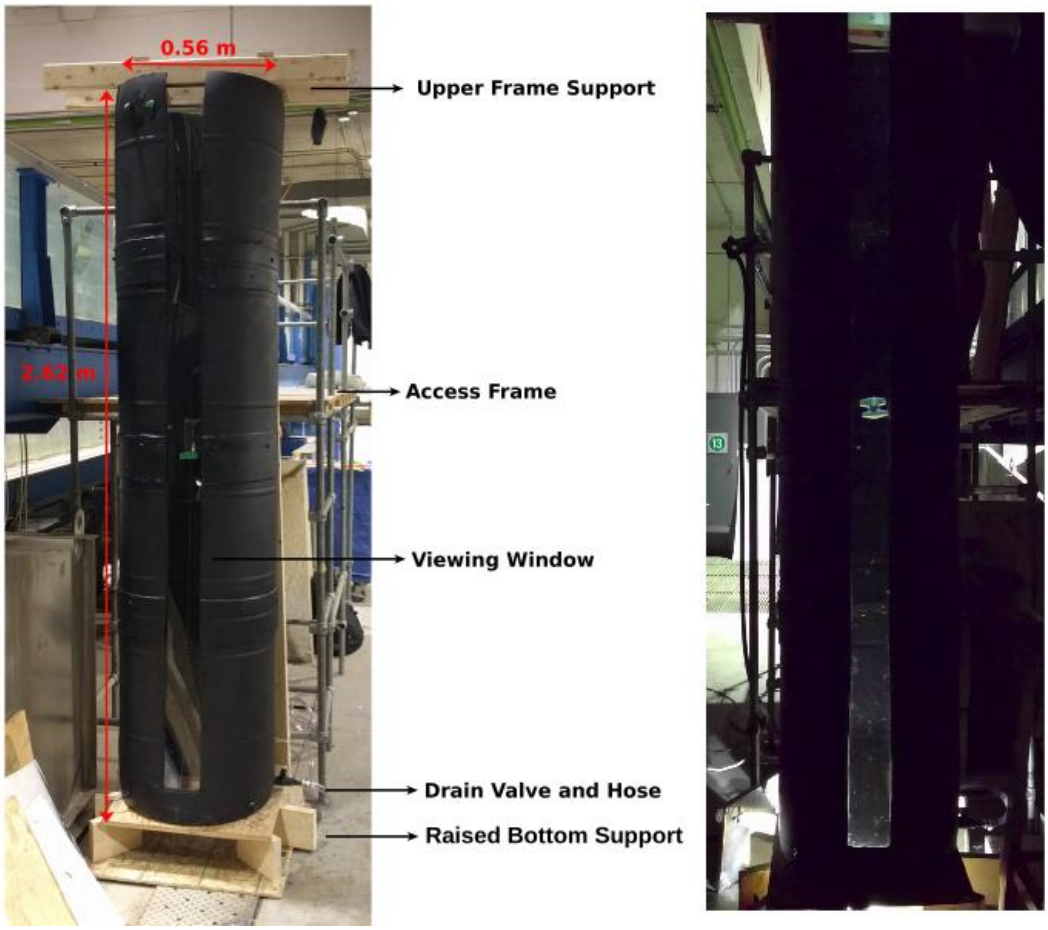


Figure 3-4: Final Experimental Setup. (a) Test Chamber Physical characteristics; (b) Frame extracted during testing, showing the contrast between the armour unit and the background achieved using LED lights.

## 3.2.2 Model Design and Setup

### 3.2.2.1 Armour Unit Orientation

Breakwaters` armour layer interlocking and packing density is affected by the techniques used for placement of concrete units. Consequently, the armour stability is influenced by the placement of

armour units. Generally, breakwaters armour layer are constructed following a set of rules or guidance specified by the inventor of each type of concrete unit. For this experiment, the Core-Loc armour unit orientations were chosen based on a quantitative research performed by Dr. John-Paul Latham et al (2013) at ICL.

The study presented new modelling and analysis methods for concrete armour unit systems using FEMDEM, based on a full scale breakwater located in San Vincente, Chile. The research was focused on the local variation of packing density, centroid spacing, unit contacts, and orientations. As a result, stereographic projection analysis of unit axis orientations was presented as a 3D representation of the Core-Loc units orientations while placed, or adopted by the units as the layer is subjected to wave action. An adaptation of such projection is shown in Figure 3-5. Since drag force is proportional to the projected area, and the shown unit orientations can be grouped into four different categories (color-coded) that are mirror images of each other, only four orientations were chosen for these experiments. The tested orientations are labeled in the upper right corner the figure. These are of interest for this research since they have different geometric properties and are common orientations associated with breakwaters constructed using Core-Loc armour units.

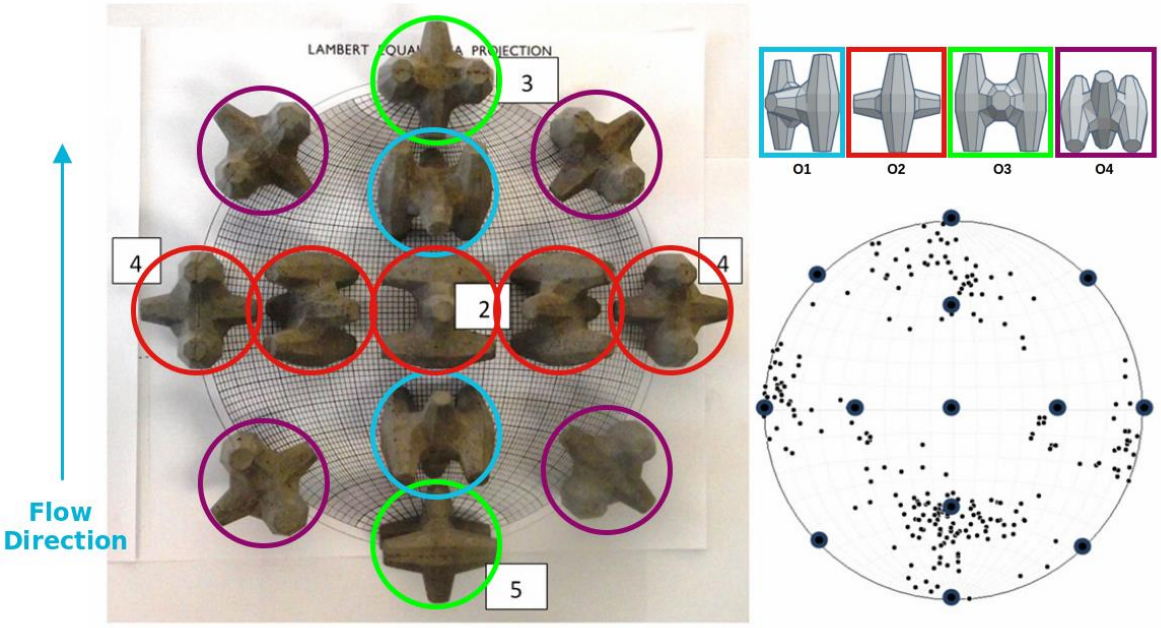


Figure 3-5: Armour unit orientation selection process (adapted from Latham et al., 2013)

### 3.2.2.2 Scaled 3D Printed CAUs

To investigate the scale effects on drag and inertia forces acting on Core-Loc armour units, down-scaling of a prototype breakwater constructed with 2.75 m Core-Loc units was done based on four different length scales. The tests were performed using four 3D-printed Core-Loc armour units with characteristic lengths of 6.1 cm, 7.9 cm, 10.9 cm, and 18.3 cm (roughly corresponding to geometric scales of ~1:45, ~1:35, ~1:25, and ~1:15, respectively). To illustrate their relative size, scaled models of the Core-Loc armour units are shown in Figure 3-6. Table 3.2 summarizes the geometric proprieties of each orientation and scale.

Table 3.2: Controlled Drop Tests Summary –Armour unit characteristic length, corresponding geometric scale and projected area normal to flow direction for each orientation

| Scale | Characteristic Length, $C_L$ (cm) | Corresponding Geometric Scale | Total Projected Area Normal to Flow Direction $\times 10^{-3}$, A ($m^2$) | | | |
|---|---|---|---|---|---|---|
| | | | O1 | O2 | O3 | O4 |
| **1** | 6.1 | 1:45 | 2.78 | 1.82 | 2.82 | 2.64 |
| **2** | 7.9 | 1:35 | 4.48 | 2.93 | 4.55 | 4.26 |
| **3** | 10.9 | 1.25 | 8.20 | 5.37 | 8.31 | 7.79 |
| **4** | 18.3 | 1:15 | 22.55 | 14.76 | 22.86 | 21.43 |

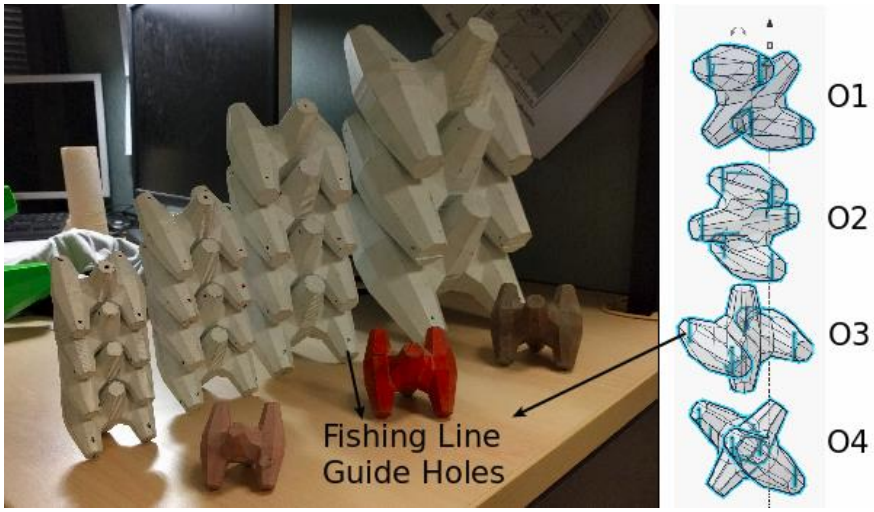


Figure 3-6: Scaled 3D printed armour units and their relative size (left to right – Scale 1,2,3,4)

The scaled models were designed in Tinkercad (free CAD design tool), and printed at the UO Richard L`Abbe Makerspace, using Ultimaker 2+ 3D printers. These printers are efficient, user-friendly and deliver consistent print results. The material used was polylactic acid (PLA), a thermoplastic polymer. The scaled models were 3D printed contrary to casting, as each orientation required different configuration for the fishing line guide holes, and the design comprised of a hollow chamber, both components shown in Figure 3-7. Four volume-averaged unit densities (1150, 1550, 1960, 2365 $kg/m^3$) were considered in order to simulate the full-range of prototype run-up velocities (2% exceeding values for run-up velocity, based on EurOtop, 2016 – refer to Section 2.3) likely to occur on the slope of a Core-Loc armored breakwater. The empirical run-up calculations were based on the 2.75 m prototype unit, placed on a 4H:3V slope (typical for rubble mound breakwaters constructed with Core-Loc units – CLI, 2012), with a water depth at the toe of the structure of 6 m. The prototype significant wave height was estimated based on the relationships between design wave height and armour unit volumes included in the CLI Core-Loc design guide tables, corresponding to 6 m. The target densities were achieved for each test case by inserting a measured amount of lead shot (lead pellets) into the interior chamber printed into the units. The required lead mass was determined by subtracting the printed PLA unit mass from the target mass for each density. A detailed summary of the

scaled units mass, lead quantities, and achieved mass during testing is provided in Appendix A.2. The target densities were successfully achieved during testing for all scales and orientations, except Scale 4, Orientation 1. This was due to the unit being damaged during testing.

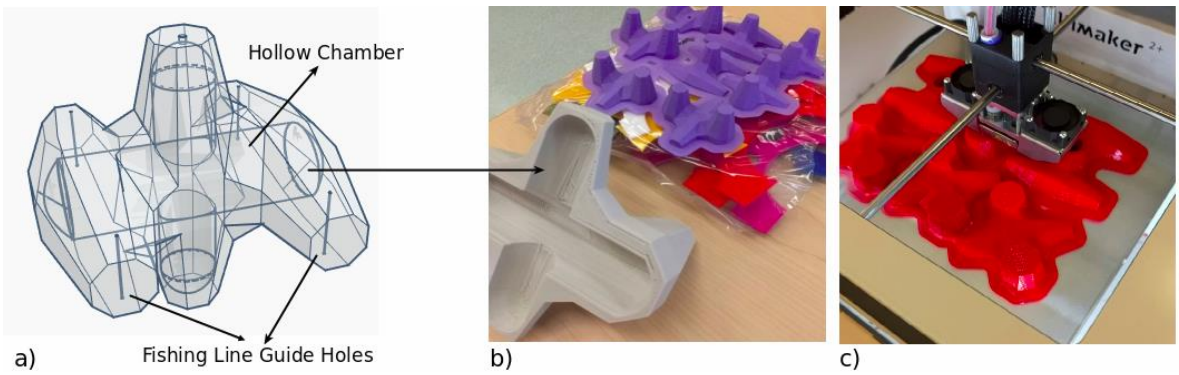


Figure 3-7: Scaled 3D printed Core-Loc Unit. (a) Tinkercad design; (b) Hollow chamber; (c) Ultimaker 2+ printing

Table 3.3. Controlled Drop Tests Summary –Armour unit characteristic length, corresponding geometric scale and comparison between target and achieved volume-averaged unit densities for each orientation

| **Scale** | **Characteristic Length, $C_L$ (cm)** | **Corresponding Geometric Scale** | **Target volume-averaged unit densities, $\rho$ $(kg/m^3)$** | **Achieved volume-averaged unit densities, $\rho$ $(kg/m^3)$** | | | |
|---|---|---|---|---|---|---|---|
| | | | | **O1** | **O2** | **O3** | **O4** |
| **1** | 6.1 | 1:45 | 1150 | 1150.0 | 1150.0 | 1150.0 | 1150.0 |
| | | | 1550 | 1555.0 | 1555.0 | 1555.0 | 1555.0 |
| | | | 1960 | 1960.0 | 1960.0 | 1960.0 | 1960.0 |
| | | | 2365 | **2365.0** | **2265.4** | **2275.3** | **2205.6** |
| **2** | 7.9 | 1:35 | 1150 | 1150.0 | 1150.0 | 1150.0 | 1150.0 |
| | | | 1550 | 1555.0 | 1555.0 | 1555.0 | 1555.0 |
| | | | 1960 | 1960.0 | 1960.0 | 1960.0 | 1960.0 |
| | | | 2365 | **2274.5** | **2203.0** | **2331.6** | **2274.5** |
| **3** | 10.9 | 1.25 | 1150 | 1150.0 | 1150.0 | 1150.0 | 1150.0 |
| | | | 1550 | 1555.0 | 1555.0 | 1555.0 | 1555.0 |
| | | | 1960 | 1960.0 | 1960.0 | 1960.0 | 1960.0 |
| | | | 2365 | **2167.7** | **2148.5** | **2286.4** | **2351.0** |
| **4** | 18.3 | 1:15 | 1150 | 1150.0 | 1150.0 | 1150.0 | 1150.0 |
| | | | 1550 | 1555.0 | 1555.0 | 1555.0 | 1555.0 |
| | | | 1960 | 1960.0 | 1960.0 | 1960.0 | 1960.0 |
| | | | 2365 | **n/a** | **2267.1** | **2299.4** | **2365.0** |

### 3.2.2.3 3D Printed Guide Plates

Prior to releasing the unit into the column of water, the guidelines were run through designated channels printed into the units that served to restrain the unit to a single orientation during the course of its fall. Interchangeable, customized top plates and bottom plates for the guide wires were fabricated for each geometric scale and orientation, providing a simple mechanism for controlling the guide wire layout appropriate to each unique test case (shown in Figure 3-8(a)). To fix the plates throughout testing, magnets were used on the bottom viewing window of the testing chamber and the custom build lid. Each plate was designed with a magnet housing compartment, as shown in Figure 3-8(b). This allowed precise alignment between the top and the bottom of the tank. During the construction phase, the centroids of the top and bottom viewing plates were marked and aligned. This ensured a consistent and constant positioning of the plates throughout the tests. Neodymium rare-earth magnets –this is the strongest type of permanent magnets made; were used to fix and secure the position of the plates. Sufficient tension was applied to the fishing line (approximately 80% of the fishing line tensile capacity, roughly 8lbs or 35N) in order to restrain the unit from deviating from its intended fall-orientation and to ensure a near-vertical trajectory between the release and resting point.

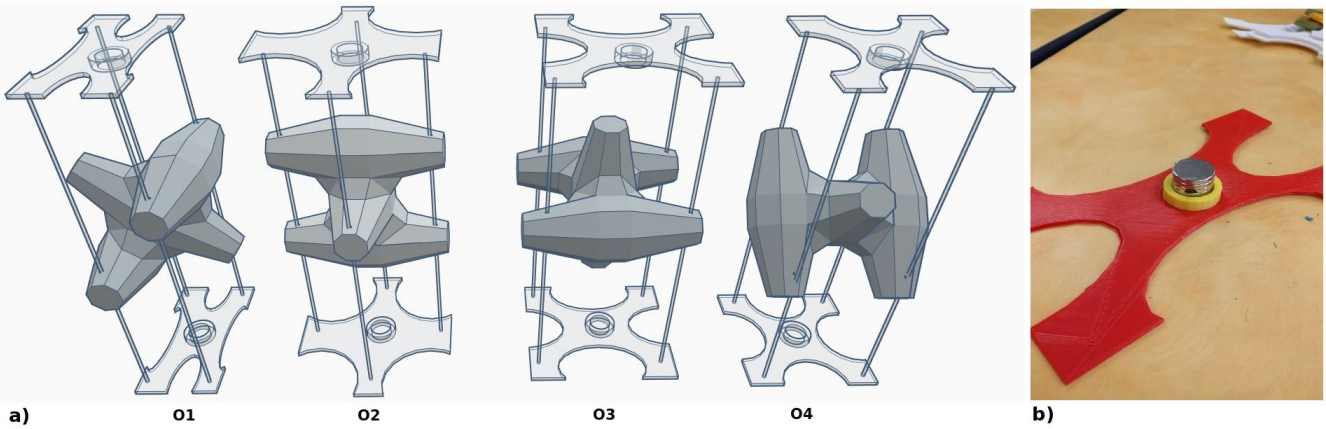


Figure 3-8: 3D printed guide plates. (a) Concept design in Tinkercad; (b) Neodymium magnets installation.

### 3.2.3 Instrumentation

A relatively simple and non-intrusive measuring technique using image-processing was used to turn the raw video footage into displacement time-histories with exceptionally high spatial and temporal resolution. A 12 megapixels (MP) camera with automatic focus adjustment (Nexus 6P, Google, Huawei) was mounted in front of the drop chamber`s viewing window on a camera stand, at a height of 1.6 meters above the ground. This video recording system allowed for high definition recordings of the tests at 60 frames per second (fps), or a sampling rate of 60 Hz. The location and height of the mount was chosen in order to capture the full height of the testing chamber, as it can be seen in Figure 3-4(b).

### 3.2.4 Experimental Procedure Methodology

#### 3.2.4.1 Controlled Drop Tests

The study comprises 320 separate tests, consisting of four different scales, densities and respective orientations, with each case being repeated five times. Throughout the experiment, the water level in the tank was maintained a constant 2.5 m.  Figure 3-9 represents the general experimental protocol used to keep identical hydraulic conditions and minimize errors introduced by changing the tested Core-Loc armour units. For each test condition, the first step consisted of lowering and fixing the bottom guide plate on the bottom of the tank. The fishing guide wires were then run-through the designated channels printed into the units. While the unit was suspended, the top guide plate was mounted, and the wires were tensioned. Once the water surface stabilized, the unit was released and the test was recorded. This was repeated five times verify test repeatability and minimize test inconsistencies. Once each test was complete, the unit was filled with lead pellets (pre-measured quantities), until the next target density was achieved. Once all four target densities were tested for one scale and one orientation, the unit was removed and the next orientation was installed.

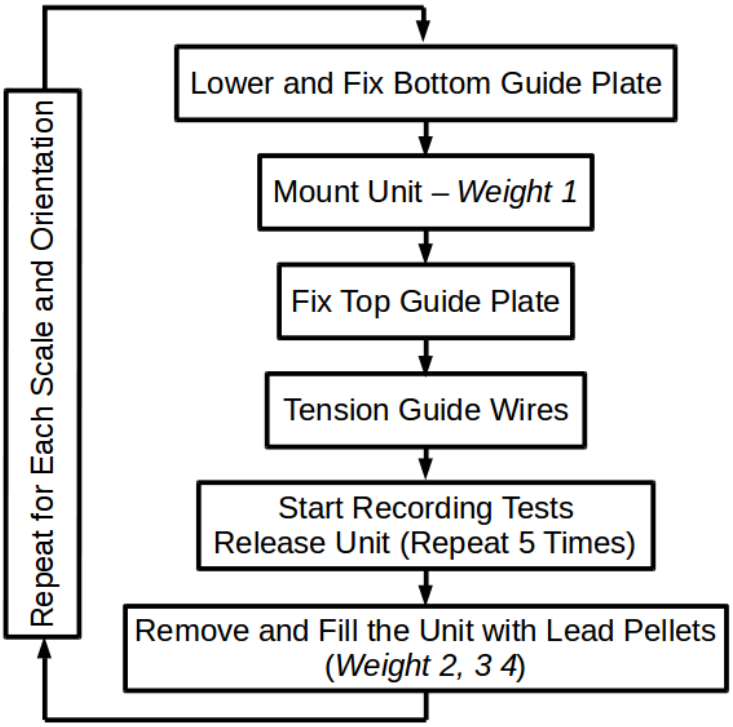


Figure 3-9: Experimental methodology diagram

#### 3.2.4.2 Data Processing and Analysis System - Octave

A simple automated process to manipulate the color field of individual frames extracted from video footage taken of the units freefalling through a column of water was devised and used to obtain detailed histories of displacement, velocity, and acceleration for the test conditions. To accomplish this, a GNU Octave data processing algorithm was developed. GNU Octave is a free numerical computation software, featuring syntactic compatibility with MATLAB.

### 3.2.4.3 Image Processing

The videos were recorded at 60 fps which yielded anywhere between 120 and 480 individual frames each of which containing a unique step in the evolution of the hydrodynamic-solid interaction unfolding. LED light sources were used at each of the extreme ends of the tank to illuminate the interior of the tank, increasing the contrast between the unit and its surroundings. This, in turn allowed for simple conversions of the original RGB-color raster to black and white images. In GNU Octave this was achieved using the "*greythresh*" and "*im2bw*" function files (part of the software`s image processing package), which converted the frames to binary images. The two functions were used to convert the individual frames initially to a grayscale image, and then to a binary black and white image. The resultant binary image consisted of all the original pixels in the input image replaced with a value of 1 and 0 based on the luminance of the pixel. A value of 1 was assigned to the white pixels, while all other pixels were given the value 0, process illustrated in Figure 3-10.

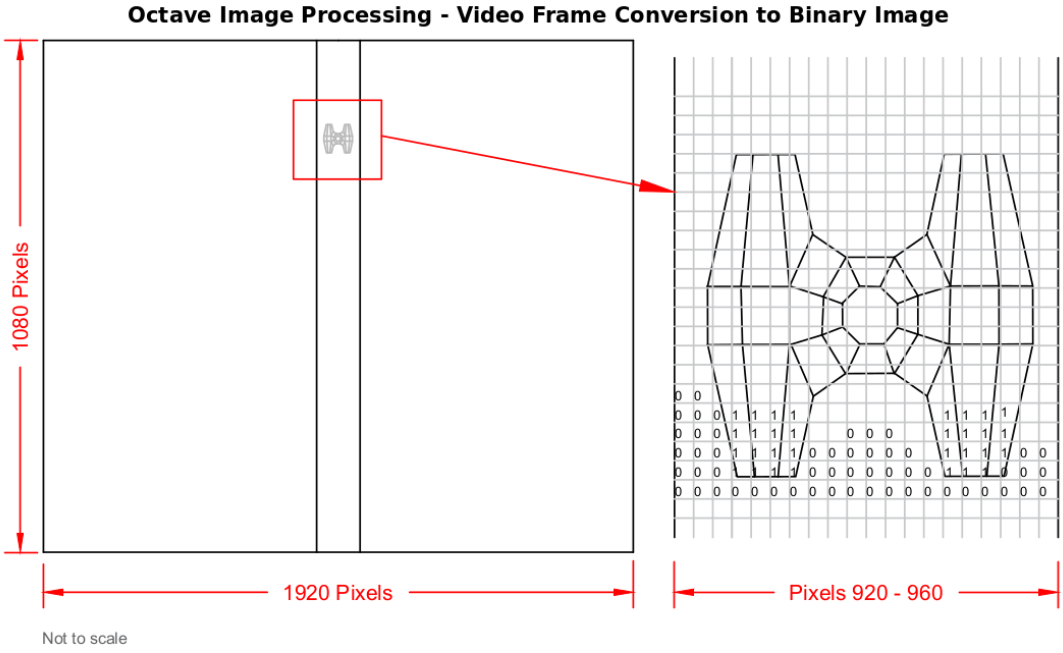


Figure 3-10: Illustrated GNU Octave frame conversion to binary image

To optimize the quality of the individual video frames prior to being processed in GNU Octave, the raw footage was edited initially in Kdenlive. This is a powerful free and open-source editing software, which was used to separate, edit and extract the individual test frames from the raw videos. This process is illustrated in Figure 3-11, showing the conversion from raw frames (a), to a color corrected image in Kdenlive (b), and finally, to a binary image (c) in GNU Octave. Since the functions used to convert the raw image to a black and white picture depend on the luminance of the pixels and the goal was to determine the location of the Core-Loc armour unit, any contamination from the additional light pixels present in the background had to be eliminated. Kdenlive was used to crop the original images and isolate the tank`s viewing window. Additionally, the image was color corrected, by dimming the original image, to facilitate the detection of the lighter pixels in GNU Octave.

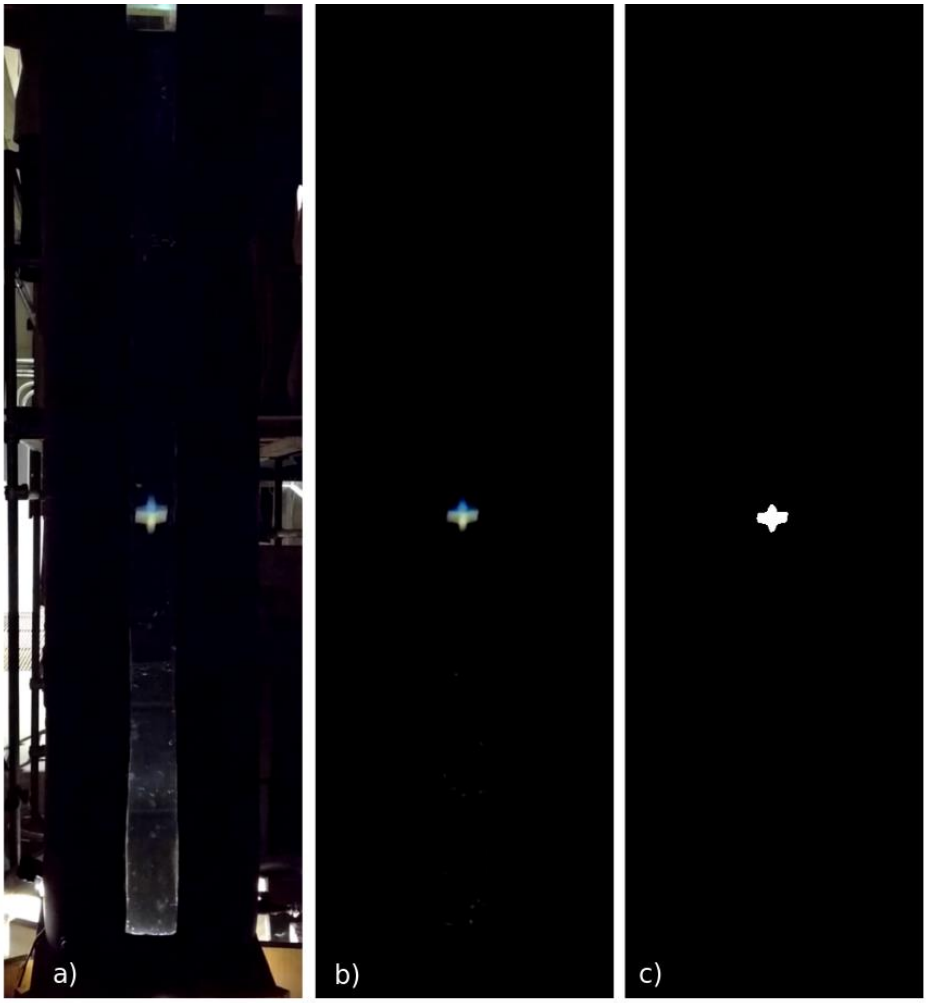


Figure 3-11: Image processing. (a) Raw footage; (b) Kdenlive color correction; (c) GNU Octave binary conversion.

### 3.2.4.4 Displacement Time History

By calibrating the conversion coefficient that is used to determine which RGB values go to white and which go to black, the entire process was automated for all the video footage captured, leaving only a single white patch of pixels on a black background. The GNU Octave script developed looped through each column and row of the binary image and returned the location of the nonzero elements (using the "*nnz*" function). From there, the displacements time-histories were constructed by locating the lowest occurring white pixel in each frame (time step) which could then be converted into a known physical location, from a calibration curve developed by using known elevations of several benchmarks also visible in the videos taken (shown in Figure 3-12). By using this calibration technique, any errors introduced by potential optical distortion from the camera lens were eliminated, as the calibration and video frames would include the same optical aberration.

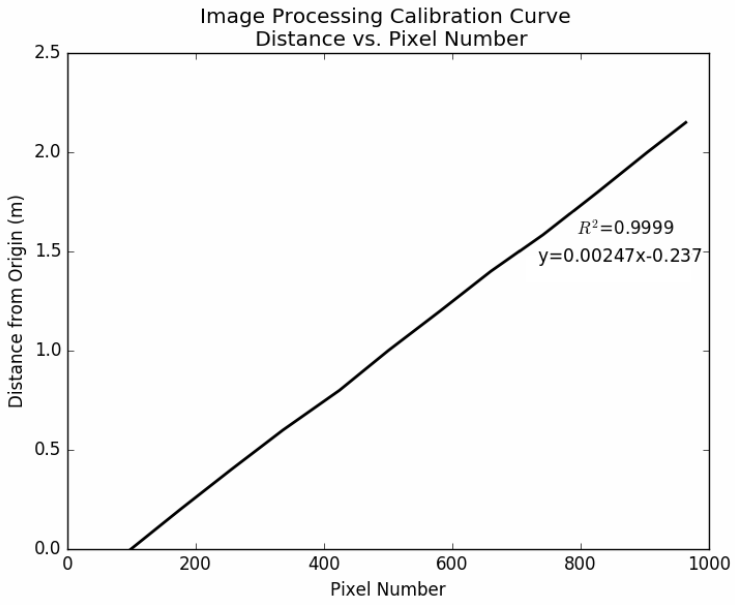


Figure 3-12: Image Processing Calibration Curve

### 3.2.4.5 Quality Control

Five runs were conducted for each unique test case to verify test repeatability and reduce the effects of inadvertent, small test inconsistencies (residual currents, straining of guidelines, etc.), potentially captured in the raw data. Image processing of the high-speed footage taken during the armour units descent yielded a unique displacement time-history for each test case, which was subsequently used to derive its velocity and acceleration time-history. The displacement time-histories obtained from the five runs performed for each test were averaged in order to remove small statistical test inconsistencies that might have arisen between runs, as shown in Figure 3-13. Drop tests without water were also performed on the scaled units to ensure that the friction contribution between the PLA material and the fishing line is negligible.

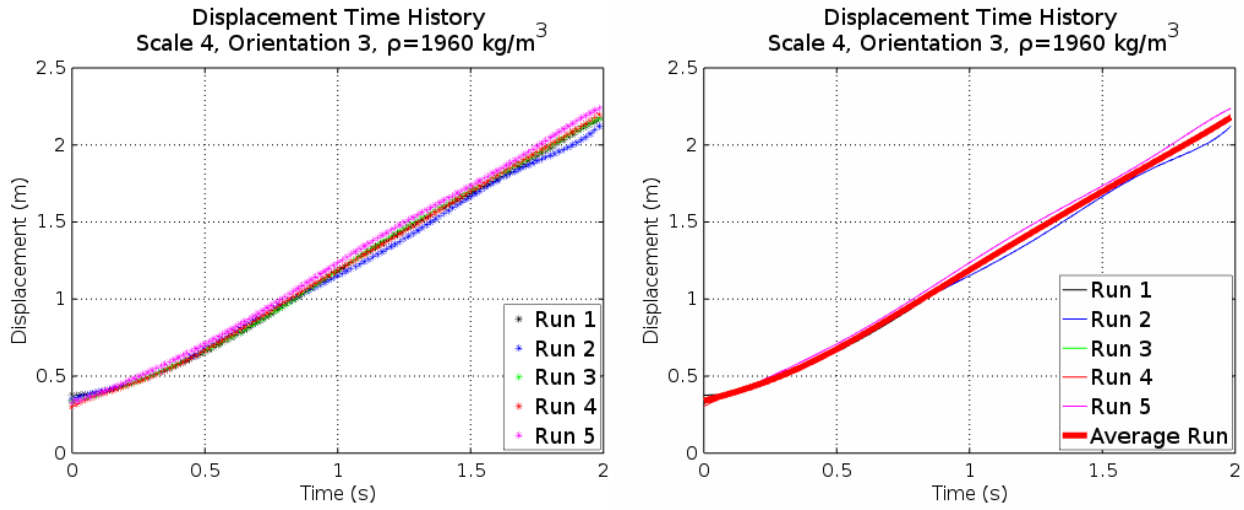


Figure 3-13: Example displacement time-history repeatability (Scale 4, Orientation 3, Density 1960 kg/m^3).

## 3.3 Results and Analysis

In this section, the results of the study are presented in more detail. For analysis purposes and due to space constraints, out of the 320 tests, only select results will be presented from now, covering all the test parameters (scale, orientation, density). These represent typical results, with the full analysis available in the appendix, referenced accordingly in text.

### 3.3.1 Displacement Time History

Accurate estimation of the Core-Loc unit's displacement-time history from the release point to the resting point at the bottom of the tank is essential for the optimization of Morison drag and inertia force coefficients. Any errors introduced by the camera footage processing will translate in inaccurate velocity and acceleration calculations, the two non-constant terms used to estimate the force coefficient. Results shown in Figure 3-14, representing the displacement time-history of Scale 2, Orientation 2 (S2O2), demonstrate that using the experimental setup designed for these experiments, the downscaled Core-Loc unit are capable of reaching terminal velocity during the short fall time. A clear region where the armour units are accelerating is visible just after the release (*t=0 s*). As the unit travels through the column of water, the slope of the displacement curve becomes linear, indicating that the unit does not accelerate. The preliminary observations of these results indicate that the drag force component can be isolated in Morison equation.

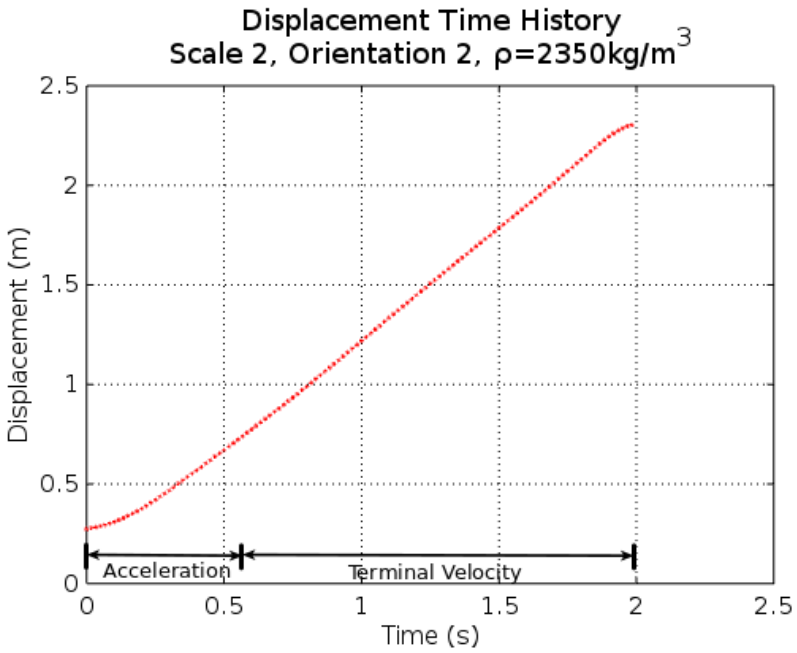


Figure 3-14: Displacement time history illustrating the acceleration and terminal velocity zones - Scale 2, Orientation 2.

As it would be expected, the unit`s density heavily influenced the differences in the total time required to traverse the column of water. These results are shown in Figure 3-15, showing a clear distinction between the travel time of the test cases with the highest density (2365 $kg/m^3$) and the cases with lower density. From the same figure, it is clear that different fall-orientations had a significant effect on the total fall time, the pattern becoming more evident as the volume-averaged density of the unit

decreased. The units with the highest density took on average between 1.9 and 2.5 seconds to reach the bottom of the tank, showing small spread of the results between different orientations. On the other hand, the spread of the travel time increases as the density of the units' decrease. This is most evident for the test cases with the lowest density (1150 $kg/m^3$), with a considerable difference between the total time to traverse the water column required by Orientation 2 (3 s) and Orientation 3, taking approximately 5.8 seconds to cover the entire water column.

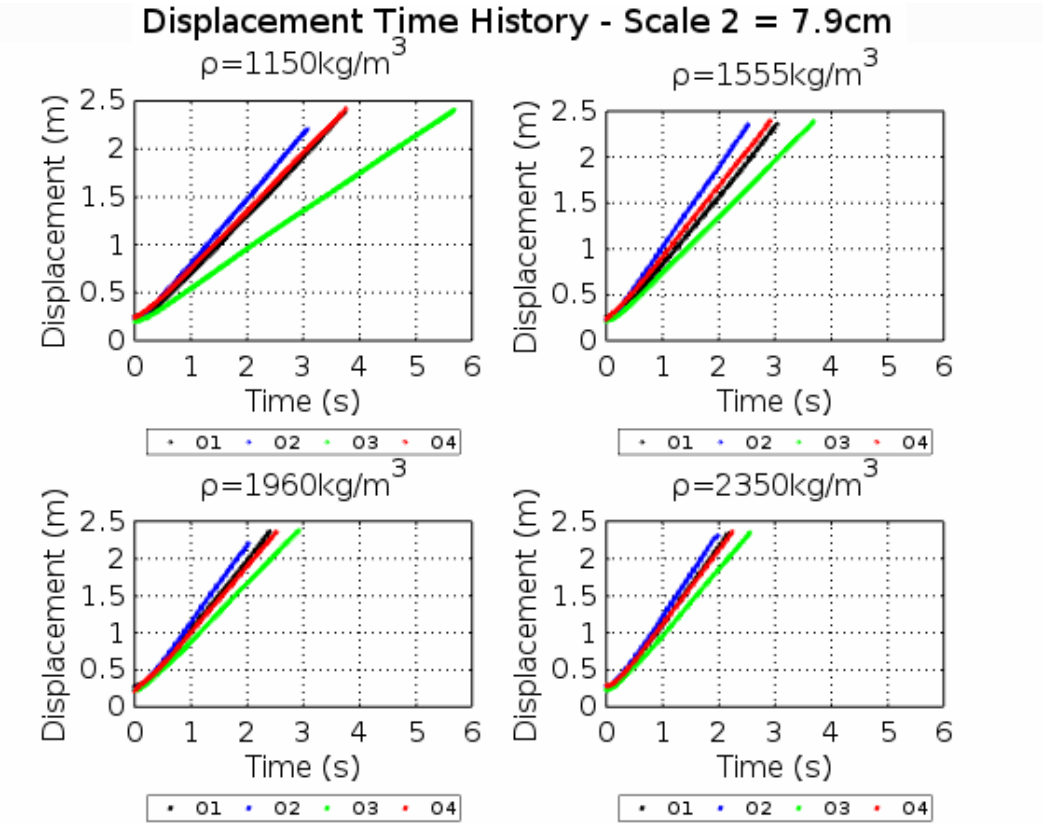


Figure 3-15: GNU Octave image processing displacement time history of all Core-Loc orientations separated by scale (Density 1960 $kg/m^3$).

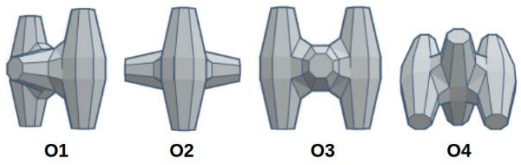


Figure 3-16: Tested Core-Loc armour unit orientations

Figure 3-16 represents the different orientations examined during this study. This image will accompany various results presented in the following sections to aid with the analysis and for illustration purposes. The figure is titled accordingly here, however no additional labels will be included from now on.

The displacement time histories results separated by unit orientation and scale, can be seen in Figure 3-17. Similarly, it is evident from these results that fall-orientation (equivalently, flow direction) had a

significant effect on the total time it took to traverse the column, indicating significantly different behavior in the development of drag and inertial forces during the fall. The difference between the slowest falling orientation (O3) and the fastest (O2) is visible for each tested scale. All results indicate little variation in the displacement time histories of Orientations 1 and 4. The discrepancy between the total fall times can be attributed to O2`s relatively smaller projected area normal to the flow direction (fall direction), compared to O3, whose total projected area is 55% larger compared to O2. The processed displacement results indicate substantial differences of flow resistance experienced by units during their fall linked to differences in projected areas normal to flow direction (subsequently flow direction). These preliminary observations can be related to stationary units inside an armour layer, which depending on flow direction and orientation can experience different hydrodynamic forces.

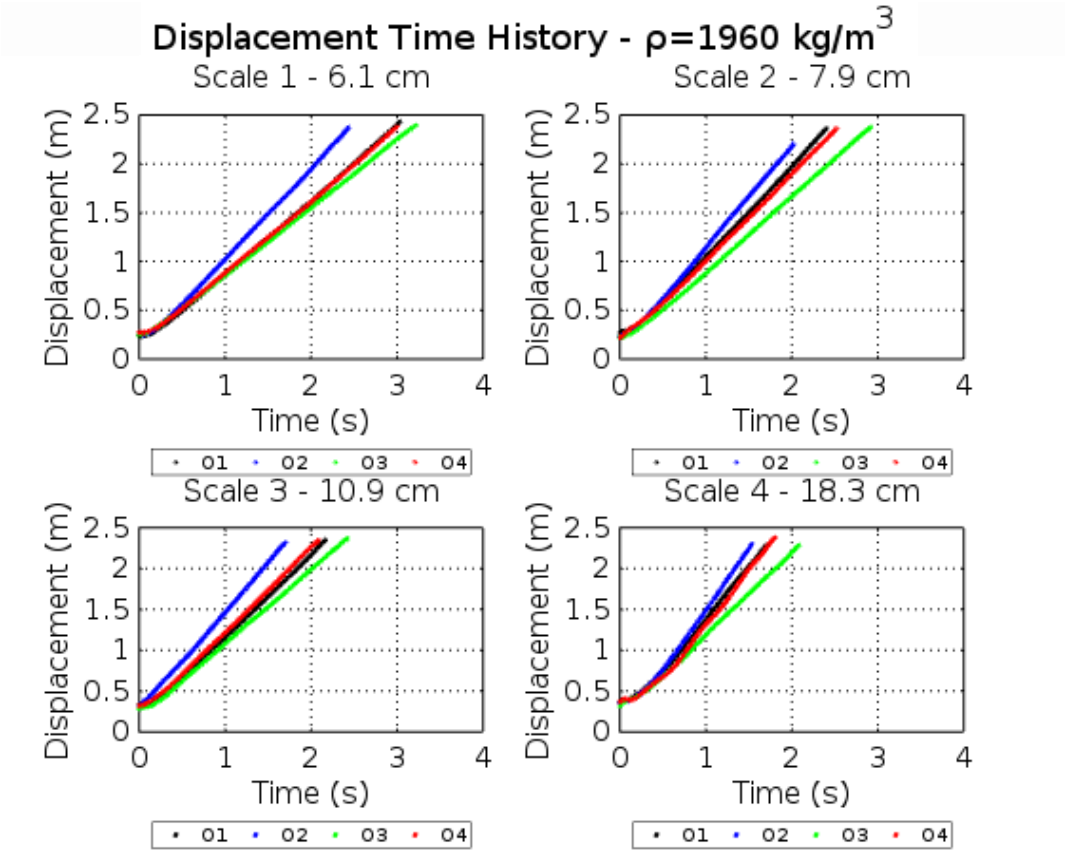


Figure 3-17: GNU Octave image processing displacement time history of all Core-Loc orientations separated by the volume-averaged densities (Scale 2 = 7.9 cm).

### 3.3.2 Armour Unit Kinetics

The velocity and acceleration time histories of the Core-Loc armour units were determined by taking the first and second derivatives ($\partial$) of the measured displacement ($d$) with respect to time, respectively, as shown below. Terminal fall velocity of an object falling though a fluid, in this case water, occurs when the sum of the resisting and buoyant forces are equal to the downward gravity force acting on an object. This state of force equilibrium corresponds to the unit having zero acceleration, in which case the velocity becomes quasi-constant. For the scope of this research, terminal velocities are associated with instances when the acceleration is lower than 0.05 $m/s^2$. The results of this analysis are shown for

each of the four orientations in Figure 3-18 and 3.19 separated by scale, and in Figure 3-20 and 3.21 separated by the four averaged volume densities tested. As it would be expected based on preliminary observations of the displacement results, O3 exhibits the lowest terminal velocity during all tests in addition to requiring the shortest amount of time to reach terminal velocity. Contrary, O2 reached the highest fall velocities in the longest amount of time. The results also indicate that all units continued to accelerate at small rates ($< 0.2\ m/s^2$), approaching terminal velocity, except orientations 1, 2 and 4 for the highest target densities and the largest scale tests (S4, 2350 $kg/m^3$), whose descent time was too short.

$$\Delta d = \int_{t_1}^{t_2} u(t)\, dt = \iint_{t_1}^{t_2} a(t) dt$$

$$u(t) = \frac{\partial d}{\eth t}\ ; a(t) = \frac{\partial u}{\partial t} \equiv \frac{\partial^2 d}{\partial t^2}$$

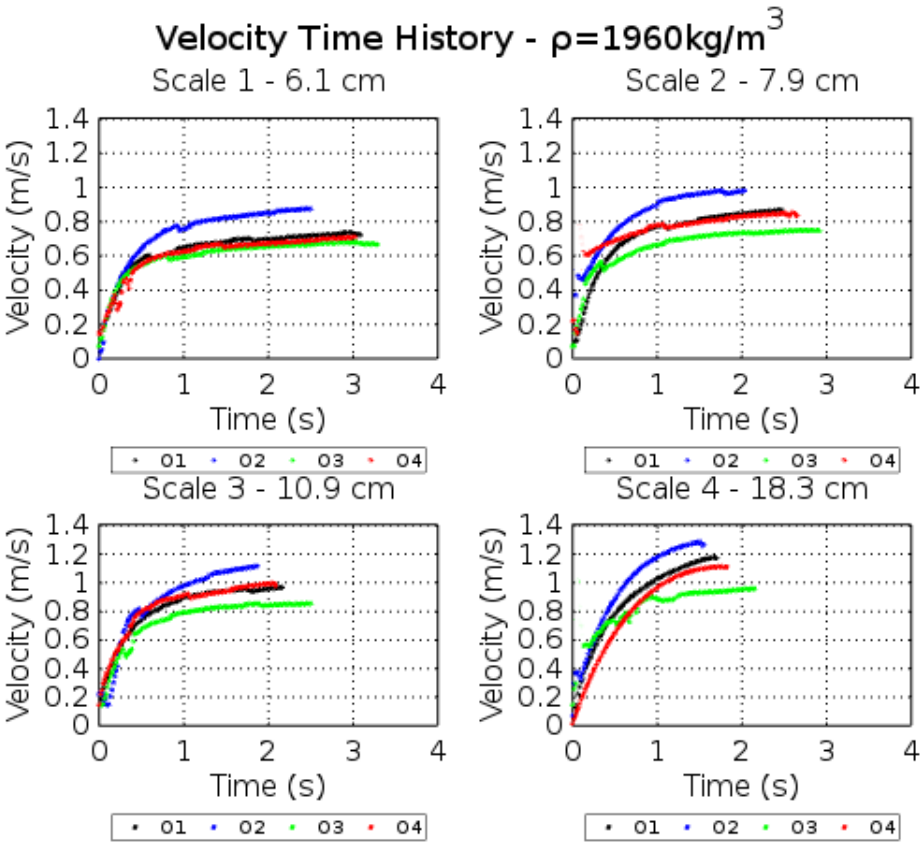


Figure 3-18: GNU Octave velocity time history of all Core-Loc orientations separated by scale (Density 1960 $kg/m^3$).

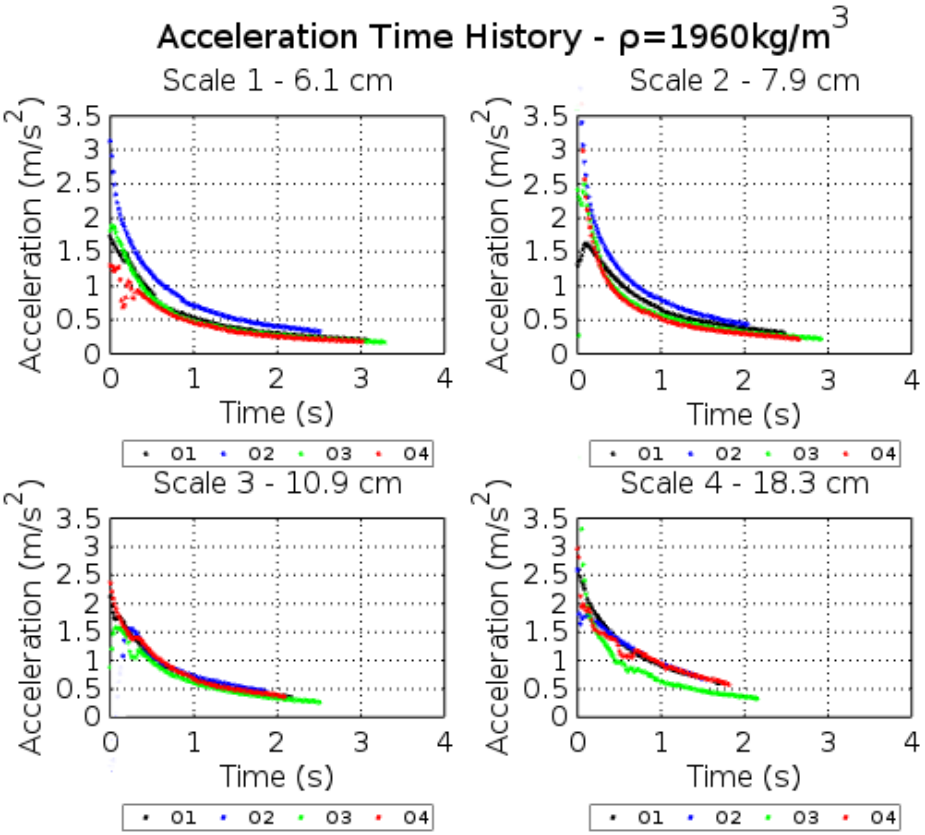


Figure 3-19: GNU Octave acceleration time history of all Core-Loc orientations separated by scale (Density 1960 $kg/m^3$).

Examining the individual orientations and the results for all averaged volume-densities, shown in Appendix A.4.2, differences in the traversal time between orientations can be observed. This is defined as the difference in time required by one unit to reach the tank bottom considering the lowest and highest densities. Based on the results, O3, O4 and O1 display the greatest spread in traversal time, listed from highest to lowest. While for O3 this is a direct result of the largest total projected area compared to the other considered orientations, for O4 and O1, this is a direct consequence of the position of the middle and exterior Core-Loc prongs, inclined at a 45º angle normal to the flow directions. As a result, these orientations experience higher lift forces during the descent, with the lift force exerted on the unit relative to the gravitational force being substantially lower at higher densities. As a result, greater portions of the gravitational force are counteracted when lower densities are deployed, resulting in reduced amounts of driving force, which causes the downward acceleration as density approaches its lowest values considered in this study.

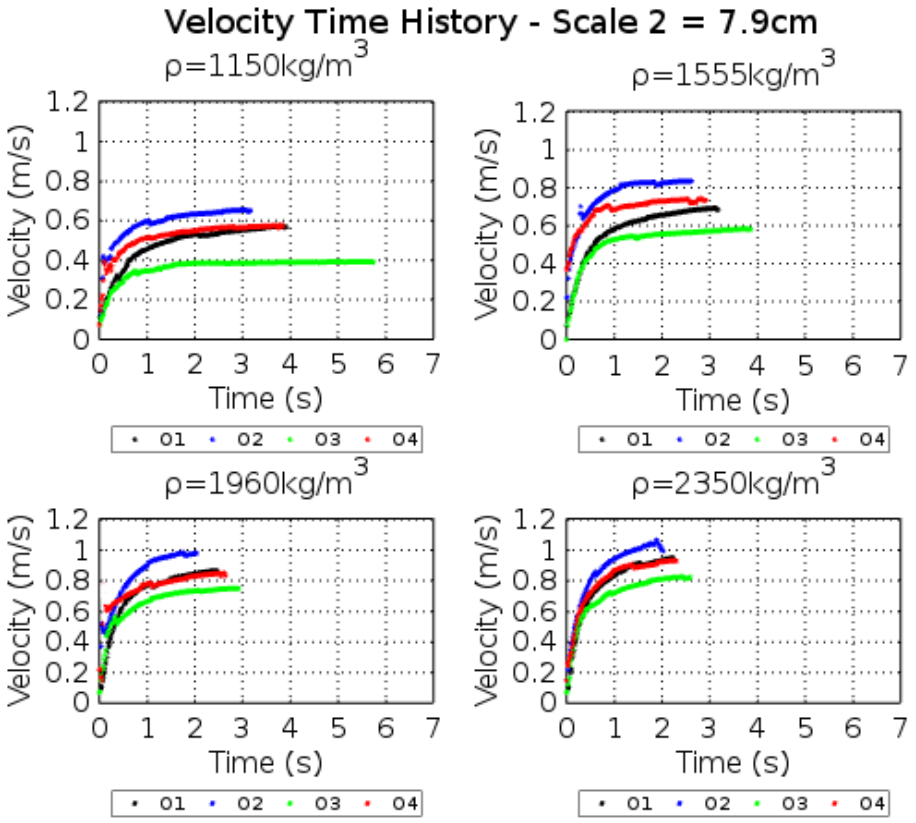


Figure 3-20: GNU Octave velocity time history of all Core-Loc orientations separated by volume-averaged densities (Scale 2 = 7.9cm ).

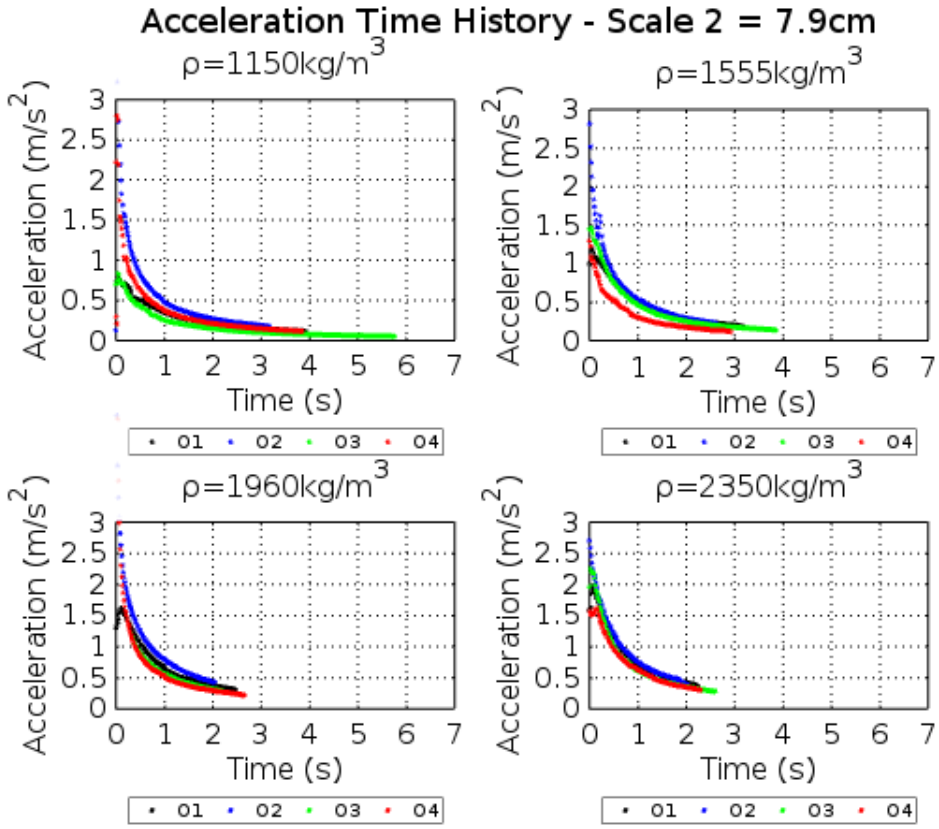


Figure 3-21: GNU Octave acceleration time history of all Core-Loc orientations separated by volume-averaged densities (Scale 2 = 7.9cm).

### 3.3.3 Drag and Inertia Force Coefficients

#### 3.3.3.1 Morison Equation Optimization

As introduced in Section 2.7.1, Morison equation is an empirical method for estimating the hydrodynamic forces acting on a submerged object. The water particle kinematics are linked to the two inline hydrodynamic force components, the drag and inertia forces, using two empirical coefficients derived from experimental data. To determine the two unknown coefficients, a basic force balance analysis of the forces acting on the unit during its gravitational fall under its own weight was performed (illustrated in Figure 3-22). The downward force of gravity was directly calculated as the product of the unit`s known mass and observed acceleration from the image processing ($F_G = m \cdot \partial u/\partial t$). The remainder of the sum of vertical forces consists of the opposing resisting forces, namely buoyancy, drag and inertia forces. As each downscaled Core-Loc model was fully submerged throughout the duration of the tests, the buoyant forces were easily determined using the models` characteristic lengths and the CLI Core-Loc volume equation. Lastly, the velocity and acceleration results extracted at each time step (frame) were used to approximate the motion terms in Morison equation. The final form of the net force balance consisted of two unknowns, the drag and inertia force coefficients, which were optimized thought an iterative process of reducing the least-squares error between the know quantities (gravity and buoyancy) and the predicted forces using Morison equation. This was done using a python algorithm (*NumPy* package was used for this step – this is a collection of high-level mathematical functions). The values were optimized at each time step such that the least-squares error is minimized.

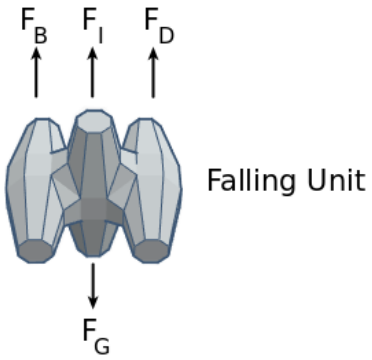


Figure 3-22: Forces acting on the falling unit.

$$F = m\frac{\partial u}{\partial t} = F_G + F_B + F_H$$

$$F_H = F_I + F_D = \rho C_M V \frac{\partial u}{\partial t} + \frac{1}{2}\rho C_D A u|u|$$

It is important to note that this iterative process of reducing the error between measured and predicted forces can arrive at multiple drag and inertia force coefficients that would satisfy the force balance. Therefore, the drag and inertia force coefficients that resulted in the smallest least-square error at each timestep was taken as the true value representative of the current state of the system. To improve the results, the coefficients should be integrated over the entire time-series of data points; however,

considering that the experiments were designed to isolate the drag force term, and the units approached terminal velocities, the errors introduced using this process were reduced.

#### 3.3.3.2 Force Coefficient Analysis

**Drag and Inertia Force Coefficients**

The best fit drag force coefficient for all tests is shown in Figure 3-23 as a function of Reynolds number. As it can be seen from the trend of the results, a sharp decrease in the drag coefficient magnitude is observed until approximately $Re = 50000$, corresponding to the flow around the units transitioning into a fully turbulent flow regime. The drag coefficient converges after to a constant value of approximately $C_D = 1.4$. A detailed quadratic and linear regression of the data sets of individual orientations (shown in red), indicates that the drag force coefficient converges towards a greater value for O2 relative to the other tested orientations as $Re$ increases. Respectively, the optimized drag coefficient for O2 converges to a $C_D$ value of 1.8 while the other tests converge to $C_D = 1.4$. Orientation 2 is the same unit that experienced the highest terminal velocity. Intuitively, it would be that the results of the optimization would yield a smaller drag coefficient. However, as O2 has a substantially smaller flow-normal total projected area compared to the other three orientations (64-68% smaller), the drag coefficient optimized for O2 had to be higher in order for the results obtained using Morison equation to produce the same motion as those observed and measured during the tests. This becomes noticeable as the $Re$ increases, and thus the dissimilarity in the drag force coefficient behavior observed between different orientations. This observation indicates that the flow development and resistance experienced by individual armour units are significantly different for the same flow conditions. In an armour layer, this could lead to an uneven distribution of forces, and ultimately to a progressive failure as individual units may be damaged. The layer stability is given by the units` interlocking forces resisting the wave action and evenly distributing the hydrodynamic forces within the layer (neighboring units). Therefore, it could be beneficial to treat O2 separately in the selection of the force coefficients for more accurate estimation of the force distribution throughout an armour layer during wave action.

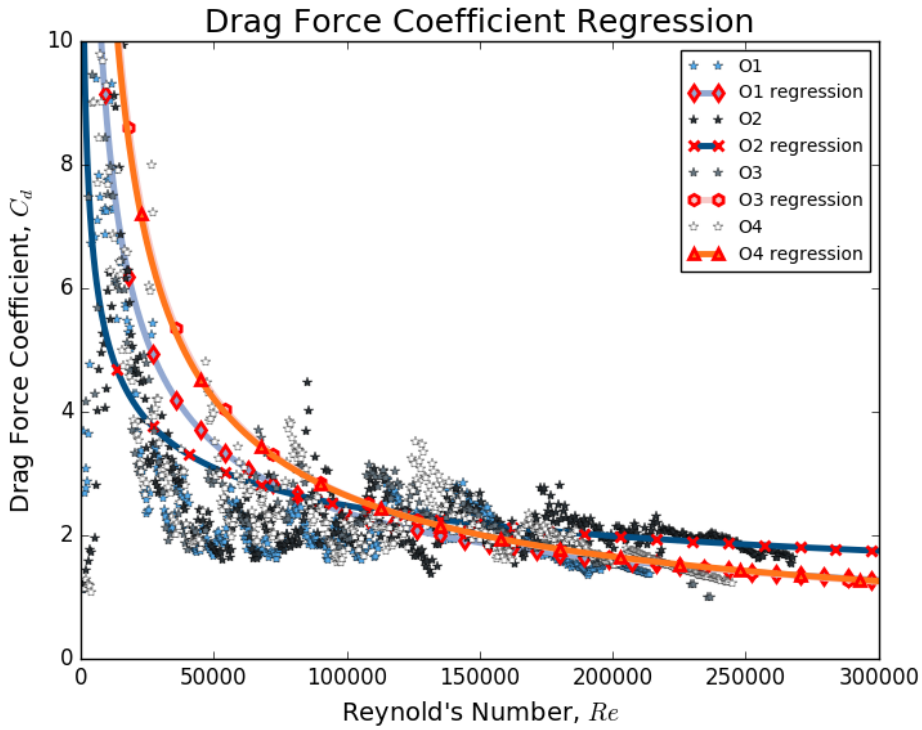


Figure 3-23: Drag force coefficient quadratic and linear regression.

The drag force coefficient results for the four orientations and volume averaged densities are shown in Figure 3-24 as functions of $Re$. Similarly, Figure 3-25 represents the same results separated by scale. The full analysis can be found in Appendix A.6. The same dissimilarity in the drag coefficient between O2 and the other three orientations can be observed. At a similar Reynold`s number, the coefficient values of O2 are visibly higher, the difference becoming more visible as Re increases. The derivation of the inertia force coefficients was beyond the purposes of this analysis, and $C_M$ values were not obtained from the analysis of the first part of the tests, when the acceleration was the highest. Therefore, the results shown for $C_D$ correspond to the analysis of the latter part of the tests, when the units approach terminal velocity.

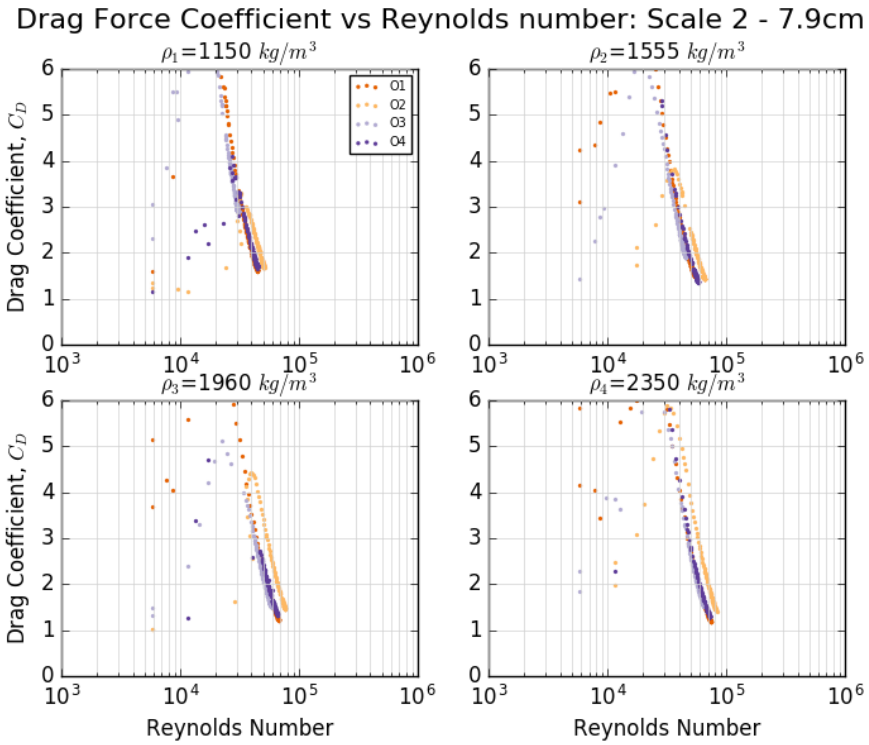


Figure 3-24: Drag force coefficient optimization results of all Core-Loc orientations separated by volume-averaged densities (Scale 2 = 7.9 cm).

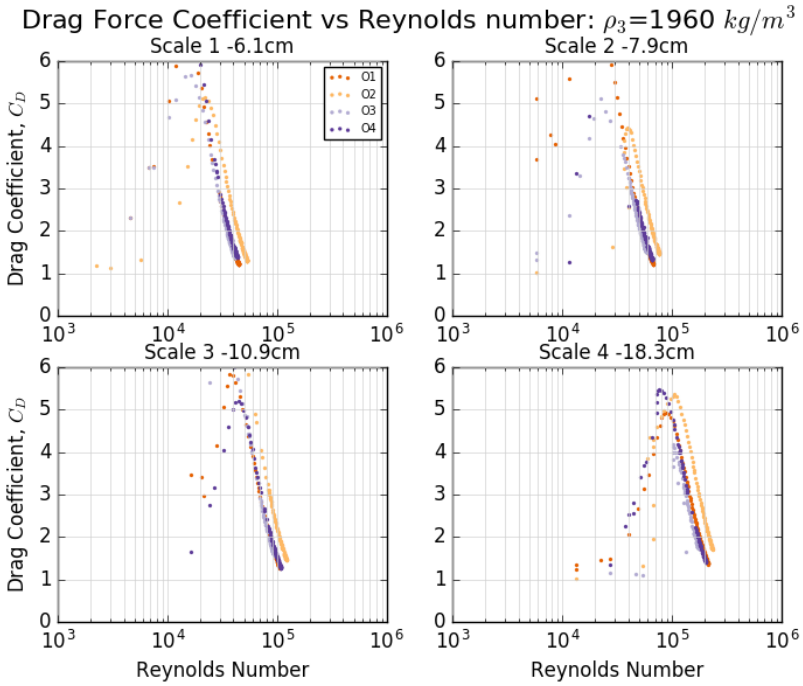


Figure 3-25: Drag force coefficient optimization results of all Core-Loc orientations separated by scale (Density 1960 $kg/m^3$ ).

## Scale Effects

The results of this study were compared with the experimental investigations on the stability of Tetrapod armour units done by Sakakiyama and Kajima (1990). Although in the original study, tests were performed under different oscillatory flow conditions, which allowed the drag and inertia force coefficients to be analyzed in terms of $K_C$ number, the results for different unit scales can be distinguished from the original figures and legends. The original plots were adapted to highlight the results of three different model scales, as shown in Figure 3-27(a) and (b). Similarly, the drag force coefficient results of the current study for different scales and orientations are shown in Figure 3-26. In both figures, the color scheme was consistently chosen such that lower or higher scales are represented by the same color in both studies. Direct comparison of the two is not feasible, as in Sakakiyama and Kajima (1990) study, the scale was simulated by varying the mass of the model armour units – in this study different geometric length scales were used. As it can be seen from both figures, both the drag and inertia force coefficients follow the same trends. Based on the variation of the force coefficients with $Re$, the results of the original study indicate that the drag forces become predominant compared to the inertia forces as $Re$ increases. This is a consequence of the acceleration decreasing as the velocity (implicitly, $Re$) increases. In other words, the drag effects become dominant as the model scales approaches prototype conditions (higher $Re$). This is evident in Figure 3-28, which represents the drag to inertia force ratio as functions of $Re$, for the four tested scales. Similar conclusions were made by Sakakiyama and Kajima, results shown in Figure 3-27(c).

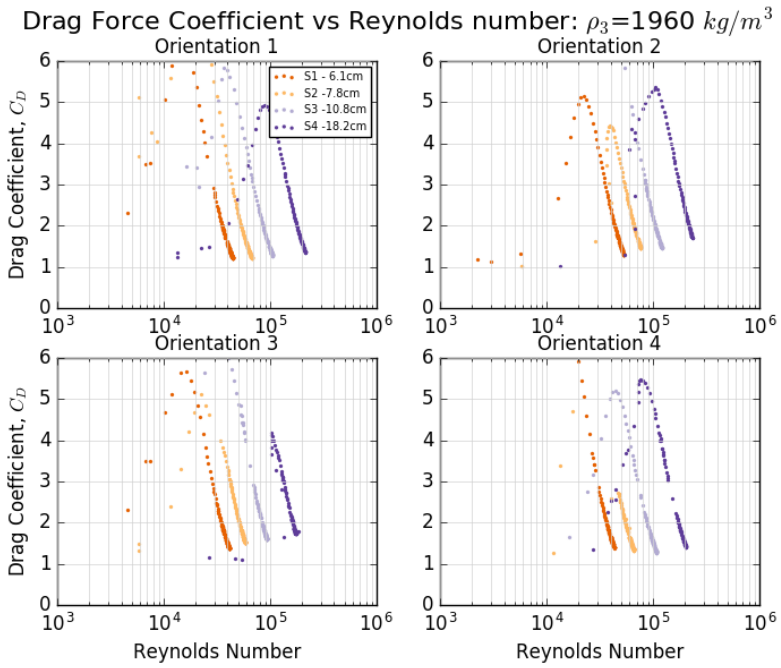


Figure 3-26: Drag force coefficient optimization results of all Core-Loc model scales separated by orientation (Density 1960 $kg/m^3$).

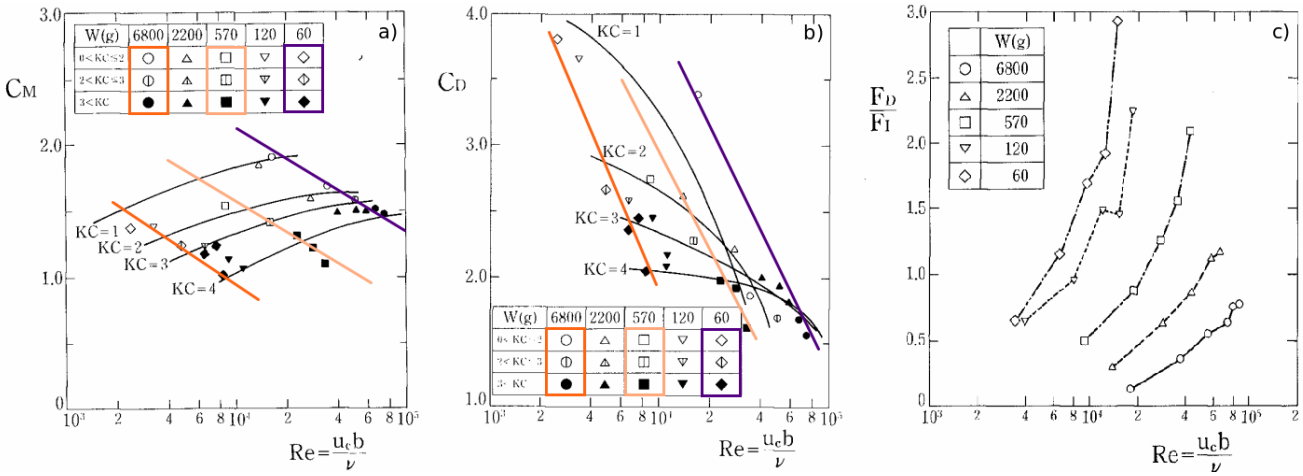


Figure 3-27: Adaptation of the original force coefficient results from Sakakiyama and Kajima (1990), highlighting the Morison empirical coefficients based on different model scales. (a) Inertia coefficient; (b) Drag Coefficient; (c) Drag to inertia force ratio.

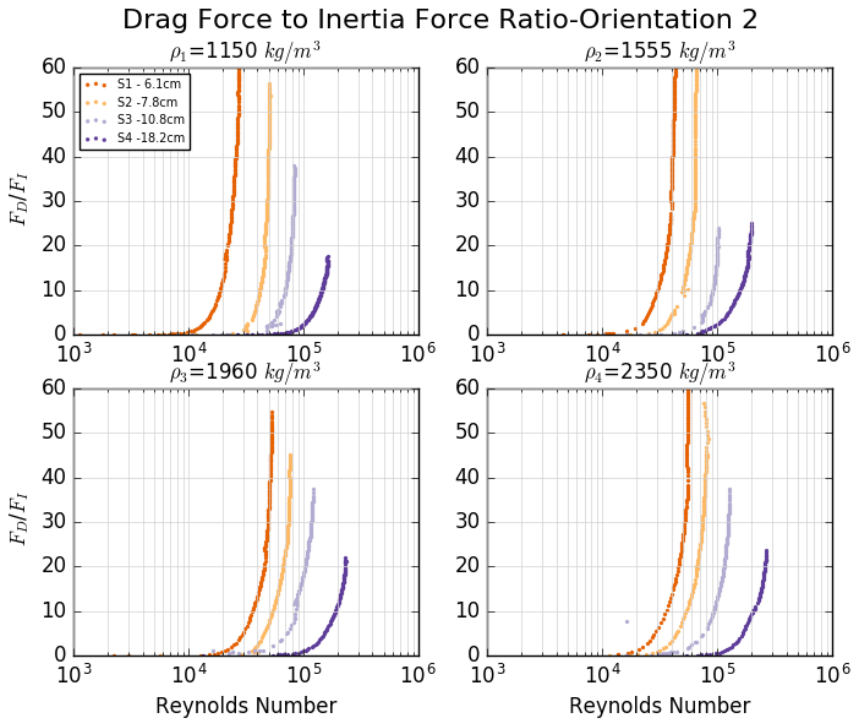


Figure 3-28: Scale effect - Drag to inertia force ratio versus Re (Orientation 2).

### 3.3.3.3 Discussion

The current rubble mound breakwater design provisions ignore the influence of the structural parameters that contribute to the armour layer stability – the interlocking and friction forces between individual armour units. The layer`s hydraulic stability is evaluated using a non-dimensional stability number dependent on empirical coefficients derived from limited scaled experiments. Due to the complex flow through the structures porous layer, the hydrodynamic forces acting on individual armour units during wave loading are difficult to quantify experimentally or theoretically. Because of the

limited studies conducted on the stability of individual armour units, the conducted study was intended to aid the current understanding of the interaction between waves and rubble mound structures. In order to isolate and analyze the individual hydrodynamic forces experienced by individual armour units, controlled drop tests were performed on Core-Loc armour units. As different unit orientations were chosen for this study, the primary concern arises from maintaining a constant falling orientation during the units' descent through the water column. For this, the model units were provided with unique sets of small holes that slide onto four anchored guide lines. This proved to be a simple and efficient way to maintain a constant falling orientation.

The data used in this study is solely derived from a simple non-intrusive camera-based tracking system. Therefore, the accuracy of the results is highly dependent on the quality of the images processed. The experiments discussed here were performed under controlled conditions, which combined with raw video footage quality enhancement, increased the contrasts between the model Core-Loc units and its surroundings. This in turn allowed for an accurate conversion of the original RBG-color raster to black and white, color scheme that is used by the developed tracking algorithm to trace unit displacement. The experimental setup was designed such that the falling downscaled model unit reach terminal velocity, which in turn allowed the eliminations the inertia force component in Morison equation, optimizing the drag force coefficient results. Since four different averaged volume densities were tested, it is intuitive that the total time required to traverse the column of water is reduced by increasing the armour unit density. The displacement time-history results indicated that different fall-orientations, and implicitly flow direction, also have a significant effect on the total falling time. Based on qualitative analysis of the different orientations paths of motion, distinctive flow developments were observed for different orientations. Orientation 2 proved to be the fastest falling unit, attributed to its relative smaller projected area normal to the flow direction and streamlined geometry compared to the other orientations.

The hydrodynamic forces were estimated in this study using Morison equation, using least squares optimization of the drag and inertia force coefficients. Originally, the Morison equation was derived and applied using theoretical approximations of the water particles kinematics. For this study, this data was derived directly from the displacement results. Therefore, to potentially increase the accuracy of the final results, weighted least squares optimization of the two coefficients can be used, as this method puts more emphasis on the experimental measurements. Alternatively, the Morison force coefficients can be estimated using the time-average value of the forces acting on the falling model unit. However, the coefficients determined using this method represent a mean value, fundamentally different than the drag coefficient used in Morison`s equation (Konstantinidis et al. 2021), and their relationship with $Re$ cannot be observed. This method is particularly helpful in oscillatory flow conditions, where the time-averaged coefficients variation with different $K_c$ numbers can be studied.

Previous studies reported that WLS method only increased the accuracy of the results by small margins compared to LS, and therefore for the purposes of this work the LS method was preferred due to its simplicity. Discrepancies observed in the results of force development on the Core-Loc units, depending on their orientation relative to the flow highlights the importance that placing patterns can

have on the overall stability of an armour layer. Based on the analysis, O2, which coincides with the unit that experienced the greatest terminal velocity, yielded larger drag force coefficients relative to the other orientations tested. In order for the predicted forces obtained via the Morison Equation to produce the same motion as those observed and measured during the tests, the drag coefficient for O2 had to be higher as a consequence of O2 having a substantially smaller flow-normal projected area compared to the other three orientations. Additionally, considering the bulk mass distribution of O2 around the unit`s primary axis (x, y, and z), the orientations geometry relative to the flow will result in a higher moment of inertia around its transversal axis (y-axis) relative to the other orientations, as illustrated in Figure 3-29. This will in turn increase the overall stability of O2 in the longitudinal direction (x-axis).

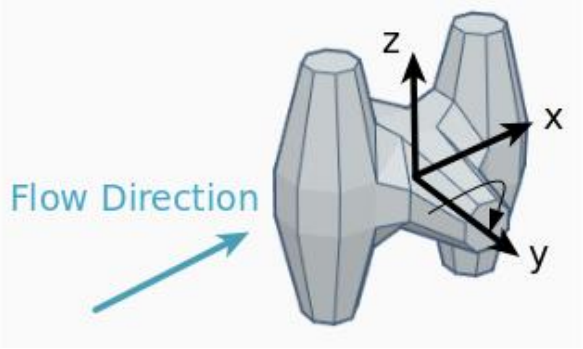


Figure 3-29: Orientation 2 illustration of the moment of inertia around the units y-axis relative to the flow direction

The drag force component in Morison proposed method of estimating the hydrodynamic forces is proportional to the velocity squared and the object`s projected area perpendicular to the flow. Due to the complex three dimensional geometry of Core-Loc units, using the projected area parameters in the original formulation may not be an accurate representation of the real interaction between the flow field and the unit. This limitation is important for O2 case, where one of the exterior prong is directly behind the prong that is perpendicular to the flow direction. In this case, any flow separation behind the first prong will be translated into a force exerted on the back of the unit. Due to the small size of the units and the streamline geometry of O2, this is believed to not have affected the final results. Furthermore, the Morison equation does not account for the influence of vortex shedding. For the case of Core-Loc units, which are designed with six distinct prongs, the flow separation behind each prong depending on the orientation can have influence on the hydrodynamic force experienced by the unit. For this study, the velocity and acceleration of the model was assumed to be representative of the flow field around the unit. Due to the unit`s complex geometry, this assumption is not an accurate representation of the water kinematic across the unit`s surface, and therefore a more accurate method of estimating the distribution of these parameters would improve the accuracy of the results.

The experimental study examined the influence of geometric scale, Reynold`s number, and unit orientation (alternatively, flow direction) on the hydrodynamics and response of Core-Loc armour units in unsteady flow conditions. The work is limited to four individual unit orientations and by its scale, as realistic rubble mound breakwaters are constructed using multiple large-sized armour units. Although the influence of the surrounding units on the flow development and implicitly the hydrodynamic response of Core-Loc units cannot be assed using this experimental setup, the study is an attempt to

increase the understanding of the interaction between waves and rubble mound structures. The world-unique, cost-effective, and non-intrusive unit displacement tracking system developed for this research can be extended to other armour shapes. Knowledge of the different hydraulic response of different unit orientations can provide further insights on the importance of placing patterns on the rubble mound armour layer stability.

## 3.4 Summary and Conclusions

The study presents series of hydrodynamic drop tests performed to yield accurate estimates for force coefficients for a Core-Loc armour unit with varying geometric scales, flow direction, and flow velocity. Aside from the experimental program, the work involved the development of a non-invasive camera-based tracking system. A simple automated process to manipulate the color field of individual frames extracted from video footage taken of the units' freefalling through a column of water was devised and used to obtain detailed histories of displacement, velocity, and acceleration for a wide-range of test conditions. To cover a wide range of prototype velocities, four different averaged unit volume densities were simulated using different quantities of lead pellets. The different unit orientations examined in this work were maintained constant throughout the unit`s descend through the water column using a simple set of guidelines and holes installed in the vertical tank and units. The hydraulic response of different units was estimated using Morison`s method of estimating the hydrodynamic forces acting on submerged structures. Based on the analysis of data and optimization of the drag and inertia force coefficients, dissimilarities in the drag coefficient behavior were observed for high Reynolds numbers between the four unit orientations tested. This indicated significant differences in flow development and resistance experienced by individual units in similar flow conditions, highlighting the importance of accurate estimations, and understanding of the force distribution through an armour layer. Another parameter of interest for evaluating the stability of individual armour units was the distribution of the moments of inertia around the unit's axis relative to the flow direction, which can act such that the overall stability of specific orientations is improved. The scale effects were assessed based on the results of four different geometric scales tested under the same conditions. The analysis indicated that as the flow velocity increase, and implicitly the acceleration decreases, the drag effects become predominant. Therefore, as scale increases and the flow conditions approach prototype conditions, the drag forces become predominant over inertia forces, consistent with other literature sources.

## 3.5 Link to Chapter 4

The hydrodynamic response of individual armour units within a rubble mound armour layer is a complex multivariate process. To describe the relative importance of drag forces over inertia forces, the original study was extended to multiple Core-Loc armour unit orientations based on the analysis of the controlled drop tests. The hydrodynamic analysis of Core-Loc armour units under oscillatory flow conditions is presented in detail in Chapter 4.

# Chapter 4 Core-Loc Hydrodynamic Analysis Under Oscillatory Flow

## 4.1 Introduction

The hydraulic tests were performed in the Ocean, Coastal, and River Engineering Research Center at the National Research Council of Canada, located in Ottawa. Through extensive expertise in physical and numerical modelling, this organization in the Canadian federal government conducts applied research and provides technical services related to civil engineering hydraulics, coastal science and engineering, and cold-region technologies. The wave flume used during the experiments has a length of 64 m, a width of 1.2 m , and a height of 1.2 m, making it an ideal experimental setting for scaled two-dimensional studies of coastal processes and wave-structure interactions. The flume is equipped with a wave generator capable of generating a wide range of wave conditions with heights up to 0.25 m, depending on the water depth (maximum achievable still water level is 0.9 m). The wave generator is equipped with an active wave absorption (AWA) system which corrects the paddle motion to absorb incoming reflected waves. A cross section of the flume (facing the wave maker) is shown in Figure 4-1 at the testing location, which is equipped with large glass windows on both sides, allowing visual observations during testing.

Figure 4-1: NRC-OCRE Steel Wave Flume (SWF) and wave generator.

## 4.2 Facilities, Instrumentation and Testing Program

To conduct the hydrodynamic analysis of Core-Loc armour unit under oscillatory flow, a physical model was used to simulate different flow conditions acting on a submerged armour unit. The model consisted of a downscaled Core-Loc armour unit, installed on a six-axis force transducer and outfitted with pressure sensors.

### 4.2.1 OCRE-National Research Center Steel Wave Flume

#### 4.2.1.1 Steel Wave Flume

The physical model constructed for this experiment was incorporated in the existing artificial bathymetry of the flume, located 38.7 m away from the wave maker. This testing location corresponded with the beginning of the horizontal section of the bathymetry, allowing sufficient distance from the wave generator for the natural transformation of waves. A detailed cross-section of the bathymetry is shown in Figure 4-3, consisting of two sloping regions corresponding to a 1V:25H and a 1V:20H slope, followed by a horizontal section elevated 0.25 m from the flume bottom. In addition to the wave maker AWA capabilities, multiple vertical layers of perforated metal sheeting were located at the end of the flume ("artificial beaches"). These were used as wave absorbing devices, as the porosity of each layer reduced the effects of the reflected waves.

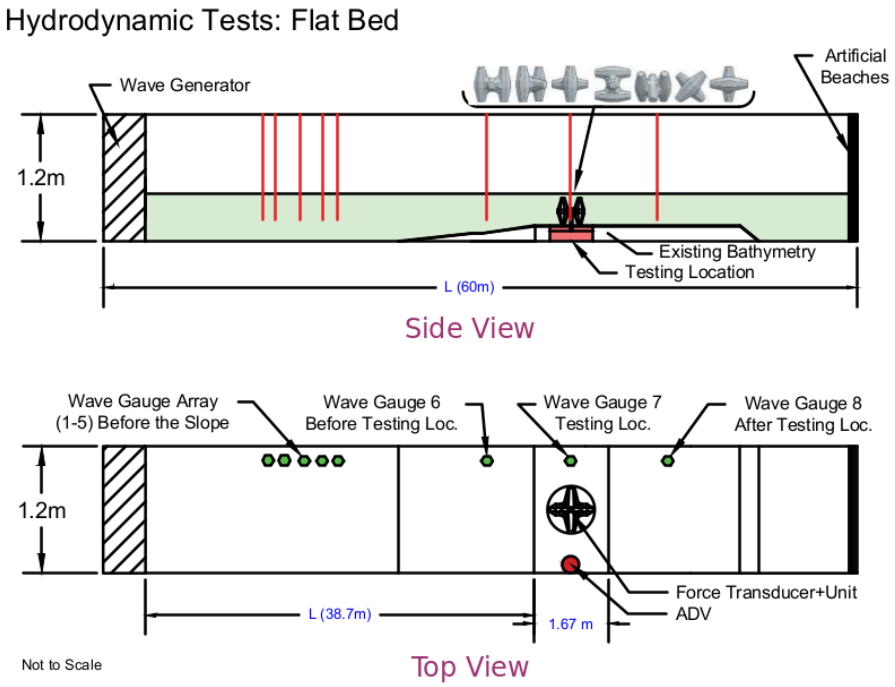


Figure 4-2: SWF test setup and instrument locations in plan and top view.

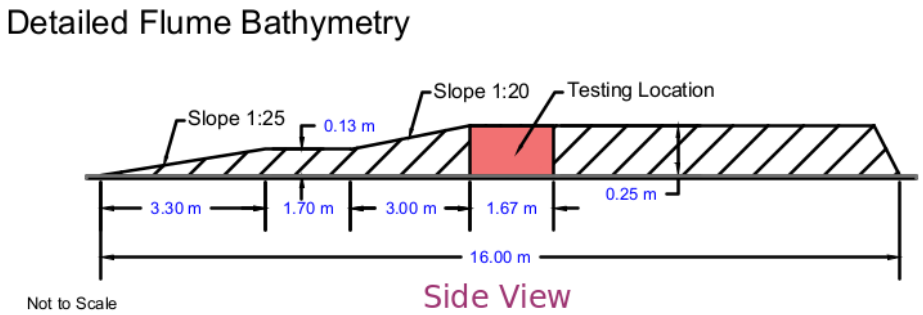


Figure 4-3: SWF detailed flume bathymetry cross-section.

#### 4.2.1.2 Testing Location – Pressure Board and Frame

Figure 4-4 and Figure 4-5 depict the removal of a 1.67 m bathymetry section and the installation of a pressure board and frame used at the testing location. The frame was built to be later used to simulate a breakwater slope onto which a force transducer and eight pressure sensors were installed. The frame was build using stainless steel and consisted of a rigid bottom structure that was pressure fixed to the bottom of the flume, and a top section, which supported a PVC board. The two sections were connected using a stainless hinge. A full technical drawing of the design and construction of the frame is available in Appendix B.1. The hollow bottom of the frame was used to mount the force and pressure instruments (the pressure instruments were installed at a later stage of the project), while the hinge allowed a 90º rotation of the PVC board for easy access to the instruments.


Figure 4-4: Testing location. (a) Removal of a 1.67m bathymetry section; (b) Installation of the pressure board and frame.

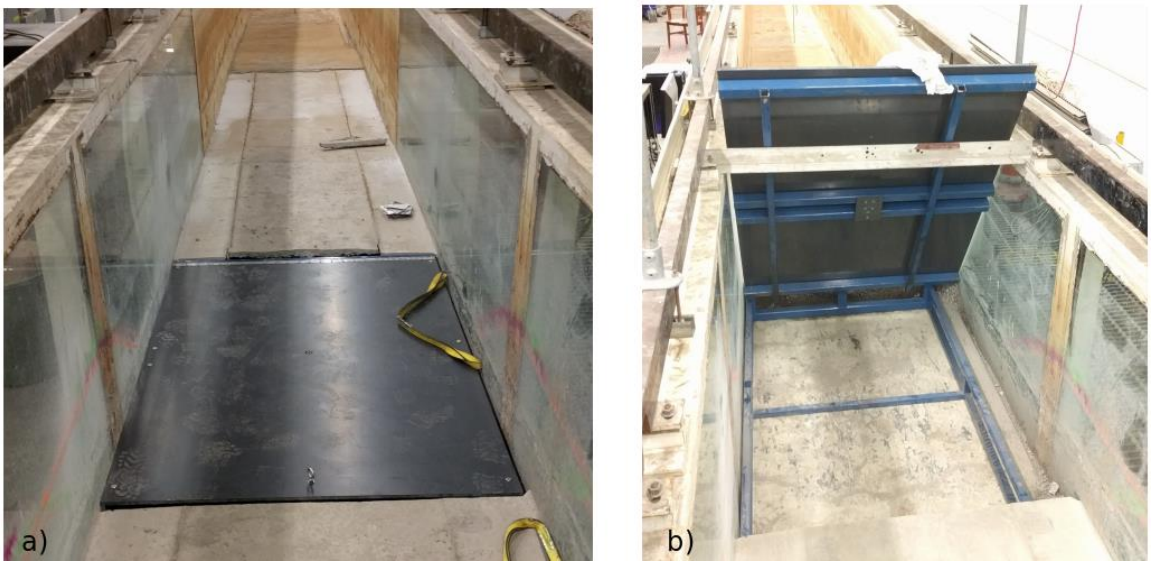


Figure 4-5: Pressure board. (a) Final installation inside the existing bathymetry; (b) Example of the hinge mechanism and bottom access.

### 4.2.2 Instrumentation

Figure 4-2 details the position of the instrumentation used for these tests, installed in the wave flume to measure wave elevations, flow velocity, and hydrodynamic forces on the scaled model Core-Loc armour unit. NRC-OCRE`s GDAC data acquisition system (DAQ) was used to collect the data from the instruments used. The following sections will cover the details regarding the instrumentation and software used.

#### 4.2.2.1 Wave Gauges

For this study, eight capacitance-type wave height gauges (manufacturer Akamina, model AWP-24-3) were mounted at various positions in the wave basin, sampling at a rate of 50 Hz and connected to the GDAC data acquisition system. A five wave gauges' array was placed before the beginning of the bathymetry section, numbered WG1 to WG5, as shown in Figure 4-6. The wave probes array was used in a later stage of the project to determine the reflection coefficient from the breakwater structure. The probes were numbered in increasing order in the direction of wave propagation. A sixth wave gauge was used to record the water level at the beginning of the second slopped section of the bathymetry, located at 35.7 m from the wave machine. The most important sensor for the purposes of this project, WG7, was located at the testing location. An eighth sensor was mounted 4 m after the testing location.

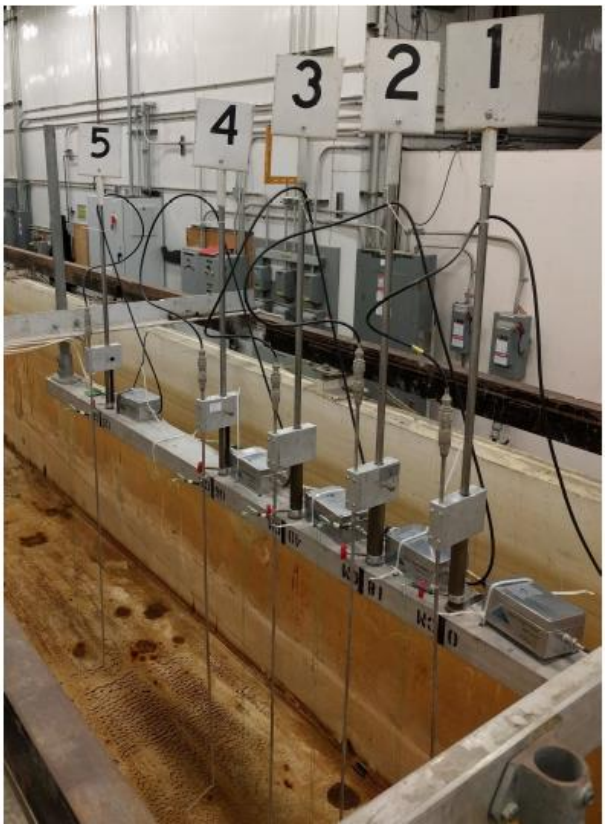


Figure 4-6: Five wave gauges' array and probe labeling

Capacitance-wire wave gauges operate by measuring the change in capacitance of the sensing wire resulting from changes in immersion depth. The probes are connected to an electric circuit linked to the

data acquisition system, which stores and converts the gauge output (in volts) into a time series of water surface elevations. All wave sensors were calibrated against a laboratory caliper prior to installation, and operated with their sensor head constantly submerged to ensure a continuous electric circuit during the passage of a wave trough. These wave gauges yielded calibration errors less than 0.5% of the calibration range throughout the experiment duration. As a quality control, the probes were calibrated at the beginning of every testing week, and re-zeroed every testing day.

#### 4.2.2.2 Force Transducer

To record the time-histories of the force exerted on a submerged Core-Loc model, a six-degree-of-freedom force transducer was used. The force sensor, model ATI Mini45 (US-60-80), was installed under the PVC board and securely fit mounted between two members of the rigid steel supporting frame. The sensor was connected to the data acquisition system via a wireless F/T device from the same manufacturer. Using this configuration, the DAQ system collected data from the force sensor at a sampling rate of 50 Hz. The dynamometer was able to measure forces up to 267 N in the x and y directions, 533 N in z, and 9 N/m of torque in all three Cartesian coordinates. The model used was provided with IP68 rating, allowing the dynamometer to withstand continuous submersion during testing which prevented any waterproofing issues that could damage the equipment and the measurements.

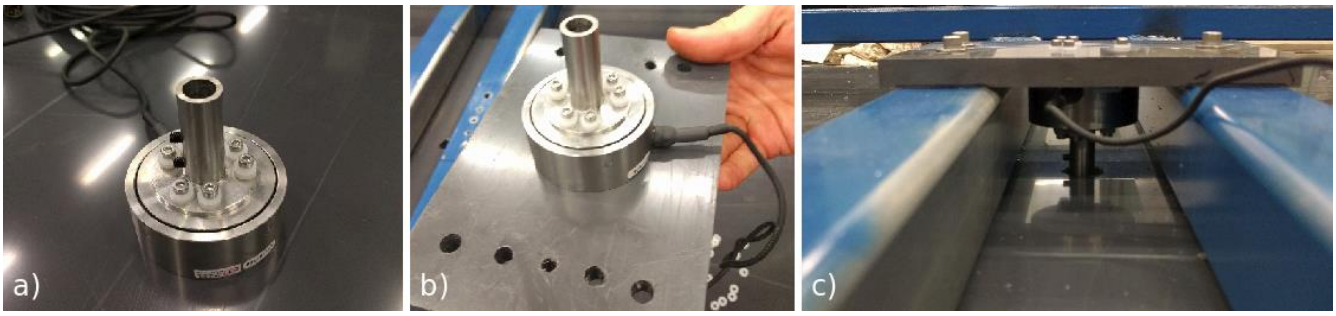


Figure 4-7: Force Transducer. (a) ATI Mini45 force sensor – rated IP68 and custom stainless steel mount; (b) Rigid PVC board mount; (c) Final installation to the pressure board and frame.

To accurately transfer the fluid forces exerted on the model to the force transducers, a stainless steel mount that connects the sensors tooling adapter plate to the PVC board was designed and machined (design provided in Appendix B.4). The role of the mount was to minimize the gap between the board and the force sensor, and to provide a secure and flush connection between the model and the transducer. Two set screws, visible in Figure 4-7, were installed on the side to secure the armour unit model during testing. The transducer was connected to a second PVC support, shown in Figure 4-7(b), which was bolted to the board frame. As it can be seen from Figure 4-7(c), showing the final connection, a 3 to 5 mm gap was left between the PVC board and the sensor mount to avoid any interference between the two that would result in inaccurate force measurements. The dynamometer configuration is also visible in Figure 4-5(b), depicting how the frame was lifted to adjust the model and tighten the set screws.

#### 4.2.2.3 ADV

A Nortek Vectrino high-resolution acoustic velocimeter was used to measure the wave induced flow velocities at the testing location. The instrument consists of one transmitter, located in the center of the probe head visible in Figure 4-8, that sends short fixed frequency acoustic pules to a sampling volume, located 5 cm away from the probe. When the pulse travel through the focus point, the four receivers of the probe record the acoustic waves reflected from moving particles present in water. Any changes in frequency are then processed and converted into water velocity in the x, y and z directions, principle known as Acoustic Doppler Velocimetry (ADV).

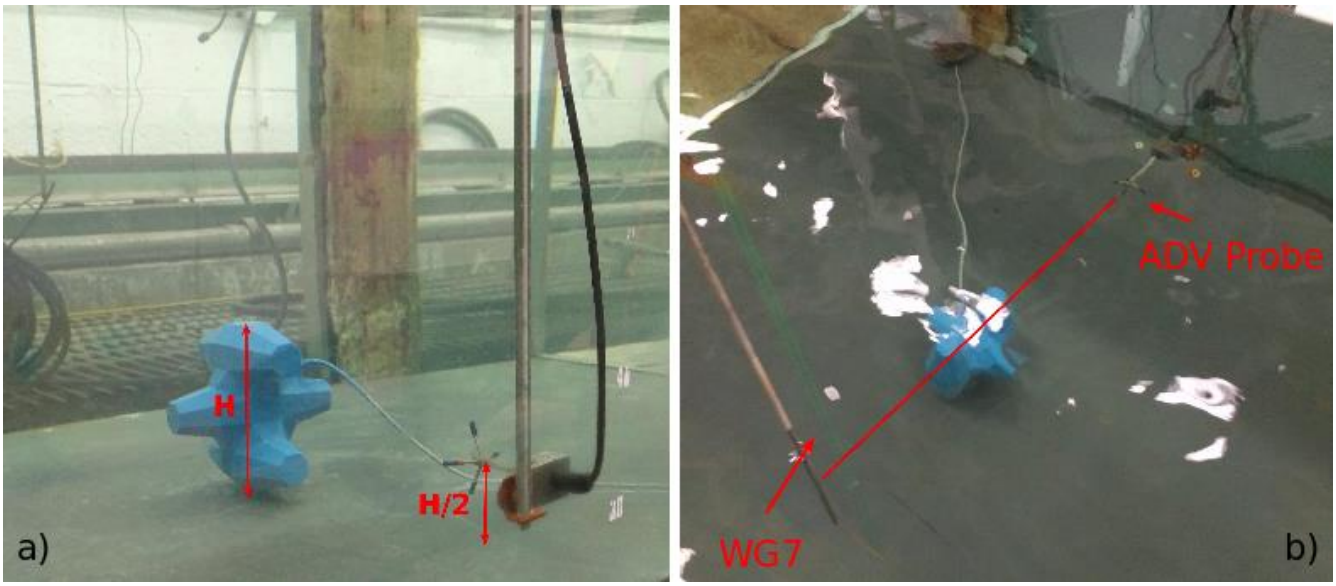


Figure 4-8: Northek Vectrino velocimeter. (a) Sampling location with respect to the centroid of the model unit; (b) Wave gauge 7, model Core-Loc and ADV probe head alignment.

The velocity measurements were sampled at a 50 Hz rate from a sample volume located beside the centroid of the Core-Loc model as depicted above. This arrangement was chosen to obtain an estimate of the undisturbed flow field at the centroid of the Core-Loc unit. The ADV probe head was aligned with the centroid of the model and kept at a sufficient distance from the unit to ensure accurate flow velocity measurements undisrupted by the presence of the model. To do so, a non-intrusive support was build which pointed the Vectrino probe head towards the centroid of the unit.

#### 4.2.2.4 Data Acquisition System – NDAC

The data acquisition system setup is shown in Figure 4-9(a), which recorded real-time data from all the instruments used during the experiment. The analog signals from the sensors were connected to an analog-to-digital converter on different channels, which transmitted the digital version of the signals to the NDAC system running on a computer. NDAC is a data-acquisition and experiment-control software developed by NRC, used to control sampling, data conversion and storage in digital form for analysis. All instruments were synchronized to begin recording at a sampling rate of 50 Hz when the wave maker was activated.

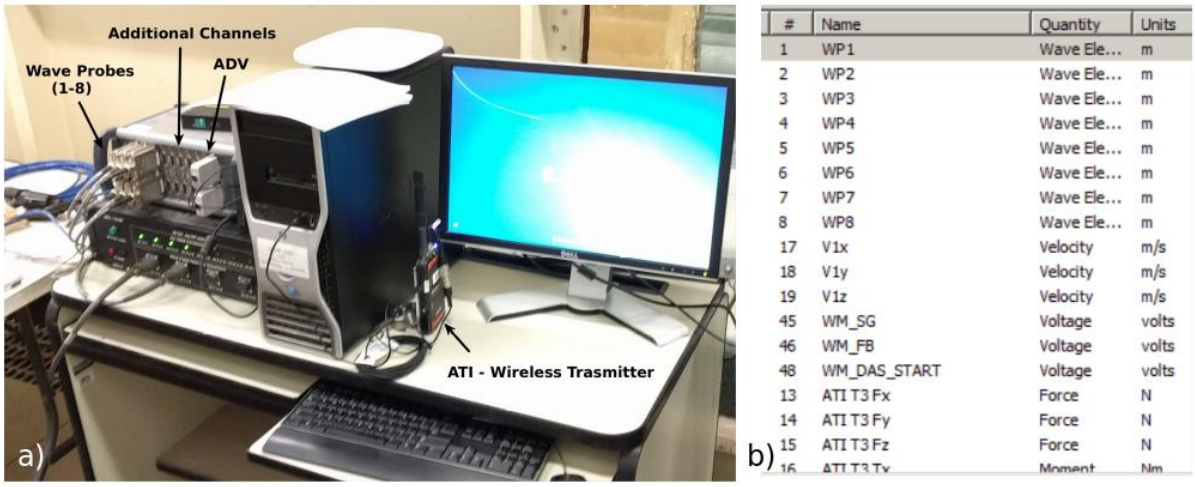


| # | Name | Quantity | Units |
|---|---|---|---|
| 1 | WP1 | Wave Ele... | m |
| 2 | WP2 | Wave Ele... | m |
| 3 | WP3 | Wave Ele... | m |
| 4 | WP4 | Wave Ele... | m |
| 5 | WP5 | Wave Ele... | m |
| 6 | WP6 | Wave Ele... | m |
| 7 | WP7 | Wave Ele... | m |
| 8 | WP8 | Wave Ele... | m |
| 17 | V1x | Velocity | m/s |
| 18 | V1y | Velocity | m/s |
| 19 | V1z | Velocity | m/s |
| 45 | WM_SG | Voltage | volts |
| 46 | WM_FB | Voltage | volts |
| 48 | WM_DAS_START | Voltage | volts |
| 13 | ATI T3 Fx | Force | N |
| 14 | ATI T3 Fy | Force | N |
| 15 | ATI T3 Fz | Force | N |
| 16 | ATI T3 Tx | Moment | Nm |

Figure 4-9: Data Acquisition system (a) NDAC server and computer connections; (b) Software interface showing the channels sampled and their corresponding instruments.

### 4.2.2.5 Sign Convention

Figure 4-10 depicts the sign convention used for all instruments throughout this experiment. The positive x direction was chosen in the direction of wave propagation, z represents the depth, and positive y is the transversal direction originating from the centroid of the Core-Loc model.

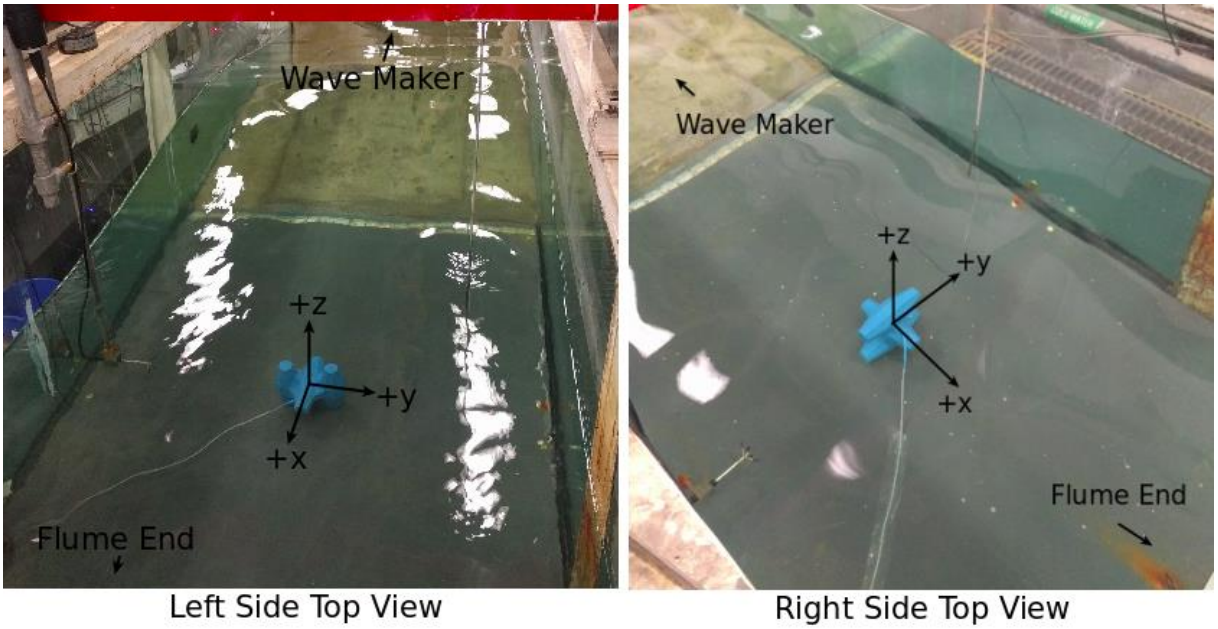


Figure 4-10: Sign convention.

### 4.2.3 Instrumented Armour Unit

To investigate the hydrodynamics of Core-Loc armour unit under oscillatory flow conditions, two scaled model units were designed and 3D printed. The objectives of the experiment were to investigate the effect of different orientation and scales of Core-Loc armour units on the forces exerted due to different wave loadings. To record the forces from passing waves, the model was mounted on a load cell resting under a frame embedded in the flume bathymetry. The designed model Core-Loc unit was

outfitted with pressure sensors and includes a self-contained data acquisition system that transmits pressure data to a Raspberry Pi 3, a credit card size computer. This data was used for a different area of the project. The following sections will cover the design and construction details of the scaled unit, which due to its state-of-the art instrumentation was given the nickname “smart unit” or “instrumented armour unit”.

#### 4.2.3.1 Armour Unit Orientation

Based on the preliminary observations from the controlled drop tests (Chapter 3) which indicated that the development of drag and inertia forces is depended on the Core-loc unit orientation, for these set of experiments, seven orientations were tested. In addition to the four tested orientations, another three were chosen based on their relative unique geometric and spatial characteristics. The chosen configurations are shown below.

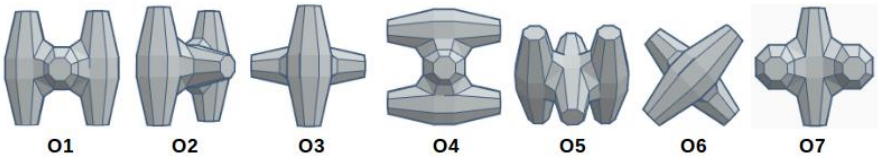


Figure 4-11: Core-Loc armour unit tested orientations.

Table 3.1 summarizes the geometric properties of each orientation used, and their corresponding orientation from the Controlled Drop Test. Orientations 1,2,3 and 5 are equivalent to orientations 3,1,2 and 4, respectively, used for the previous study. The remaining orientations were based on a Core-Loc armour layer simulated numerically using FEMDEM (Figure 4-12), published by Latham et al. in 2014. Orientation 4 is characteristically orientation 1 rotated 90º, chosen to investigate potential effect of the different flow pattern development due to the opposite position of the two Core-Loc exterior prongs. Similarly, orientations 3 and 6 share the same projected area, with orientation 6 tilted 45º. This causes a much smaller gap between the side prongs and the flume floor, likely leading to different flow patterns around the two orientations. Lastly, orientation 7 corresponds to a Core-Loc unit resting on its central prong. Orientations 3 and 7 have a similar projected area, but different location of the unit`s exterior legs.

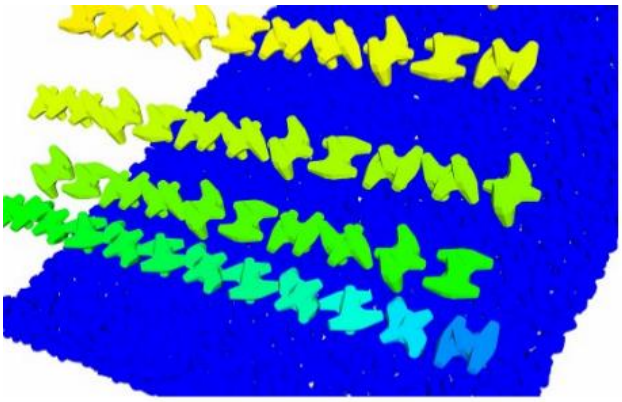

Figure 4-12: Core-Loc placement orientation patter used for the construction of an armour layer using FEMDEM (Latham et al., 2014).

For these set of tests two scaled Core-Loc models with characteristic lengths 0.18 m and 0.12 m were used. The geometric length of the models was based on tests that will be performed with these units on a slopped breakwater section. For the current experiments, choosing a prototype would be unrealistic as the unit rests on a horizontal section. Despite the arbitrary scale, the model`s dimensions were checked against Morison`s equation applicability range, whose hydrodynamic force predictions are valid when the structures size is small relative to the waves length ($C_L/L$ <0.1). The test parameters are covered in Section 4.3.2.

Table 4.1: Scaled Core-Loc model geometric properties and corresponding unit orientations from the controlled drop experiments.

| **Scale - Armour Unit Characteristic Length, $C_L$ (m)** | **Unit Orientation (Corresponding Controlled Drop Tests Orientation)** | **Projected Area, $A$ ($m^2$)** |
|---|---|---|
| 1 – 0.18 m | 1 (O3) | 0.0224 |
| | 2 (O1) | 0.0210 |
| | 3 (O2) | 0.0145 |
| | 4 | 0.0224 |
| | 5 (O4) | 0.0221 |
| | 6 | 0.0145 |
| | 7 | 0.0177 |
| 2 – 0.12 m | 1 (O3) | 0.0112 |
| | 2 (O1) | 0.0095 |
| | 3 (O2) | 0.0066 |
| | 4 | 0.0112 |
| | 5 (O4) | 0.0100 |
| | 6 | 0.0066 |
| | 7 | 0.0081 |

#### 4.2.3.2 Scaled Armour Unit

The two smart units were designed in Tinkercad such that all the tests conducted can be completed using a single Core-Loc model for each scale, in order to ensure identical dimensions and weights between tests, and minimize manufacturing errors and construction costs. As mentioned in the introductory section, the downscaled 3D printed models were outfitted with pressure sensors and wired with a unique electric circuit connected to a Raspberry PI3 computer. Building one smart unit for each seven orientations and both scales was unfeasible, and thus the final design of the unit was optimized in

order that one separate model for each scale can be used for each future test, while ensuring enough space and covered for the pressure sensors and electric connections.

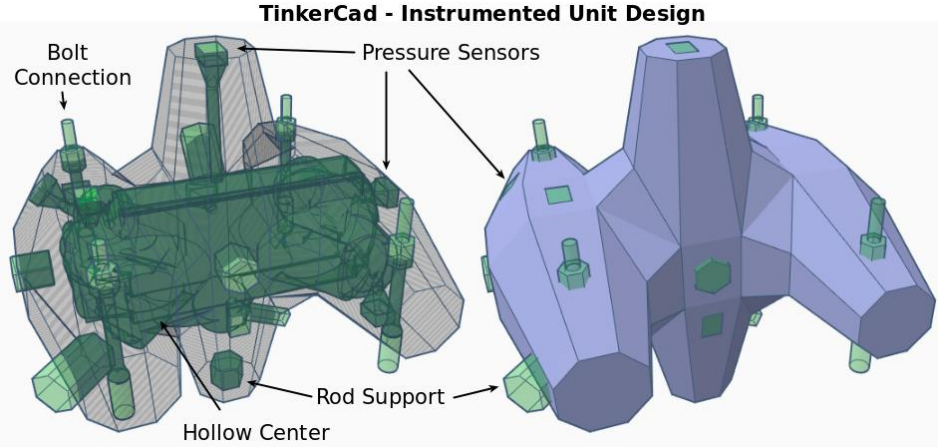


Figure 4-13: Instrumented Core-Loc armour unit Tinkercad design

Each smart unit was connected to the force transducer using a threaded rod, that extended from the unit to the transducer mount. To ensure that the unit orientation does not change throughout testing, the rod was fastened to the unit using nylon hex jam nuts. These nuts are internally threaded with a nylon insert, which prevented the rod from loosening from vibrations, and cross threads, which secured the rod from backing off. For each orientation (some orientations share the same fastener), the hex shaped nuts were aligned with the centroid of the unit and perpendicular to the force transducer mount, visible in Figure 4-13, which depicts the various positions of the fasteners (labelled as rod supports). In the same figure, the other design components of the design can be seen. The hollow center was used to store the wiring and electrical components of the circuit. Although technical details are not provided in this thesis about the pressure sensors, 8 and 6 Honeywell Basic TBF Series Pressure Sensors were used to build the smart unit for scale 1 and 2, respectively. These are small flush diaphragm sensors, chosen due to their small size, which allowed their installation without affecting the Core-Loc shape.

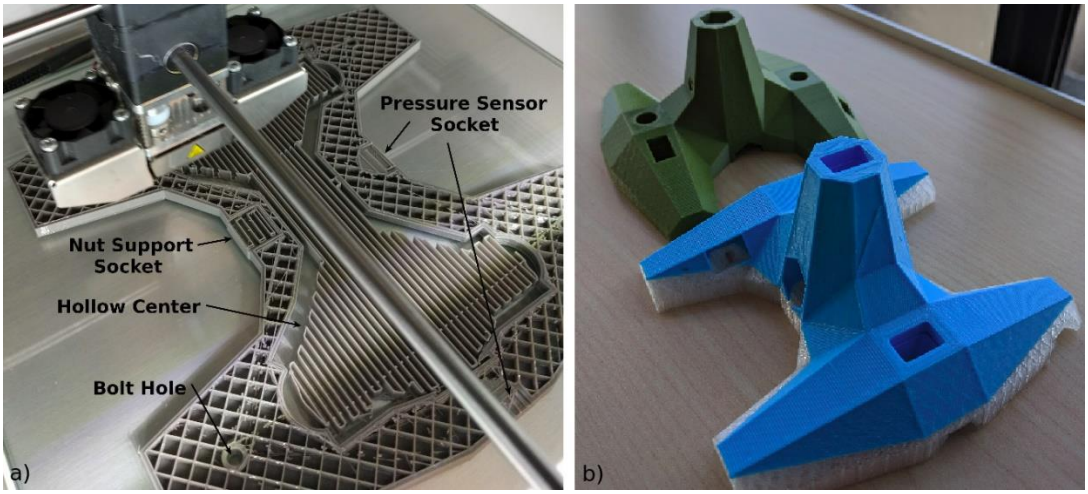


Figure 4-14: Scaled Core-Loc model. (a) 3D printing and design components; (b) Final model sections.

Due to 3D printing size and technological limitations, the model had to be printed in two separate parts as shown in Figure 4-14(b). This is due to the Core-Loc complex geometry and complexity of the final model design, which required 3D printing support structures. Whenever a model feature is at an angle higher than 45º, the printer requires a material support beneath it. Otherwise, the layer adhesion will sag and deform the model. These supports are visible in Figure 4-14(a), represented by the perpendicular material structure located in the center of the model, meant to support the hollow center ceiling. These supports are easily removable once the prints are done and do not affect the final shape. Since the downscale modelled Core-loc consisted of two parts, four additional bolt connections were design to connect the two sections once the model wiring was complete.

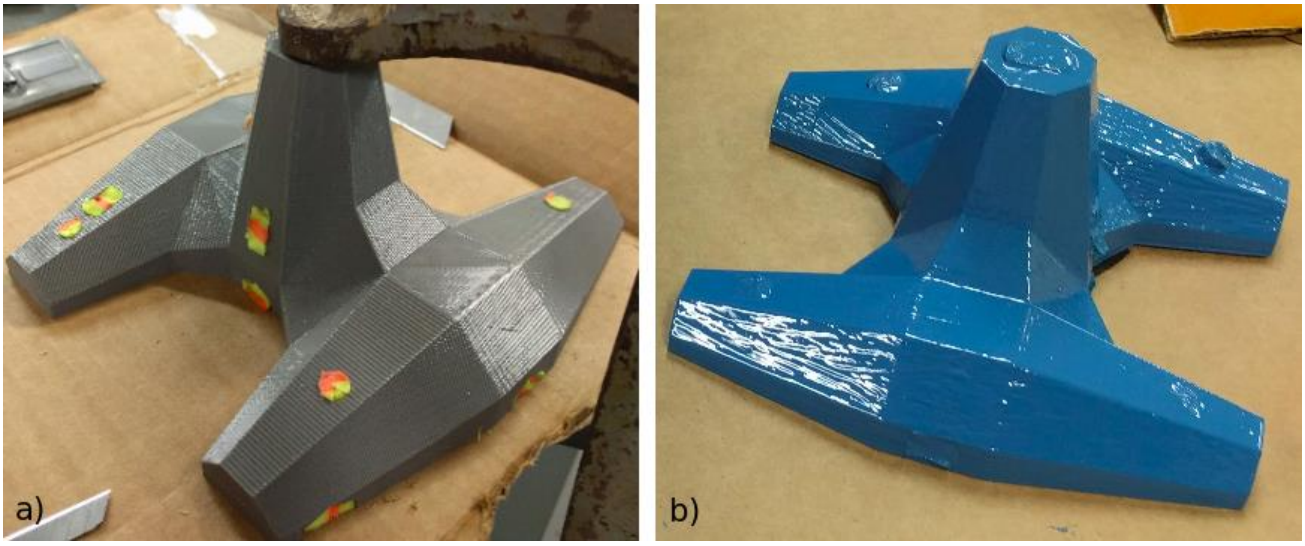


Figure 4-15: Model waterproofing. (a) Foam application; (b) Marine epoxy coating.

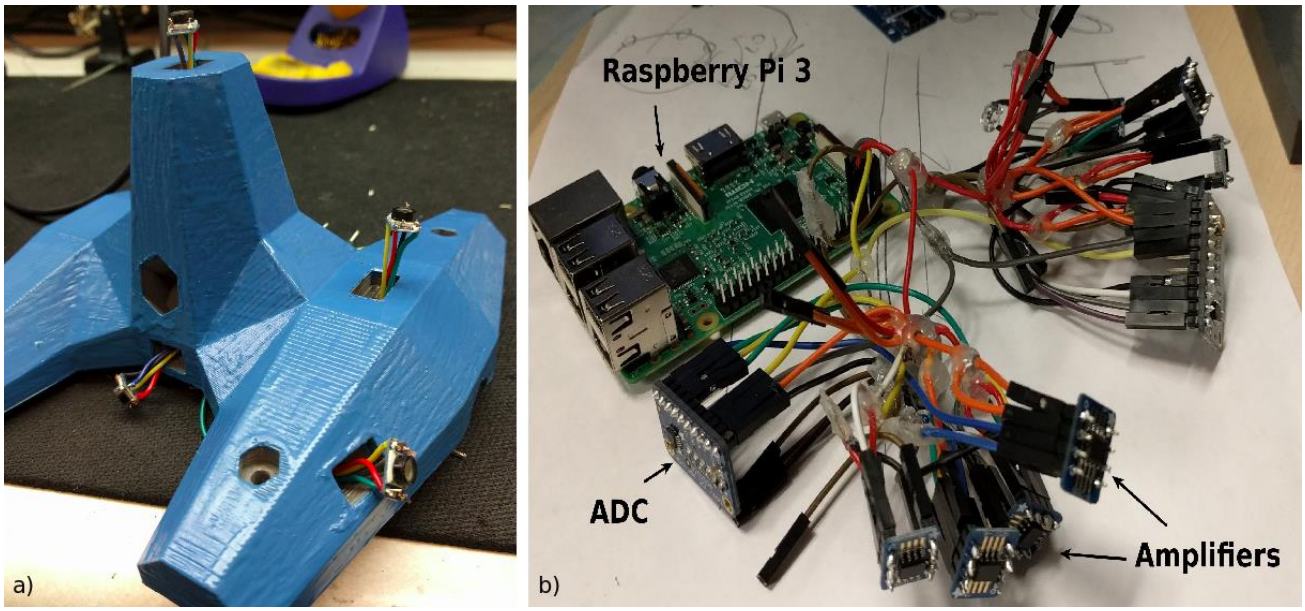


Figure 4-16: Scaled Model. (a) Honeywell TBF Series pressure sensors installation; (b) Electric circuit (pressure sensors connections, amplifiers, and analog to digital converters –ADC) and Raspberry Pi3 controller.

The same plastic material used to 3D print the models for the drop tank experiment was used for these units (PLA). When 3D printing parts, the model is build layer by layer. Due to layer adhesion and temperature variations during the printing process, indiscernible gaps exist in the structure of the printed parts. These can easily damage the final model, as water molecules will infiltrate over time between these gaps and damage the electric circuit. To mitigate this, the final printed parts were covered in marine epoxy paint, as depicted in Figure 4-15, which creates a 1-2 mm water resistant coating. The Tinkercad design of the Core-Loc was based on the exact dimensions of the parts used to build the instrumented unit, which is why the various holes in the model were covered in foam prior to applying the coating. This ensured a flush finish of the Core-Loc unit. Between the two printed sections, a custom-made silicon gasket was build (shown in appendix B.3), to prevent water leaking inside the unit. The same coating was applied at the end over all connections, leaving only the sensors exposed, as shown in Figure 4-17.

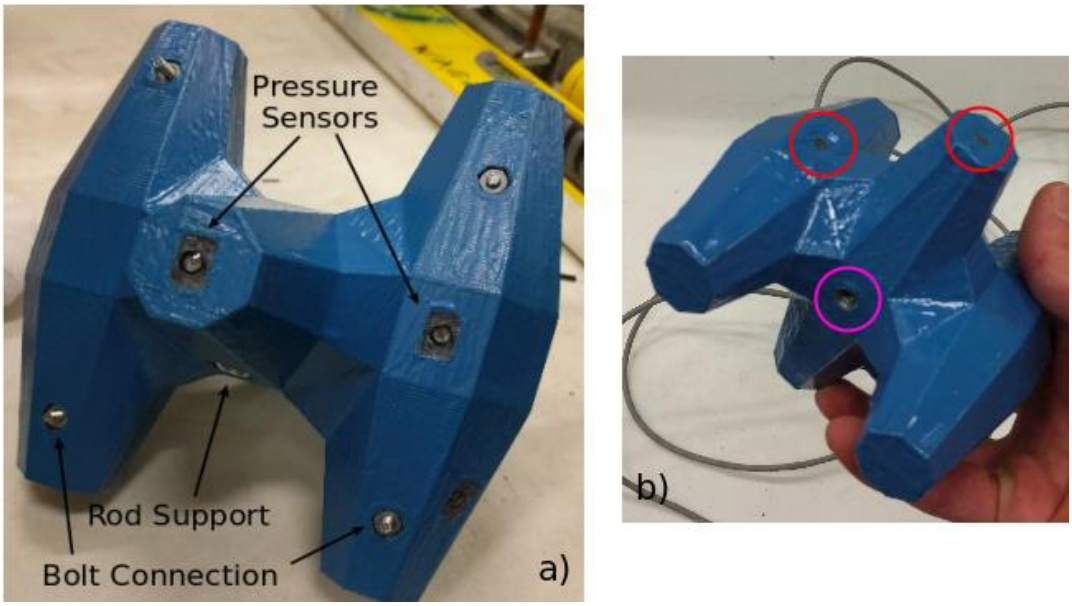


Figure 4-17: Final Instrumented Core-Loc Model. (a) Scale 1-0.18m; (b) Scale 2- 0.12m.

## 4.3 Experimental Procedure

In the following sections, the experimental methodology and test parameters are covered in details.

### 4.3.1 Instrument Calibration

#### 4.3.1.1 Wave Gauge Calibration

As mentioned in Section 4.2.2, the wave gauges were calibrated at the beginning of every testing week, and re-zeroed every day. Each day, the flume water level was adjusted to the desired level, which was marked using a measure tape fixed on the glass wall at the testing location. This was done to account for any potential leaks and evaporation of water when deemed necessary. The NDAC system is equipped with a wave gauge calibration feature, which updated the calibration data of the server and allowed real-time monitoring of the errors. The wave probes were calibrated using three water elevations, by fixing the wave gauges on the supports at a fixed and known elevation using spacers and

recording the output voltage. This was repeated for three water elevations during each calibration, 0.2 m above, at, and below the still water level. This procedure ensured calibration errors less than 0.5% during the duration of the experiments.

#### 4.3.1.2 Force Transducer Calibration

The force transducer and wireless F/T transmitter were factory calibrated by the manufacturer, ATI Industrial Automation, compliant with the ISO9001 standards. The sensor`s hardware was temperature compensated, thus no corrections were required due to the water temperature variation during the experiment. The sensor measurements were recorded by the data acquisition system NDAC and Manual removal of the zero values was required for analysis. The force transducer was also verified on site prior to the beginning of the experimental program by applying measuring weights in the x, y, and z directions. The NDAC recordings were then compared with the applied known mass of the weights to ensure measurement accuracy, linearity, and no cross-talk between the sensor`s channels. The instrument was considered successfully calibrated as the results indicated accurate force readings.

#### 4.3.1.3 ADV calibration

The Nortek Vectrino velocimeter was automatically calibrated using the calibration sheet and software provided by the manufacturer, according to which, the individual ADV channels (x, y, and z) contained errors of less than 0.002%. On site calibration was not possible.

### 4.3.2 Wave Synthesis and Generation

#### 4.3.2.1 Test Plan and Sequence

To investigate the hydrodynamics of Core-Loc armour units, a test program featuring different wave conditions was developed for both tested scales, summarized in Table 4.2. The program covered four regular and two irregular wave signals for each scale. The regular signals were defined by their wave height ($H$) and period ($T$), while the irregular signals were referenced with respect to their significant wave height ($H_s$) and peak period ($T_p$). The tested parameters covered different ranges of wave heights and periods, ensuring a relatively broad range of flow velocities and therefore resultant forces on the Core-Loc model. In order to simplify the relationships between the characteristics of the incident waves and the wave-induced forces, only the regular signals were analyzed for the optimization of the hydrodynamic force coefficients. The irregular signals results will be used for the validation of a new wave model developed by ICL. Each regular wave test was run for a duration of 5 minutes, time in which between 150 and 400 waves were generated per test. The irregular test signals were simulated for 15 minutes, time predefined during the wave synthesis. This duration was sufficient to generate hundreds of individual waves including many different combinations of wave period and wave height. The test plan was executed for all seven Core-Loc armour unit orientations and for both scales, yielding 84 unique tests. Before each test, the data acquisition system was armed and linked to the wave maker, ensuring that all instruments were initiated and synchronized with the wave generation. A local computer host was used to control the wave generation system and software.

Table 4.2: Summary of the experimental program and wave parameters.

| Drive Signals | Scale 1 – 0.18 m | | | | | |
|---|---|---|---|---|---|---|
| | **Water Depth, D (m)** | **Wave Height, H, $H_S$ (m)** | **Wave Period, T, $T_p$ (s)** | **Wave Length, L (m)** | **Wave Steepness, H/L** | **Iribarren Number, $\xi$** |
| **Regular** | 0.80 | 0.100 | 1.50 | 3.22 | 1.95 | 3.66 |
| | | | 4.00 | 10.83 | 0.58 | 6.71 |
| | | 0.200 | 1.70 | 3.88 | 1.62 | 2.84 |
| | | | 3.00 | 7.90 | 0.80 | 4.06 |
| **Irregular** | 0.80 | 0.075 | 4.00 | | | |
| | | 0.150 | 1.70 | | | |
| | **Scale 2 – 0.12 m** | | | | | |
| **Regular** | 0.62 | 0.067 | 1.22 | 2.19 | 2.86 | 3.69 |
| | | | 3.27 | 7.75 | 0.81 | 6.94 |
| | | 0.133 | 1.39 | 2.70 | 2.33 | 2.91 |
| | | | 2.45 | 5.62 | 1.12 | 4.19 |
| **Irregular** | 0.62 | 0.050 | 3.33 | | | |
| | | 0.100 | 1.38 | | | |

For scale 1, the water depth was kept at 0.8m at the testing location for all tests. Based on the wave maker`s capabilities, two sets of regular wave heights were tested (0.1 m and 0.2 m), each signal corresponding to a short and a longer period as shown in Table 4.2. Froude scaling laws were used to determine the scale 2 wave parameters required to match the ones used for scale 1, resulting in a water depth of 0.62 m for scale 2. The downscaling of the wave parameters was based on the of the length scale ($n_L = 2/3$) as shown below. This length scale corresponds to the ratio of the characteristic lengths of each instrumented unit ($C_{L-Scale\ 1}/C_{L-Scale\ 2} = 2/3$).

Wave height and depth: $H_{Scale\ 2} = H_{Scale\ 1} n_L$

Wave period: $T_{Scale\ 2} = T_{Scale\ 1} n_L^{0.5}$

### 4.3.2.2 Wave Generation and Synthesis

To create waves, the wave maker required a drive signal, indicating the paddle motion required to achieve specific wave conditions. After the selection of the test parameters, the drive signals were synthesize using the locally available GEDAP package, which provides an extensive range of software used for signal synthesis. The software, based on the input water depth and target wave height and period, automatically creates the regular signals. It allows the user to initiate and stop the wave generation, and to adjust the test duration.

### 4.3.2.3 Wave Calibration

All wave signals were calibrated based on the testing location measurements from WG7 prior to the installation of the Core-Loc model. Each initial signal showed discrepancies between the target and the generated waves` parameters. This was assessed by running a zero-cross analysis on the measured data

(part of the same GEDAP package) after each signal, and compare the measured with the target wave height. The initial synthesis signals generated waves close to the target, but adjustments due to shoaling and flume friction were required. Based on the percentage difference between the measured and desired wave heights, the initial signal gain setting was adjusted (either lower or higher) and the test was repeated until the target wave height was met. The drive signal was then run three times to ensure repeatable results.

## 4.4 Data Processing and Analysis

The NDAC data-acquisition software collected and stored the data from all instruments used in the model in digital format. After the completion of each test, the files were converted to a CSV file format (comma-separated values). These files were used to delineate the measurements into separate columns, containing an identical format of the time-series recordings of each wave gauge, force components, and velocity. All data was then analyzed using the GNU Octave software. The following sections will cover the individual instruments data analysis details.

### 4.4.1 Data Analysis System – GNU Octave

#### 4.4.1.1 Force Data

The zero value from the raw measurements of the ATI force transducer was Manually removed by taking the recordings average value during the first 20 s, time during which the waves did not reach the modelled Core-Loc. An example of this is shown in Figure 4-18(a), for a wave height of 0.133 m and period of 1.39 s. This procedure ensured that the data used for further analysis is representative of the forces experienced by the model, and was repeated for each force channel ($F_x$, $F_y$, and $F_z$). Each data set was then passed through a Butterworth low pass filter using the signal-processing package available in GNU Octave. This was used to remove high frequency noise from the measurements, as shown in Figure 4-18(b), representing a comparison between the raw and the filtered signal. The force time histories of each orientation in the direction of wave propagation were then used for the drag and inertia force coefficient optimization.

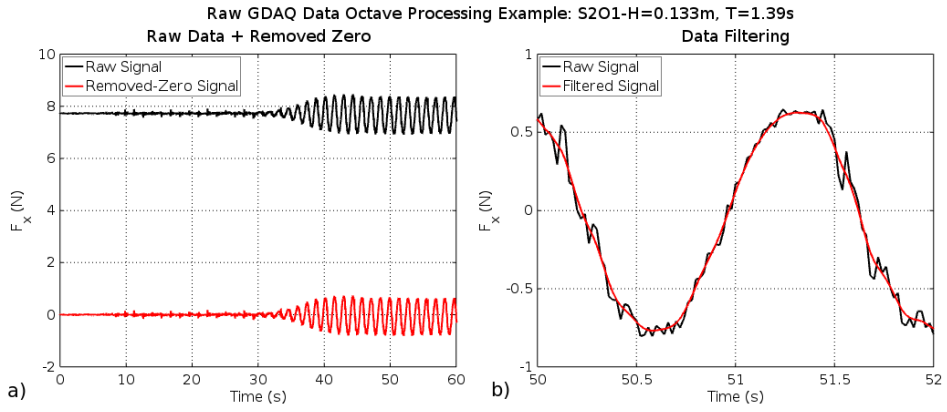


Figure 4-18: Raw GDAQ data processing in GNU Octave. (a) Example zero removal from ATI force transducer recordings; (b) Butterworth low pass filter application and results compared to the raw signal.

#### 4.4.1.2 Wave Data

The wave data was not directly required for the force coefficient analysis. As mentioned in Section 4.2.2, the WG7 data was used for the analysis and calibration of the wave conditions and did not require filtering.

#### 4.4.1.3 Velocity and Acceleration Data

Similarly, the velocity measurements at the centroid of each orientation were passed though the same low pass filter. The movement of water particles time history was then checked against wave transformation theories. Since the testing conditions corresponded to transitional to shallow waters, the particles should follow an elliptical orbit, flatter near the bottom of the flume. Figure 4-19(a) represents the orbital motion of the water particles based on the ADV measurements (for sign convention, refer to Figure 4-10). Based on the spatial asymmetry and magnitude of the velocity components shown, a clear elliptical particle orbit typical to transitional to shallow water conditions can be seen, indicating accurate velocity measurements. The local acceleration time history was then determined based on the first derivative of the velocity data with respect to time ($a = \partial u/\partial t$). The phase relationship between the velocity and acceleration was checked by comparing the two data sets, as shown in Figure 4-19(b). The 90º phase difference can be clearly observed, indicating a maximum acceleration when the velocity is at a minimum.

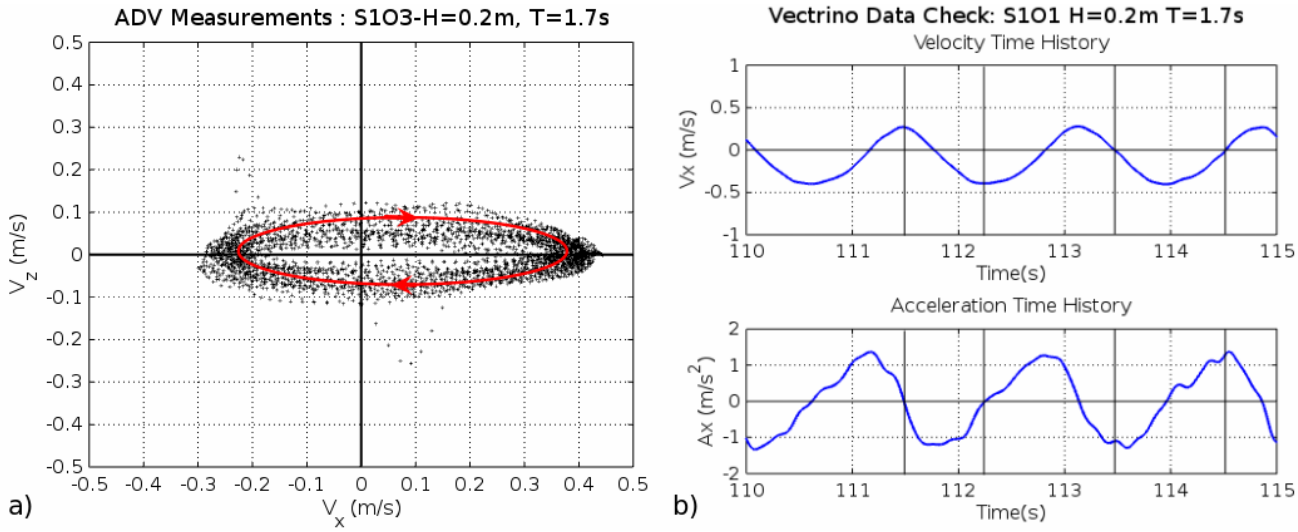


Figure 4-19: Example of the ADV measurements quality check based on a wave height of 0.2m and period 1.7s. (a) Elliptical orbital motion of the water particles; (b) Velocity and acceleration phase relationship check.

### 4.4.2 Quality Control

#### 4.4.2.1 Repeatability and output Variance of Instruments

The NDAC interface allowed for real-time observations of the instrument measurements. After each test, the time histories were reviewed to ensure that the instruments and data acquisition system function properly. Any unrealistic results were discarded and the test was repeated. Once a test was considered successful and the flume water level settled, a new drive signal was loaded and the next

tests were initiated. The repeatability of the test results was unfortunately not documented due to time constraints. Several tests should have been repeated 3 to 5 times to ensure that the instruments output similar trends and values for the same drive signal. The results of this step were not recorded during the experiments, as many of the drive signals were repeated throughout the testing period and visual observations of the NDAC outputs indicated reasonable repeatability. Specific tests were repeated because of the second data acquisition system used, recording the pressure time history from the model Core-Loc, which mal-functioned occasionally.

#### 4.4.2.2 Output Data

Once the GNU Octave raw data processing was complete, the wave profile and velocity and forces time histories of each test were subject to a quality control. The velocimeter, force transducer, and WG7 alignment was illustrated in Figure 4-8. The three instruments were mounted based on visual observations; however, any deviation from the centroid of the unit, which was mounted on the force transducer, results in phase offset measurements. For this reason, the wave profile recorded forces and velocities, and the derived accelerations of each test were plotted and compared, as shown in Figure 4-20. Based on the results, the velocity and wave elevation time series were adjusted Manually in GNU Octave to match the required phase frequency of the force transducer. This step was necessary where the wave prove or the velocimeter was a few millimeters off from the model`s centroid, which caused a phase drift of less than 0.02 seconds.

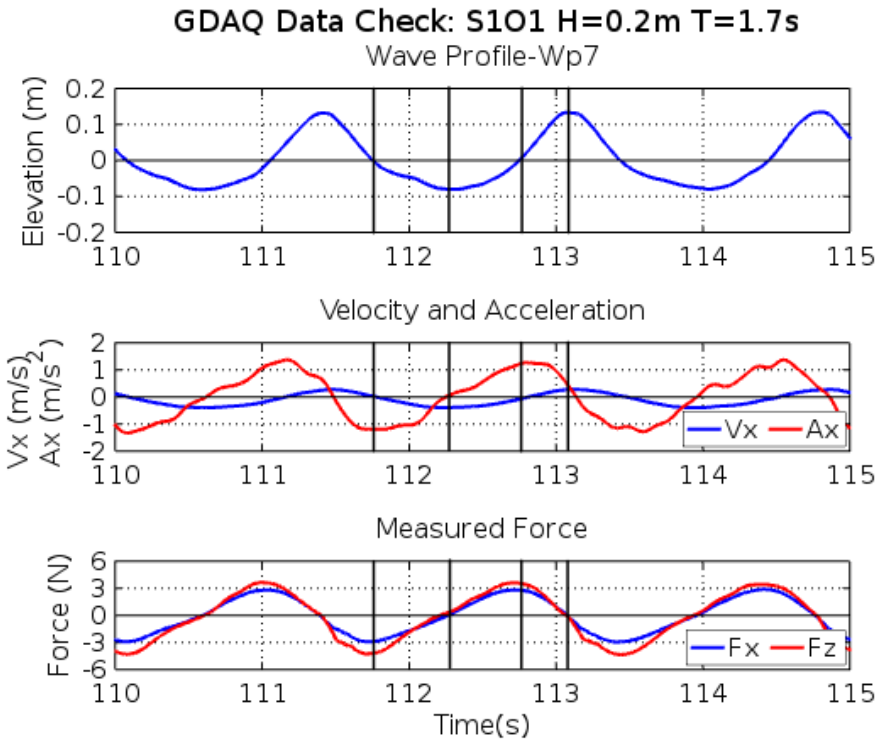


Figure 4-20: Testing location alignment control and phase offset corrections instruments (WG7, ADV, ATI force transducer).

## 4.5 Results and Analysis

The following section will cover the hydrodynamic analysis results of the seven Core-Loc orientations tested under different oscillatory wave conditions. The recorded force time histories of each test will be evaluated in more detail to uncover any discrepancies in the force and flow development around different unit orientations. The optimized drag and inertia force coefficients will be covered in the second part of the analysis.

### 4.5.1 Force Analysis and Orientation Effects

Following the GNU Octave processing of the raw force time histories, the results of each tested orientation (Figure 4-22) were grouped together based on the different wave signals used, and split into the three directional components – x, y and z. The longitudinal force ($F_x$) time histories are shown in Figure 4-21(a) and (b) for scale 1 and 2, respectively. The forces recorded during the tests were relatively small, with maximum values ranging from 0.4 N to 3.5 N depending on the wave conditions and scale. Because of the small force magnitudes, the time series show small variations of the forces between different Core-Loc orientations. The differences become more distinct as the period and wave height increases. On average, a 0.5 N difference can be observed between different orientations, with largest differences corresponding to the highest waves and longest periods, of 1.5 N for scale 1 and 0.5 N for scale 2. The largest forces were recorded for O1 and O4, the orientations with the largest projected area normal to the wave propagation direction. Orientation 2 and 5, which also shares a large projected area relative to other orientations were expected to experience larger longitudinal forces. A closer look at the longer waves data indicates that as the wave height increased, for both scales, larger forces are acting on O2; this was not observed for O5. This discrepancy is believed to be due to the position of the middle prong, which facilitates the uprush of the flow, decreasing the overall resistance of O5 compared to O1, 2 and 4. The smallest forces were recorded for O3 and O6, except for test with a wave height of 0.1 m and 1.5 s period. For that case, O4 corresponds to the smallest forces in the direction of wave propagation; however, due to the significant offset time history at the time of the wave trough relative to the other tests, this data set is not considered accurate. Orientations 3 and 6 share the same streamlined geometry and smallest total projected area, coinciding with the orientation that experienced the least resistance during the controlled drop tests discussed in Chapter 2 (O2).

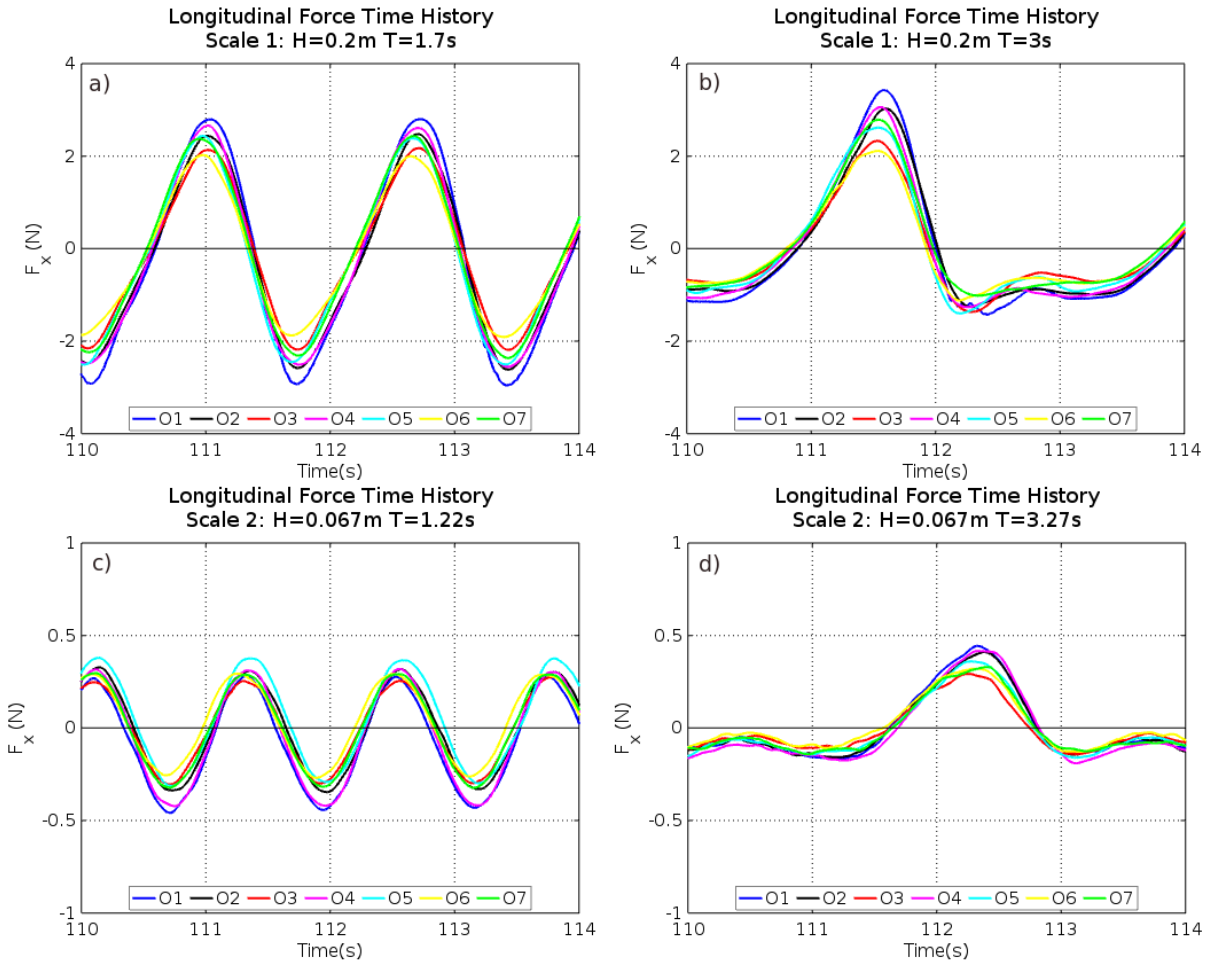


Figure 4-21: Longitudinal force time history recorded for each orientation. (a) Scale 1 –H=0.2m, T=1.7s; (b) Scale 1 –H=0.2m, T=3.0s; (c) Scale 2 –H=0.067m, T=1.22s; (d) Scale 2 –H=0.067m, T=3.27s.

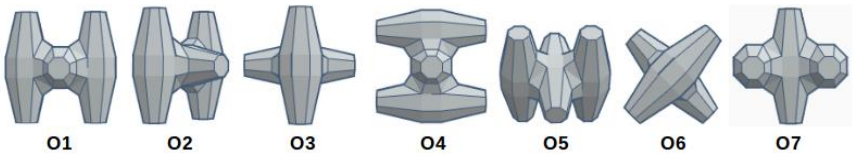


Figure 4-22: Tested Core-Loc armour unit orientations.

Although the analysis of the transversal forces ($F_y$) is beyond the scope of this work, the recorded time histories for each orientation and wave conditions are shown in Appendix B.5. As most orientations were symmetric to the direction of wave propagation, small forces were measured in this direction, with magnitudes less than 0.1 N on average for both scales. From all tests, O2 and O4 experienced slightly higher forces relative to the other orientations. This was expected for O2, which is tilted 45º relative to the flow, however, transversal forces were not expected for O4. The small variations recorded are associated with imperfect alignment of the unit's middle prong, which would cause a different flow development on the sides of the unit, as well as potential influences due to vortex shedding behind the model unit.

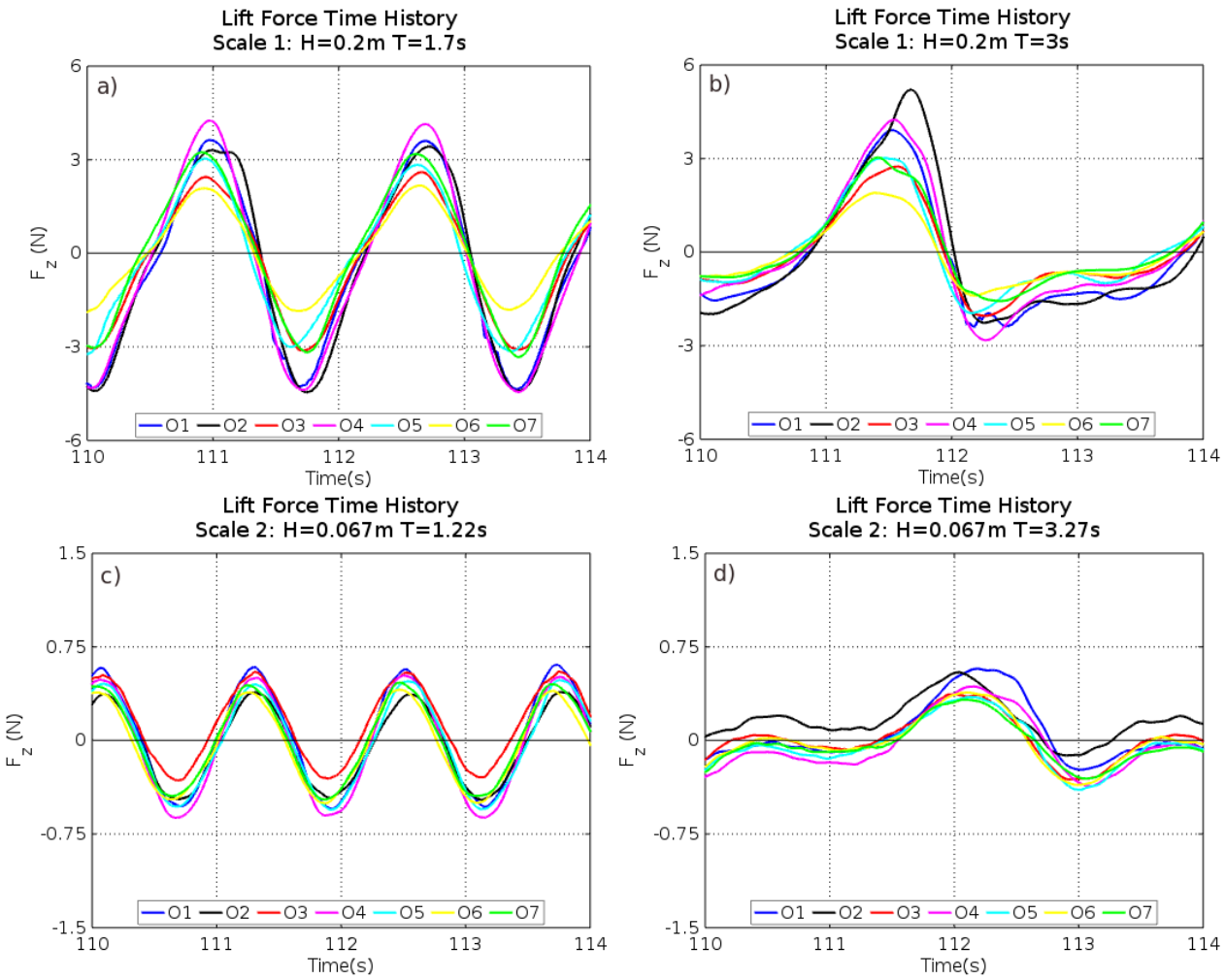


Figure 4-23: Lift force time history recorded for each orientation. (a) Scale 1 –H=0.2m, T=1.7s; (b) Scale 1 –H=0.2m, T=3.0s; (c) Scale 2 –H=0.067m, T=1.22s; (d) Scale 2 –H=0.067m, T=3.27s.

The lift force ($F_z$) measurements are shown in Figure 4-23(a&b) and (c&d), for scale 1 and 2, respectively. The measured magnitudes are to a certain degree larger than the longitudinal forces. This is believed to be attributed to a construction error of the PVC board hole through which the threaded rod connecting the model Core-Loc unit to the ATI force transducer was installed. This hole was made slightly bigger, to prevent any interference between the rod and the PVC board. Due to an initial misalignment during the construction, the hole had to be re-drilled, leading to a considerable larger gap between the rod and the board then what was intended. To further investigate this, the similarity of the peak forces of the scale 1 and 2 data sets were compared, by assessing the quantile-quantile (Q-Q) distribution of the lift to longitudinal force ratios. Figure 4-24 represents Q-Q plot, showing the $F_z/F_x$ ratio of scale 1 on the y axis, and scale 2 on x. The shape of the dataset (falling on a straight line) indicates that the measurements of both scales have identical distributions. This implies that the differences in forces measured are consistent throughout the experiment. It was suggested that the larger lift forces are associated with a difference in the pressure between the bottom and top of the unit. Due to Core-Loc`s geometry, flow will be rushed through the various gaps between the unit`s prongs. This is associated to an increase in flow velocity around the prongs of the unit. If the flow velocities

under and above the unit are different, the resultant pressure difference will create lift forces acting on the unit. Further analysis of the lift force time history relative to the wave profiles (an example is shown in Figure 4.20) supports the idea that the cross-flow through the PVC board below the unit influenced the measurements in z-direction. Small oscillations of the PVC board were observed during testing as the wave crests passed the testing location, despite the heavy metal frame. The board flexing downward would cause the water to rush through the gap, causing a direct uplift force on the unit. This is supported by the observed trends, where an uplift force can be observed as the wave crest passes. Similarly, the opposite is expected during the wave trough, where the difference in elevations causes the board to lift and water to fill the open space under the frame (associated with a downward force on the unit).

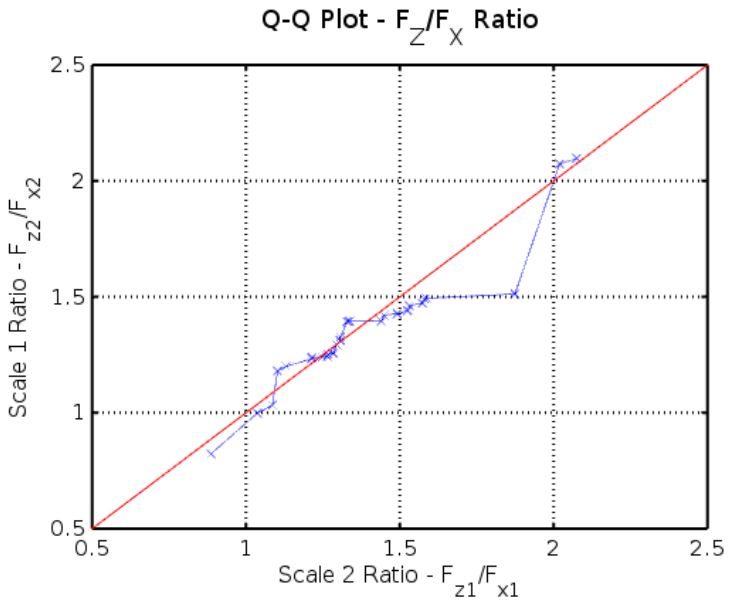


Figure 4-24: Quantile-Quantile probability plot comparing the lift to longitudinal peak forces ratios between Scale 1 and Scale 2

The large lift measurements compared to the longitudinal forces are believed to be associated with the construction error that allowed cross-flow through the PVC board below the unit. The force transducer was manually calibrated in all directions as discussed in Section 4.3, however, this was performed with the flume dry. To accurately pin-point the source of the problem, the measured data should be compared with the lift forces recorded under the same wave conditions, but without the unit mounted on the transducer. Unfortunately, these tests were not performed, as the error was observed after the testing setup was modified for a different stage of the project. Although the pressure variation across the Core-Loc unit seems a reasonable explanation, the magnitude and distribution of forces does not support that theory. Due to this reason, the z-data is considered erroneous.

### 4.5.2 Drag and Inertia Force Coefficients

#### 4.5.2.1 Morison Equation Optimization

The poor quality of the force measurements through the test program precluded the analysis of lift forces and coefficients. However, it is assumed that this error did not affect the other force measurements, and therefore only the analysis of the longitudinal forces was conducted – this force component was more critical for the determination of the drag and inertia coefficients, the scope of these experiments.

The drag and inertia force coefficients were empirically determined from the experimental force time series recorded for different wave conditions and Core-Loc unit orientations. The units loading response was theoretically estimated using Morison`s equation and the wave kinematics data recorded by the ADV instrument. The $C_D$ and $C_M$ values have been determined using least squares optimization of the difference in total error between the measured longitudinal force ($F_{measured}$) and the force prediction of Morison`s equation. This step was easily implemented using a python algorithm (once again using the same *NumPy* library) in terms of the error term ($\sigma$), as shown below. Using this technique, the only two unknowns are the drag and inertia coefficients, which are optimized to provide the best fit at each time step, over the entire time record.

$$\sigma^2(C_D, C_M) = \int_0^t \left[F(t)_{measured} - F(t, C_D, C_M)_{computed}\right]^2 dt$$

$$\sigma^2(C_D, C_M) = \left[F_x - \left(\rho C_M V \frac{\partial u}{\partial t} + \frac{1}{2}\rho C_D A u|u|\right)\right]^2$$

#### 4.5.2.2 Force Coefficient Analysis

As oscillatory flow reverses direction every half wave cycle, the raw force coefficients extracted for each time step from the least squares optimization were sorted according to an ascending order of the time step`s corresponding Reynolds number. This was done such that the data could be interpolated and interpreted in a meaningful way. Typical results of the drag and inertia force coefficients are shown in Figure 4-25 for each orientation as a function of $Re$. These correspond to the highest waves and longest period of both scales (*Scale 1- H=0.2m, T=3s; Scale 2- H=0.133m, T=2.45s*), with the results of other tests shown in Appendix B.6. For this section, the $Re$ number was calculated using the instantaneous velocity measurements and the characteristic length of the scaled Core-Loc unit. As part of the force coefficients analysis, Keulegan-Carpenter number was calculated for each flow condition. To estimate the velocity amplitude in the $K_c$ formulation ($K_c = uT/L$), the maximum recorded fluid particle velocity of each wave signal and its corresponding wave period was used. Similarly, to the $Re$ calculations, the characteristic length scale of the object was based of the characteristic length of each unit ($L = C_L$). The force coefficient results are shown in Figure 4-26 as a function of $Re$, for one orientation (O2) and different $K_c$ numbers.

#### 4.5.2.3 Drag and Inertia Force Coefficients

The results shown in Figure 4-25 indicate that different Core-Loc unit orientations did not affect the optimization results of both the drag and inertia force coefficients. Considering the little variation observed in the magnitude of the longitudinal forces, this is expected. Further determination of the $K_c$ number for each wave signal reveal that the data is not well conditioned to determine the drag coefficients. As covered in the literature review, the force coefficients vary with respect to different $Re$ and $K_c$ numbers. For low $K_c$ numbers there is not enough time for flow separation or wake to form behind an object before flow reversal (oscillatory flow reverses direction every half cycle). In these conditions, the only significant contribution to the total drag force is due to viscous shear forces; however, these are small compared to the inertia forces (Lin, 1980). Therefore, for $K_c$ numbers less than 5, the regime is dominated by inertia forces and the drag effects can be neglected. The short period waves generated for this experiment correspond to small $K_c$ numbers, and therefore the drag coefficient results are not considered reliable. Figure 4-26 shows the drag and inertia coefficients results for the different $K_c$ values generated as a function of the $Re$ number. Sapkaya (1976) published the most comprehensive and detailed study of the $C_D$ and $C_M$ variations as function of $Re$ and $K_c$. Generally, it was shown that the $C_D$ decreases with increase in $K_c$, while $C_M$ increases with increase in $K_c$. Both figures clearly indicate that $C_D$ decreases with increasing $Re$ to a value of approximately 0.25 after which the results increase as $Re$ number increases. Contrary, the inertia coefficients increase with increasing $Re$ number, but stabilize at around a value of 1.75. For $K_c$ values larger than 5, the drag effects increase – this is evident from the $C_M$ results for the same wave height with different periods, as longer period waves correspond to larger $K_c$ numbers. For both scales and all four wave signals, the results for the same wave height with a longer period correspond to a decrease in the inertia coefficient. For example, for *Scale 1: H=0.1m, T=1.5s,* $K_c = 2.4$, $C_M$ converges to around 1.7, while for the same wave height with *T=4s,* $K_c = 6.7$, $C_M$ converges towards 1.3. The same trends between $K_c$ numbers and the distribution of the inertia force coefficients are observed for scale 2, however, the coefficients converge to lower values as the magnitude of the recorded forces and achieved $Re$ numbers are much smaller. Moreover, since scale 2 corresponds to smaller $K_c$ numbers, the coefficient results has been observed to be more scattered – which has been reported in other literature sources (Sarpkaya, 1976), and therefore the interpolation of the results has been more difficult for these conditions. As it is visible in Figure 4-26, the interpolation results of $K_c = 1.9$ and 4.5 are notably noisier at higher $Re$ numbers compared to the same tests but with higher $K_c$ numbers.

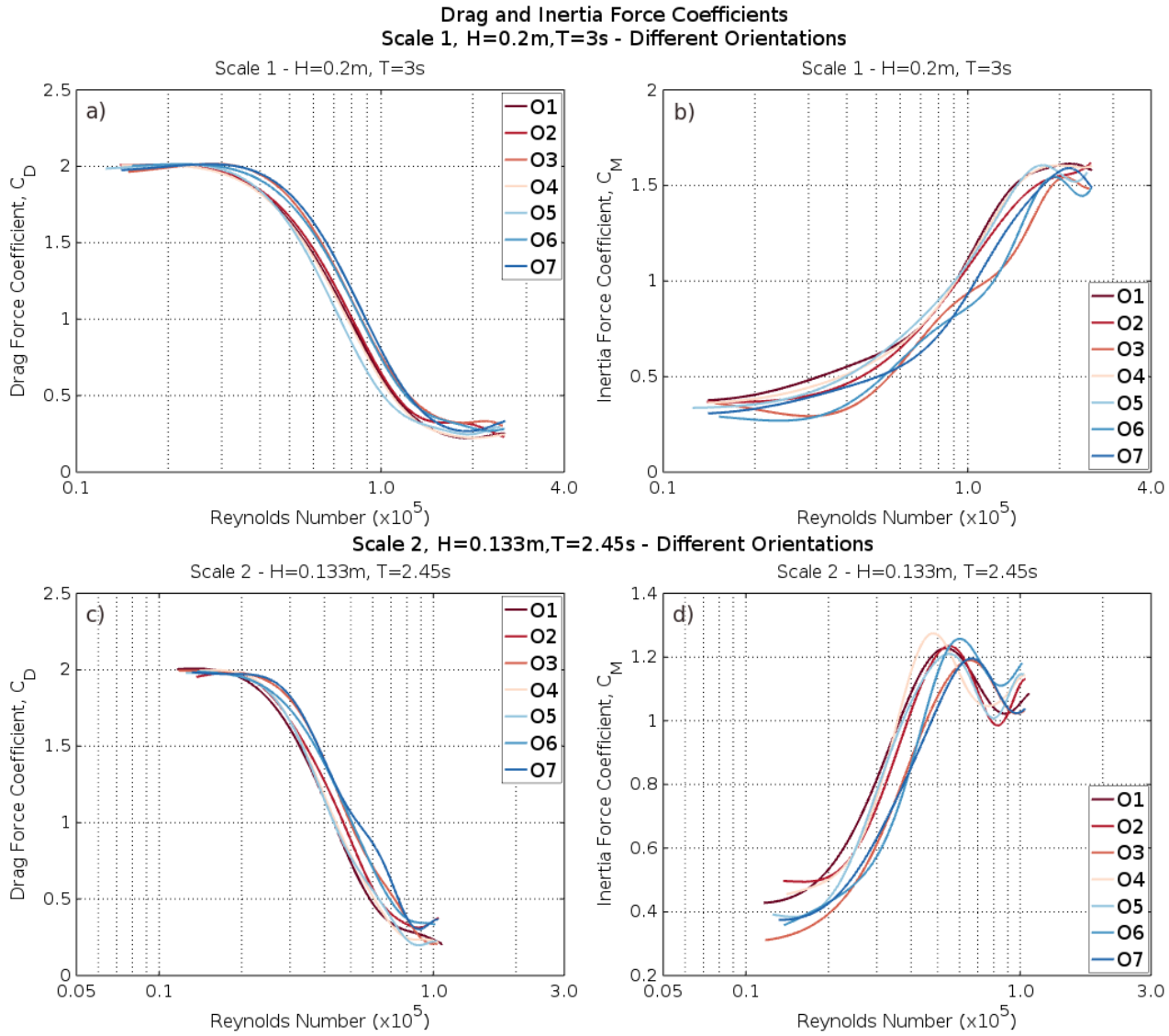


Figure 4-25: Morison force coefficients results for different Core-Loc orientations as a function of Reynolds number. (a) Drag coefficient: Scale 1 –H=0.2m, T=3.0s; (b) Inertia coefficient: Scale 1 –H=0.2m, T=3.0s; (c) Drag coefficient: Scale 2 –H=0.133m, T=2.45s; (d) Inertia Coefficient: Scale 2 –H=0.133m, T=2.45s.

In addition to the smaller force variations recorded, the inertia force component in Morison`s equation is proportional to the fluid acceleration and unit volume, and the influence of unit orientation on the inertia force coefficients is not represented. The only parameter linking the structure geometry to the inertia force is the unit volume, which is constant throughout the tests regardless of orientation. Although it has been shown that the drag coefficient data is not reliable, this study covered $K_c$ numbers of up to 8.3, with half of the tests in inertia dominated regimes. For this reason, it is believed that the inertia force coefficient results are accurate, and a value of $C_M = 1.6$ is considered representative for the Core-Loc unit at high $Re$ numbers. The inertia coefficient converges towards a value of 1.2 for scale 2, however for these tests the range of $Re$ numbers achieved is lower compared to the scale 1 tests. As it can be seen from Figure 4-25, these values show an increasing trend as $Re$ increases. Note that this value is representative for inertia dominated flow regimes, and it would decrease as the drag effects become significant. Based on the different variations of the two empirical coefficients at

different $K_c$ numbers, it would be expected that the drag coefficients would be higher for higher $K_c$ numbers. Although this can be generally observed from the results with small differences between the $C_D$ value at high $Re$ numbers, the trend is not consistent for all tests. For larger $K_c$ numbers ($K_c > 5$), it has been shown that the magnitude of the transverse forces on the structure is appreciable, and therefore Morisons force predictions underestimate the total force (Morison equation does not account for the transversal influences) (Meyers, 1975). The same wave, but with longer period and sequent larger $K_c$ number, will have smaller fluid particle velocities. However, even if the velocities are different between the two wave periods, the accelerations can undergo at the same rate of motion change – acceleration is the change in velocity with respect to time. It is believed that the inconsistencies in the drag calculations at $K_c > 5$, in addition to the underestimation of Morison equation, are due to similar rates of change in velocity between the same wave signal for a short and a long period. This causes the inertia force component (proportional to the acceleration) to remain relatively constant, while the drag component is underestimated by the Morison prediction at these $K_c$ conditions – consequently, the drag coefficients will be smaller.

Similar to the iterative process of reducing the error between measured and predicted forces used to estimate the force coefficients in the first experiment (Chapter 4), the accuracy of the results can be improved by considering the entire time-series of measurements, or over one wave cycle. Using the current approach, the solution of the force balance can arrive at multiple guesses of inertia and drag coefficients – it is for this reason why the solution that corresponded to the smallest least-square error was considered the true result at individual time steps. For a better interpretation of the results in relation with $K_C$ number, the empirical force coefficients may be computed as a time-averaged value of the total in-line force over a number of flow cycles. Using this approach, a meaningful trend can be produced with respect to a changing $K_C$ number. Considering the limited range of wave conditions used during this experiment proved this method of estimating the empirical coefficients would not provide any further insights of their dependence on the $K_C$ numbers.

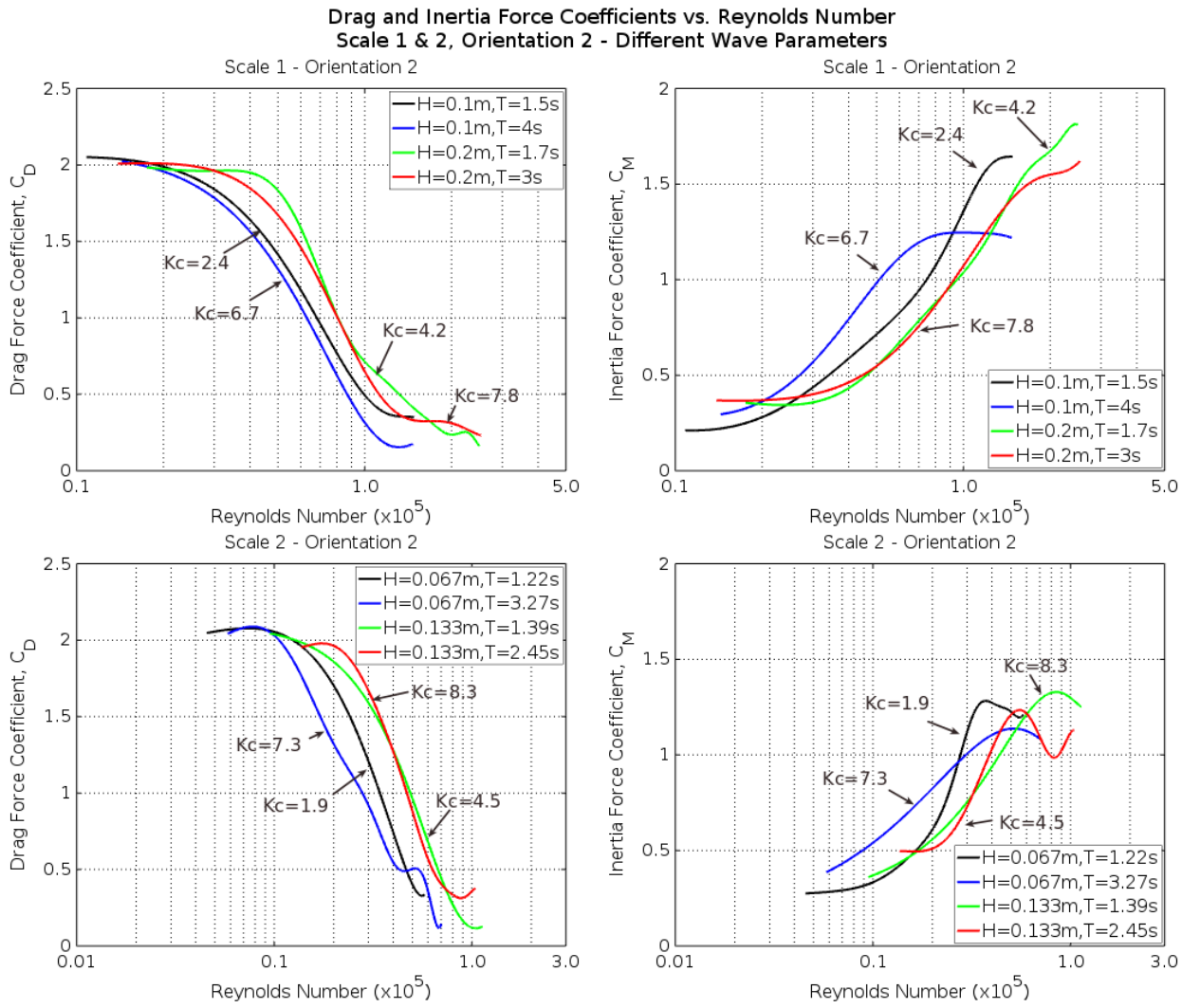


Figure 4-26: Morison force coefficients results as a function of Reynolds number for constant $K_c$ values. Data based on the tests performed with orientation 2. (a) Drag coefficient- Scale 1; (b) Inertia coefficient- Scale 1; (c) Drag coefficient- Scale 2; (d) Inertia Coefficient- Scale 2.

### 4.5.2.4 Comparison Between Morison Equation and Measured Force Results

In Figure 4-27, the measured in-line forces are compared to the in-line hydrodynamic force predictions of Morison model using the derived $C_D$ and $C_M$ empirical coefficients as functions of $Re$ number, discussed in the previous section and the measured fluid kinematics. The results are shown for each wave condition for one scale and one orientation (S1O2), with the complete comparison included in Appendix B.7. Generally, the Morison equation force model yields relatively accurate approximation of the measured forces. However, it can be observed that the theoretical hydrodynamic forces are not always accurately estimated at the peaks of the force time histories. The velocity and acceleration time histories relative to the occurrence of peak forces, shown in Figure 4-20, show that the peak longitudinal forces occur when the velocity is zero, and acceleration is largest. Therefore, in these conditions the peak forces will be based solely on the inertia force contribution. Comparing the

predicted longitudinal hydrodynamic force between different wave periods, it is clear that Morison`s equation underestimates the forces more as the period of the waves increases.

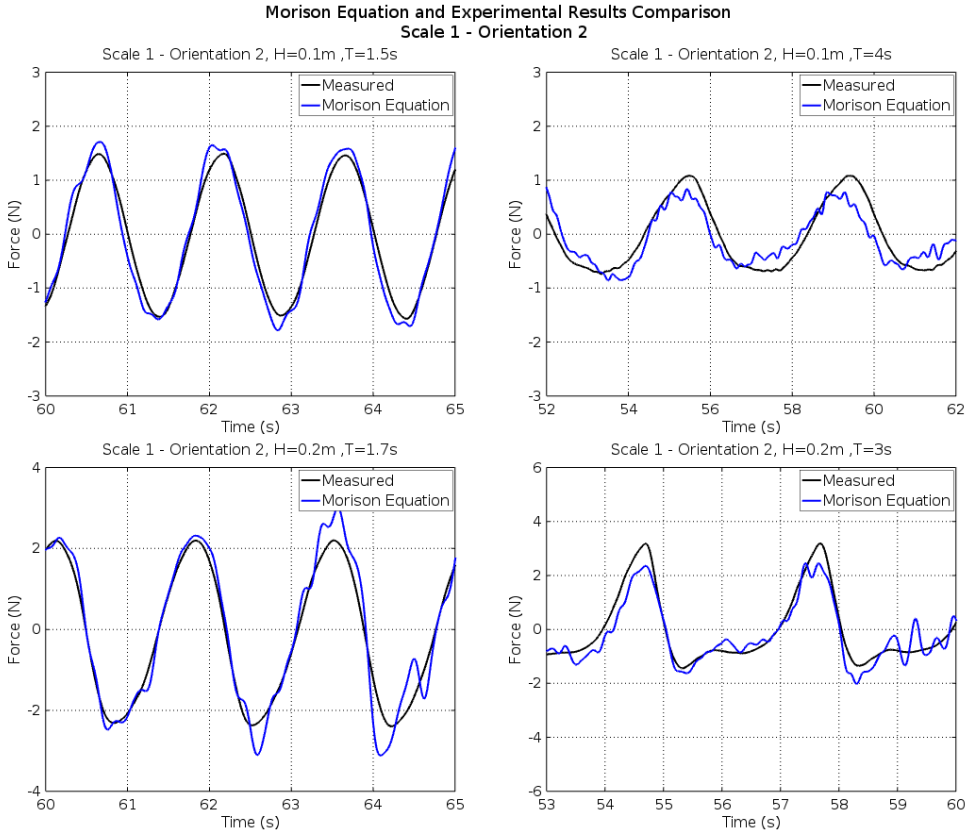


Figure 4-27: Comparison between the measured in-line unit response and total hydrodynamic force estimated using Morison equation and the derived $C_D$ and $C_M$ coefficients for each regular wave signal– Scale 1, Orientation 2.

### 4.5.3 Lift Force Coefficients

The hydraulic stability of the armour layer of a breakwater governs its capability to withstand wave loading. The literature review conducted on this topic summarized the main forces that contribute to the layer`s stability under the destabilization forces as a result of wave motion (run-up and run-down) on the structure`s slope. Two important forces that undermine the stability of the armour layer are the drag and inertia forces, which were covered in previous sections. Another important destabilization force is the lift force, acting perpendicular to the slope as a result of the flow. The analysis of the lift forces was planned for the current work, however the poor quality of the force results in the vertical direction of the wave propagation (z), impeded their further use in the determination of the empirical lift force coefficients for different Core-Loc unit orientations and flow conditions. The lift forces determined experimentally for each unit configuration were to be analyzed, based on the lift coefficient results from the lift formulation shown below.

$$F_L = 0.5 C_L \rho_w u^2 A_L$$

### 4.5.4 Discussion

Over the range of flow conditions included in the test program, the results indicate that the total measured inline hydrodynamic forces are mostly influenced by the wave period and wave height rather than orientation. Based on the results presented, shorter period waves show little variation between the force results for different Core-Loc orientations, while increased variations were noticed for waves with longer period and higher height. However, the overall recorded force magnitudes were small throughout testing, with maximum in-line force of 3.5 N. The measured magnitudes represent a small percentage of the ATI force transducer range, and therefore can be subject to measurement uncertainty; however, the built-in threshold detection system that detected small changes of the applied load indicate that the transducer accuracy did not affect the results. The smallest in-line forces were recorded for orientations 3 and 6, which share the same streamlined geometry and have the smallest total project area normal to the wave propagation direction. These orientations correspond with the orientation that experienced the least resistance in the first experiment. The optimization of the force coefficients for these orientations in the previous study concluded that the flow development around this unit is significantly different, and thus a higher drag force coefficient was determined. However, this was simply a result of the Morison equation used to predict the forces, for which to reproduce the experimental measurements for the small projected area of these orientations, the optimized term $C_D$ had to be higher. A closer look at the geometry of these orientations relative to the flow indicates that these orientations exhibit a high moment of inertia around the transversal axis (*y-axis*). Therefore, due to their bulk mass distribution around the units three primary axis (*x, y, z*), their stability is overall increased along the longitudinal direction (*x-axis*). The largest forces were recorded for O1 and O4, which have the largest projected area relative to the other orientation. O2, which also has a larger area, was observed to developed larger in-line forces as the wave height and period increases.

The empirical drag and inertia force coefficients were then fitted to the measured data by minimizing the least squares error between the measured in-line forces and Morison`s predictions for all orientations and wave signals. The complete results from this analysis are shown in Figure 4-25 and Figure 4-26 for different orientations and Keulegan-Carpenter number, respectively. As the force coefficient differences were little for different Core-Loc configurations, no meaningful differences between the results of different orientations were noted. This result was also a consequence of the flow regime used that was dominated by the inertia forces. Morison's method assumes that the force can be estimated by the sum of the individual drag and inertia force components. The inertia term is proportional to the fluid acceleration and unit volume, and therefore the effects of unit orientation is not represented. The calculated $K_c$ numbers for the wave signals used ranged between 1.9 and 8.3. Keulegan-Carpenter numbers smaller than 5 correspond to inertia dominated regime, while drag effects become significant for higher $K_c$ numbers. The inertia force coefficients decreased as the wave period increased for the same wave height ($K_c$ number increases). The trends of the fitted force coefficient results showed good agreement with previous results published by other researchers – notably, Sarpkaya`s comprehensive study (1986) on the relative importance of drag forces over inertia forces in oscillatory flow for constant values of $K_c$. The drag coefficients were expected to increase for higher $K_c$ numbers; however, results did not show a consistent trend. Between different tests, several

inconsistencies were observed where the drag coefficient value for smaller $K_c$ numbers was either the same or slightly higher. The drag force coefficients could not be reliably determined at low $K_c$ numbers because the drag forces were insignificant. At $K_c$ numbers larger than 5, their contribution becomes significant and therefore the predicted forces are underestimated.

The analysis concluded that the drag coefficient results are unreliable, however, since the flow regimes used during this study are predominantly dominated by the inertia effects, the inertia coefficients are relatively accurate. Furthermore, previous studies indicated that the $C_M$ estimations for $K_c$ numbers larger than 15 are not reliable (all tests corresponded to $K_c < 15$), as these conditions are dominated by drag. From the analysis of the force data under oscillatory flow conditions, the empirical coefficients used in Morison`s equation have been identified to be dependent on $Re$ and $K_c$ numbers, as shown in Figure 4-25 and Figure 4-26. The fitted coefficients were used in subsequent comparison between the measure total in-line forces and the Morison`s estimates. Generally, good agreement was observed between the two data sets. It was concluded that Morison's equation underestimates the peak forces for longer period waves, which are associated with higher $K_c$ numbers.

Another limitation of Morison`s formulation is that forces are calculated using the fluid velocity and acceleration that would occur at the centerline of the submerged structure, ignoring the effects of flow disturbance due to the structure`s presence. Notably, as it was covered during the literature review, the flow separation, vortex and wake formation behind the structure are not accounted for in the proposed formulation for the total hydrodynamic force acting on a submerged structure. Morison`s prediction of the wave induced forces acting on a submerged structure relies on accurate kinematics inputs (velocity and acceleration). These are estimated using wave theories where direct measurements of the fluid motion are not available, introducing the problem of selecting the appropriate wave theory from a design wave height or from wave surface elevation time histories. The accuracy of Morison`s equation force predictions using wave theories such as airy wave, stokes, solitary wave or stream function has been subject of many experimental investigations, however the theoretical kinematics predictions have been proved to have their own limitations and ranges of applicability on accurately describing the fluid motion.

For the complex geometry of a Core-Loc unit, or any CAUs, the velocity measured at the centroid of the unit, which the fluid motion would experience if the unit was not present, does not correctly represent the spatial and temporal variation of the complex fluid kinematics that occurs near the unit`s surface. Therefore, the drag and inertia forces estimated using Morison's method should not be expected to be 100% accurate – the drag is proportional to the velocity squared in the equation. Similarly, the inertia forces are proportional to the instantaneous fluid acceleration, which is dependent on the rate of change in velocity. This is a fundamental limitation of Morison`s equation, which neglects the dependence of the force upon both the instantaneous and preceding flow condition by using the instantaneous fluid particle velocity and acceleration. Despite being developed as an empirical method to predict wave loads on submerged cylinders, this thesis has shown that the Morrison equation, with appropriate force coefficients, can also provide a reasonable prediction of wave loads on an isolated Core-Loc unit resting on the seabed.

## 4.6 Summary and Conclusions

The study conducted at NRC consisted of a series of experimental investigations on Core-Loc armour units' hydrodynamics under oscillatory flow conditions. The temporal variation of force variations of seven different unit orientations was analyzed under different regular wave conditions and two scales. The wave loading in the direction of wave propagation was theoretically estimated using Morison`s equation by fitting the drag and inertia force coefficients to match the measured forces. The theoretical predictions were obtained using the recorded kinematics beside the centroid of each unit. Despite the results of this study being affected by limitation of Morison`s equation and the limited range of flow conditions examined, nonetheless, this work provides a complementary analysis of the force coefficients determined from the previous experiment. The analysis of the flow regime used throughout testing concluded that the data was best suited for the estimation of inertia coefficients, while the results from the controlled drop test were derived on the condition that the drag forces approach a constant value as the unit approach terminal velocities towards the end of the tests. Comparing the empirical and measured force data sets it was observed that Morisons model was able to provide a reasonable prediction of the longitudinal force for some conditions, but not in all. The model underestimates the peak forces, with increasing inaccuracy as the flow transitions from an inertia dominated to a drag dominated regime. The model was originally developed and applied for cylindrical piles, and despite numerous limitation, Morison`s equation remains a standard accepted method of estimating wave-loading on structures. Its applicability for estimating the hydrodynamic forces acting on individual armour units is questionable, as the geometry of any CAU and the flow development around the unit are much more complex to be accurately represented by the parameters used to calculate the inertia and drag force components in the current form.

# Chapter 5 Conclusions and Recommendations for Future Work

## 5.1 Conclusions

The application of Morison`s equation in predicting the hydrodynamic loads on Core-Loc armour units with different orientations and scales has been studied through a series of laboratory tests. Based on the analysis of the drag and inertia force coefficients of Core-Loc units under unsteady and oscillatory flow conditions, the following conclusions can be drawn.

### 5.1.1 Hydrodynamic analysis of Core-loc armour units under unsteady flow conditions

The experimental setup presented a simple system to maintain a constant falling unit orientation throughout testing. The guideline system used proved to be an efficient method to analyze the flow developments of different unit orientations.

- This study presented a novel non-intrusive camera-based tracking system utilizing image-processing techniques to track the armour unit motion. The algorithm converts the original footage into binary images that produce accurate and highly repeatable estimation of the unit`s displacement time histories.
- The results of the camera-based tracking system produced accurate estimation of the armour unit kinetics, which are required in the estimation of the drag and inertia force components using Morison`s equation.
- The initial drag and inertia force coefficient results showed discrepancies between the force development of different Core-Loc orientations. One particular orientation proved to experience greater velocities relative to the other tested orientations. In turn, the fitted drag coefficients for these tests were higher, highlighting the importance that placing patterns can have on the over stability of a breakwater armour layer. Further observations indicate that the distribution of the inertia moments relative to the flow play an important role on the stability of individual units.
- It was determined from the least squares optimization of the error between the measured data and Morison`s equation predictions that in fully turbulent flow regimes, a drag coefficient of $C_D = 1.4$ is representative for the Core-Loc geometry. No estimates of the inertia coefficients were possible, as the tests were performed in a drag dominated regime.
- The results of geometric scale influence on the hydrodynamic response of Core-Loc units were consistent with other literature sources. Comparing the drag and inertia force component of four different unit geometric scales, showed that drag forces become predominant as the flow conditions approach prototype conditions (larger scale, higher flow velocity).

- The applications of the vertical tank built for this experiment and the novel tracking system developed can be further extended to analyze the effects of unit orientations and scale of any CAU.

### 5.1.2 Hydrodynamic analysis of Core-Loc armour units under oscillatory flow conditions

- Over the range of oscillatory flow conditions included in the test program, it was shown that the inline hydrodynamic forces are mostly influenced by the wave height and period rather than unit orientations. This is mainly due to the relative importance of inertia forces over drag observed for the simulated flow conditions.
- The results from this experiment generally fall within inertia dominated regimes and therefore the effects of unit orientation were relatively small. However, this study provided estimates of the inertia force coefficients of Core-Loc units for low $K_c$ numbers (corresponding to inertia dominated flow regimes), complementing the results of the previous experiment.
- The use of Morison`s method for estimating the hydrodynamic loads on submerged cylindrical structures or objects has been extended in this study to CAUs. The results indicate that the method contains can provide reasonable estimates of the in-line l,oads on isolated Core-Loc units in some oscillatory flow conditions, but that the method has limitations, which can lead to erroneous predictions in other flow conditions.
- The complex fluid kinetics along the Core-Loc`s surface were oversimplified in this study, and represented by the instantaneous velocity and acceleration measurements besides the centroid of the model units. The flow field around complex CAUs geometries such as the Core-Loc unit are not accurately represented by this assumption.
- For the given flow conditions, the force coefficients were analyzed for constant values of Keulegan-Carpenter numbers. Despite unreliable drag coefficient results, the inertia results were consistent with other literature sources for small $K_c$ numbers. For a more detailed analysis of the dependence of drag and inertia forces on $Re$ and $K_c$ numbers, tests should be performed with a wider range of wave conditions.

The analysis of the drag and force coefficients discussed herein helps identify some of the primary variables that must be considered in the evaluation of wave induced loading on CAUs. The findings of the presented work provided a general understanding of the hydrodynamics load on individual Core-Loc armour units, and the effect of geometric scale, and orientation. The study highlighted some fundamental limitations of Morison`s method of estimating the in-line hydrodynamic of individual armour units, which must be further evaluated in future studies. The relationships between the flow kinetics along the complex geometry of CAUs and the parameters used to estimate drag and inertia force components need to be investigated.

While this study provided a good initial experimental investigation of the hydrodynamic loading of individual Core-Loc armour units, it provides no information regarding the influence of surrounding armour units and interlocking forces. This is a fundamental limitation of the application of the current work, and further collaborative studies involving UO, NRC-OCRE, Bairds W.F & Associates and ICL that will employ a more realistic breakwater section. As part of this ongoing collaboration, tests were performed at the NRC-OCRE research-center using a single instrumented unit located on a slope (Figure 5-1(a)) and subject to wave action. The analysis of this second study is undertaken by a different master's student. Ongoing tests will be performed using the same systems after a full breakwater section is constructed, current progress shown in Figure 5-1(b).

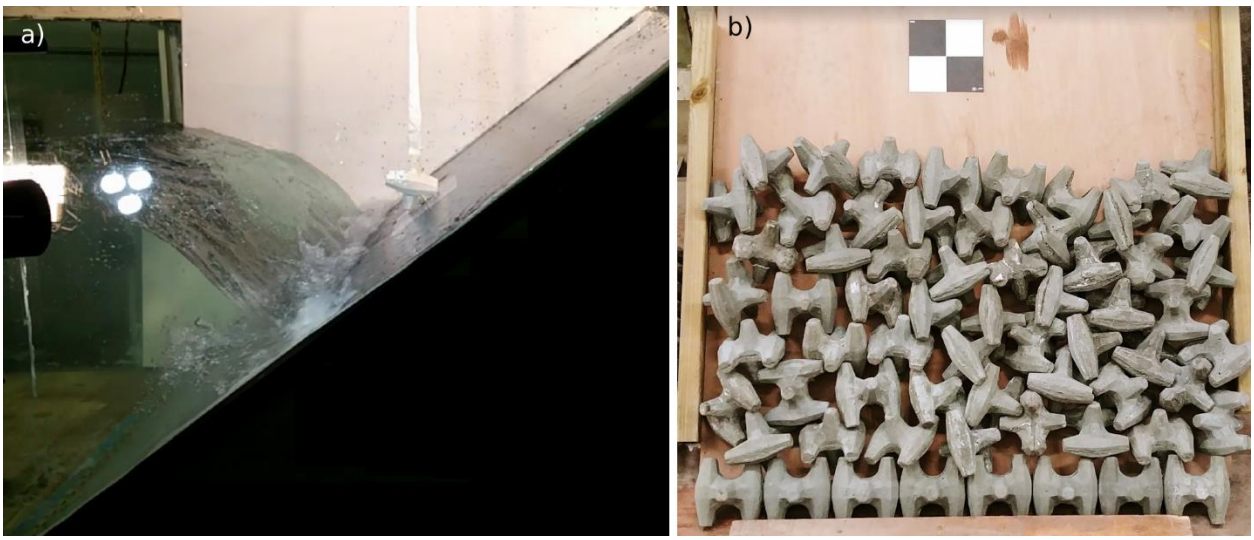


Figure 5-1: Ongoing research performed in the NRC-SWF. (a) Single instrumented Core-Loc unit on a slope; (b) Current placing progress of a breakwater armour layer constructed with Core-Loc armour units – casted onsite.

## 5.2 Recommendations for Further Research

Throughout this study, several aspects were identified that could be explored further in more detail to create a more comprehensive understanding of the hydrodynamic loading of CAUs. Several suggestions for future work are recommended, as follows:

- The camera-based unit tracking algorithm can be further improved. Currently, the quality of the results relies on controlled contrast differences between the unit and its surroundings. The thresholding function that detects the changes in pixels' luminosity can be further improved to detect changes from multiband rendered images. This would extend the applicability of the tracking algorithm to other engineering fields.
- A detailed investigation of the force coefficients and the influence of a wider range of $K_c$ numbers should be performed. Studies such as those performed by Sarpkaya (1986), showed the dependence and unique relationships of the drag and inertia coefficients on $Re$ and specific $K_c$ values. Moreover, studies should be performed using a full breakwater model section, with a

more sensitive force transducer, over a broader range of test conditions. The analysis could be then extended to the lift and transversal force components in addition to the in-line force analysis. Furthermore, the empirical drag and inertia force coefficients can be computed as a time-averaged value of the in-line forces over several flow cycles and wider range of flow conditions. This method will enable a more detailed conclusion with respect to the coefficient's dependency on different $K_C$ numbers.

- This study attempted to establish Morison equation force coefficients for isolated Core-Loc armour units located both away from and close to a solid boundary, and then apply the Morison equation to predict in-line hydrodynamic loads due to oscillatory flow. The Morison equation, while simple to use, has fundamental limitation and does not accurately represent the physical relationships between armour unit geometry, response and flow kinetics. Particularly, investigations should focus on the flow field around the units. The velocity and acceleration terms representative for armour units should be investigated, to further increase the accuracy of Morison`s equation. The instrumented unit developed as part of this study can be used in this regard, providing information of the spatial and temporal distribution of pressures, and consequently kinematics, as well as a PIV system.

The current work is just the initial stage of a comprehensive experimental and numerical investigation of the force development within a breakwater armour layer, and thus, some of the issues discussed here will be evaluated in future studies. Nonetheless, the study revealed some of the many challenges that coastal engineers face in the evaluation of the complex nature of wave induced loading on the armour layer of rubble mound breakwaters. This is still at large a very complex phenomenon to quantify experimentally, which was the primary reason that lead to empirical breakwater design provisions, ignoring at large the actual physical processes that generate forces within these structures.

# Bibliography

Ahrens, J.O., 1987. Characteristics of Reef Breakwaters. *Technical Report* CERC-87-17, U.S. Army Corps of Engineers, Waterways Experiment Station, Vicksburg, MS.

Allshop, N.W.H., 1983. Low-crest Breakwaters, Studies in Random Waves. *Proceedings of Coastal Structure `83*, Arlington, VA.

Baba, A., 2014. Concept of Hydrodynamic Load Calculation on Fixed Jacket Offshore Structures – An Overview of Vertically Mounted Cylinders. *American Journal of Engineering Research*, 3(3), 65-74.

Bairds W.F. & Associates., n.d.. Kaumalapau Breakwater Repair. Picture available at www.baird.com.

Battjes, J.A., 1974. Surf Similarity. *Proceedings of the 14th International Conference on Coastal Engineering*. Copenhagen, Denmark, ASCE, New York, 466-480.

Castro, E., 1933. Diques de Escollera. *Revista de Obras Publicas*. Madrid: 183-185.

Chanson, H. (2004). The Hydraulics of Open Channel Flow. Elsevier. ISBN 978-0-08-047297-3.

CIRIA, CUR, CETMEF, 2007. The Rock Manual: The Use of Rock in Hydraulics Engineering (2nd edition). C68, CIRIA, London.

CLI, 2012. Core-Loc Practical Aspects. *Concrete Layer Innovations*, Online resources available at www.concretelayer.com

CLI, 2012. Guidelines for Design: Core-Loc Design Table. *Concrete Layer Innovations*, Online resources available at www.concretelayer.com

Core-Loc-Africa, n.d.. Application of Core-Loc to Parts of Africa and Adjacent Islands. Picture of Port St. Francis Breakwater, available at www.core-loc.africa.com

De Graauw, A., 2007. Core-Loc Breakwater Armour Unit. Copyright Free Image.

Domingo, V.A.M., 2012, Evaluation of Concrete Armour Units Used to Repair Damaged Dolos Breakwater. *Master`s Thesis*, Delft University of Technology Faculty of Civil Engineering and Geoscience, Hydraulic Engineering.

EurOtop, 2016. Manual on Wave Overtopping of Sea Defenses and Related Structures. *An Overtopping Manual Largely Based on European Research, but for Worldwide Application.* Van Der Meer, J.W., Allsop, N.W.H., Bruce, T., De Rouck, J., Kortenhaus, A., Pullen, T., Schüttrumpf, H., Troch, P. And Zanuttigh, B., www.overtopping-Manual.com.

FEMA, 2005. Wave Run-Up and Overtopping. Coastal Flood Hazard Analysis and Mapping Guidelines-*Focused Study Report*.

Frostick, L.E., McLellan, S.K., Mercer, T.G., 2011. User Guide to Physical Modelling and Experimentation: Experience of the HYDRALAB Network. *IAHR Design Manual*, CERC Press, Balkema, Leiden, The Netherlands.

Hudson, R.Y., 1953, Wave Forces on Breakwaters. *Transactions of the ASCE*, 118, 653-674.

Hudson, R.Y., 1958. Design of Quarry Stone Cover Layer for Rubble Mound Breakwaters. *Research Report* No. 2-2, CERC, WES, Vicksburg, MS.

Isaacson, M., Baldwin, J., Niwinski, C., 1991. Estimation of Drag and Inertia Coefficients From Random Wave Data. *Journal of Offshore Mechanics and Arctic Engineering*, 113, 128.

Jackson, R.A., 1968. Limiting Heights of Breaking and Nonbreaking Waves On Rubble Mound Breakwaters. *Technical Report* No H-6803, USACE, WES, Vicksburg, MS.

Keulegan, G.H., Carpenter, L.H., 1958. Forces on Cylinders and Plates in an Oscillating Fluid. JBS Report No. 4821. *Journal of Research of the National Bureau of Standard*, 605, 423-440.

Konstantinidis, E., Dedes, A., and Bouris, D. (2017). Drag and Inertia Coefficients for a Circular Cylinder in a Steady Plus Low-Amplitude Oscillatory Flow. 10th International conference on Flow-Induced Vibration. Vol. 65, pp. 219-228. https://doi.org/10.1016/j.apor.2017.04.010

Latham, J.P, Mannion, M.N., Poole, A.B., Bradbury, A.P. Allsop, N.W.H., 1988. The Influence of Armour Stone Shape and Rounding on the Stability of Breakwater Armour Layer. *Report* 1, Coastal Engineering Group, Queen Mary College, University of London, UK

Latham, J.P, Xiang, J., Anastasaki, E., Guo, L., Karantzoulis, N., Vire, A., Pain, C., 2014. Numerical Modelling of Forces, Stresses and Breakages of Concrete Armour Units. *34th Conference on Coastal Engineering*, 1-13.

Latham, J.P., Anastasaki, E., Xiang J., 2013. New Modelling and Analysis Methods for Concrete Armour Units Systems Using FEMDEM. *Journal of Coastal Engineering*, 77, 151-166.

Latham, J.P., Anastasaki, E., Xiang, J., 2013. New Modelling and Analysis Method for Concrete Armour Unit Systems Using FEMDEM. *Coastal Engineering*, 77, 151-166.

Melby, J.A., Turk, G.F., 1994. Concrete Armour Unit Performance in Light of Recent Research Results. *ASCE/WPCO Seminar on Case Histories of Design, Construction and Maintenance of Rubble Mount Structures*, ASCE, New York.

Melby, J.A., Turk, G.F., 1997. Core-Loc Concrete Armour Units: Technical Guidelines. *Technical Report* CHL-97-4. WES, USACE, Vicksburg, MS.

Meyers, D.W., 1975. Transverse Oscillations of a Circular Cylinder in Uniform Flow. *Master's Thesis*, Naval Postgraduate School, Monterey, California.

Milthaler, F.M., Pavlidis, D., Xiang, J., Latham, J., Pain, C.C., Vire, A., Piggott, M.D., Farrell, P.E., 2013. The Immersed Body Method Combined with Mesh Adaptivity for Fluid-Solid Coupling. *Coastal Structures 2011*- Proceedings of the 6th International Conference. Vol 1, pp 277-283.

Morison, J.R., Obrien, M.P., Johnson, J.W, Schaaf, S.A, 1950. The Force Exerted by Surface Waves on Piles. *Petroleum Transactions*, American Institute of Mining Engineers, 189, 149-154.

Palmer, G.N., Christian, C.D., 1998. Design and Construction of Rubble Mound Breakwaters. *Transactions of the Institution of Professional Engineers New Zealand*: Civil Engineering Section, 25(1), 19-30.

Postma, G.M., 1989. Wave Reflection from Rock Slopes Under Random Wave Attack. *PhD Thesis*, Delft University of Technology, Faculty of Civil Engineering and Geoscience, Hydraulic Engineering.

Powell, K.A., Allsop, N.W.H., 1985. Low-crest Breakwaters, Hydraulic Performance and Stability. *Hydraulics Research*, Wallingford. Report SR 57.

Sakakiyama, T., Kajima, R., 1990. Scale Effect of Wave Forces on Armour units. *Proceedings of the 22nd Coastal Engineering Conference*, ASCE, 2, 1716-1729.

Sarpkaya, T., 1976. In-line and Transverse Forces, on Cylinders in Oscillatory Flow at High Reynolds Numbers. *Technical Report* No. NPS-69-SL76062, Naval Postgraduate School, Monterey, CA.

Sarpkaya, T., 1976. Vortex Shedding and Resistance in Harmonic Flow About Smooth and Rough Cylinders at High Reynold's Numbers. *Technical Report* No. NPS-59SL76021. Naval Postgraduate School, Monterey, CA.

Sarpkaya, T., 2010. Wave Force on Offshore Structures. *Cambridge University Press*, Cambridge, UK.

Seelig, N.W., 1983. Laboratory Study of Reef-Lagoon System Hydraulics. *Journal of Waterway, Port, Coastal, and Ocean Engineering*, 9(4).

Seelig, W.N., 1980. Two-dimensional Tests of Wave Transmission and Reflection Characteristics of Laboratory Breakwaters. *Technical Report* 80-1, CERC, WES, Vicksburg, MS.

Seelig, W.N., Ahrens, J.P., 1981. Estimation of Wave Reflection and Energy Dissipation Coefficients for Beaches, Revetments and Breakwaters. *CERC Technical Paper* 81-1, Fort Belvoir, USACE, Vicksburg, MS.

Ten Oever, E., 2006. Theoretical and Experimental Study on the Placement of Xbloc. *Master`s Thesis*. Delft University of Technology Faculty of Civil Engineering and Geoscience, Hydraulic Engineering.

Thomson, D.M., Shuttler, R.M., 1975. Riprap Design for Wind Wave Attack, a Laboratory Study in Random Waves. *JRS Wallingford*, Report EX 707.

Trenhaile, A.S., Lakhan, V.C. (1989). Applications in Coastal Modeling. Elsevier. pp. 54–. ISBN 978-0-08-087087-8.

U.S.A.C.E, 2002. Coastal Engineering Manual (CEM). *Engineering Manual* 1110-2-1100, U.S. Army Corps of Engineers, 6 Volumes, Washington, DC.

Van der Meer, J.W., 1987. Stability of Breakwater Armour Layers-Design Formulae. *Coastal Engineering*, 11, 219-239.

Van Der Meer, J.W., 1988. Stability of Cubes, Tetrapods and Accropode. Design of Breakwaters, Thomas Telford, London, 71-80.

Van der Meer, J.W., 1990. Data on Wave Transmission Due to Overtopping. *Delft Hydraulics Report* H986.

Van Der Meer, J.W., 1995. Conceptual Design of Rubble Mound Breakwaters. Design and Reliability of Coastal Structures, *Short Course During the 23rd ICCE*, Venice, Italy.

Van der Meer, J.W., 1998. Rock Slopes and Gravel Beaches Under Wave Attack. *Phd Thesis*, Delft University of Technology. Also: *Delft Hydraulics Communication,* No. 396.

Van Der Meer, J.W., 1999. Design of Concrete Armour Layers. *Coastal Structures*, A.A. Balkema, Rotterdam, 213–221.

Van Der Meer, J.W., 2011. Design Aspects of Breakwaters and Sea Defences. *5th International Short Conference on Applied Coastal Research.*

Van Der Meer, J.W., Stam C.J., 1998. Wave Run-Up and Overtopping*. Chapter 8 in Seawalls, Dikes and Revetments*, Edited by K. W. Pilarczyk, Balkema, Rotterdam.

Van Gent, M.R.A, 2004. On the Stability of Rock Slopes. *Proceedings NATO-Workshop on Environmental Friendly Coastal Protection Structures*, Varna, Bulgaria.

Van Gent, M.R.A., D`Angremond, K., Triemstra, R., 2001. Rubble Mound Breakwaters: Single Armour Layers and High-Density Concrete Units. *Coastlines, Structures and Breakwaters*, ICE, London, UK.

Van Gent, M.R.A., Smale, A., Kuiper, C., 2003. Stability of Rock Slopes with Shallow Foreshores. *Proceedings of Coastal Structures*, ASCE, Portland, OR.

Verdegaal, I., 2013. The Influence of Core Permeability on the Stability of Interlocking Single Layer Armour Units. *Master`s Thesis*. Delft University of Technology, Faculty of Civil Engineering and Geosciences, Hydraulic Engineering.

Wolfram, J., Nagipour, M., 1999. On the Estimation of Morison Force Coefficients and Their Predictive Accuracy for Very Rough Circular Cylinders. *Applied Ocean Research*, 21, 311-328.

Woodward-Clyde Consultants, 1980. Assessment of the Morison Equation. U.S. Navy, Civil Engineering *Laboratory Report* CR 80.022

Zanuttigh, B., Van der Meer, J.W., 2006, Wave Reflection from Coastal Structures. *Proceedings of the International Conference of Coastal Engineering*, 30, San Diego, CA.

# Appendix

## A Core-Loc Hydrodynamic Analysis via Controlled Drop Tests

### A.1 Vertical Drop Test Tank Technical Details

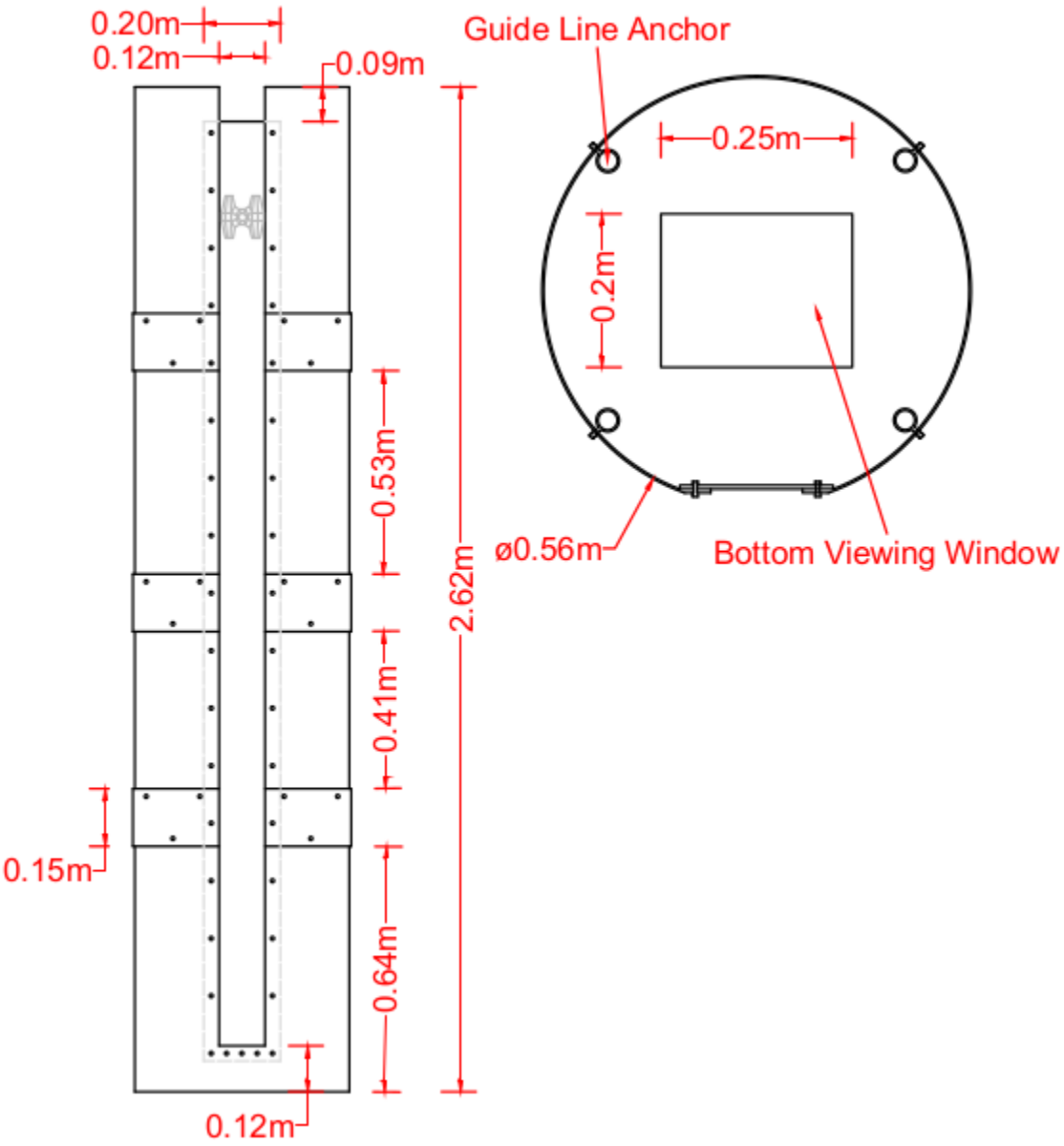

## A.2 Test Series Summary

| | Plastic Mass (g) | S1 | 26.50 | 28.00 | 26.00 | 28.50 |
|---|---|---|---|---|---|---|
| | | S2 | 43.50 | 44.50 | 42.50 | 36.50 |
| | | S3 | 83.00 | 95.50 | 91.00 | 79.00 |
| | | S4 | 470.00 | 406.50 | 292.50 | 432.00 |
| **Target Mass (g)** | **Scale** | **Led Req. (g)** | **O1** | **O2** | **O3** | **O4** |
| 57.71 | S1 | W1 | **31.21** | **29.71** | **31.71** | **29.21** |
| 78.04 | | W2 | 20.33 | 20.33 | 20.33 | 20.33 |
| 98.36 | | W3 | 20.33 | 20.33 | 20.33 | 20.33 |
| 118.69 | | W4 | 20.33 | 20.33 | 20.33 | 20.33 |
| 120.66 | S2 | W1 | 77.16 | 76.16 | 78.16 | 84.16 |
| 163.16 | | W2 | 42.49 | 42.49 | 42.49 | 42.49 |
| 205.65 | | W3 | 42.49 | 42.49 | 42.49 | 42.49 |
| 248.14 | | W4 | 42.49 | 42.49 | 42.49 | 42.49 |
| 329.28 | S3 | W1 | 246.28 | 233.78 | 238.28 | 250.28 |
| 445.24 | | W2 | 115.96 | 115.96 | 115.96 | 115.96 |
| 561.21 | | W3 | 115.96 | 115.96 | 115.96 | 115.96 |
| 677.17 | | W4 | 115.96 | 115.96 | 115.96 | 115.96 |
| 1532.85 | S4 | W1 | 1062.85 | 1126.35 | 1240.35 | 1100.85 |
| 2072.68 | | W2 | 539.83 | 539.83 | 539.83 | 539.83 |
| 2612.52 | | W3 | 539.83 | 539.83 | 539.83 | 539.83 |
| 3152.35 | | W4 | 539.83 | 539.83 | 539.83 | 539.83 |

| | Achieved Unit Mass for each test (g) | | | | | |
|---|---|---|---|---|---|---|
| | Plastic Mass (g) | S1 | 26.50 | 28.00 | 26.00 | 28.50 |
| | | S2 | 43.50 | 44.50 | 42.50 | 36.50 |
| | | S3 | 83.00 | 95.50 | 91.00 | 79.00 |
| | | S4 | 470.00 | 406.50 | 292.50 | 432.00 |
| **Target Mass (g)** | **Scale** | **Led Mass (g)** | **O1** | **O2** | **O3** | **O4** |
| 57.71 | S1 | W1 | 57.71 | 57.71 | 57.71 | 57.71 |
| 78.04 | | W2 | 78.04 | 78.04 | 78.04 | 78.04 |
| 98.36 | | W3 | 98.36 | 98.36 | 98.36 | 98.36 |
| 118.69 | | W4 | 118.69 | 113.69 | 114.19 | 110.69 |
| 120.66 | S2 | W1 | 120.66 | 120.66 | 120.66 | 120.66 |
| 163.16 | | W2 | 163.16 | 163.16 | 163.16 | 163.16 |
| 205.65 | | W3 | 205.65 | 205.65 | 205.65 | 205.65 |
| 248.14 | | W4 | 238.64 | 231.14 | 244.64 | 238.64 |
| 329.28 | S3 | W1 | 329.28 | 329.28 | 329.28 | 329.28 |
| 445.24 | | W2 | 445.24 | 445.24 | 445.24 | 445.24 |
| 561.21 | | W3 | 561.21 | 561.21 | 561.21 | 561.21 |
| 677.17 | | W4 | 620.67 | 615.17 | 654.67 | 673.17 |
| 1532.85 | S4 | W1 | 1532.85 | 1532.85 | 1532.85 | 1532.85 |
| 2072.68 | | W2 | 2072.68 | 2072.68 | 2072.68 | 2072.68 |
| 2612.52 | | W3 | 2612.52 | 2612.52 | 2612.52 | 2612.52 |
| 3152.35 | | W4 | n/a | 3021.85 | 3064.85 | 3152.35 |

## A.3 Displacement Time History Results

### A.3.1 Individual Scales and Averaged-Volume Densities

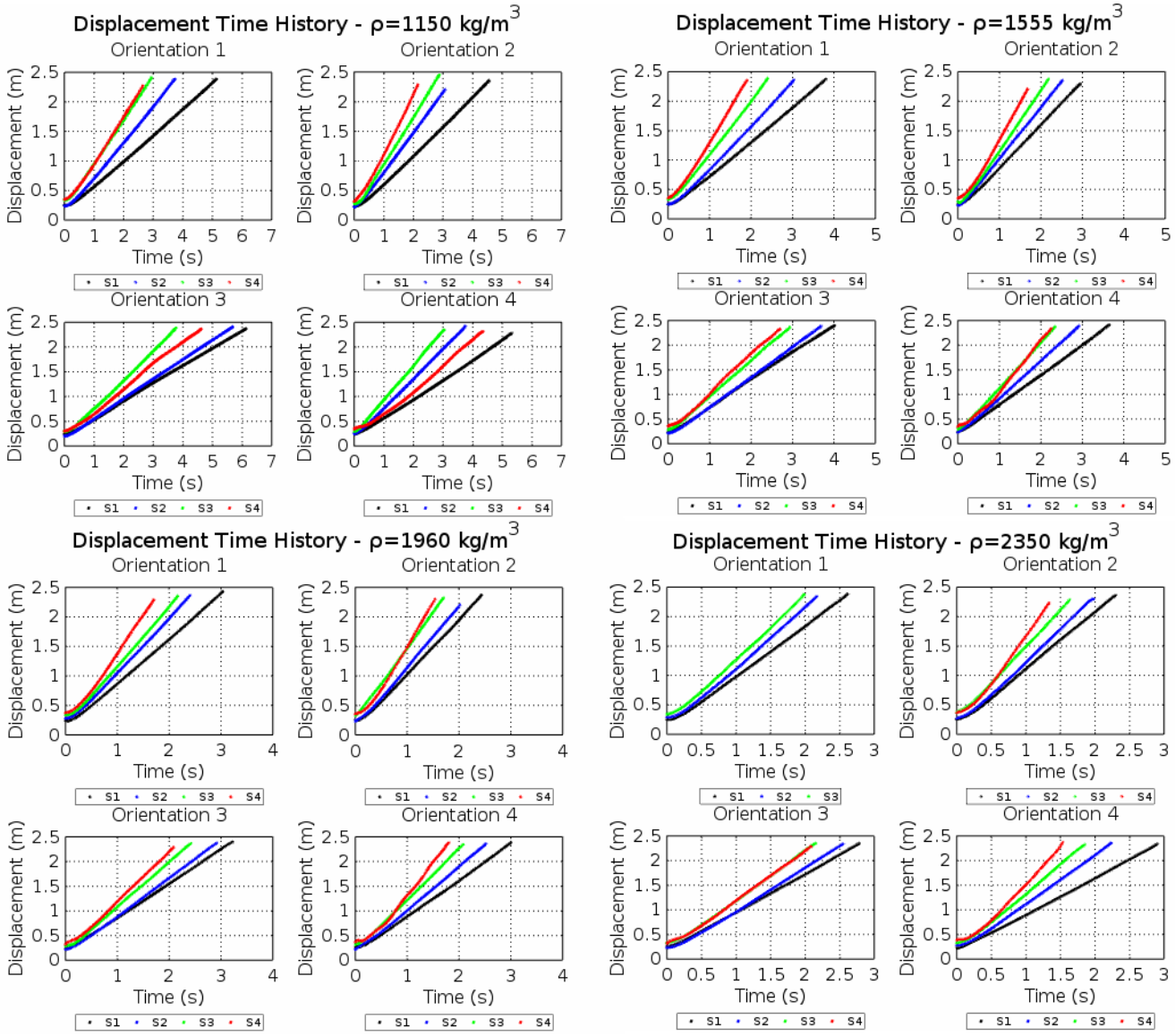

## A.3.2 Individual Orientations and Averaged-Volume Densities

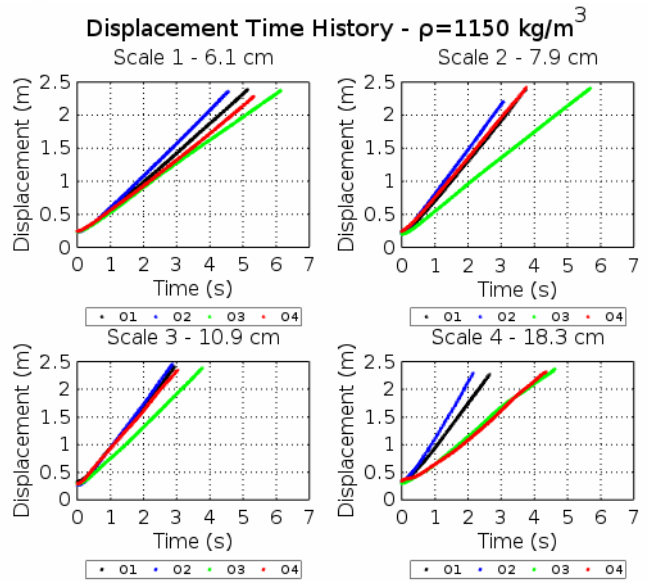


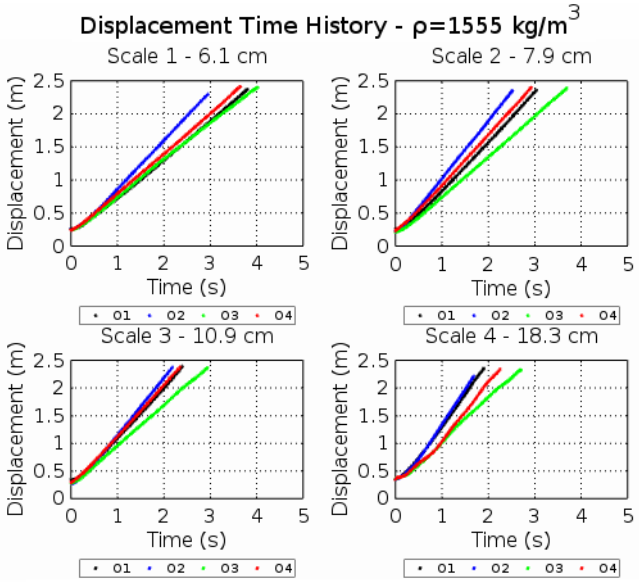


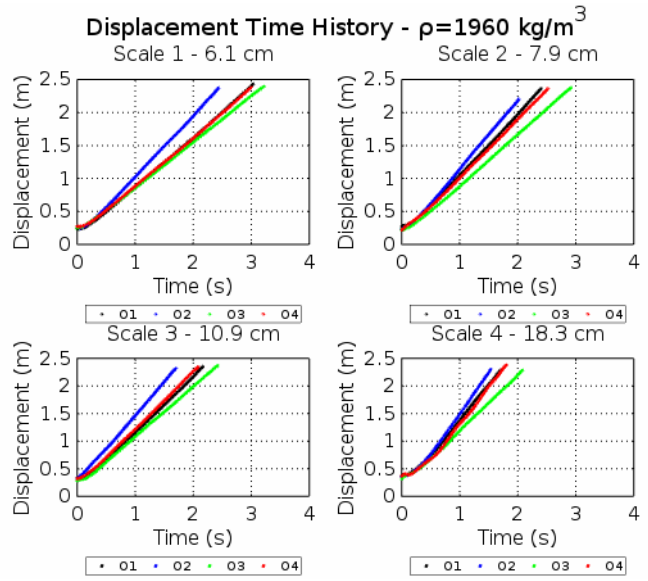


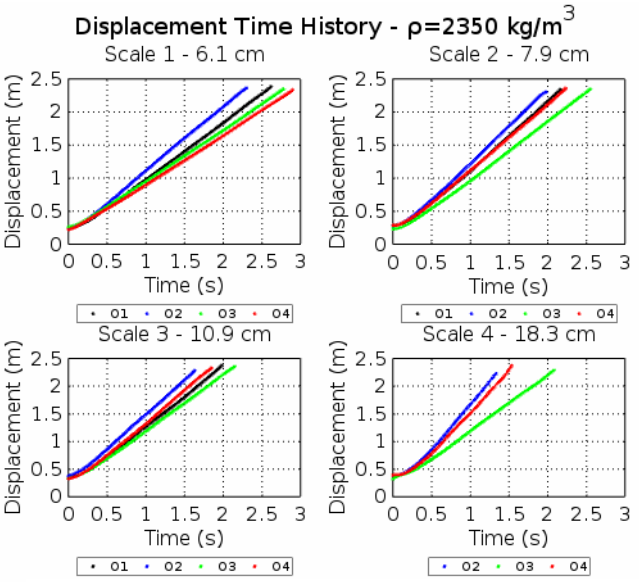

### A.3.3 Individual Orientations and Scales

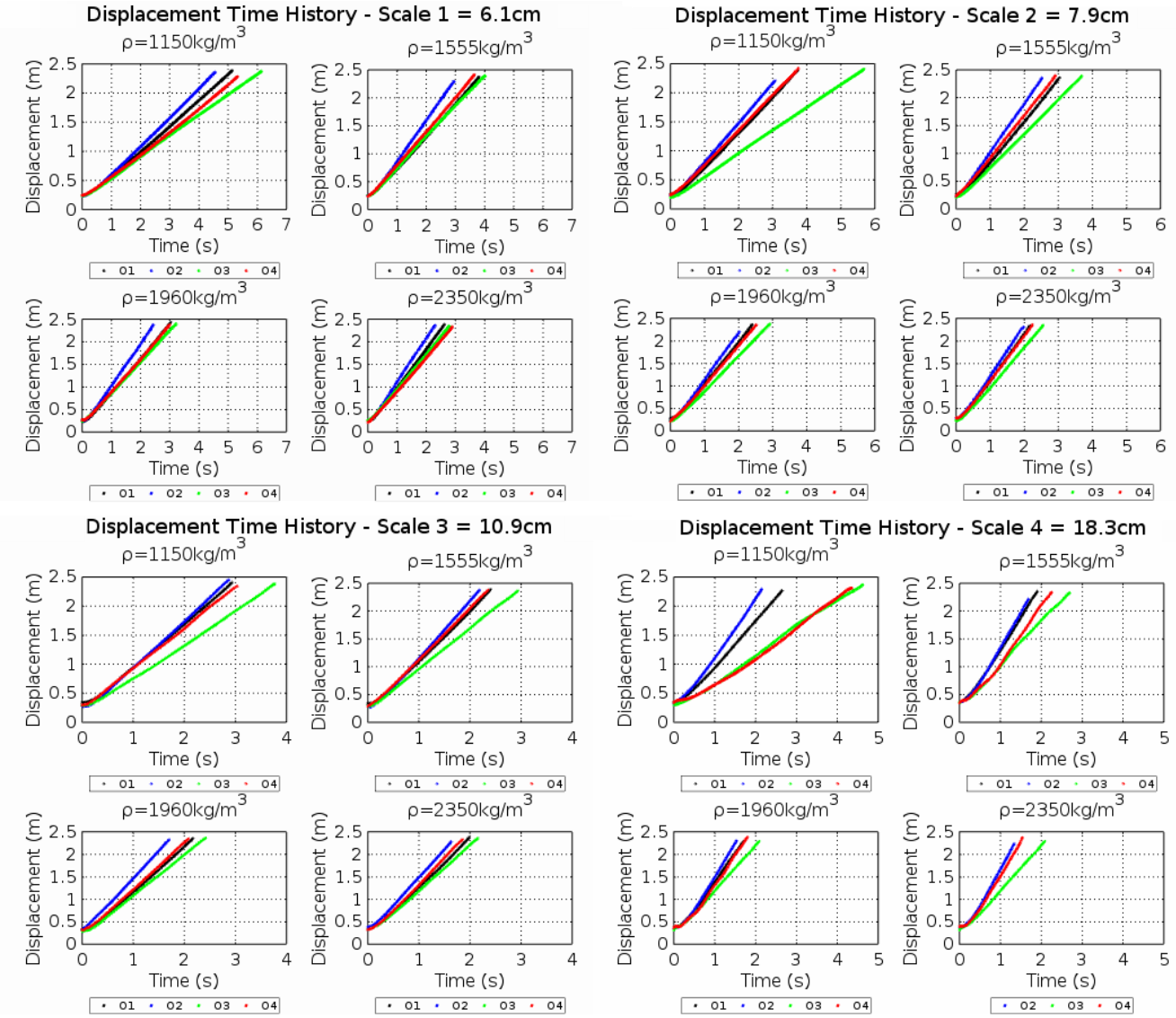

## A.4 Velocity Time History Results

### A.4.1 Individual Scales and Averaged-Volume Densities

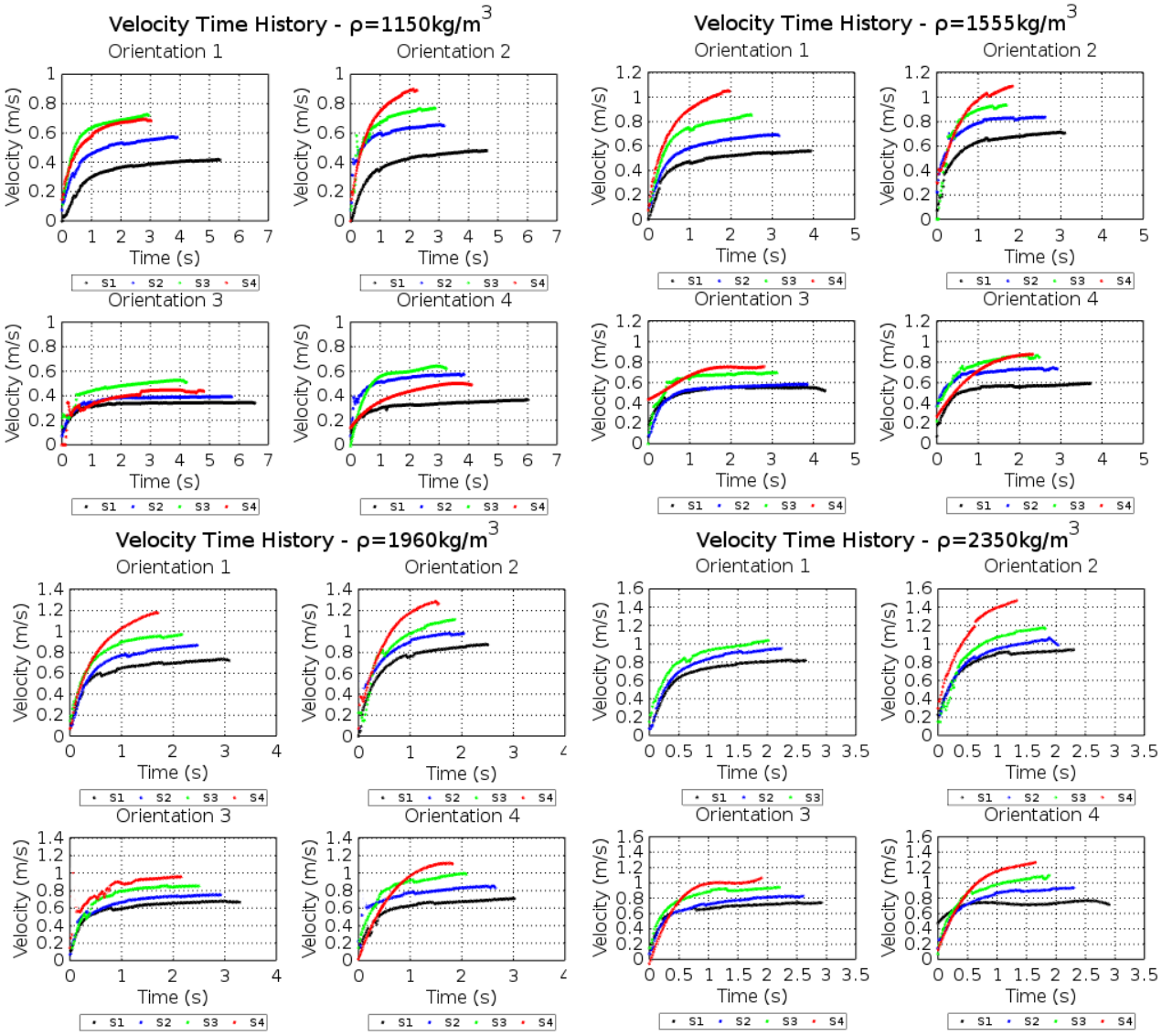

## A.4.2 Individual Orientations and Averaged-Volume Densities

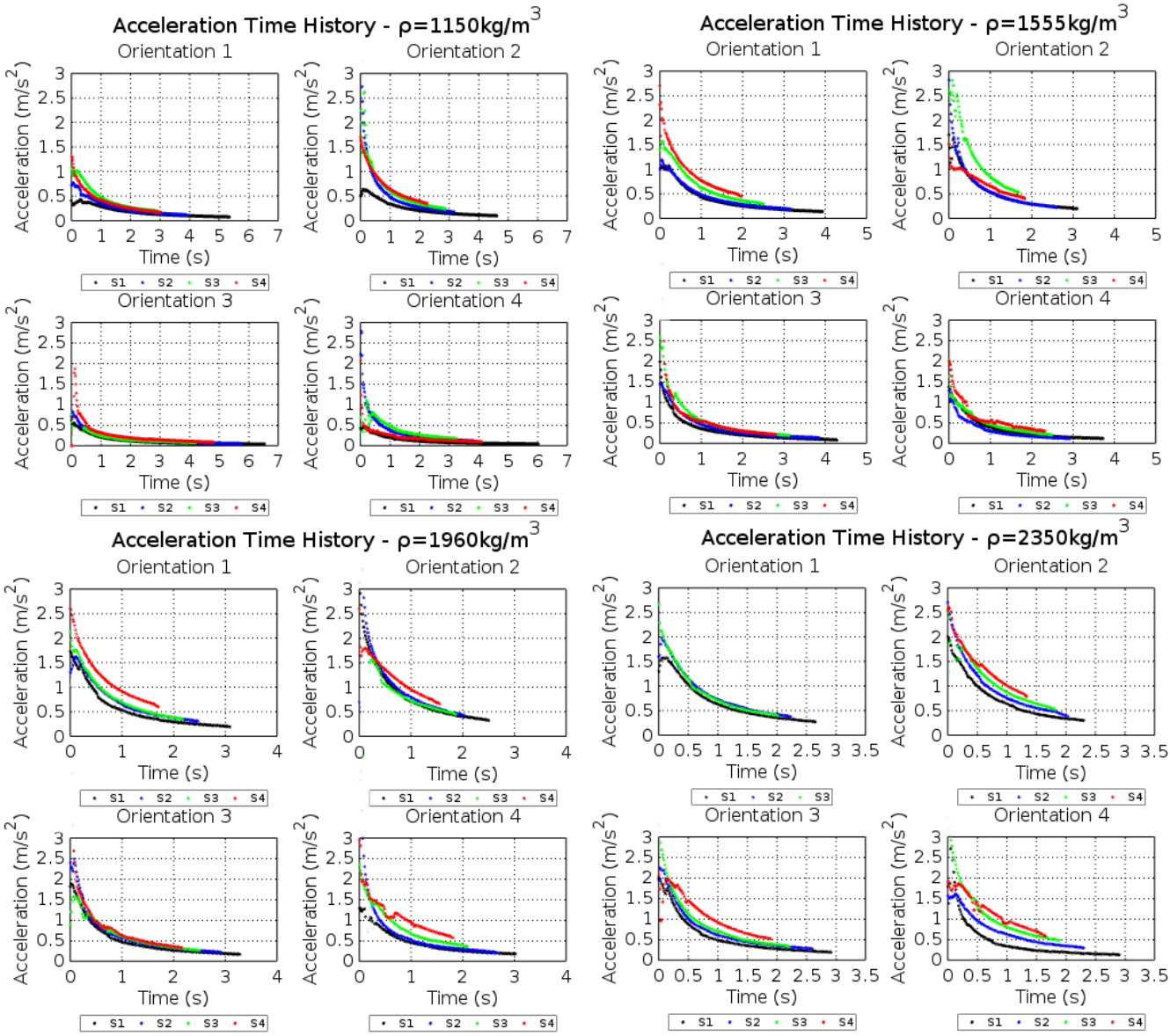

### A.4.3 Individual Orientations and Scales

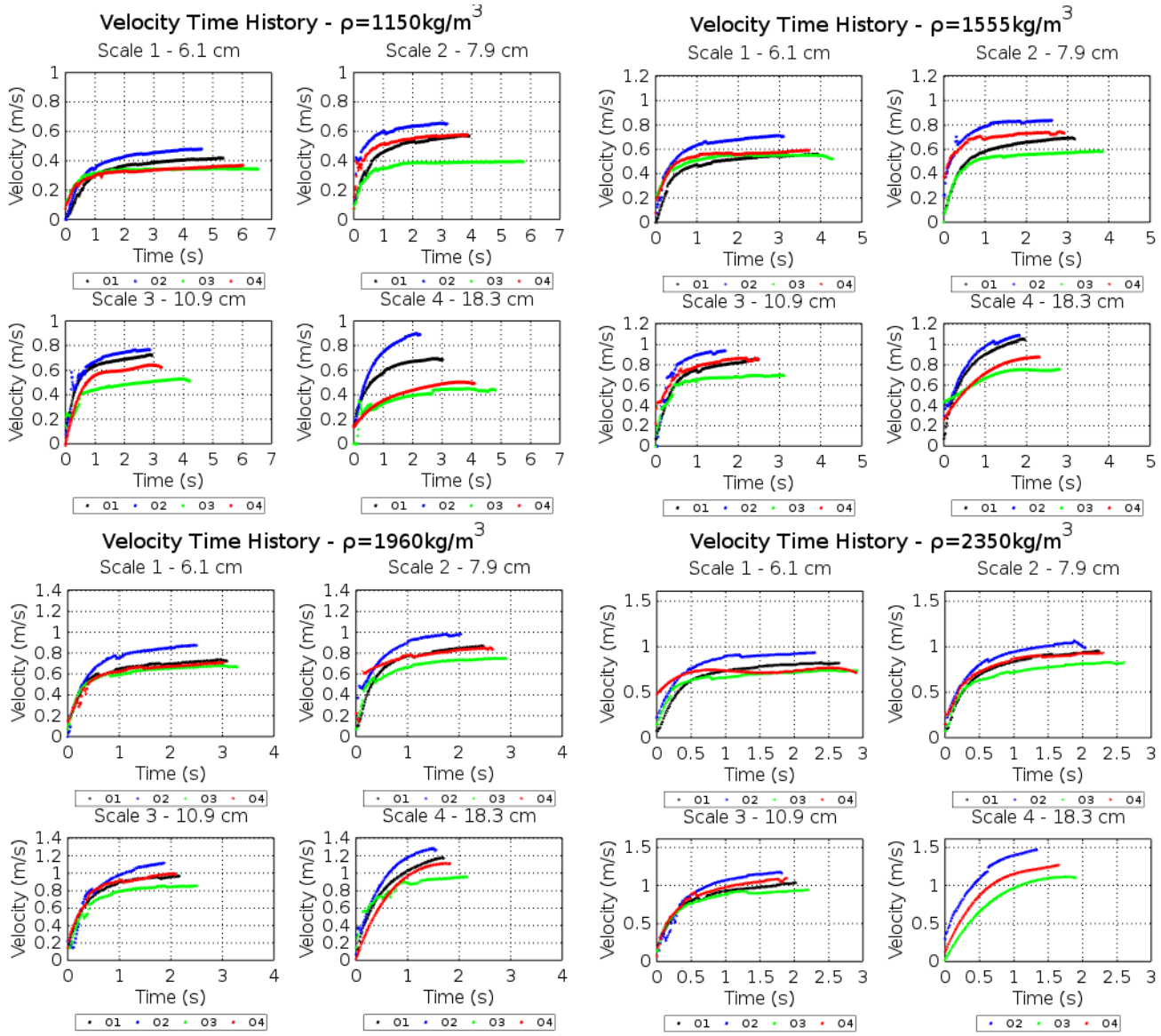

## A.5 Acceleration Time History Results

### A.5.1 Individual Scales and Averaged-Volume Densities

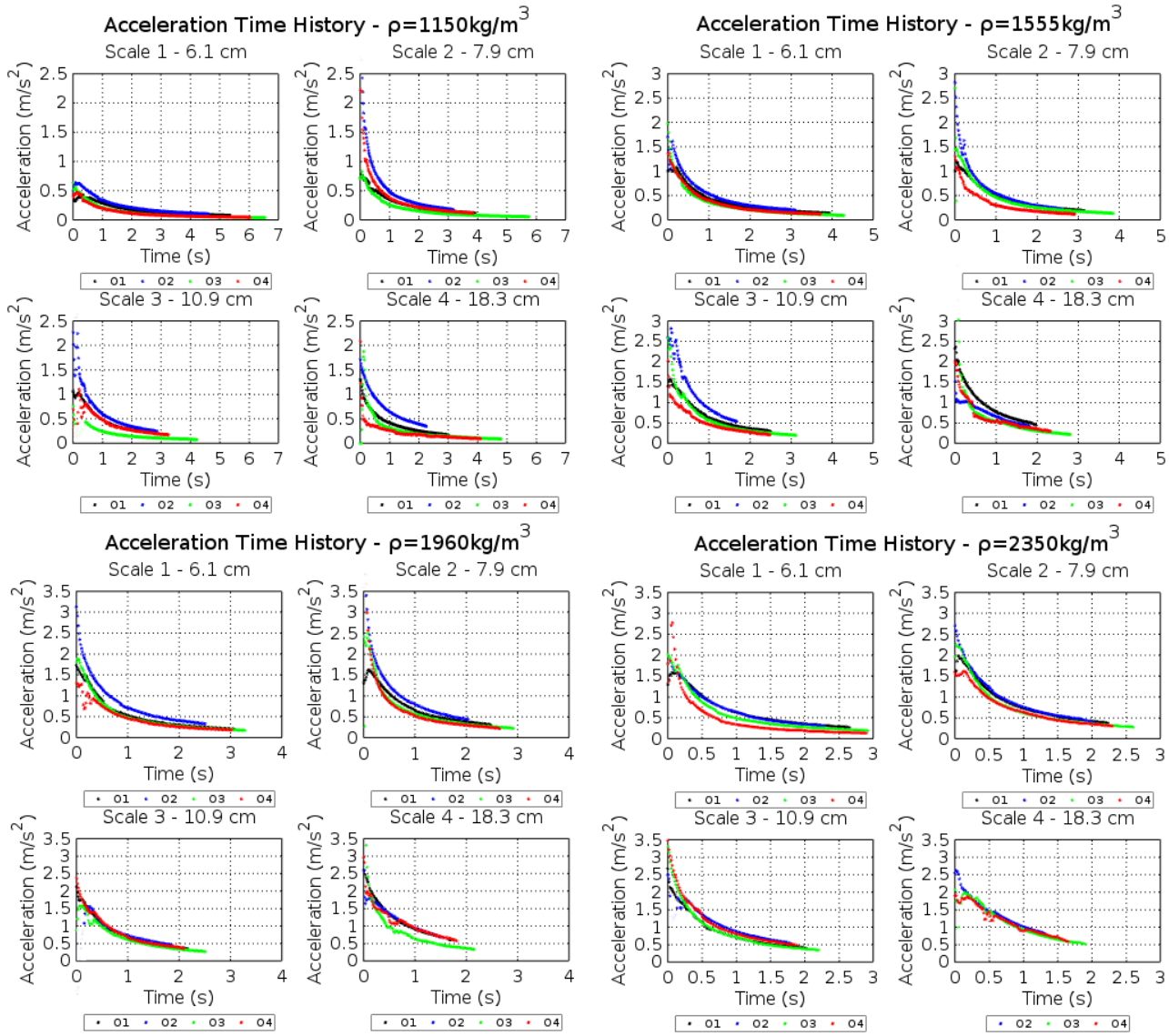

## A.5.2 Individual Orientations and Averaged-Volume Densities

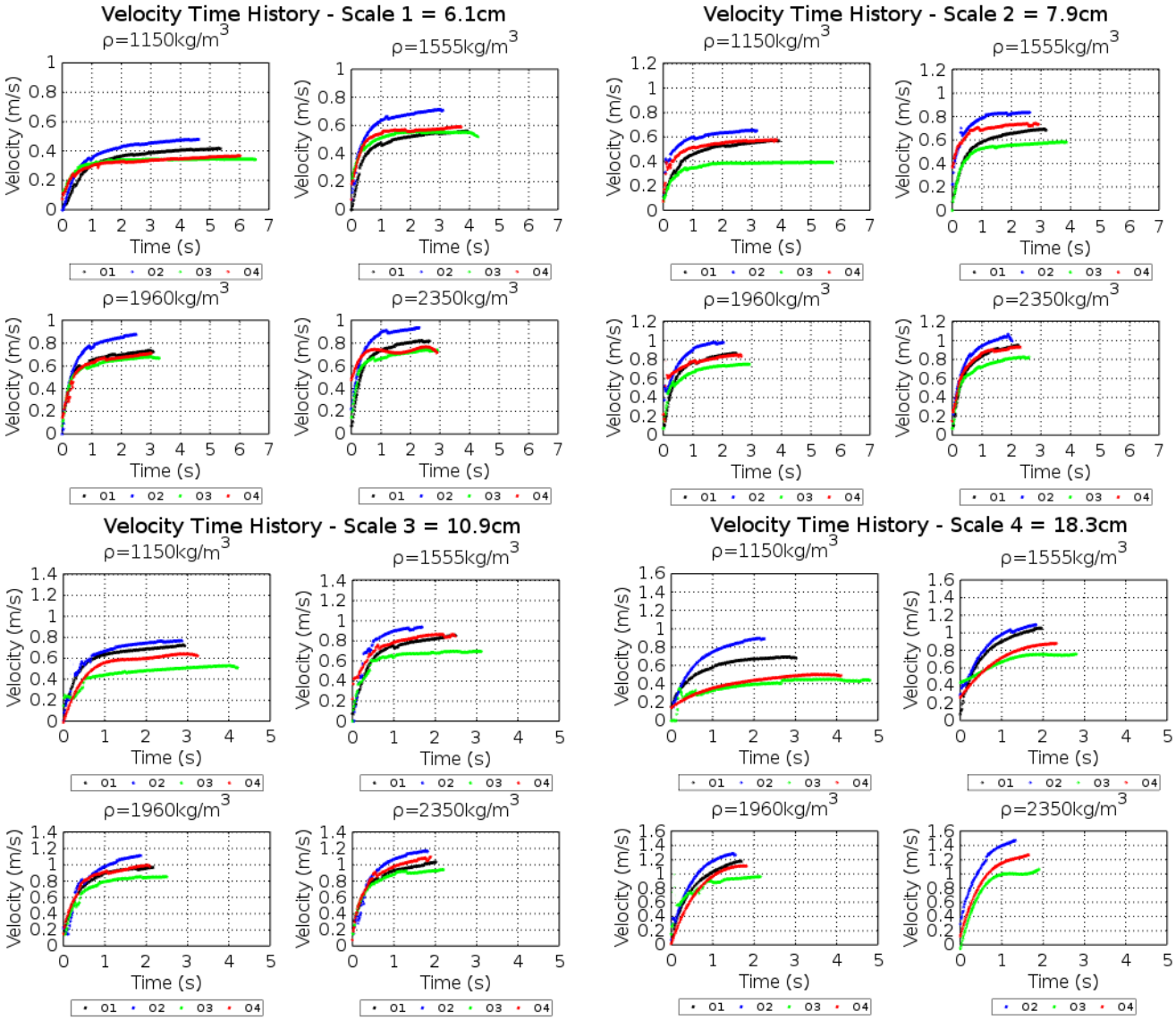

## A.5.3 Individual Orientations and Scales

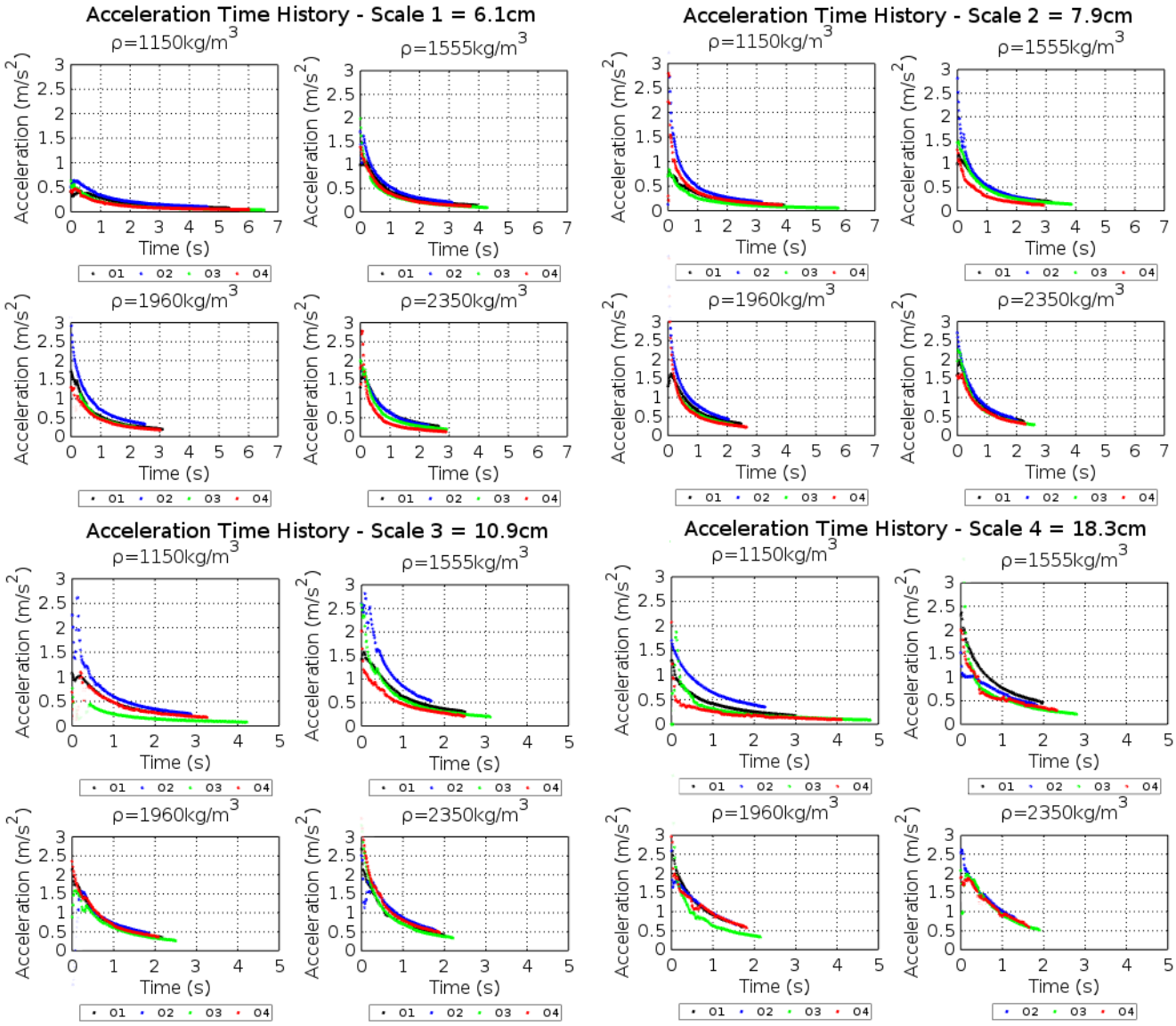

## A.6 Drag Force Coefficient Results

### A.6.1 Individual Scales and Averaged-Volume Densities

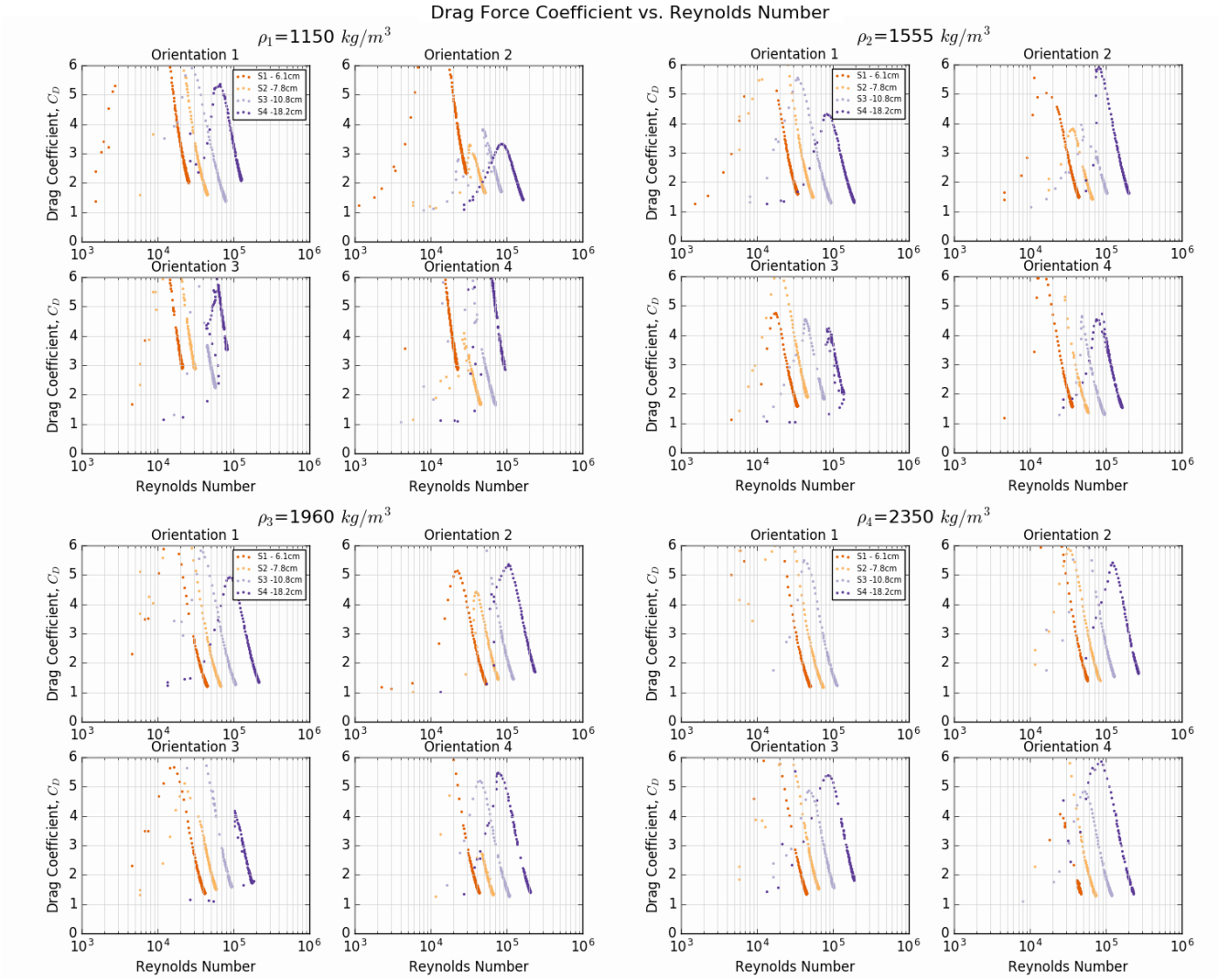

## A.6.2 Individual Orientations and Averaged-Volume Densities

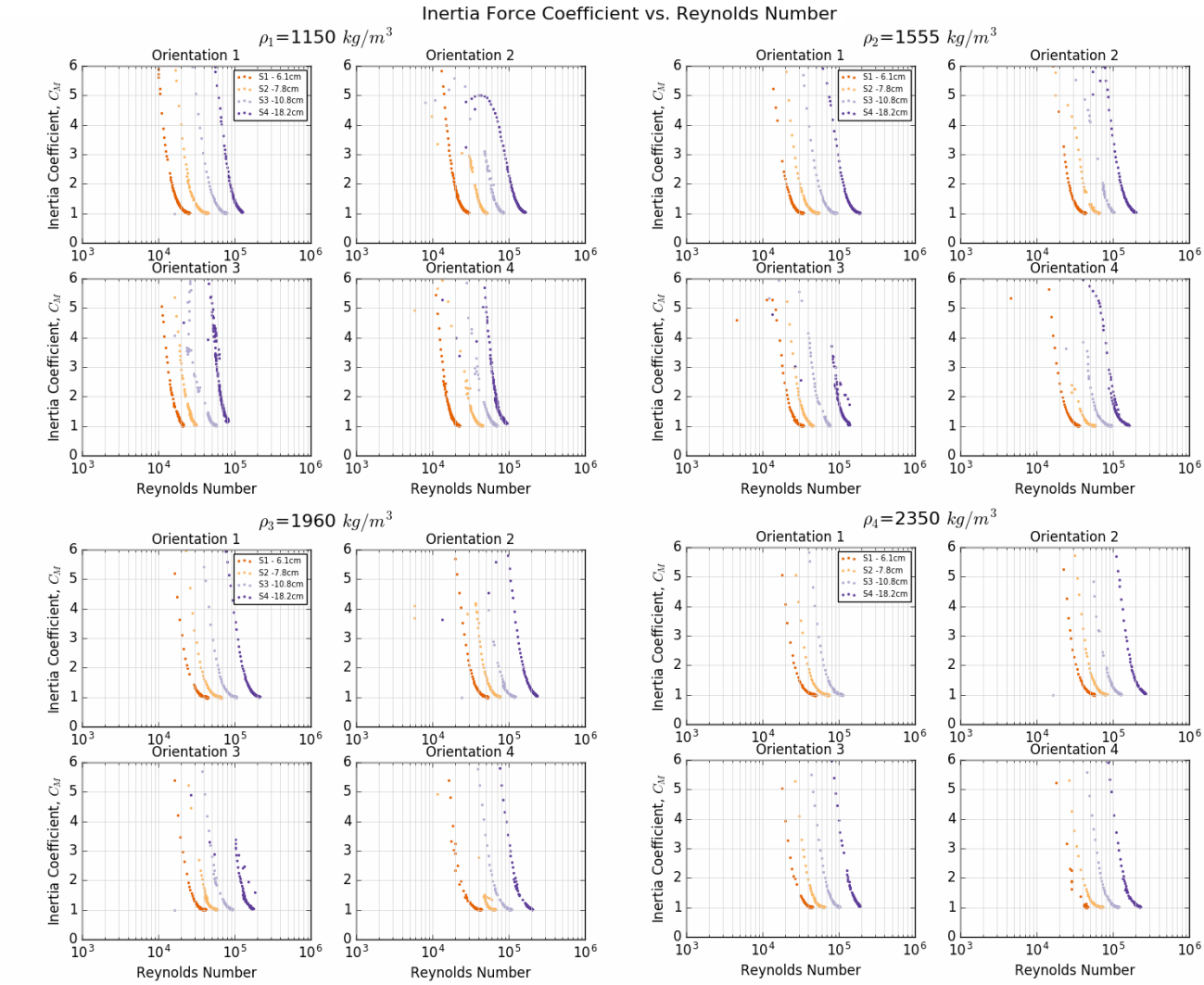

## A.6.3 Individual Orientations and Scales

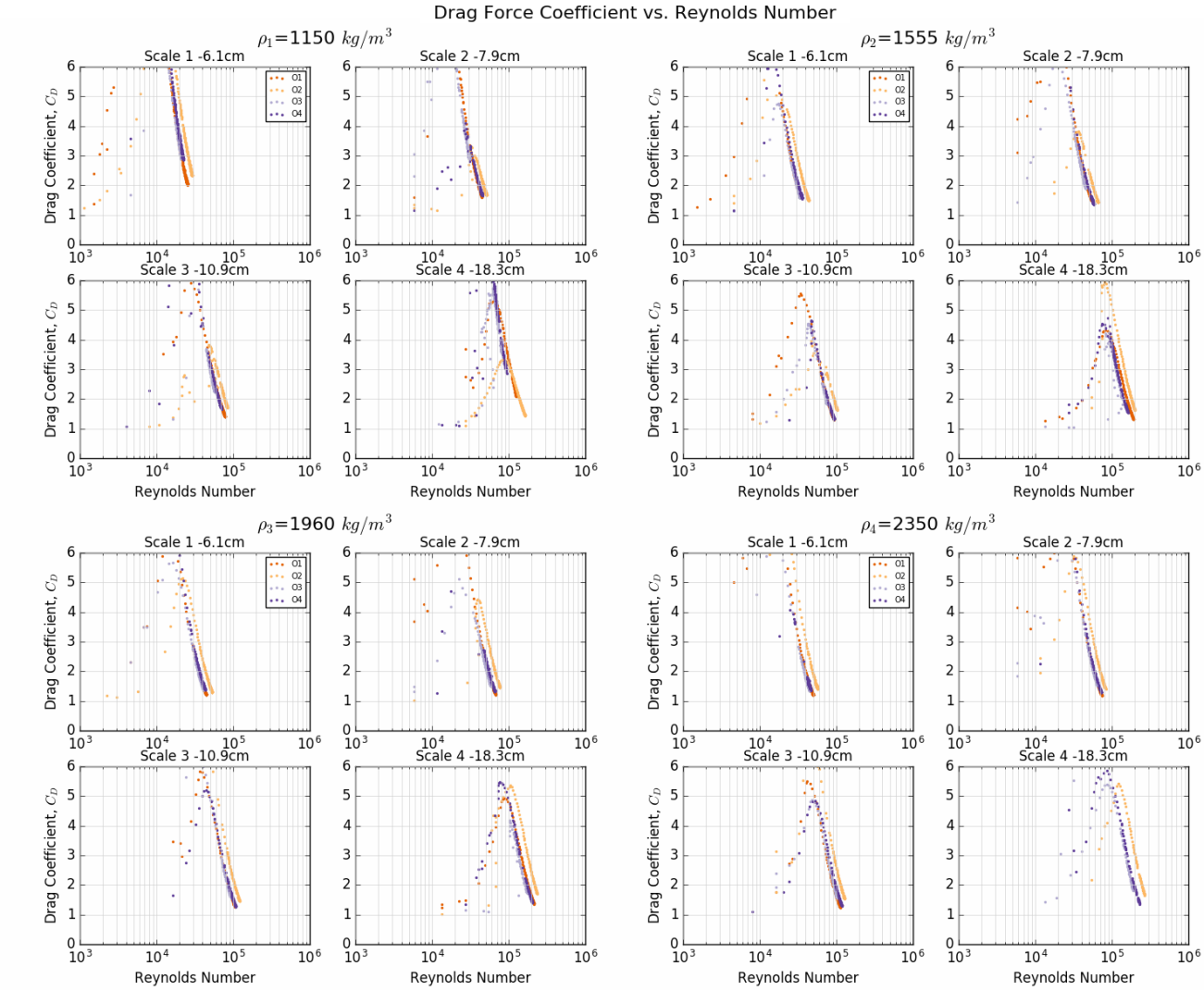

## A.7 Inertia Force Coefficient Results

### A.7.1 Individual Scales and Averaged-Volume Densities

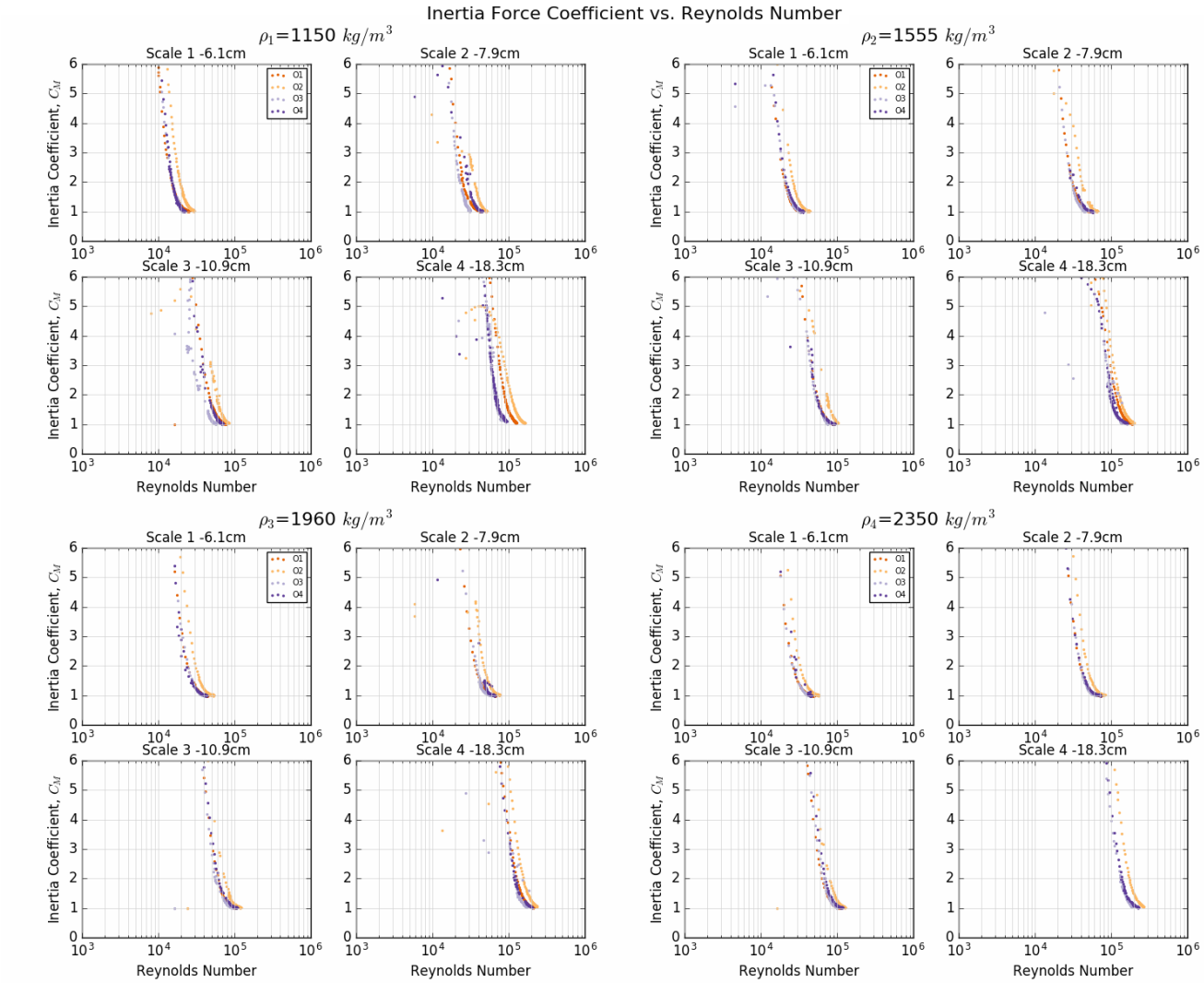

## A.7.2 Individual Orientations and Averaged-Volume Densities

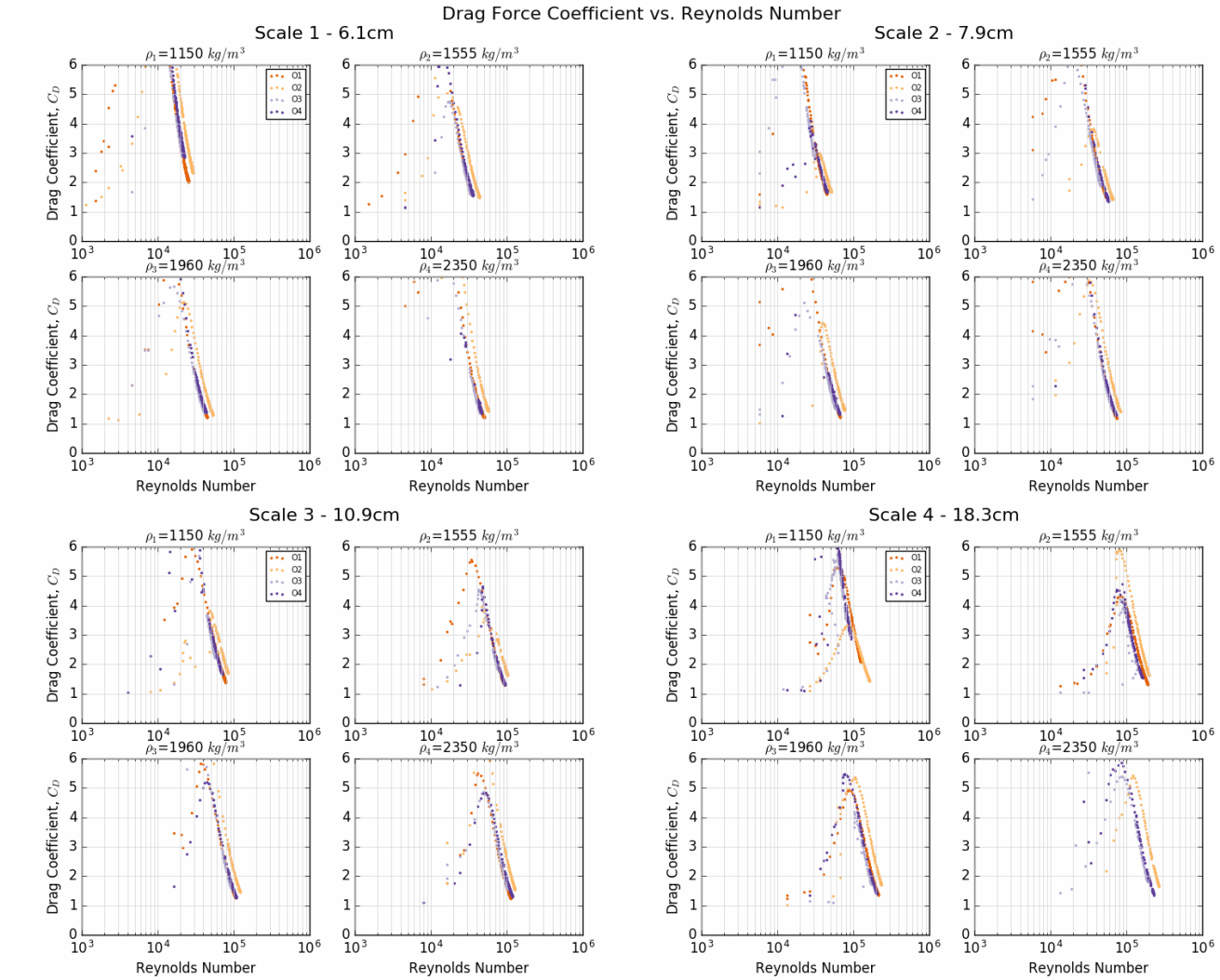

## A.7.3 Individual Orientations and Scales

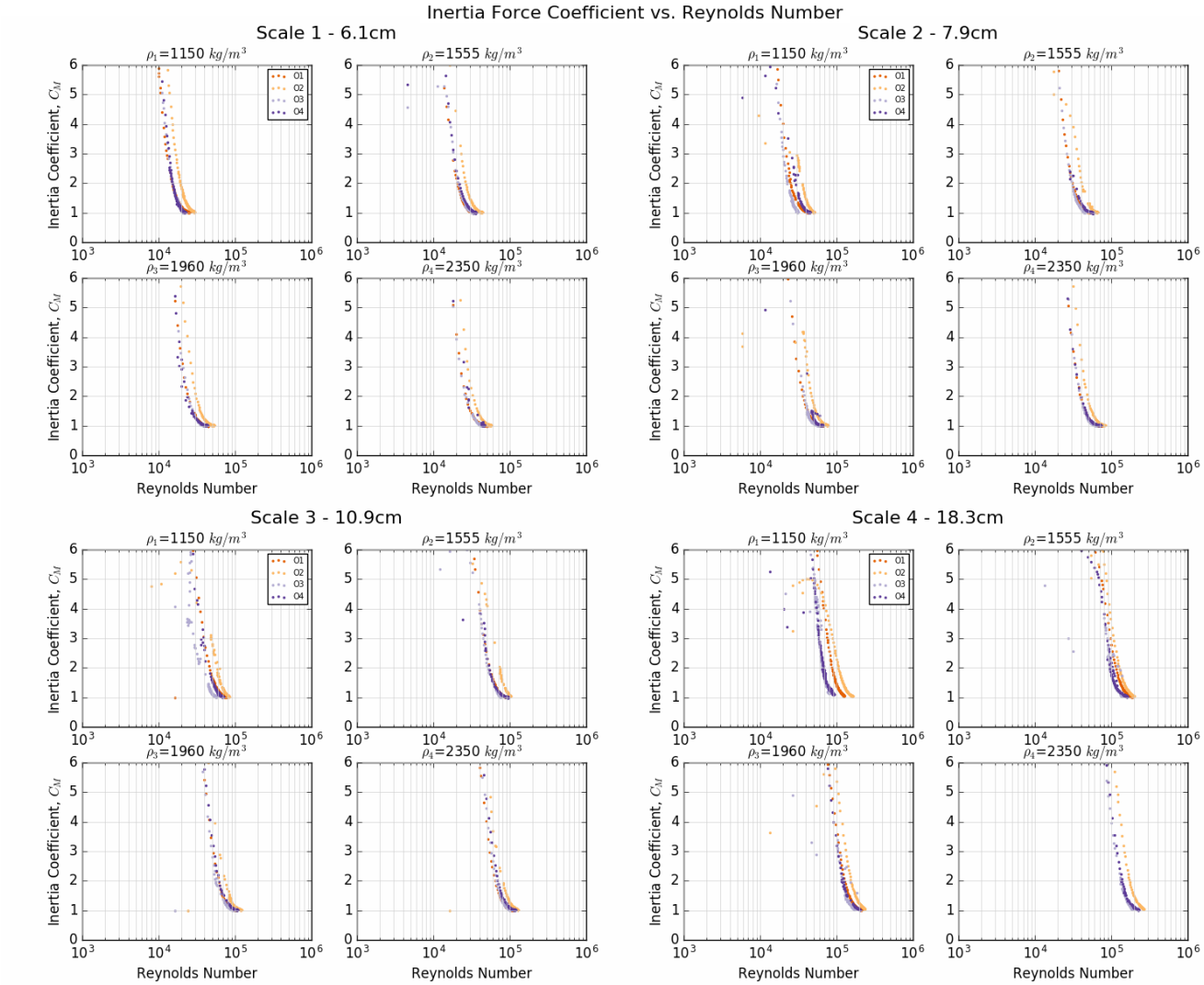

## A.8 Drag to Inertia Force Ratio Results

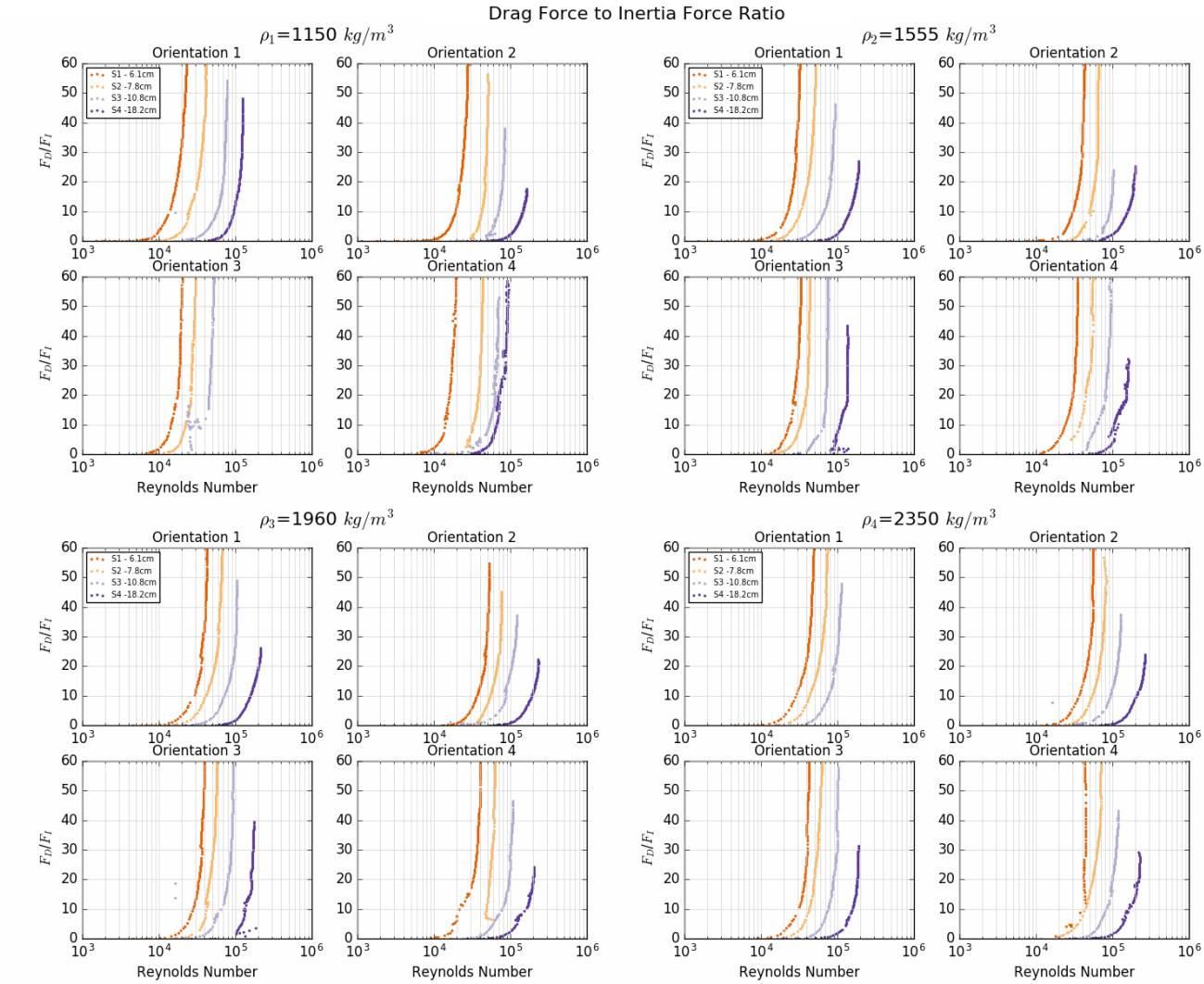

# B Core-Loc Hydrodynamic Analysis Under Oscillatory Flow

## B.1 Bathymetry Frame and Board Design

Pressure Board- Metal Frame

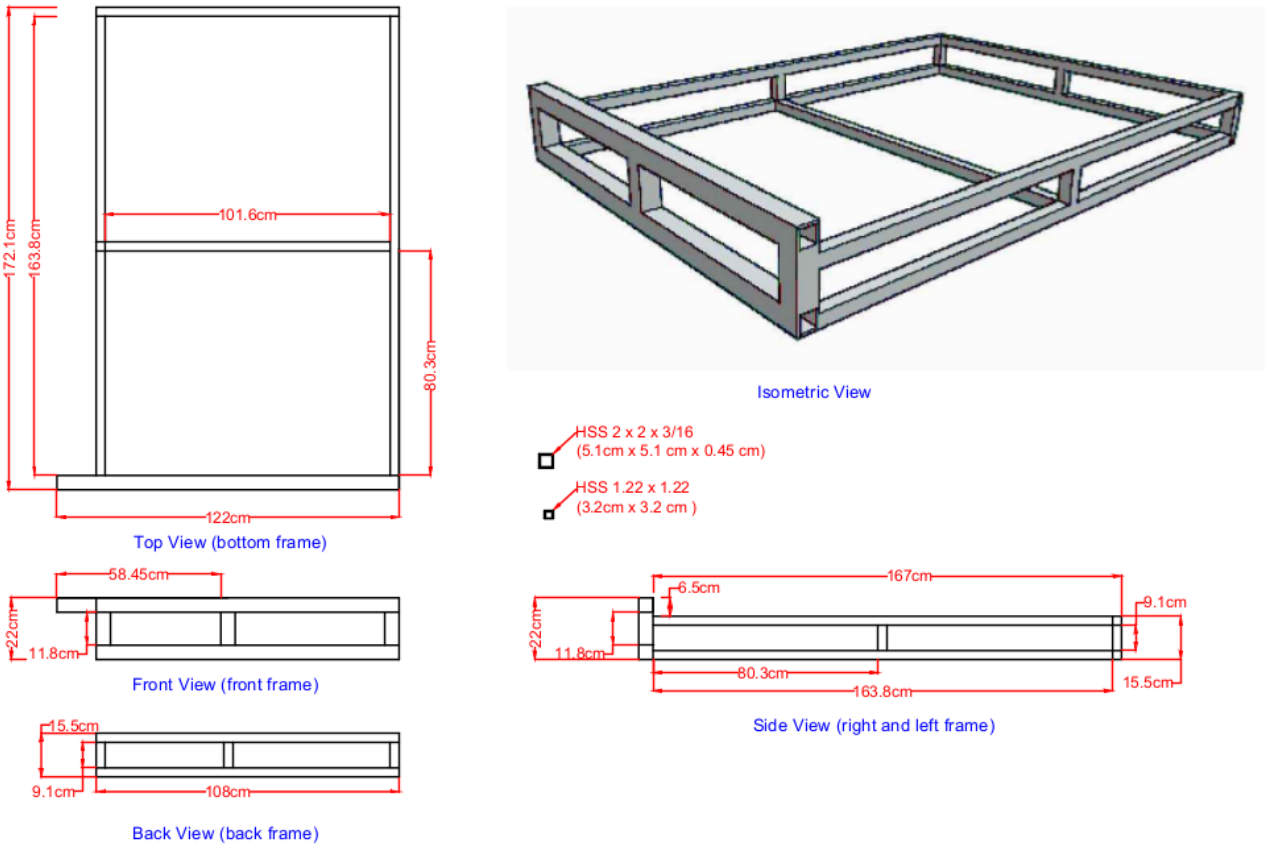


Pressure Board Design - Board

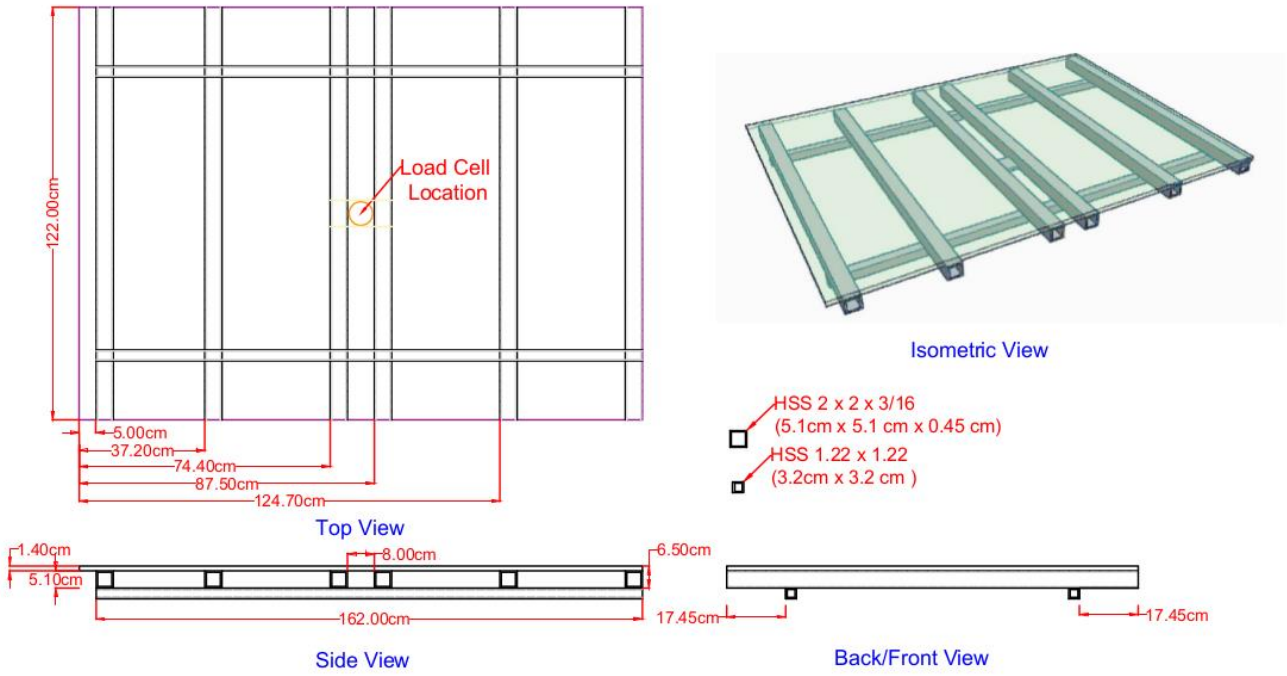

## B.2 Construction Process

## B.3 3D Printed Core-Loc Model Gasket

## B.4 Force Transducer Mount

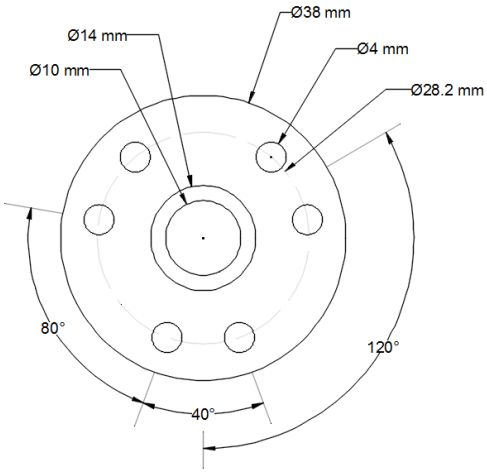


Top View

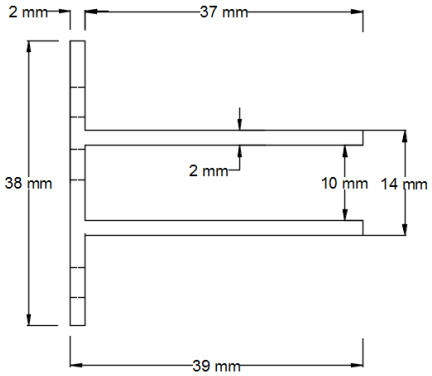


Side View

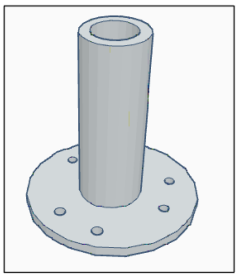

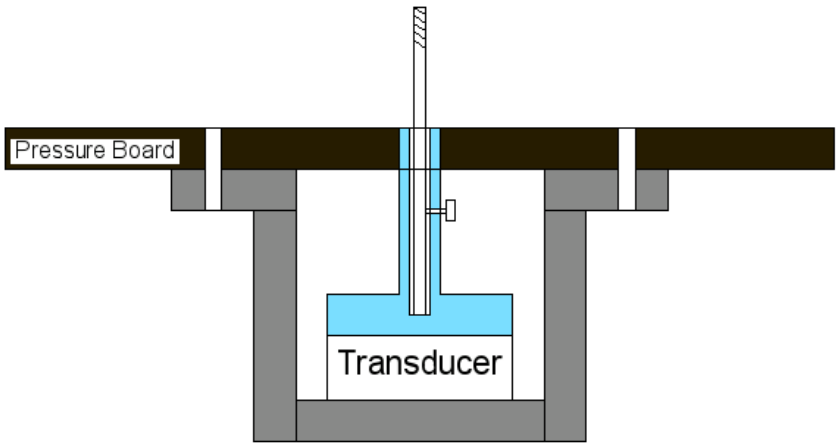

## B.5 Force Time History Results

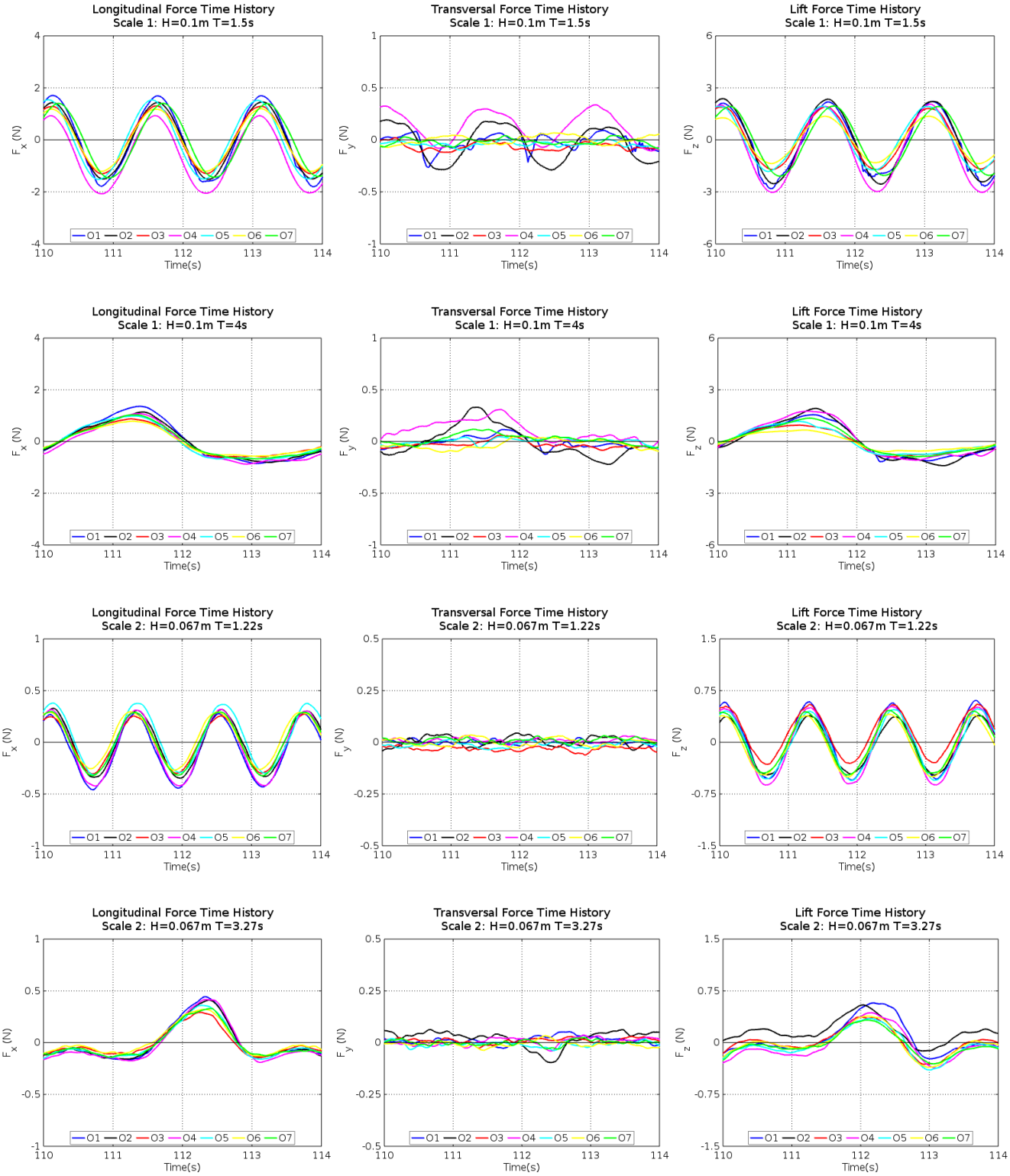

# Appendix

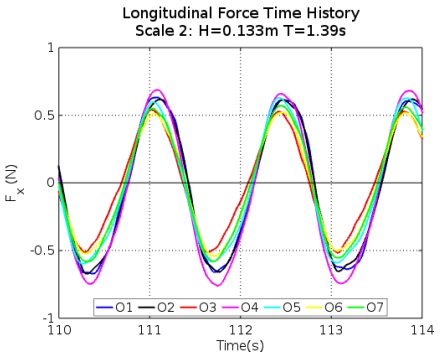
Longitudinal Force Time History
Scale 2: H=0.133m T=1.39s
F_x (N)
Time(s)
O1 O2 O3 O4 O5 O6 O7

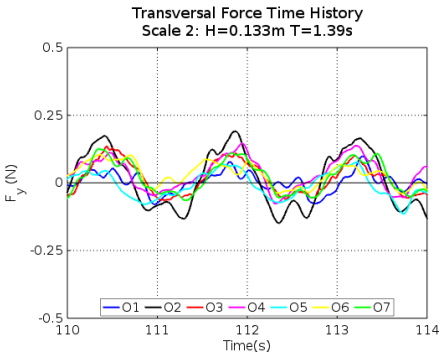
Transversal Force Time History
Scale 2: H=0.133m T=1.39s
F_y (N)
Time(s)
O1 O2 O3 O4 O5 O6 O7

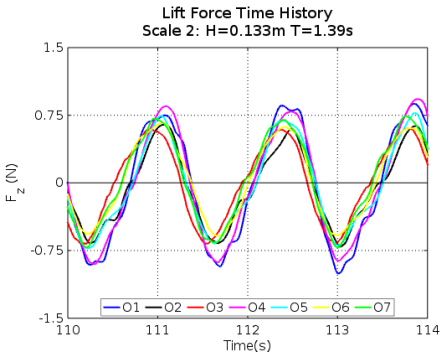
Lift Force Time History
Scale 2: H=0.133m T=1.39s
F_z (N)
Time(s)
O1 O2 O3 O4 O5 O6 O7

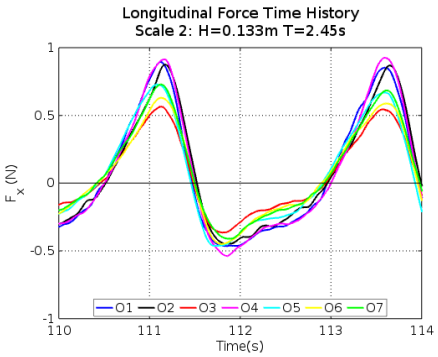
Longitudinal Force Time History
Scale 2: H=0.133m T=2.45s
F_x (N)
Time(s)
O1 O2 O3 O4 O5 O6 O7

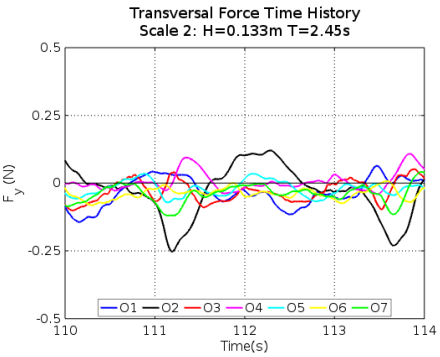
Transversal Force Time History
Scale 2: H=0.133m T=2.45s
F_y (N)
Time(s)
O1 O2 O3 O4 O5 O6 O7

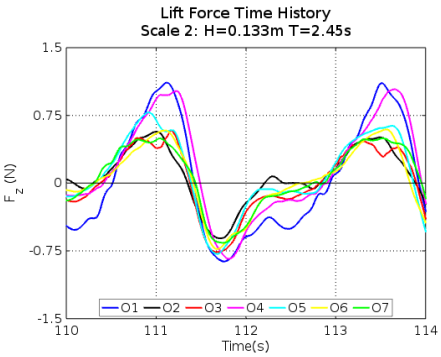
Lift Force Time History
Scale 2: H=0.133m T=2.45s
F_z (N)
Time(s)
O1 O2 O3 O4 O5 O6 O7

## B.6 Drag and Inertia Force Coefficient Results

### B.6.1 Orientation Effect – Scale 1

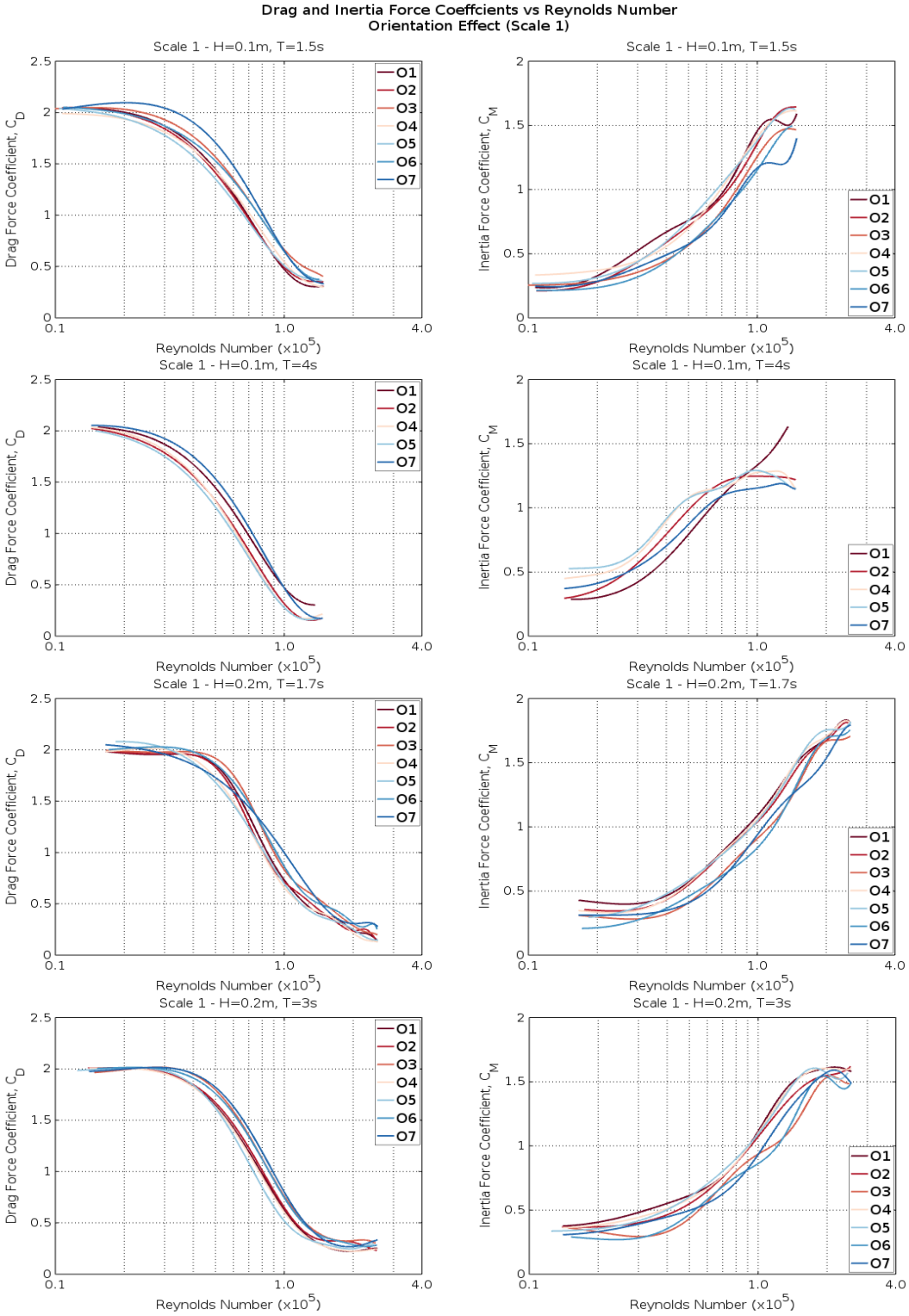

## B.6.2 Orientation Effect – Scale 2

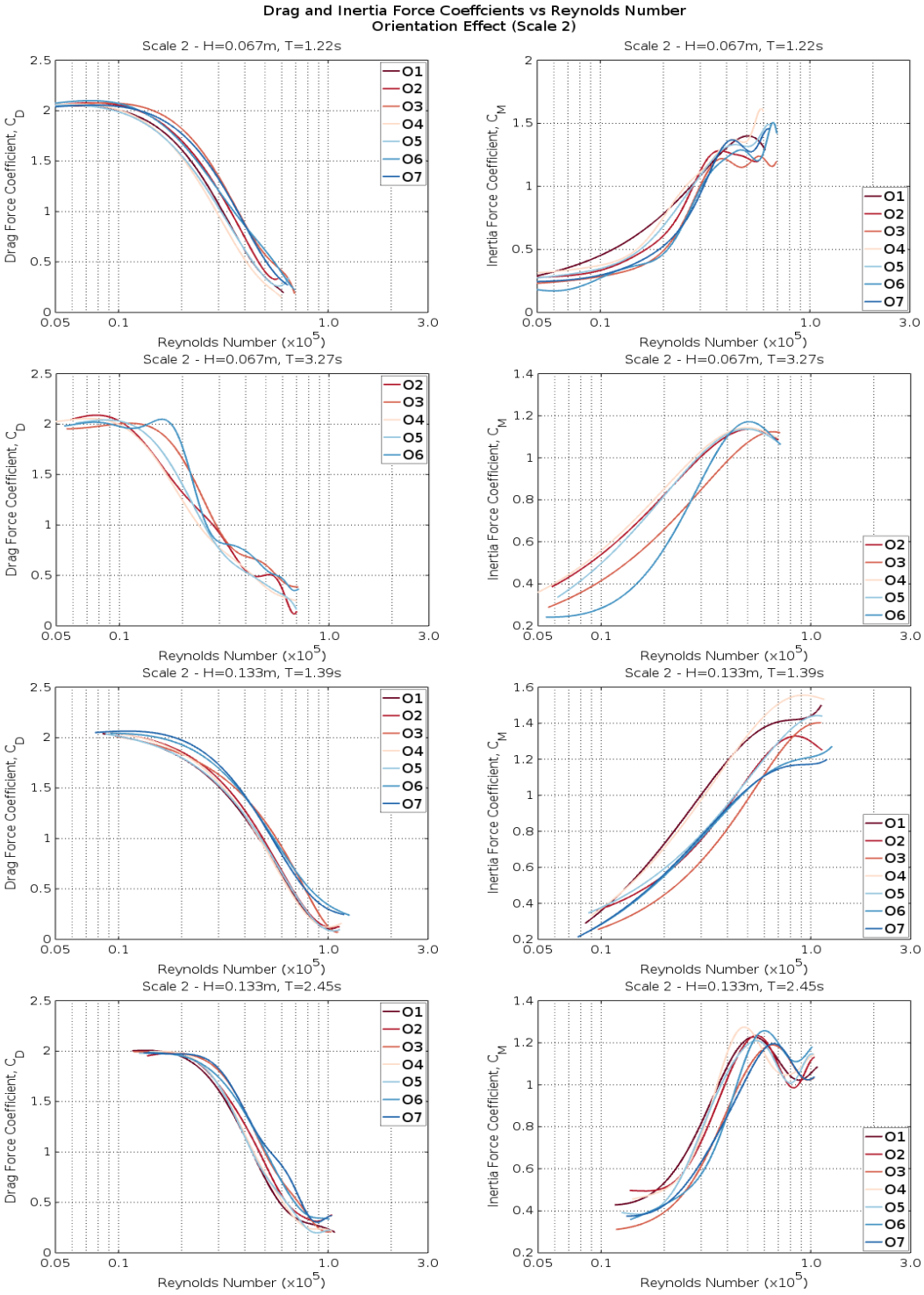

## B.6.3 Drag Coefficient vs. Reynolds Number for Different Wave Signals – Scale 1

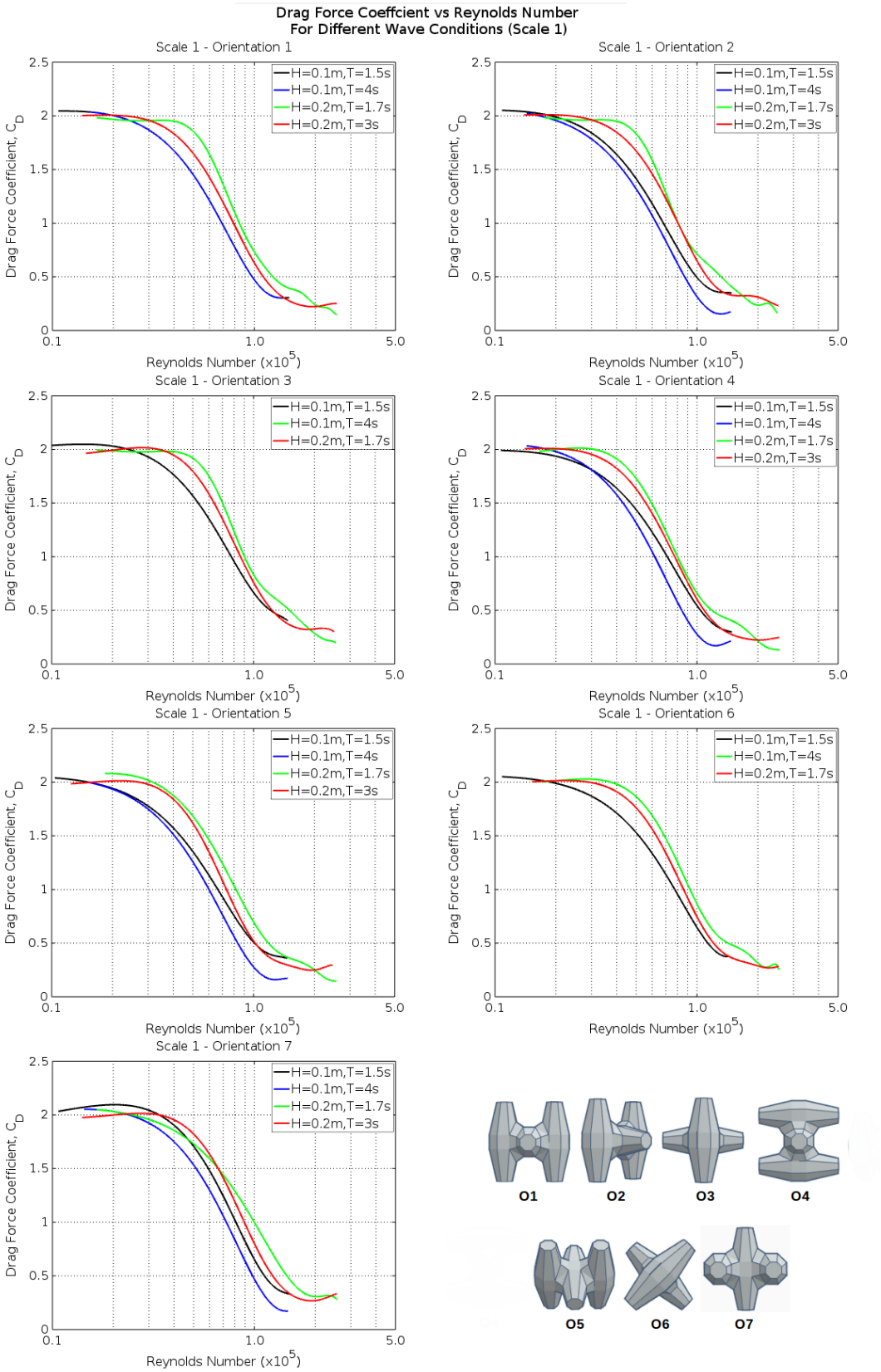

## B.6.4 Inertia Coefficient vs. Reynolds Number for Different Wave Signals – Scale 1

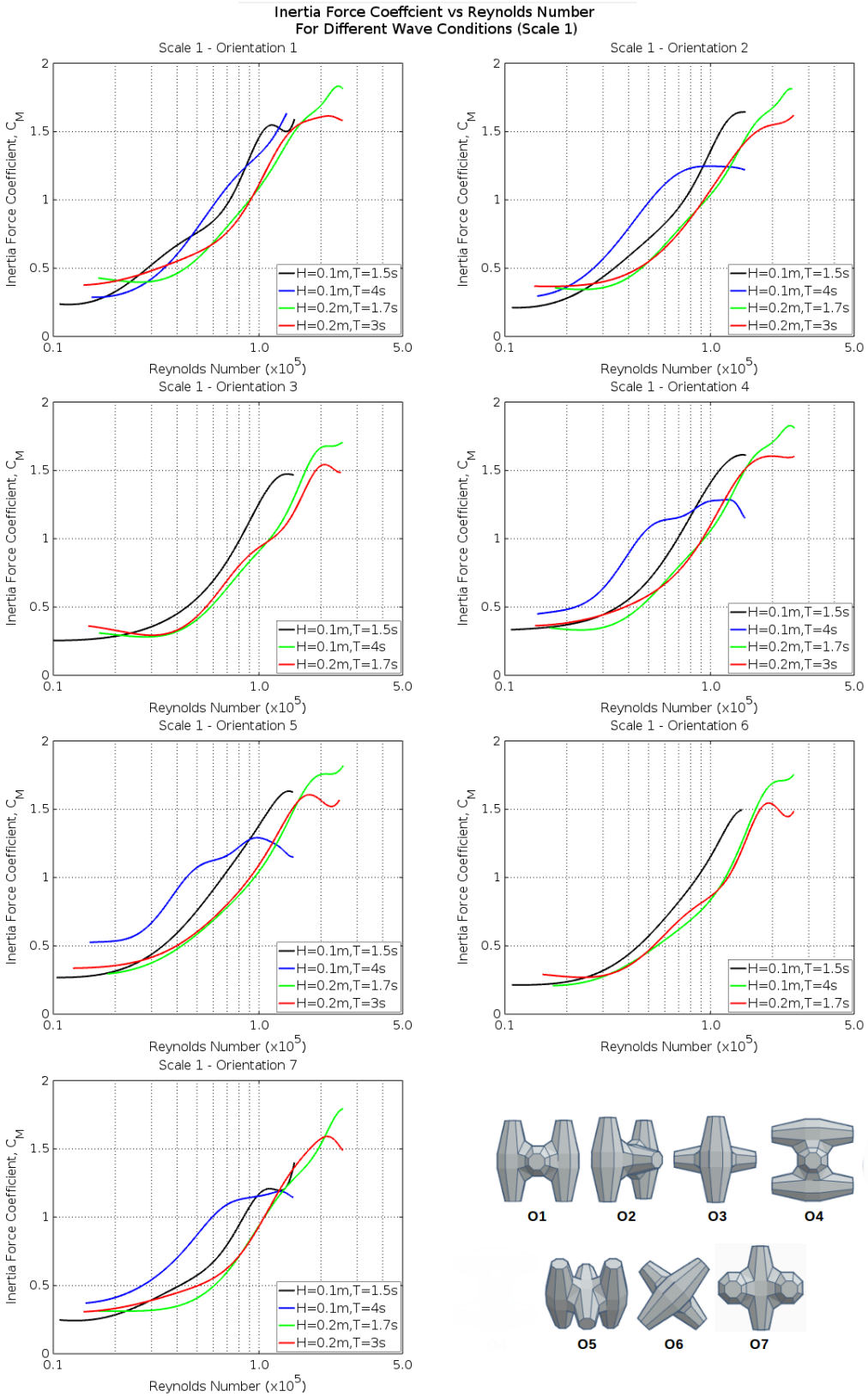

## B.6.5 Drag Coefficient vs. Reynolds Number for Different Wave Signals – Scale 2

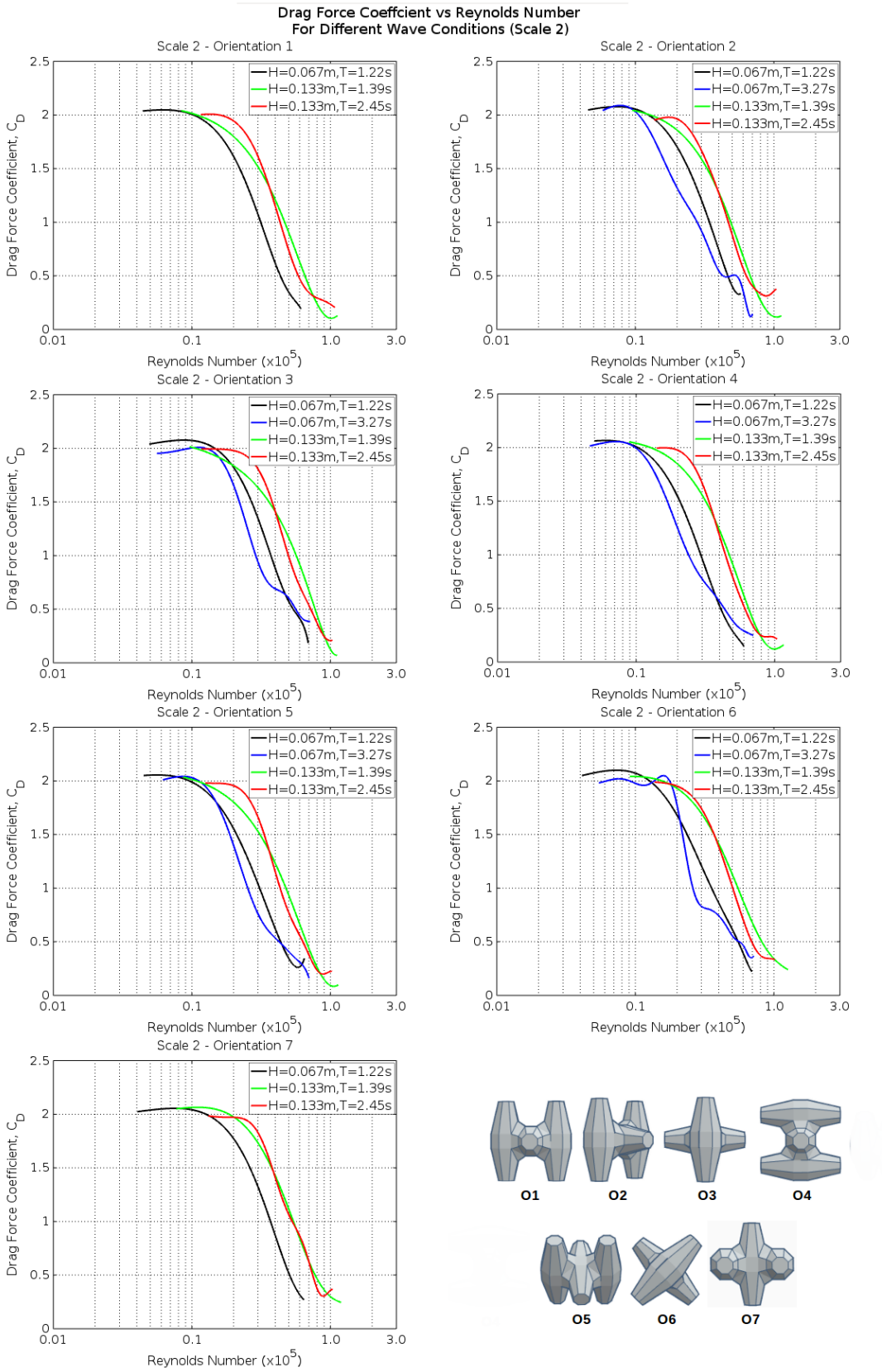

## B.6.6 Inertia Coefficient vs. Reynolds Number for Different Wave Signals – Scale 2

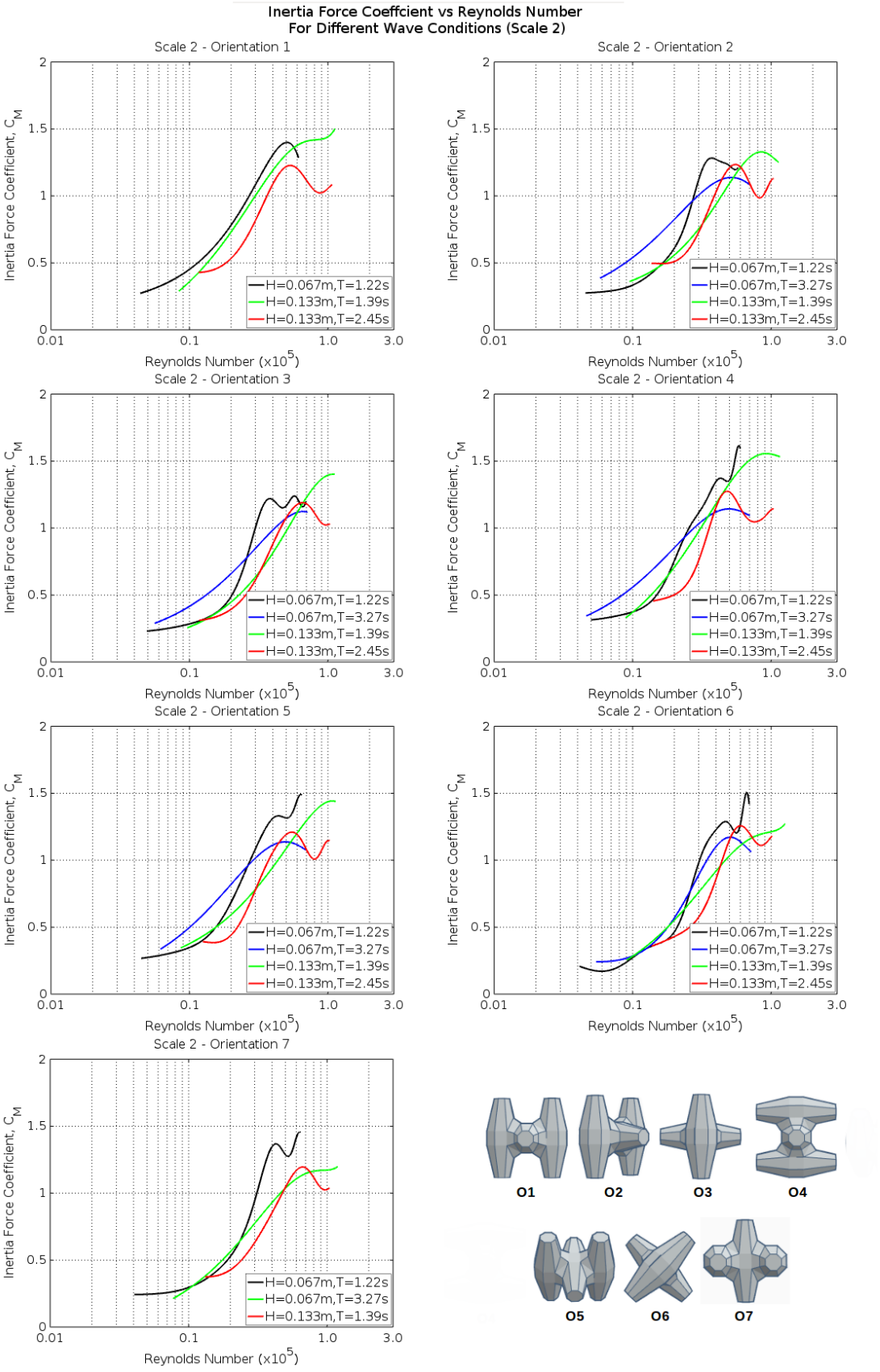

## B.7 Comparison Between Morison Equation and Experimental Results

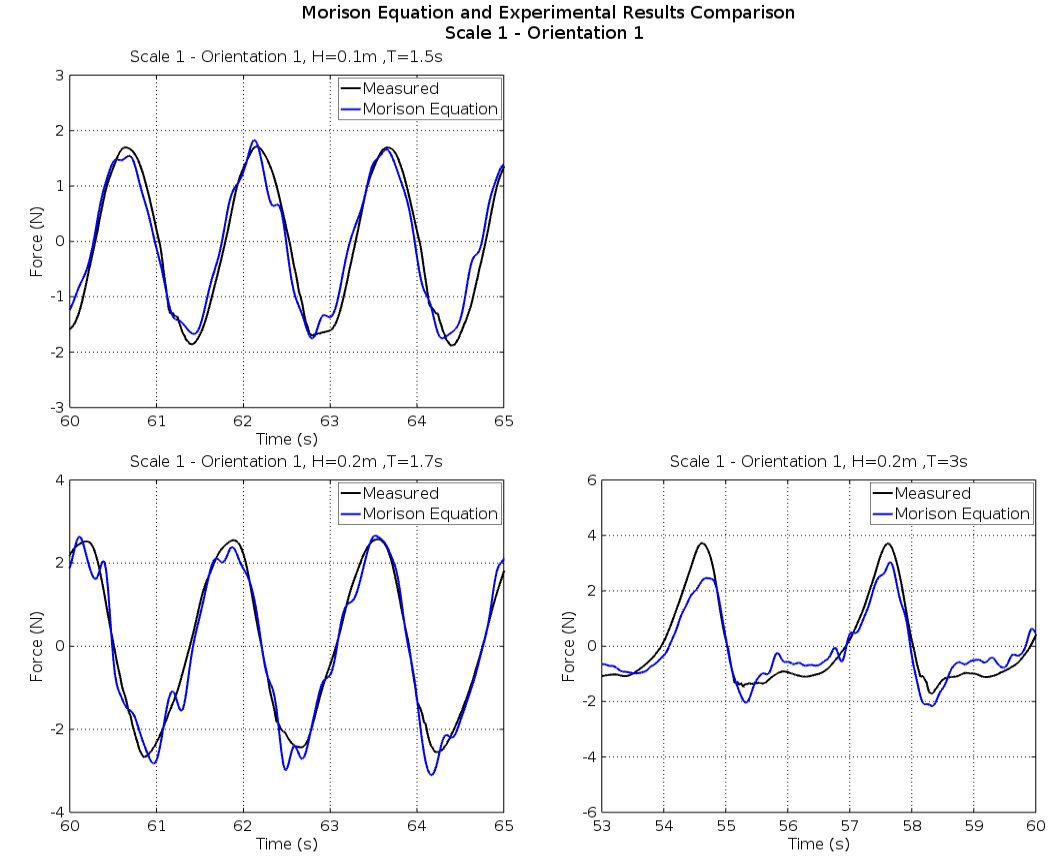


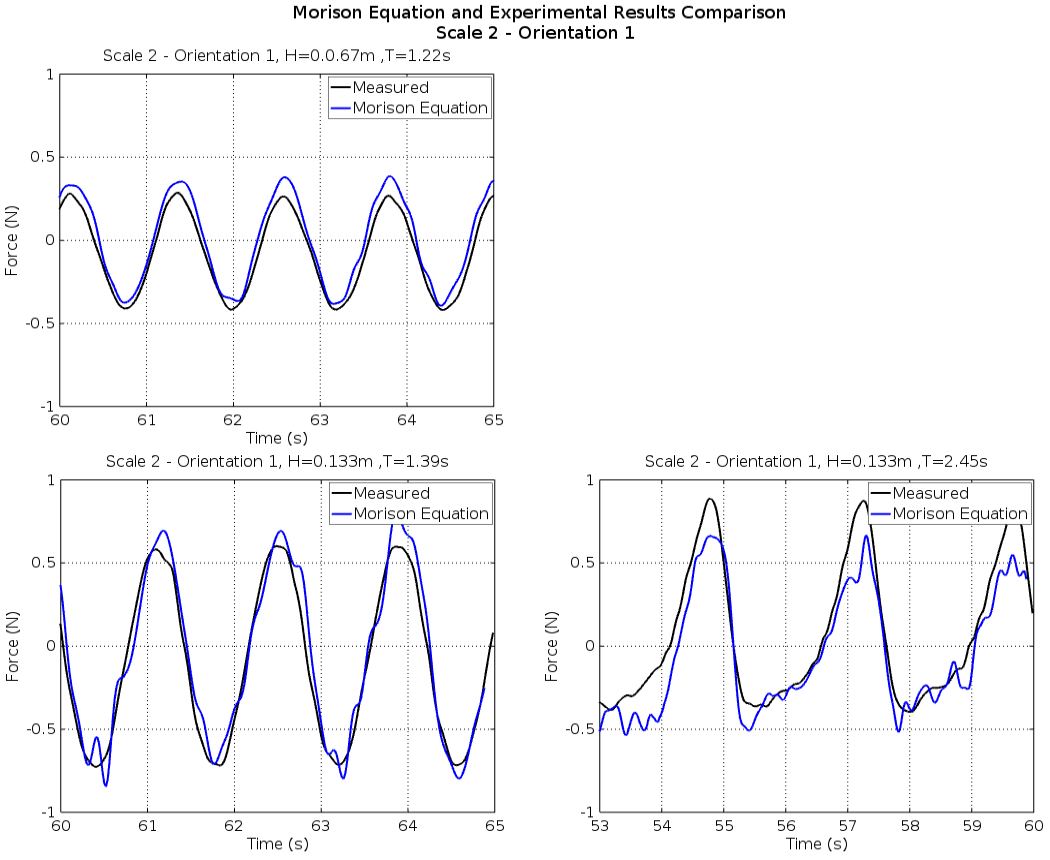


o2

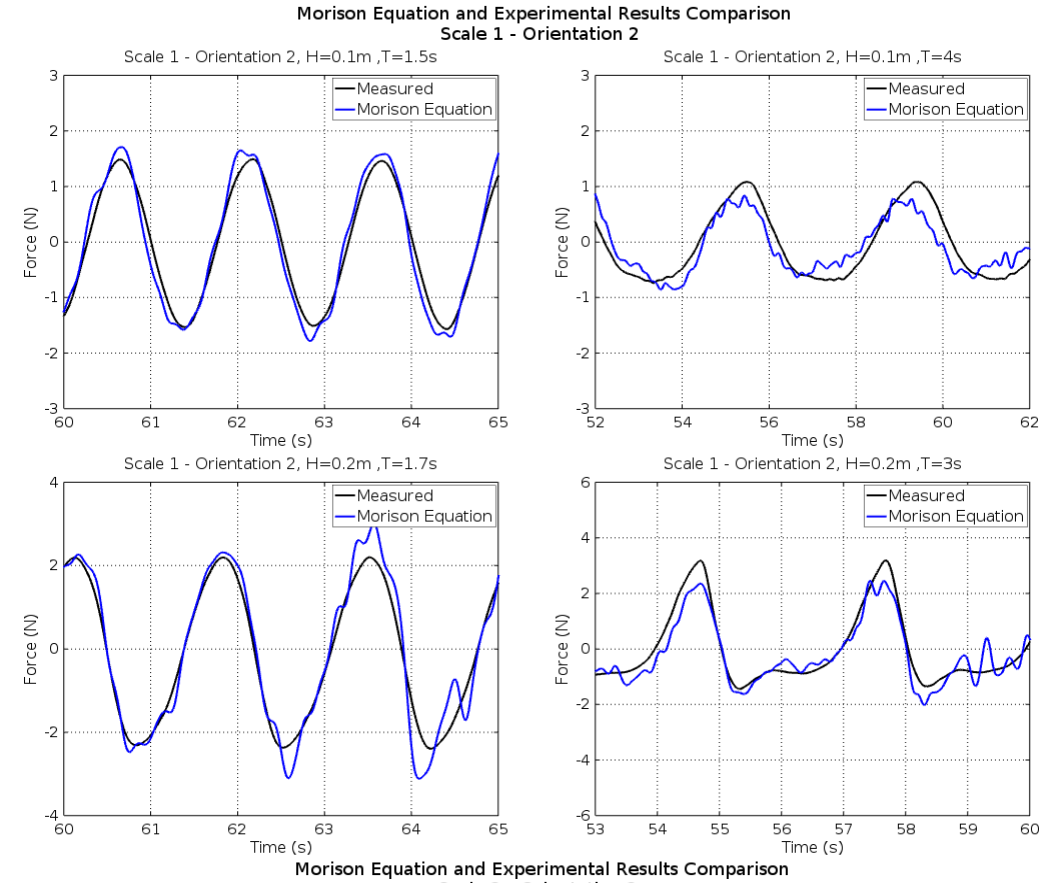
Morison Equation and Experimental Results Comparison
Scale 1 - Orientation 2
Scale 1 - Orientation 2, H=0.1m ,T=1.5s
Scale 1 - Orientation 2, H=0.1m ,T=4s
Scale 1 - Orientation 2, H=0.2m ,T=1.7s
Scale 1 - Orientation 2, H=0.2m ,T=3s
Measured
Morison Equation
Force (N)
Time (s)

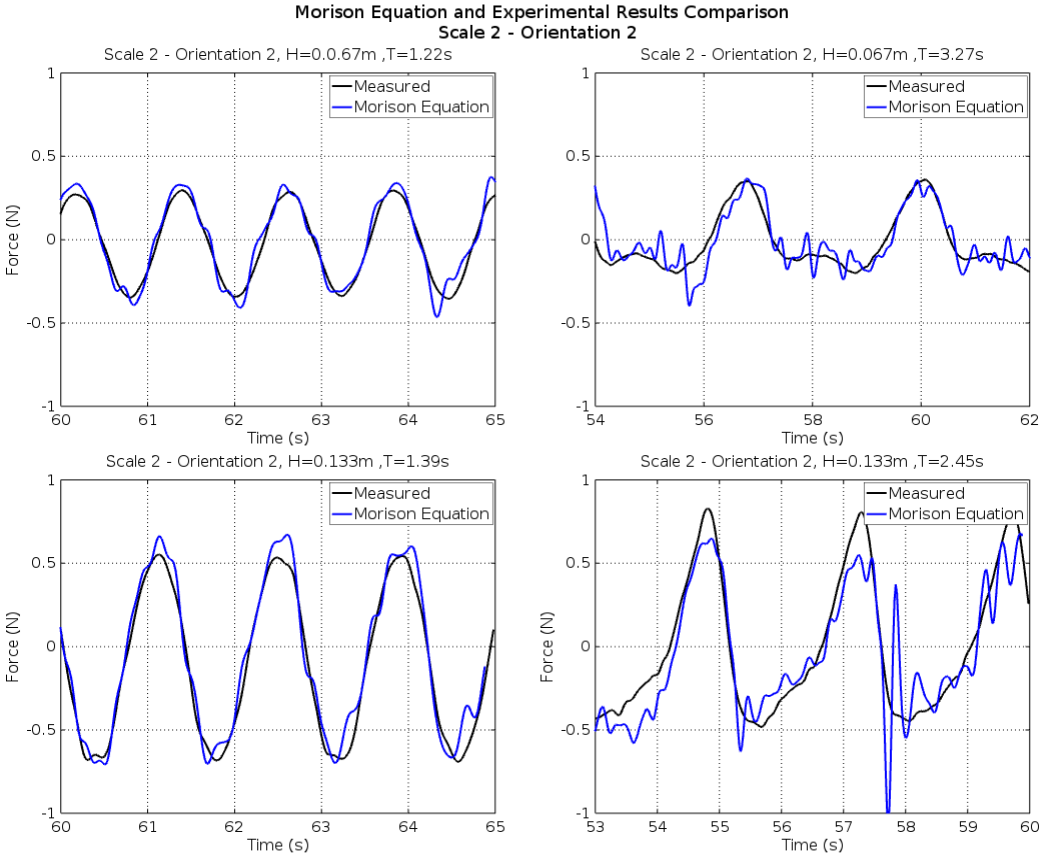
Morison Equation and Experimental Results Comparison
Scale 2 - Orientation 2
Scale 2 - Orientation 2, H=0.0.67m ,T=1.22s
Scale 2 - Orientation 2, H=0.067m ,T=3.27s
Scale 2 - Orientation 2, H=0.133m ,T=1.39s
Scale 2 - Orientation 2, H=0.133m ,T=2.45s
Measured
Morison Equation
Force (N)
Time (s)

o3

**Morison Equation and Experimental Results Comparison**
**Scale 1 - Orientation 3**

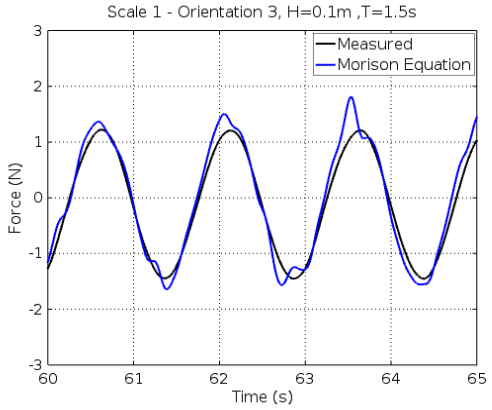


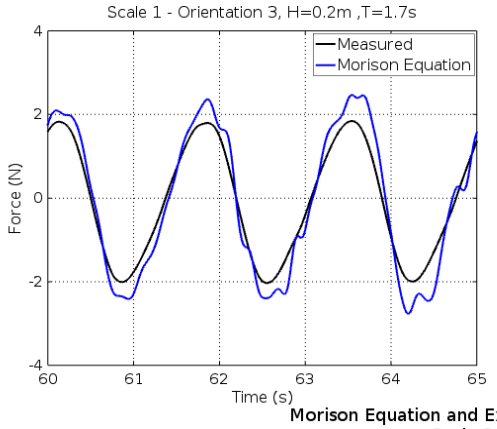


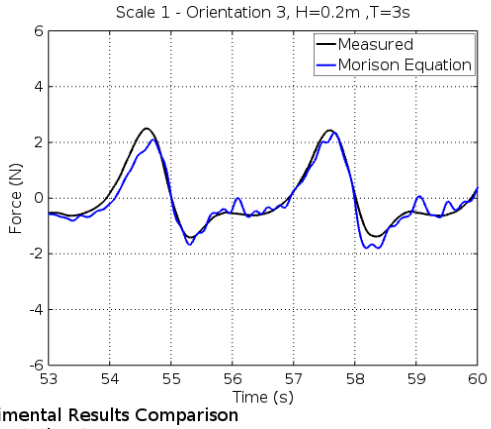


**Morison Equation and Experimental Results Comparison**
**Scale 2 - Orientation 3**

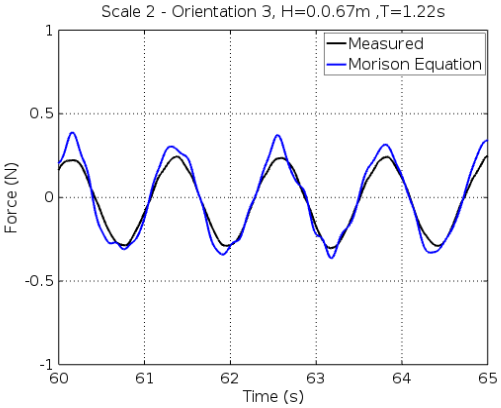


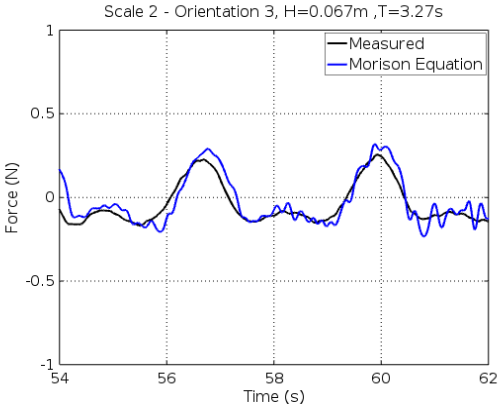


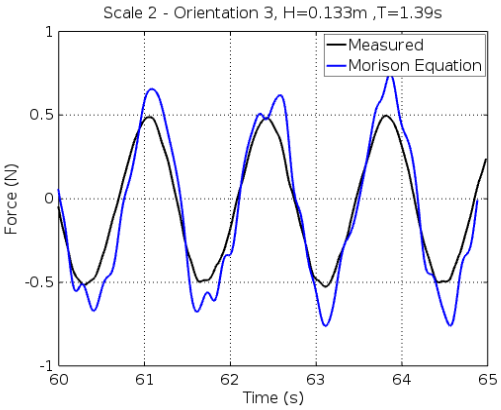


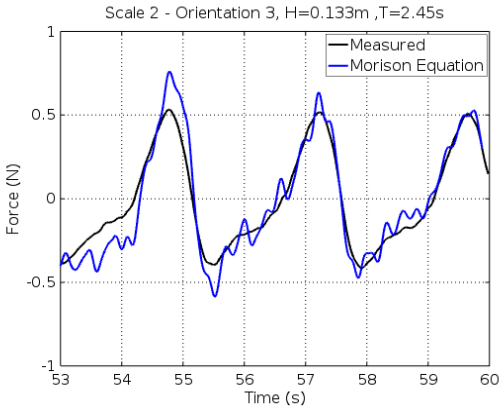


o4

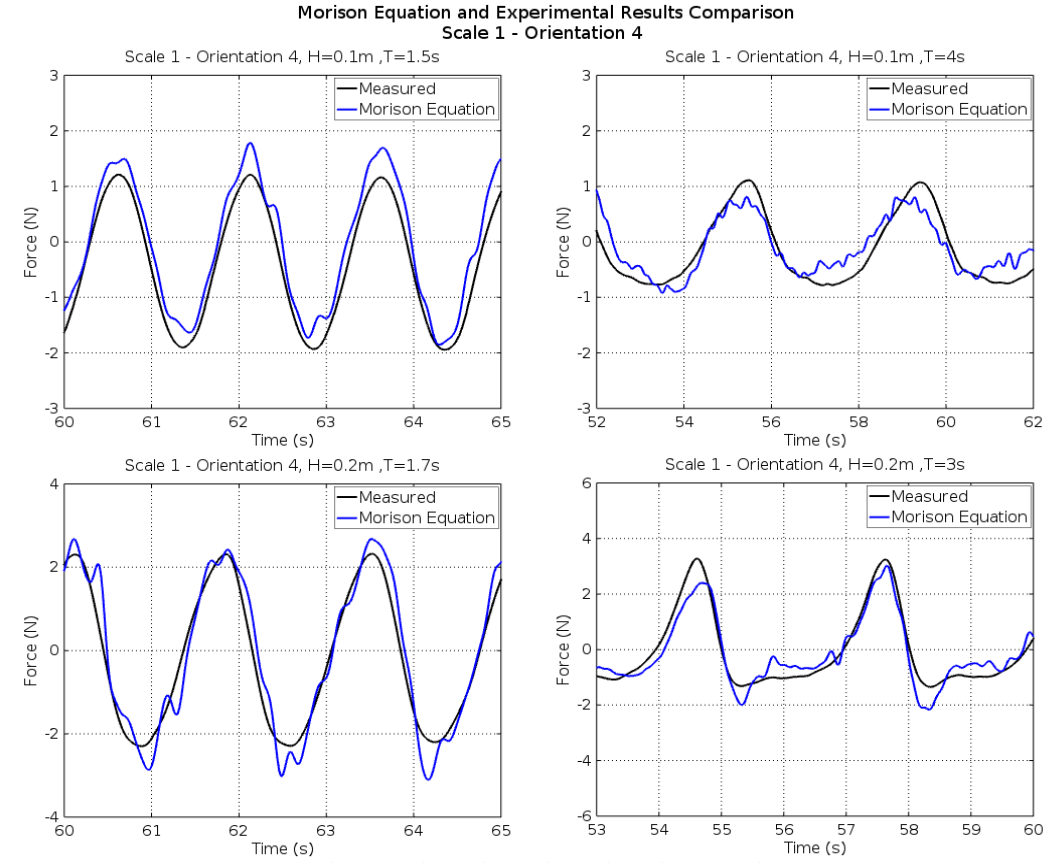
Morison Equation and Experimental Results Comparison
Scale 1 - Orientation 4
Scale 1 - Orientation 4, H=0.1m ,T=1.5s
Scale 1 - Orientation 4, H=0.1m ,T=4s
Scale 1 - Orientation 4, H=0.2m ,T=1.7s
Scale 1 - Orientation 4, H=0.2m ,T=3s
Measured
Morison Equation
Force (N)
Time (s)

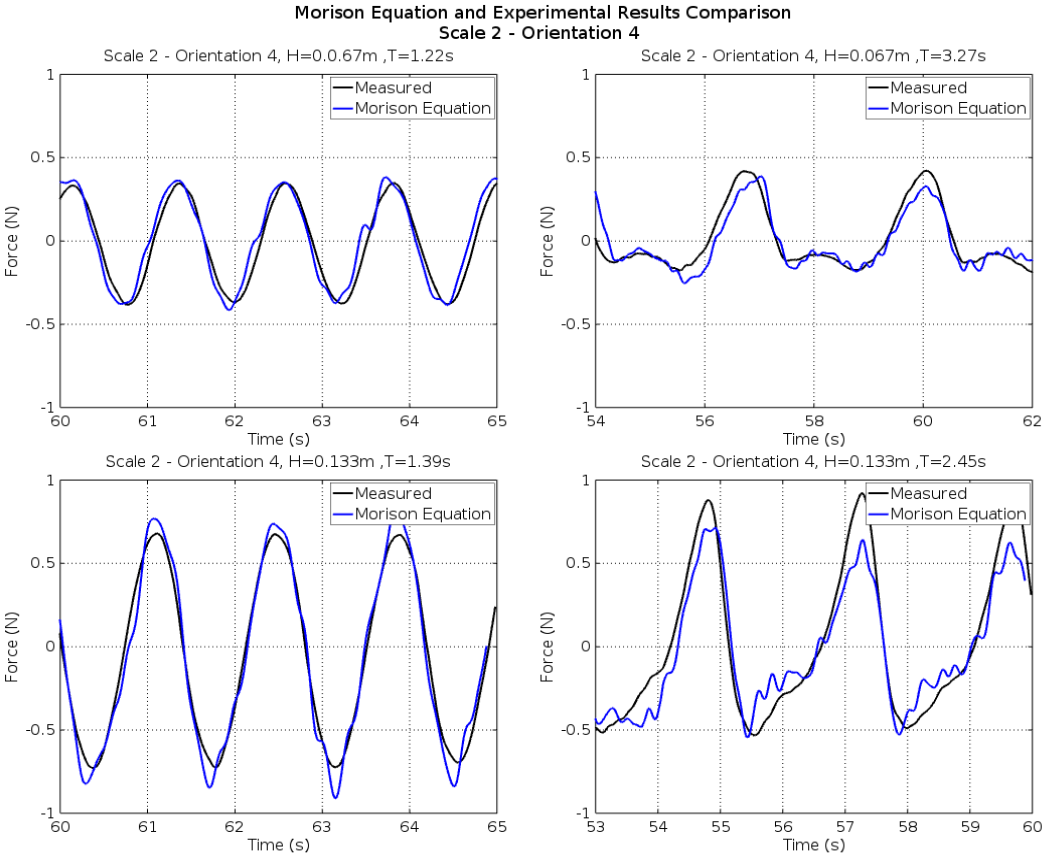
Morison Equation and Experimental Results Comparison
Scale 2 - Orientation 4
Scale 2 - Orientation 4, H=0.0.67m ,T=1.22s
Scale 2 - Orientation 4, H=0.067m ,T=3.27s
Scale 2 - Orientation 4, H=0.133m ,T=1.39s
Scale 2 - Orientation 4, H=0.133m ,T=2.45s
Measured
Morison Equation
Force (N)
Time (s)

o5

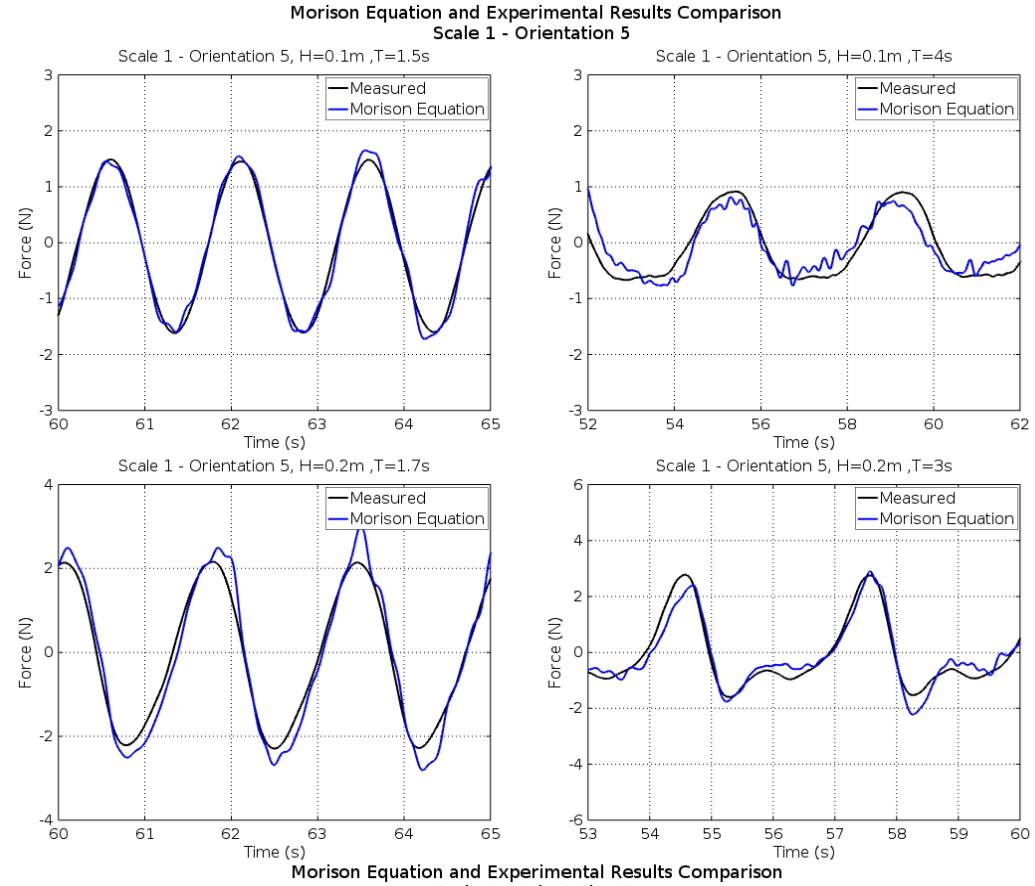
Morison Equation and Experimental Results Comparison
Scale 1 - Orientation 5
Scale 1 - Orientation 5, H=0.1m ,T=1.5s
Scale 1 - Orientation 5, H=0.1m ,T=4s
Scale 1 - Orientation 5, H=0.2m ,T=1.7s
Scale 1 - Orientation 5, H=0.2m ,T=3s
Measured
Morison Equation
Force (N)
Time (s)

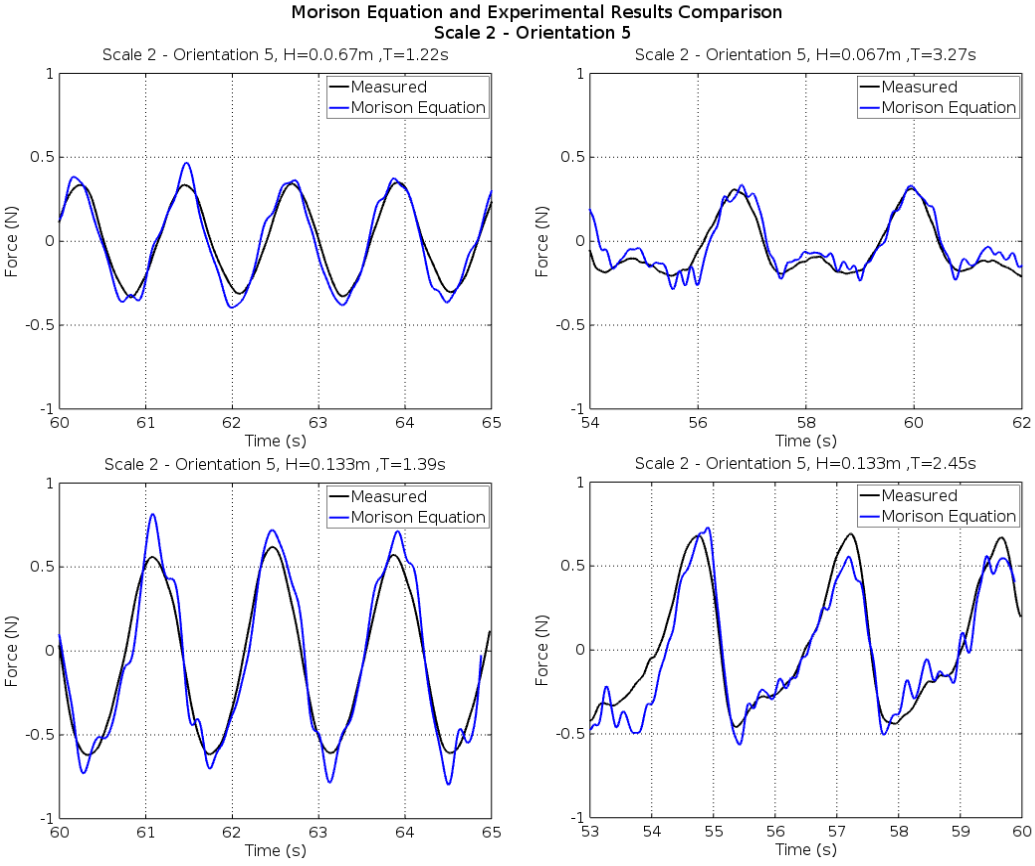
Morison Equation and Experimental Results Comparison
Scale 2 - Orientation 5
Scale 2 - Orientation 5, H=0.0.67m ,T=1.22s
Scale 2 - Orientation 5, H=0.067m ,T=3.27s
Scale 2 - Orientation 5, H=0.133m ,T=1.39s
Scale 2 - Orientation 5, H=0.133m ,T=2.45s
Measured
Morison Equation
Force (N)
Time (s)

o6

Morison Equation and Experimental Results Comparison
Scale 1 - Orientation 6

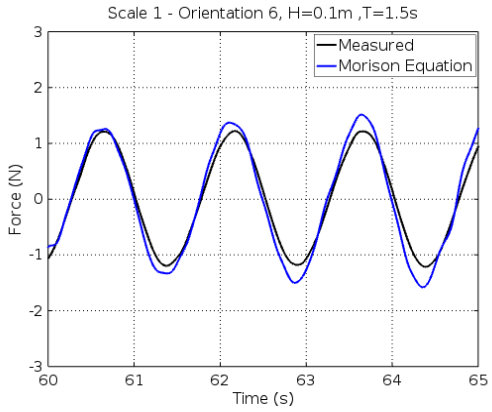


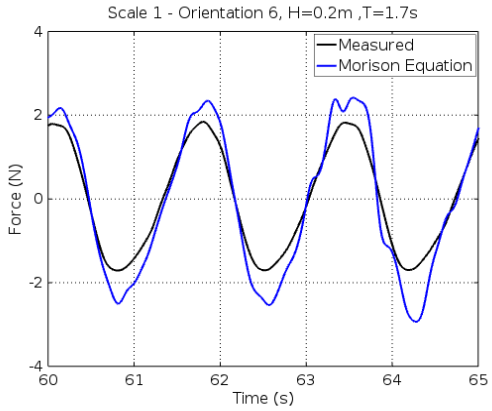


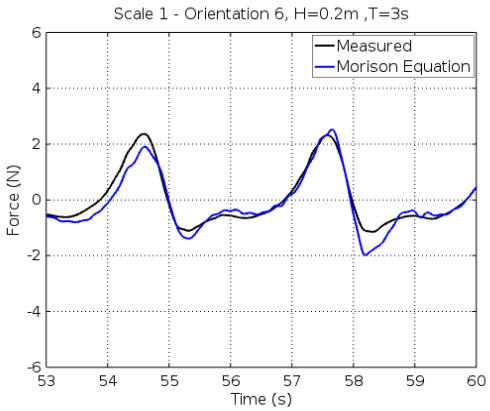


Morison Equation and Experimental Results Comparison
Scale 2 - Orientation 6

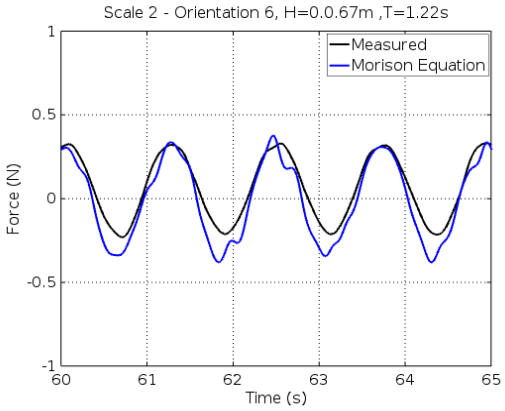


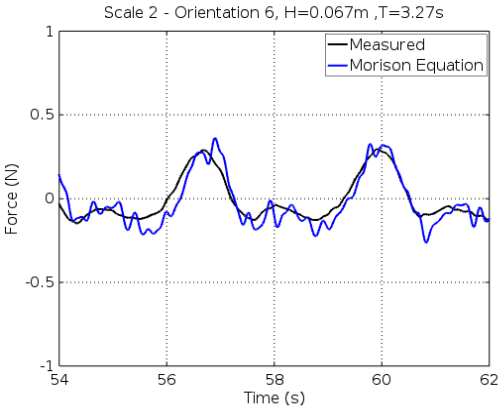


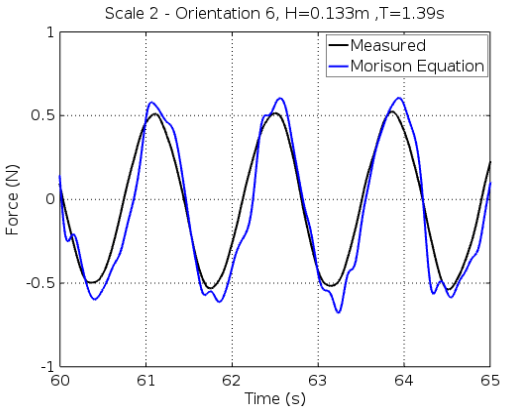


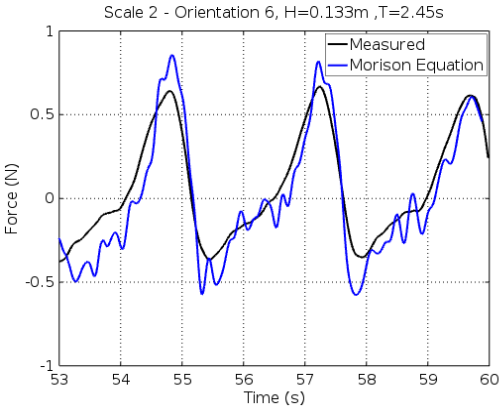


o7

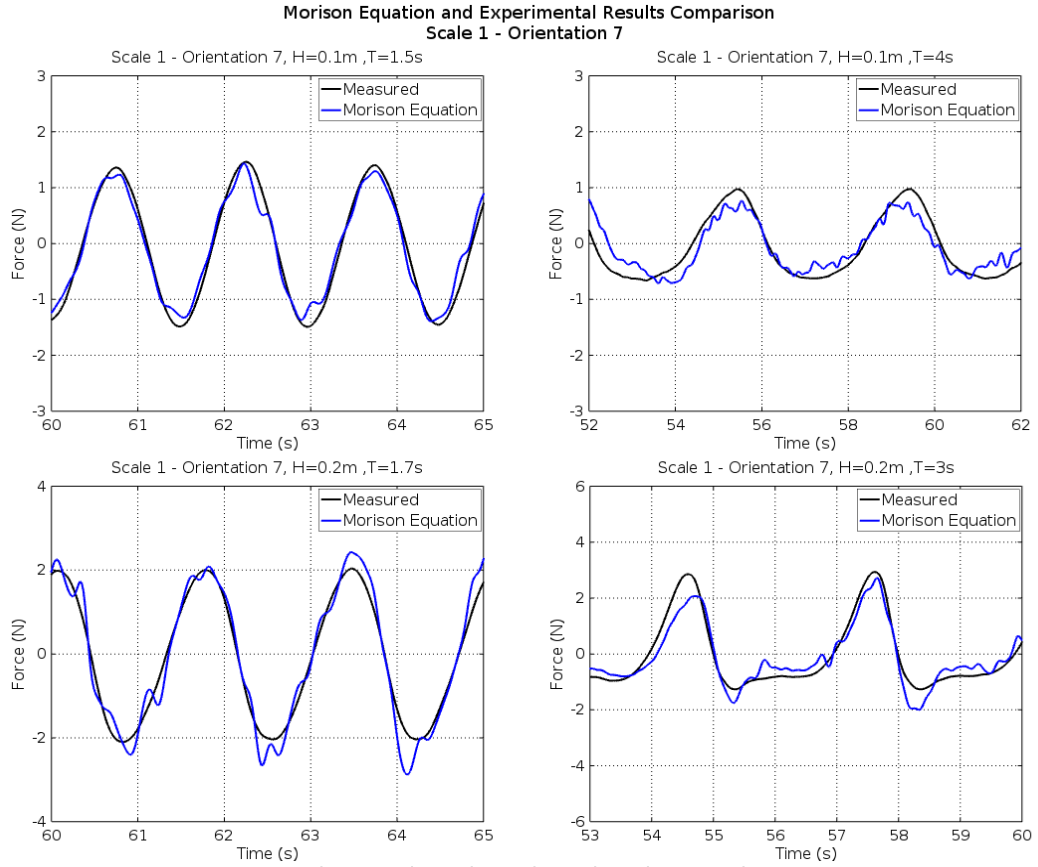
Morison Equation and Experimental Results Comparison
Scale 1 - Orientation 7
Scale 1 - Orientation 7, H=0.1m ,T=1.5s
Scale 1 - Orientation 7, H=0.1m ,T=4s
Scale 1 - Orientation 7, H=0.2m ,T=1.7s
Scale 1 - Orientation 7, H=0.2m ,T=3s
Measured
Morison Equation
Force (N)
Time (s)

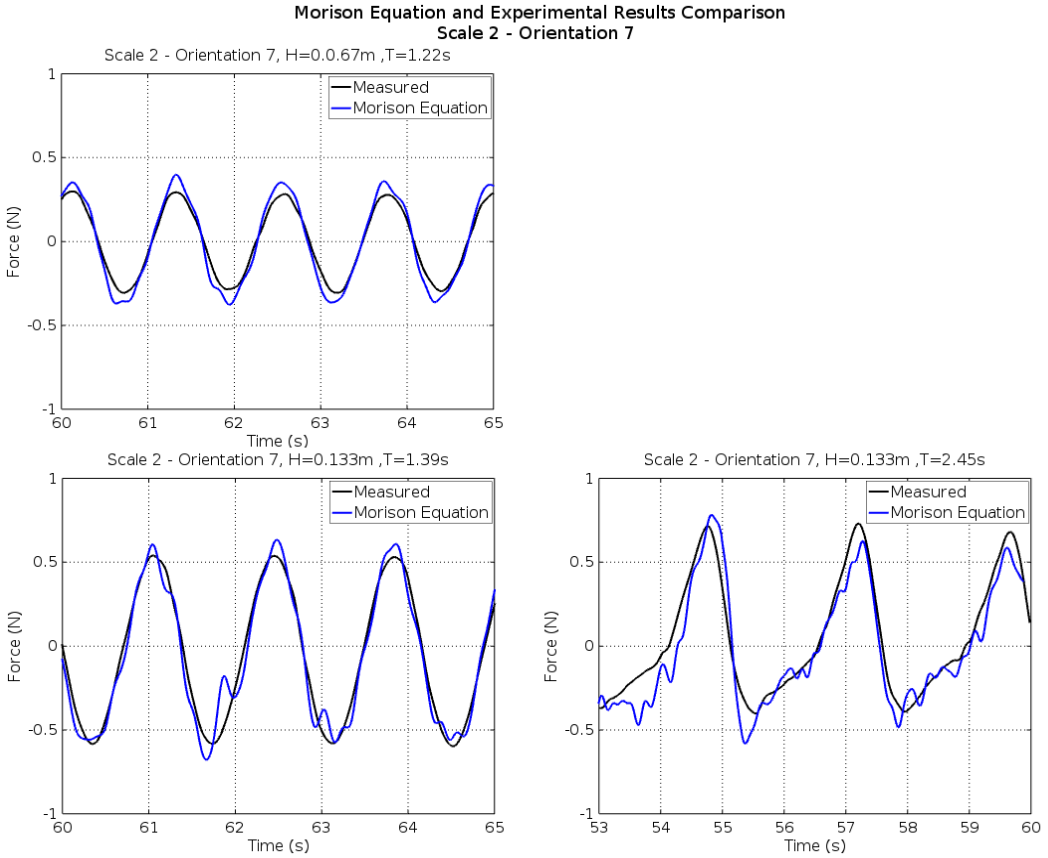
Morison Equation and Experimental Results Comparison
Scale 2 - Orientation 7
Scale 2 - Orientation 7, H=0.0.67m ,T=1.22s
Scale 2 - Orientation 7, H=0.133m ,T=1.39s
Scale 2 - Orientation 7, H=0.133m ,T=2.45s
Measured
Morison Equation
Force (N)
Time (s)